Percolation and Homogenization Theories for Heterogeneous Materials

by

Ying Chen

B.S., Materials Science and Engineering
Tsinghua University, 2004

SUBMITTED TO THE DEPARTMENT OF MATERIALS SCIENCE AND ENGINEERING
IN PARTIAL FULFILLMENT OF THE REQUIREMENTS FOR THE DEGREE OF

DOCTOR OF PHILOSOPHY IN EMERGING, FUNDAMENTAL, AND COMPUTATIONAL STUDIES IN MATERIALS SCIENCE
AT THE
MASSACHUSETTS INSTITUTE OF TECHNOLOGY

JUNE 2008

MASSACHUSETTS INSTITUTE OF TECHNOLOGY
JUN 16 2008
LIBRARIES

© 2008 Massachusetts Institute of Technology. All rights reserved.

ARCHIVES

Signature of Author: _____
Department of Materials Science and Engineering
May 23, 2008

Certified by: _____
Christopher A. Schuh
Danae and Vasilios Salapatas Associate Professor of Metallurgy
Thesis Supervisor

Accepted by: _____
Samuel M. Allen
POSCO Professor of Physical Metallurgy
Chair, Departmental Committee on Graduate Students

Percolation and Homogenization Theories for Heterogeneous Materials

by

Ying Chen

Submitted to the Department of Materials Science and Engineering
on May 23, 2008 in Partial Fulfillment of the Requirements for the Degree of
Doctor of Philosophy in Emerging, Fundamental, and Computational Studies in Materials Science

ABSTRACT

Most materials produced by Nature and by human beings are heterogeneous. They contain domains of different states, structures, compositions, or material phases. How these different domains are distributed in space, or in other words, how they connect to one another, determines their macroscopic properties to a large degree, making the simple rule-of-mixtures ineffective in most cases. This thesis studies the macroscopic effective diffusion, diffusional creep, and elastic properties of heterogeneous grain boundary networks and composite solids, both theoretically and numerically, and explores the microstructure-property correlations focusing on the effects of microstructural connectivity (topology). We have found that the effects of connectivity can be effectively captured by a percolation threshold, a case-specific volume fraction at which the macroscopic effective property undergoes a critical transition, and a set of critical scaling exponents, which also reflect the universality class that the property belongs to. Using these percolation quantities together with the generalized effective medium theory, we are able to directly predict the effective diffusivity and effective diffusional creep viscosity of heterogeneous grain boundary networks to a fairly accurate degree. Diffusion in composite solids exhibits different percolation threshold and scaling behaviors due to interconnectivity at both edges and corners. Continuum elasticity suffers from this complexity as well, in addition to the complicating factor that each phase is always characterized by several independent elastic constants. These issues are each addressed in detail. In addition to studying all the above properties for a random distribution of grain boundaries or phases, we have also studied the effects of correlations in spatial distributions. This topic is especially important in materials science, because virtually no materials exhibit random phase distributions. We have examined the percolation of effective properties for correlated microstructures spanning between the random distribution and the perfectly periodic distribution. An important result of this work is new understanding about what correlations may be considered small, or inconsequential, to the percolation scaling behavior, and which are large or long-range, and lead to a loss of universality. Finally, a rigorous, and easy-to-use, analytical homogenization method is developed for periodic composite materials.

Thesis Supervisor: Christopher A. Schuh
Title: Danae and Vasilios Salapatas Associate Professor of Metallurgy

Acknowledgments

First of all, I would like to thank my thesis advisor, Christopher A. Schuh. In addition to being a knowledgeable and insightful researcher, Chris is also an excellent advisor and friend with whom I have shared so much joy of research (as well as ). It is really rewarding to see someone excited about some research I did, and even more so to have many enlightening conversations with someone who is similarly enthusiastic and ambitious in science as I am. I was very eager to do good research when I entered MIT, and thanks to Chris, I now still have a strong desire to make a difference in a few materials science fields. Working with Chris makes me a lucky graduate student.

I also want to thank my thesis committee members, Professor Samuel M. Allen and Professor W. Craig Carter, for their encouragements and advices both before and after becoming members of my thesis committee. They have offered a lot of useful suggestions on my thesis. They are just nice people to talk to whenever there is a chance.

I am very grateful for the education I received from MIT. It is not necessarily all about knowledge, but more about the people here, the exhaustive resources, the inspirations, and most importantly, what have happened to me. Four years ago the scientific world was very mysterious to me. It is incredible for me now to start discovering and working on cutting-edge research problems. I am becoming a scientist!

I dedicate this thesis to my family. My dad, Weiping Chen, and my mom, Demei Wang, have been caring for and supporting me throughout my life. They have paid tremendous attention to my study and have worked very hard to ensure I can pursue my dream without any worries. I cannot be who I am today without them. My younger sister, Li Chen, has also been a good friend and a big support for me.

I wish to thank all of my friends for their endless support. There are many ups and downs in my life in the past few years. My dear friends have helped me through some extremely difficult times. Things change over time, but I know friendship never does.

Finally, I want to thank all of our past and present group members. Everyone in the group is very nice. I have had a wonderful time working in the group. I particularly want to thank Megan Frary, Vee, Alan Lund, and Andrew Detor for helping me get started with the research in my first year. I also want to thank Corinne Packard, Jason Trelewicz, Shiyun Ruan, Jeremy Mason, Eric Homer, Tiffany Ziebell, and Tim Rupert for all the help and the many pleasant conversations.

Contents

List of Tables

Chapter 1. Introduction

1.1. Effective Properties of Heterogeneous Materials

We rarely see a perfectly homogeneous material in nature, one that appears the same everywhere on any length scale above the molecular dimensions. Most often a material is heterogeneous, or in other words, disordered in some way. Heterogeneous materials contain domains of different material phases, compositions, or states on one length scale* or on multiple length scales. Common examples of heterogeneous materials include bones, which are made of mineral crystals and collagen fibers and are hierarchical structures extending across many length scales, wood, polycrystalline materials with grains of different orientations, fiber-reinforced or particulate composite materials, porous and cellular materials, concrete, and many others. Even some seemingly uniform materials can have local fluctuations in their densities or compositions, making them dynamically heterogeneous [1].

The macroscopic properties of heterogeneous materials are seldom the averages of their constituent properties over volume. For example, consider a two-phase composite material with phase fractions p_1 and p_2, and phase properties K_1 and K_2, respectively. The effective property of the composite material, K_{eff}, is only equal to $p_1K_1 + p_2K_2$ in some rare cases, and more often is much lower than $p_1K_1 + p_2K_2$ because of the specific spatial distribution of the two phases. K_{eff} depends on both the *geometry*, the shape and size of individual particles, and the *topology*, the connectivity among individual particles [2]. An understanding of the effects of both the phase geometry and the topology, on the one hand, can allow predictions of the macroscopic properties of materials with known microstructural arrangements, and on the other hand, can provide guidance for microstructure design to aim for optimal materials performance.

While efforts have been made to understand the geometric effects for over a century, the role of topology in materials properties has only started to be addressed quantitatively in the most recent few decades. This is because it is difficult to take into account or predict the effects of connectivity rigorously. A critical transition named the *percolation transition* [3] (which I will elaborate on in section 1.3) makes it difficult to directly generalize the solution for a simple system containing just one second-phase particle to the solution for heterogeneous media containing many overlapping or touching particles. The analytical solutions for the effective properties available today are mostly based on the mean field theory and are generally referred to as *homogenization theories* [1, 4-6]. These models are becoming more and more sophisticated because many higher-order terms are needed in order to accurately capture microstructural information. Unfortunately, coefficients for higher-order terms are difficult to calculate, and even if possible, there is no guarantee that a limited number of terms can properly capture the key microstructural information—the connectivity. The good news, though, is that percolation theory as a statistical tool to describe the topology of heterogeneous systems has been well developed in different

* In this thesis, all length scales are above the molecular dimensions so that the materials or phases can be described with macroscopic parameters.

fields of physics. The ultimate solution might be to incorporate percolation theory into traditional homogenization theories, or the other way around. More communication between the two fields could possibly lead to the next-generation topology-sensitive homogenization theories.

The field could have also benefited from more communication among communities working on different effective properties. Although it has been recognized for a long time that formulations for a variety of transport processes are mathematically analogous, advances in understanding one effective property have not always been noticed or appreciated by researchers concerned with other analogous properties. Some common analogous properties [2, 7] are listed in Table 1. For example, for the same microstructure, the determination of effective thermal conductivity can be directly translated into the derivation for effective mass diffusivity. The elastic properties have not been included in Table 1 because the effective stiffness matrix is a fourth-rank tensor, different from the second-rank effective tensors presented in Table 1.

Table 1. Steady-state effective transport properties which are mathematically analogous.

Average Flux =	Effective Property •	Average Field
Electric Current	Electrical Conductivity	Electric Field (Electric Potential Gradient)
Heat Flux	Thermal Conductivity	Temperature Gradient
Mass Flux	Mass Diffusivity	Concentration Gradient
Magnetic Induction	Magnetic Permeability	Magnetic Field
Electric Displacement	Dielectric Constant	Electric Field

Next, a brief review of some of the most widely used homogenization and percolation theories will be given in the context of diffusion and effective diffusivities of heterogeneous materials, followed by discussions of some challenges for predicting effective properties of real, complicated microstructures. At the end, the objectives of our work, together with an overview of this thesis, will be provided.

1.2. Classical Homogenization Theories

When the material size is much larger than the length scales of the inhomogeneities, the heterogeneous material can generally be treated as a homogeneous one with effective properties. In other words, the material is macroscopically homogeneous and its effective properties are independent of the sample size. The process of deriving the effective properties for heterogeneous materials is usually termed *homogenization* [1, 2, 8], which is schematically shown in Figure 1.

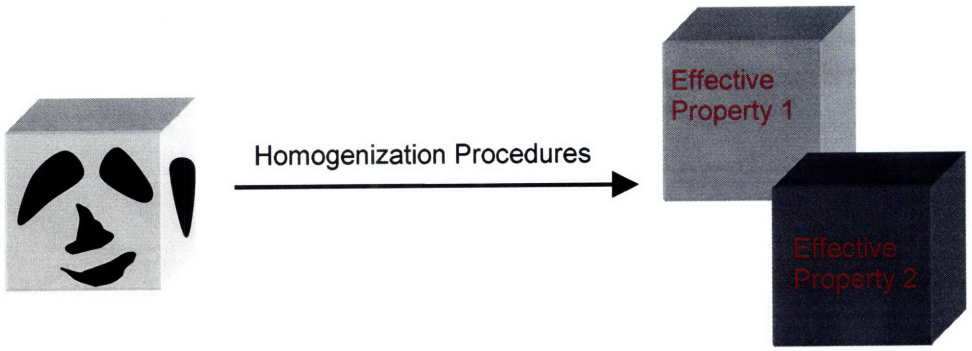

Figure 1. The goal of homogenization theories is to derive the effective properties for heterogeneous materials so that the material can be viewed as homogeneous on the macroscopic scale for the property of interest. The effective properties (in gray on the right) are usually bounded by the properties of individual phases (white and black on the left). The specific value for one effective property (the gray level on the right) could be different from one another, e.g., for some properties the material may behave more like the white phase and for other properties it could behave more like the black phase.

1.2.1. Upper and Lower Bounds

There are certain geometric arrangements among the phases for which the effective properties are exactly solvable. Take diffusion for example. When the phases are arranged in parallel, the effective diffusivity of the composite material is simply the linear or harmonic average of individual phase diffusivities when the diffusional flux is parallel or perpendicular to the phase alignment, respectively (see Figure 2(a) and (b) and the corresponding equations Eqs. (1) and (2)). When the composite material comprises of one concentric-shell structure with one phase coating the other or many such coated-spheres of different sizes to fill the space, the effective diffusivity can be accurately described by the Hashin-Shtrikman (HS) equation [9, 10] (see Figure 2(c) and (d) and the corresponding equations Eqs. (3) and (4)).

The geometries shown in Figure 2 are only extreme cases for all possible phase arrangements. For example, one phase either always connects to opposite sides of the sample at all phase fractions, while the other phase never does. The above equations (Eq. (1) to (4)) thus turn out to be bounds on effective properties of heterogeneous materials of general microgeometries. The linear and harmonic average in Eq. (1) and (2) correspond to the upper and lower Wiener bounds [11], respectively. Eq. (3) and (4) were derived by Hashin and Shtrikman [9] using variational principles and are upper and lower bounds for effective diffusivities for any two-phase isotropic composite materials. The Hashin-Shtrikman (HS) bounds are more restrictive and tighter than the Wiener bounds because they require isotropy. But the differences between the two types of bounds are only significant when the phase contrast ratio (D_2/D_1) is very low (Figure 3(a)). When the phase contrast ratio is high, the upper and lower Wiener bounds and HS bounds are similarly far apart and thus do not provide useful information about possible values of the effective diffusivities (Figure 3(b)).

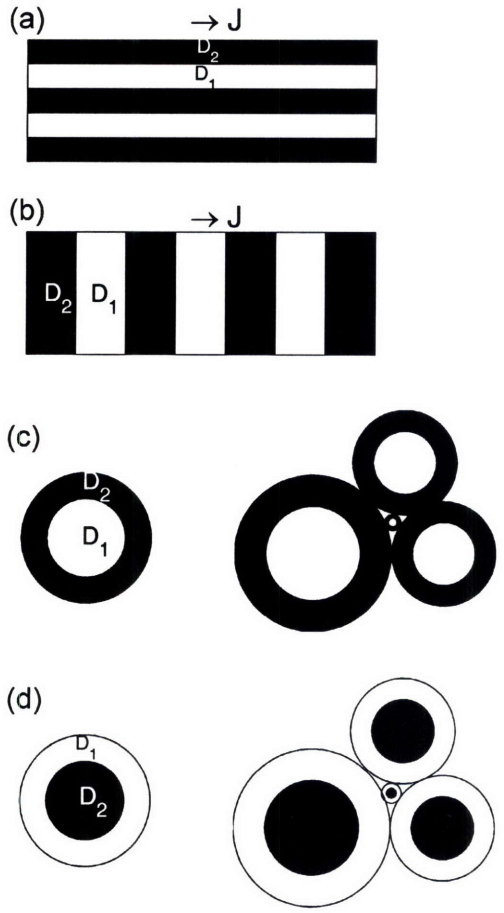

$$D_{eff}(\|) = (1-p)D_1 + pD_2 \tag{1}$$

$$D_{eff}(\perp) = \frac{1}{\frac{1-p}{D_1} + \frac{p}{D_2}} \tag{2}$$

$$D_{eff}(HS^+) = D_2 + \frac{1-p}{\frac{1}{D_1 - D_2} + \frac{p}{dD_2}} \tag{3}$$

$$D_{eff}(HS^-) = D_1 + \frac{p}{\frac{1}{D_2 - D_1} + \frac{1-p}{dD_1}} \tag{4}$$

Figure 2. Examples of some simple geometries for which the effective diffusivities can be solved exactly. The exact equations are written on the right side of the corresponding geometries. p is the fraction of the phase with diffusivity D_2 and d is the dimensionality.

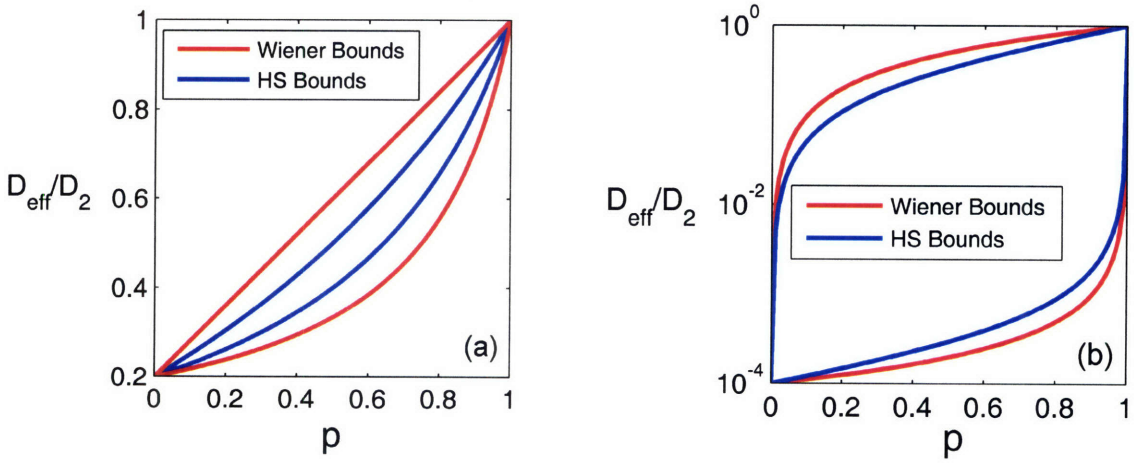

Figure 3. Wiener and Hashin-Shtrikman (HS) upper and lower bounds for composite materials of phase 1 and 2 with $D_2/D_1 = 5$ in (a) and $D_2/D_1 = 10^4$ in (b) in two dimensions. p is the fraction of phase 2.

There are also a lot of works attempting to tighten the Wiener bounds for anisotropic materials and the HS bounds for isotropic materials by including higher-order terms [12-16]. These terms are rather difficult to calculate. Even if it is possible to calculate them for certain microstructures, they are only minor modifications and do not much narrow down the orders-of-magnitude difference between the upper and lower bounds when the phase contrast ratio is high (such as in Figure 3(b)). Therefore, various types of bounds are in general not very useful for composite materials with high contrast in the phase properties. It is for this reason the so-called effective medium theories are also widely used, as will be described in the next section.

1.2.2. Effective Medium Theories

Various Effective Medium Theories (EMT) [17, 18] for estimating effective properties of two or multi-component composite materials are based on the exact solution for one single spherical or ellipsoidal inclusion embedded in an infinite medium [19]. For example, consider placing a sphere of radius r_0 with diffusivity D_2 into an infinite matrix with diffusivity D_1 in a uniform concentration gradient ∇C. The induced perturbation in the concentration field outside the sphere, ΔC, is

$$\Delta C(r) = -\frac{D_2 - D_1}{D_2 + (d-1)D_1}\left(\frac{r_0}{r}\right)^d C(r) \tag{5}$$

where r is the distance from the center of the sphere and d is the dimensionality. So $d = 3$ for the present case of a spherical inclusion in a three-dimensional matrix. Eq. (5) with $d = 2$ applies to a circular disk embedded in a two-dimensional matrix.

There are two fundamental types of effective medium theories. The first is the asymmetric effective medium theory derived from a composite material containing dilute spherical particles. Suppose the composite itself is a large sphere of radius R_0 containing a matrix material with diffusivity D_1 and dilute spherical particles with diffusivity D_2. Now insert the whole composite sphere into an infinite medium of the matrix material with diffusivity D_1 in a uniform concentration gradient ∇C (see Figure 4(a)). If we assume the small spherical particles are sufficiently dilute that there are not any interactions among the fields of these particles, then the total induced perturbation due to the presence of these particles is

$$\Delta C(r) = -p\frac{D_2 - D_1}{D_2 + (d-1)D_1}\left(\frac{R_0}{r}\right)^d C(r) \tag{6}$$

where p is the volume fraction of the inclusion particles in the composite sphere and r is the distance from the large composite sphere. Alternatively, we may neglect the microstructural details inside the large composite sphere and simply consider it as a homogeneous sphere with effective diffusivity D_{eff} (see Figure 4(b)), and then the perturbation in the concentration field should be

$$\Delta C(r) = -\frac{D_{eff} - D_1}{D_{eff} + (d-1)D_1}\left(\frac{R_0}{r}\right)^d C(r) \tag{7}$$

Eq. (6) and Eq. (7) should be equivalent, requiring

$$\frac{D_{eff} - D_1}{D_{eff} + (d-1)D_1} = p\frac{D_2 - D_1}{D_2 + (d-1)D_1} \tag{8}$$

Note that Eq. (6) results from a simple superposition of the individual perturbation fields of each spherical particle, so there is no requirement on the size distribution of these particles. For the same volume fraction p, a uniform or nonuniform size distribution of the particles will result in the same perturbation field in Eq. (6). The final equation for calculating the effective diffusivity, Eq. (8), thus applies to composite materials containing dilute spherical inclusions regardless of their size distribution. Eq. (8) is usually referred to as the asymmetric effective medium equation or the Maxwell-Garnett equation [20]. Interestingly, Eq. (8) coincides with the Hashin-Shtrikman equation (Eq. (4)), so it is basically the lower HS bound when $D_2 > D_1$ and the upper HS bound otherwise. This coincidence can be easily understood from the composite geometry shown in Figure 2(d) for which Eq. (4) is exact. If we neglect the thin black lines which are represented merely to show the coated sphere geometry, Figure 2(d) is simply a dispersion of spherical inclusions, equivalent to the composite geometry shown in Figure 4(a).

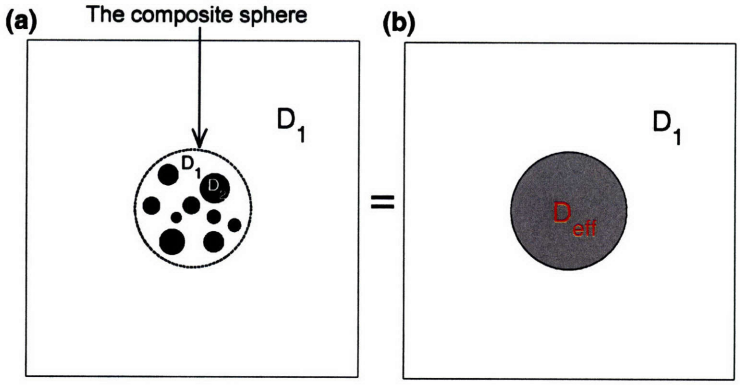

Figure 4. Illustration of the composite geometries used to derive the *asymmetric* effective medium theory.

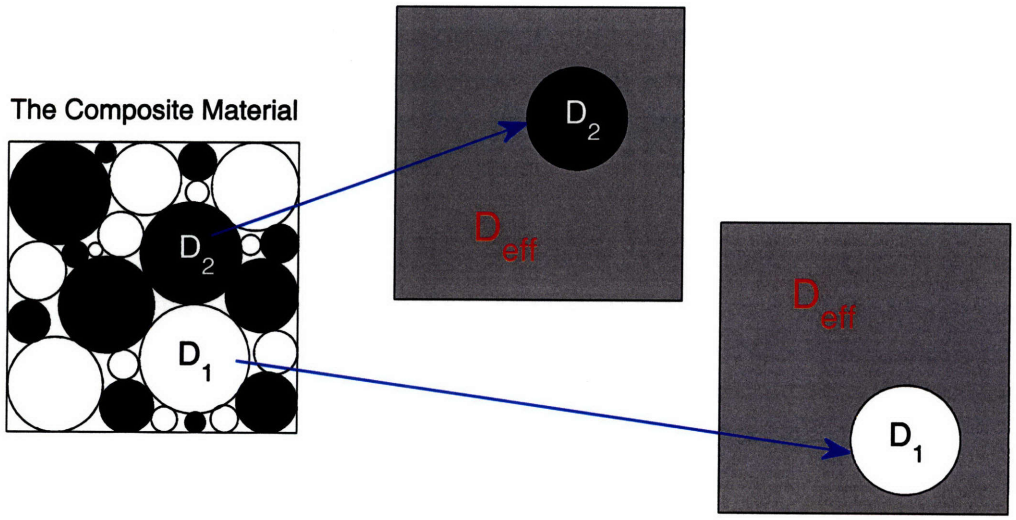

Figure 5. Illustration of the composite geometries used to derive the *symmetric* effective medium theory.

The second type of EMT is the symmetric effective medium which treats each phase independently and equally; there is no obvious matrix or inclusion in the composite system. As illustrated in Figure 5, each particle, regardless of its phase, can be considered to be embedded in an effective medium with diffusivity D_{eff}. Such insertion of a particle of either phase 1 or 2 into the effective medium will induce a change in the previously uniform concentration field, which can be described by Eq. (5). If we neglect the interactions among the particles, the average perturbation caused by inserting the particles into the effective medium is the simple superposition of the perturbation caused by individual particles.

$$\Delta\overline{C}(r) = \left[(1-p)\frac{D_1 - D_{eff}}{D_1 + (d-1)D_{eff}} + p\frac{D_2 - D_{eff}}{D_2 + (d-1)D_{eff}}\right]\frac{1}{r^d}C(r) \tag{9}$$

Here the distance r is large compared to the composite size and p is the volume fraction of phase 2. The overall result of these individual insertion processes is equivalent to directly inserting the whole composite material into the effective medium with diffusivity D_{eff}. Because the effective diffusivity of the composite material is equal to D_{eff}, inserting the composite into the effective medium will not cause any perturbation in the field:

$$\Delta\overline{C}(r) = 0 \tag{10}$$

The equivalence between Eq. (9) and (10) gives

$$(1-p)\frac{D_1 - D_{eff}}{D_1 + (d-1)D_{eff}} + p\frac{D_2 - D_{eff}}{D_2 + (d-1)D_{eff}} = 0 \tag{11}$$

Eq. (11) is usually referred to as Bruggeman's symmetric effective medium approximation [6, 18, 21]. It is basically derived from the self-consistency requirement.

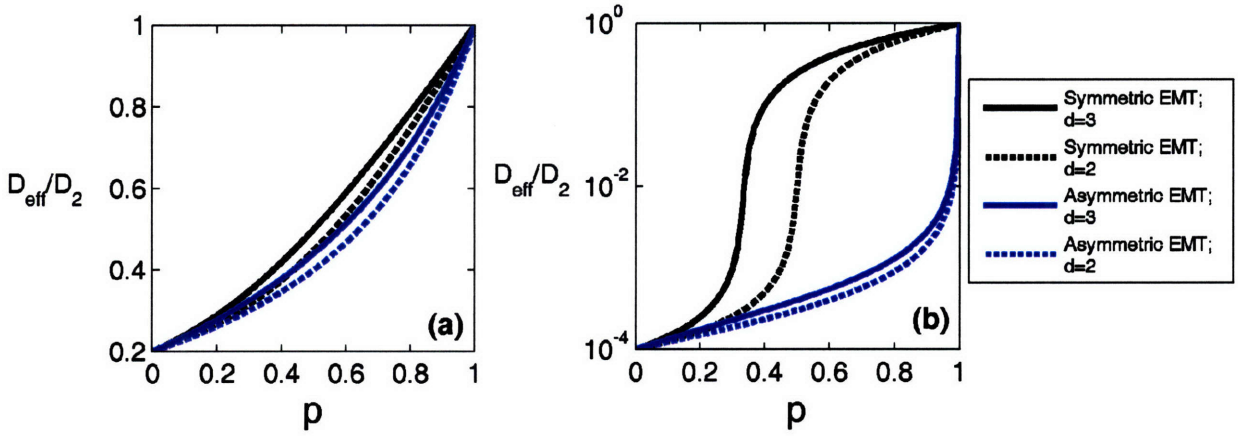

Figure 6. Predictions of the symmetric EMT equation (Eq. (11)) and the asymmetric EMT equation (Eq. (8)) for a composite material composed of phase 1 and 2 with $D_2/D_1 = 5$ in (a) and $D_2/D_1 = 10^4$ in (b). d = 2 and 3 corresponds to two and three dimensions, respectively.

Figure 6 compares the predictions from the symmetric EMT equation (Eq. (11)) and the asymmetric EMT equation (Eq. (8)) for both a low ($D_2/D_1 = 5$) and a high ($D_2/D_1 = 10^4$) phase diffusivity ratio. It seems that predictions from the symmetric and asymmetric EMTs are fairly close when D_1 and D_2 are of similar magnitude, but are significantly different when D_1 and D_2 are different by several orders of magnitude. In particular, as plotted in black lines in Figure 6(b), the symmetric EMT predicts a sudden increase in the effective diffusivity at $p = 1/3$ in three dimensions and at $p = 1/2$ in two dimensions. Another difference between the two types of EMT theories is that the symmetric EMT equation (Eq. (11)) can be easily generalized to multi-component composites as

$$\sum_i p_i \frac{D_i - D_{eff}}{D_i + (d-1)D_{eff}} = 0 \tag{12}$$

in contrast to the asymmetric EMT equation (Eq. (8)).

The asymmetric EMT equation (Eq. (8)) and the symmetric EMT equation (Eq. (11)) are only written for spherical inclusions. However, both equations have been used widely in the literature for various particle geometries and microstructural arrangements. The equations have also been modified to describe ellipsoids, but they become much more complex and more difficult to solve numerically. In addition to the geometric limitations, another obvious disadvantage of both equations is that they have been derived by neglecting all possible interactions among the particles. These interactions can be very strong when the particles are close to each other, and should be taken into account in more realistic models.

1.2.3. Series Expansion Approaches

As effective medium theories assume that the particles do not interact with each other, they can be considered as low-order approximations. Higher-order terms can be introduced by gradually taking into account many-body interactions such as pair interaction, triplet interaction, and so on. This approach is usually termed the *cluster expansion* method [22-24]. The resulting expressions for the effective properties are usually polynomials of the phase volume fraction. However, many-body interactions are too intricate to be calculated analytically; it is already very difficult to obtain pair and triplet interactions among particles of general shapes. Therefore the idea of incorporating many-body interactions is very difficult to implement in practice. In fact, the existing cluster expansion expressions are mostly derived for spheres or ellipsoids at perfect phase contrast (e.g., $D_2/D_1 \to 0$ or ∞) only. They rarely extend beyond first or second order in phase fractions, and thus do not provide substantial additional useful information over the predictions from effective medium theories. For example, consider a matrix of diffusivity D_1 containing dilute spheres of diffusivity D_2. The cluster expansion method could at best lead to

$$D_{eff} = D_1 + \frac{dD_1(D_2 - D_1)}{D_2 + (d-1)D_1} p + O(p^2) \tag{13}$$

where p is the sphere volume fraction and d remains to be the dimensionality. If we neglect the terms in $O(p^2)$, Eq. (13) is equivalent to the asymmetric EMT equation (Eq. (8)) or the Hashin-Shtrikman bound equation (Eq. (4)). Unfortunately, second or higher-order terms are seldom attainable.

Another type of series expansion approach is the *contrast expansion* method [25-27], which usually expresses the effective properties as the powers of some functions of the individual phase properties. When the phase diffusivities are of similar magnitude (e.g., D_2/D_1 is low), the effective diffusivity D_{eff} can be expressed as powers of the difference in the two phase diffusivities, $D_2 - D_1$.

$$D_{eff} = D_1 + D_1 \sum_{n=1}^{\infty} a_n \left(\frac{D_2 - D_1}{D_1} \right)^n \tag{14}$$

where a_n are the expansion coefficients that generally depend on the microstructure. Eq. (14) is usually referred to as the *weak-contrast* expansion. In Eq. (14), $a_1 = p$, the fraction of phase 2. So the first-order expansion is simply the linear volumetric average of the individual diffusivities, $D_{eff} = (1-p)D_1 + pD_2$. a_2 depends on the complex two-point microstructure correlation function and does not generally reduce to simple analytical forms. But when the composite material is macroscopically isotropic, a_2 reduces to $a_2 = -p(1-p)/d$. Thus the expansion to the second-order for isotropic composites is

$$D_{eff} = D_1 + p(D_2 - D_1) - \frac{p(1-p)(D_2 - D_1)^2}{dD_1} \tag{15}$$

Expressions at third- or higher-orders depend on more complicated n-point ($n \geq 3$) microstructure correlation functions which are in general analytically intractable.

When the phase contrast is high (high D_2/D_1 value), we can turn to the *strong-contrast* expansion [25], which expresses the effective diffusivity D_{eff} in powers of the d-dimensional scalar β.

$$\beta = \frac{(D_2 - D_1)}{D_2 + (d-1)D_1} \tag{16}$$

$$p^2\beta^2 \frac{D_{eff} + (d-1)D_1}{D_{eff} - D_1} = p\beta - \sum_{n=2}^{\infty} A_n \beta^n \tag{17}$$

where A_n are the expansion coefficients that also depend on the microstructure. In fact, A_n are related to the expansion coefficients a_n in the weak-contrast expansion Eq. (14), as both sets of coefficients are functions of the n-point microstructure correlation functions. Again A_n are complicated integrals of the correlation functions and do not usually assume explicit analytical forms as a function of the individual volume fractions and phase diffusivities. But when the composite is isotropic, $A_2 = 0$. So when truncated after the second-order, the strong-contrast expansion reduces to

$$\frac{D_{eff} - D_1}{D_{eff} + (d-1)D_1} = p\beta = p\frac{(D_2 - D_1)}{D_2 + (d-1)D_1} \tag{18}$$

which coincides with Eq. (8), the asymmetric EMT equation, or Eq. (4), one of the Hashin-Shtrikman bounds. The fact that Eq. (18) coincides with the asymmetric EMT (or the Hashin-Shtrikman bound) is actually not surprising. The expansion has been derived from first placing the heterogeneous material into an infinite homogeneous reference material (which is chosen to be either phase 1 or 2 for simplicity)

and then solving for the induced field. This embedding procedure is similar to the derivation of the effective medium theory, except that now the interactions among particles are captured by the higher-order terms.

As already mentioned above, the coefficients for the important higher-order terms in both types of expansions depend on the microstructural geometry and topology. They are complex functions of the *n*-point correlation functions which are usually impossible to compute analytically for even simple microstructures. As a result, the series expansion methods have seldom been applied in practice despite their theoretical soundness. Instead of trying to capture the effects of microstructural heterogeneity by adding more and more complex terms, it is the central idea of this thesis that we instead need a robust but concise means of capturing the topology of heterogeneous microstructures. We propose that percolation theory may fill this need.

1.3. Percolation Theory

1.3.1. Percolation Threshold

Percolation theory [3, 28, 29] is a well-developed statistical tool to study the probabilistic and geometric properties of connected clusters of one component in an inhomogeneous system. In particular, it focuses on the emergence of a percolating cluster that connects opposite sides of the system. The critical fraction of the component at which percolation occurs is termed the *geometric percolation threshold*, usually denoted as p_c.

Most percolation studies have focused on percolation processes on lattices (discrete systems). There are two types of lattice percolation. One is bond percolation and the other is site percolation. In bond percolation, each bond is either occupied with probability p or absent with probability 1-p. Whether a bond is present or not is independent of the presence of any other bond. Two bonds are considered connected if they directly meet at junctions or if there is a connected path between them. A set of bonds that are interconnected in this way is usually called a cluster. When p is low, there are only some small clusters separated from each other (e.g., Figure 7(a)); when p is sufficiently high, there will be a well-connected large cluster that connects opposite sides of the system, i.e., it is sample-spanning or percolating (e.g., Figure 7 (b)). Thus there must be a critical probability or fraction p_c corresponding to the percolation transition (first emergence of the percolating cluster). Similarly, in site percolation, a fraction of all available sites are randomly occupied, and two occupied sites are considered connected if they can reach each other via nearest-neighbor jumps. Again the percolation threshold p_c corresponds to the critical fraction below which there is no percolating cluster (e.g., Figure 7(c)) but above which there is (e.g., Figure 7(d)).

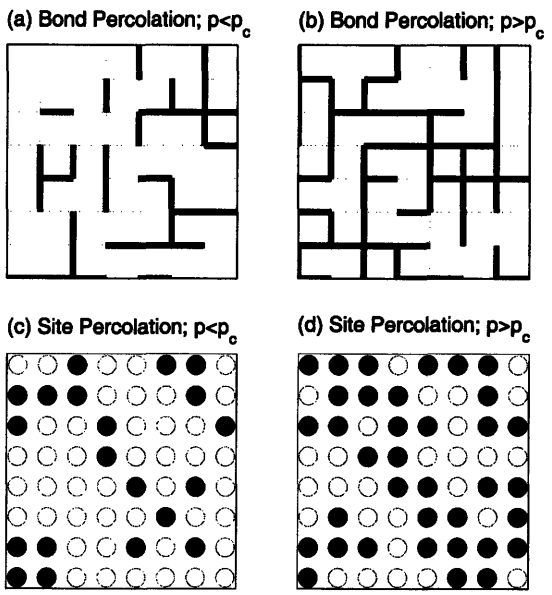

Figure 7. Illustration of discrete lattice percolation on a square lattice. (a) and (b) show the connectivity among occupied bonds (bold black lines) below and above percolation threshold p_c, respectively. (c) and (d) respectively show the clusters of occupied sites (filled in black) below and above p_c.

The specific numerical value of the percolation threshold depends on (1) the lattice type which includes dimensionality and symmetry, (2) the percolation type (bond or site), (3) the system size (being finite or infinite), and (4) correlations among the occupations (randomly occupied or not). The percolation thresholds most commonly referred to are for an infinitely large system with random occupations, and usually they are only approximations except for a few two-dimensional lattices [3] (see Table 2).

Table 2. Bond and site percolation thresholds for triangular, square, and honeycomb lattices.

Lattice	Bond Percolation	Site Percolation
Triangular	$1-2\sin(\pi/18)$* (≈0.34729)	0.50000*
Square	0.50000*	0.59275
Hexagonal (Honeycomb)	$2\sin(\pi/18)$* (≈0.65271)	0.69620

* Exact results

When the system size L[†] is not sufficiently large, there will not be one definite percolation threshold but instead a range of fractions, spanning over a width Δ, in which the percolation transition can possibly occur. As L increases, Δ decreases according to

[†] In percolation theory, the system size L is usually a unitless quantity defined as number of elements per edge or the true system dimension divided by the true element size.

$$\Delta \propto L^{-1/\upsilon} \tag{19}$$

where υ is a critical scaling exponent in percolation theory. The average percolation threshold $p_c(L)$ for one finite system size L is not necessarily the mean of all possible critical fractions, but rather the fraction at which a percolating cluster is most likely to appear. A simpler way to approximate $p_c(L)$ is to look for the fraction at which there is a 50% probability to have a percolating cluster in the system. $p_c(L)$ is usually lower than the percolation threshold p_c for infinite size, and conforms to the relationship

$$p_c - p_c(L) \propto L^{-1/\upsilon} \tag{20}$$

where υ is the same scaling exponent as the υ in Eq. (19). Therefore as the system size L increases towards infinity, the percolation transition width Δ decreases to zero and the percolation threshold $p_c(L)$ approaches p_c obeying the same scaling relationship. The scaling presented in Eq. (19) and (20) is part of the finite-size scaling scheme in percolation theory to extrapolate percolation quantities for infinite systems from those for finite systems.

Correlations among the occupation probabilities of different bonds or sites can cause a shift in the percolation threshold as well. Positive correlations promote occupations near an occupied bond or site, making it easier to form a percolating cluster of bonds or sites. The percolation threshold tends to decrease as a result of the enhanced connectivity. On the contrary, negative correlation means that the occupation probability close to an occupied bond or site is lower than average. Because this generally deters connectivity, more bonds or sites must be filled in order to form a percolating cluster. The percolation threshold will be higher than that for the case of random occupation. One common correlation the percolation community studies is to consider the connectivity among the next-nearest neighboring occupied sites in addition to the nearest neighbors. This will obviously promote the connectivity and decrease the percolation threshold. For example, for the site percolation on the square lattice, adding next-nearest-neighbor connectivity decreases the percolation threshold from ~0.59275 to ~0.4073.

1.3.2. Percolation Scaling Laws, Critical Exponents, and Universality Class

In addition to the percolation threshold p_c, the geometric properties of the system can be more specifically characterized by several other percolation quantities. For a system with bond (or site) occupation probability p, two important percolation quantities are the *percolation probability* $P(p)$, the probability that a given bond (or site) belongs to a percolating cluster, and the *backbone fraction* $P_B(p)$, the fraction of bonds (or sites) in the percolating cluster that actually contribute to transport processes, because some of the bonds are dead-ended and cannot not conduct flow. Both $P(p)$ and $P_B(p)$ follow a power law scaling right above p_c.

$$P(p) \propto (p - p_c)^{\beta} \qquad \text{for } p > p_c \tag{21}$$

$$P_B(p) \propto (p - p_c)^{\beta_B} \qquad \text{for } p > p_c \tag{22}$$

Both Eq. (19) and (20) are written only for infinitely large systems (system size $L \to \infty$) where the macroscopic properties such as $P(p)$ and $P_B(p)$ are independent of L. When L is finite, the properties will

become a function of L. One needs to infer quantities for an infinite system from the finite-size scaling technique, which is based on another important percolation property, the *correlation length* $\xi(p)$[‡]. The correlation length is defined as the typical radius of finite clusters when $p < p_c$ and the maximum size of the "holes" inside the percolating cluster when $p > p_c$. As p approaches p_c, $\xi(p)$ also follows a scaling law:

$$\xi(p) \propto |p - p_c|^{-\upsilon} \tag{23}$$

Thus ξ diverges to infinity as $p \to p_c$.

For $p > p_c$, the correlation length is the length scale over which the system can be considered macroscopically homogeneous; when the system size $L > \xi$, the percolating cluster appears homogeneous and can be simply described by the Euclidean dimension d. When $L < \xi$, however, we need to consider the fractal nature of the percolating cluster, i.e., the cluster is self-similar on many length scales. Then the cluster has to be characterized by a fractal dimension D_f which is slightly lower than the Euclidean dimension d. If we work with a finite system, ξ will eventually exceed the system size L as p_c is approached (Eq. (23)). In this case, L becomes the dominant length scale in the system and also the cluster needs to be characterized by the fractal dimension D_f. Thus the total number of bonds or sites in the percolating cluster would be proportional to L^{D_f}, resulting in an average density or probability

$$P(p,L) \propto \frac{L^{D_f}}{L^d} = L^{D_f - d} = L^{-\beta/\upsilon} \quad \text{for } p > p_c \text{ and } L < \xi(p) \tag{24}$$

where the last equality results from partitioning an infinite system into many finite cells in order to obtain the relationship between D_f and d. Eq. (24) applies to small systems while Eq. (23) works for infinite systems. We can combine them to obtain a scaling equation for any system size:

$$P(p,L) \propto L^{-\beta/\upsilon} \psi\left(L^{1/\upsilon}(p - p_c)\right) \quad \text{for } p > p_c \tag{25}$$

where $L^{1/\upsilon}(p - p_c) \propto [L/\xi(p)]^{1/\upsilon}$, and $\psi(x)$ is a proper analytical scaling function. For example,

$$\psi(x) \to \begin{cases} 1 & \text{when } L << \xi(p) \\ x^{\beta} & \text{when } L >> \xi(p) \end{cases} \tag{26}$$

can make Eq. (25) converge to Eq. (24) or Eq. (21) in the limits of small or infinite system size, respectively. If we already know the values for $P(p,L)$ for several finite sizes L, we can adjust the value of β to attain a power law scaling of $L^{\beta/\upsilon}P(p,L)$ with respect to $L^{1/\upsilon}(p - p_c)$ with the same scaling exponent β. This way we can evaluate β for infinite systems from data for finite systems. The scaling form in Eq. (25) has been assumed valid for essentially any other percolation properties. Their critical scaling exponents can thus be obtained in a similar fashion. The correlation length exponent υ is exactly what appears in Eqs. (19) and (20) for the scaling of the percolation threshold $p_c(L)$. In fact, Eqs. (19) and (20) have been derived from the finite-size scaling of the percolation probability using an equation similar to Eq. (25).

One of the most important concepts in percolation theory is universal scaling and the universality class [3, 30, 31]. In a certain universality class, the critical scaling exponents, such as β, β_B, and υ presented

[‡] $\xi(p)$ is a geometric property of percolating systems; it should be distinguished from the common correlation length that characterizes correlations in the literature and in later sections of this proposal.

above, are independent of the lattice type (coordination number of the lattice) and the percolation type (bond or site percolation). Many percolation quantities become insensitive to these factors near the percolation threshold. The critical exponents usually only depend on the dimensionality of the lattice. The values for the critical exponents mentioned above are given in Table 3 for two and three dimensions [3, 32].

Table 3. Geometrical critical scaling exponents in two and three dimensions.

Geometric critical exponents	$d = 2$	$d = 3$
β	5/36	0.41
β_B	0.47	1.05
υ	4/3	0.88
D_f	91/48	2.52

One factor that might affect the universal scaling behavior is the correlation among occupations of neighboring sites. In addition to shifting the percolation threshold as discussed in Section 1.3.1, correlations could also possibly change the scaling behaviors near the percolation threshold. Presently the general understanding is that short-range correlations do not change the scaling exponents, and thus the problem remains in the same universality class [29, 33, 34]. The effects of long-range correlations are less studied, but the available data show that the percolation scaling in the presence of long-range correlations might be nonuniversal, i.e., the scaling exponents become a function of the correlation length [35, 36]. Little is known about the critical length scales of correlations at which the crossover from universal to nonuniversal scaling occurs.

1.3.3. Effects of Percolation on Effective Properties

Percolation theory has been mainly used to understand and predict effective transport properties, as these properties depend on the connectivity in a straightforward way. For example, we can consider the bond percolation problem shown in Figure 7(a) and (b) as one where each missing bond is equivalent to a bond with a diffusivity $D_1 = 0$ and each existing bond has a finite diffusivity D_2 ($D_2 > 0$). The fraction of bonds of diffusivity D_2 is p. Then the effective diffusivity of the system, D_{eff}, should be zero below the percolation threshold p_c because the useful bonds are well separated and there is no diffusion path. As p increases above p_c, D_{eff} becomes finite and then keeps increasing as the percolating cluster, as an effective diffusion path, forms and grows. D_{eff} as a function of the bond occupation fraction p is illustrated in Figure 8(a). In fact, D_{eff} obeys a simple power scaling law for $p > p_c$:

$$D_{eff}(p,0,D_2) \propto (p - p_c)^t \qquad \text{for } p > p_c \tag{27}$$

Here we have assumed a perfect phase contrast, *i.e.*, one phase diffusivity being zero vs. the other being finite. Percolation theory can also well handle the opposite extreme case, a binary system where some bonds have a finite diffusivity D_1 ($D_1 > 0$) and others have an infinite one $D_2 = \infty$. Intuitively then, D_{eff} should be finite below p_c and diverge to infinity at p_c when bonds with an infinite diffusivity start to form a percolating cluster. Its divergence in the vicinity of p_c can be described by a power law as well:

$$D_{eff}(p, D_1, \infty) \propto (p_c - p)^{-s} \qquad \text{for } p < p_c \tag{28}$$

D_{eff} as a function of p is illustrated in Figure 8(b).

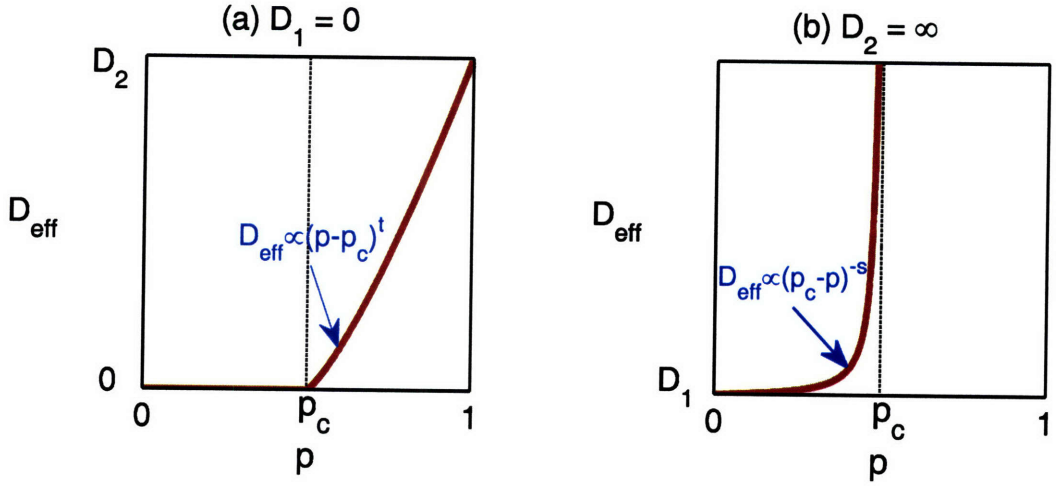

Figure 8. A schematic of the effective diffusivity of a binary network composed of bonds with diffusivities D_1 and D_2 at the perfect diffusivity contrast (a) $D_1 = 0$ and (b) $D_2 = \infty$. p is the fraction of bonds with diffusivity D_2 and p_c is the percolation threshold.

The scaling exponent s in Eq. (28) and t in Eq. (27) are actually equal to each other in two dimensions. This can be explained by inspecting the duality and phase-inversion symmetry of a square network [37].

$$D_{eff}(p, D_1, D_2) \xrightarrow{\text{Duality Symmetry}} \frac{1}{D_{eff}\left(p, \frac{1}{D_1}, \frac{1}{D_2}\right)} \xrightarrow{\text{Inversion Symmetry}} \frac{1}{D_{eff}\left(1-p, \frac{1}{D_2}, \frac{1}{D_1}\right)} \tag{29}$$

Here the reciprocity relationship due to duality symmetry can be explained as follows. If we map a network to a new one where each bond is the perpendicular bisector of an original bond but with a diffusivity reciprocal to the diffusivity of the original bond, then the effective diffusivity of the mapped network should be the reciprocal of the effective diffusivity of the original network. As square networks are geometrically self-dual, *i.e.*, geometrically invariant under the dual mapping, the effective diffusivities for the mapped networks are thus still for square networks. The phase-inversion symmetry means a randomly-distributed system should be invariant if we simultaneously interchange both the phase properties and phase fractions. Now if we let $D_1 = 0$ and D_2 = finite number, we have

$$D_{eff}(p,0,D_2) = \frac{1}{D_{eff}\left(1-p,\frac{1}{D_2},\infty\right)} \tag{30}$$

which holds for $p > p_c$. The left and right side of Eq. (30) should obey the power law in Eq. (27) and Eq. (28), respectively. And if we further consider that $p_c = 0.5$ for square networks (Table 2), we have

$$A(p-p_c)^t = \frac{1}{B[p_c-(1-p)]^{-s}} = \frac{1}{B}[p_c-(1-p)]^s \xrightarrow{p_c=0.5} \frac{1}{B}[p-p_c]^s \tag{31}$$

where A and B are prefactor constants of the scaling laws. Thus $s = t$ for square networks. Because the scaling exponents are universal percolation quantities and are independent of the lattice type and percolation type (bond or site), the relationship $s = t$ generally holds for any transport properties in two dimensions. However, the specific values for s or t in both two and three dimensions as we know them at present are only based on approximations or numerical simulations.

It is worth mentioning that s and t are unique and nontrivial critical scaling exponents in percolation theory. They are not related to the geometric scaling exponents such as those listed in Table 3 in any simple way. Although several approximations have been proposed to relate s or t to those geometric scaling exponents, they are often too simple to capture the complex physics and statistics of disordered systems. On the other hand, s and t may just be considered as independent critical scaling exponents that are determined by and conversely reflect the physical laws governing the process and their complex dependence on geometric connectivity. If certain physical processes can be described by the same set of scaling exponents, then the physical laws governing these phenomena must be fundamentally the same [2], no matter how disparate these processes seem to be from each other. For example, the values of s and t are the same for all the properties listed in Table 1 because they are mathematically analogous.

Table 4. Critical exponents for linear transport and elastic properties in two and three dimensions.

Property critical exponents	$d = 2$	$d = 3$
s (for transport coefficient)	1.3	0.73
t (for transport coefficient)	1.3	2.0
s (for elastic constant)	1.12	N/A
t (for elastic constant)	2.4±0.4	4.4±0.6

from Refs. [2, 8, 38]

A lot of effort has also been expended to understand the effects of percolation on elastic properties of spring networks [38-45]. This class of percolation problem is usually referred to as rigidity percolation to distinguish it from simple geometric percolation and percolation of linear transport properties. Usually each bond is considered an elastic spring that can be stretched or contracted. Consider a binary system composed of springs with elastic constant E_1 and E_2 with probability 1-p and p, respectively. Similar to the perfect diffusivity contrast discussed above, we first consider the case of $E_1 = 0$. The percolation

threshold for elastic constant, p_{ce}, is defined as the critical fraction at which the system becomes rigid, *i.e.*, stable under an applied stress. Because with only central forces the system can still be unstable even when the bonds form a percolating cluster, it requires a higher degree of connectivity in order to support mechanical load. Thus p_{ce} is usually much higher than the geometric percolation threshold p_c. For example, for a triangular network p_{ce} is found to be ~0.58 or ~0.64 by two independent studies [38, 40] while $p_c \approx 0.35$. The effective elastic constant E_{eff} is zero below p_{ce} and follows the same power law scaling as in Eq. (27) or Figure 8(a),

$$E_{eff}(p,0,E_2) \propto (p - p_{ce})^t \qquad \text{for } p > p_{ce} \tag{32}$$

The opposite extreme case is where E_1 is finite but $E_2 = \infty$. E_{eff} will be finite below p_{ce} and diverges to infinity as p approaches p_{ce} according to a power law similar to Eq. (28) or Figure 8(b).

$$E_{eff}(p,E_1,\infty) \propto (p_{ce} - p)^{-s} \qquad \text{for } p < p_{ce} \tag{33}$$

However, the values of s and t are different from those for linear transport properties (see Table 4), because now what are transmitted through the network are vectors instead of scalars. Thus the central-force rigidity percolation is said to belong to a different universality class.

In addition to the scaling laws in Eq. (32) and (33), we can also examine the force distributions on the elastic spring network by calculating the force moments defined as [40, 46]

$$M_F(k) = \sum F^k \tag{34}$$

where the summation runs over all springs in the network and k = 1,2,3.... Near the percolation threshold $M_F(k)$ follows a power law as well, $M_F(k) \propto |p - p_{ce}|^{\tau(k)}$. Similar to the situation described for geometric percolation, the correlation length of rigidity percolation will exceed the finite system size L when p approaches p_{ce} from either below or above. Thus L will become the dominant length scale in the system, which leads to a finite-size scaling relationship analogous to Eq. (24).

$$M_F(k,L) \propto L^{-\tilde{\tau}(k)} \quad \text{for } p = p_{ce} \text{ or very close to } p_{ce} \tag{35}$$

The set of the critical scaling exponents, $\tilde{\tau}(k)$, where k = 1,2,3..., are distinct exponents in percolation theory as well. Eq. (35) can also be used to estimate the rigidity percolation threshold p_{ce} because it only scales with L in this way for p at or very close to p_{ce}.

1.4. Predicting Effective Properties for Real Materials: Challenges and Opportunities

1.4.1. Imperfect Phase Contrast

Although percolation theory seems to work well for predicting and understanding effective properties at a perfect phase contrast, *i.e.*, the property of interest of one of the two phases is either zero or infinite, only in very rare cases can we assume such an ideal phase contrast. More often we need to deal with

systems fully occupied with bonds of different finite diffusivities, elastic constants, etc. Consider a simple binary system where bonds can have a low diffusivity D_1 or a higher one D_2 with probability 1-p and p, respectively. In this case $0< D_2/D_1 <\infty$; the phase contrast is imperfect. The effective diffusivity D_{eff} is thus nontrivial in the full range of the bond fractions. Few studies have focused on the effects of percolation on the effective properties of such binary systems. Because diffusion entirely relies on geometric connectivity and it has the same percolation threshold p_c as geometric percolation, D_{eff} is expected to increase abruptly at p_c from being closer to D_1 to being closer to D_2. If the power scaling laws in Eq. (27) and (28) should still be obeyed when $p > p_c$ and $p < p_c$, respectively, D_{eff} as a function of p should be some proper combination of these two scaling laws. This is illustrated in Figure 9, which can be formed by merging Figure 8(a) and (b). The effective elastic constant should show a similar trend as well but with its own percolation threshold p_{ce} and scaling exponents s and t.

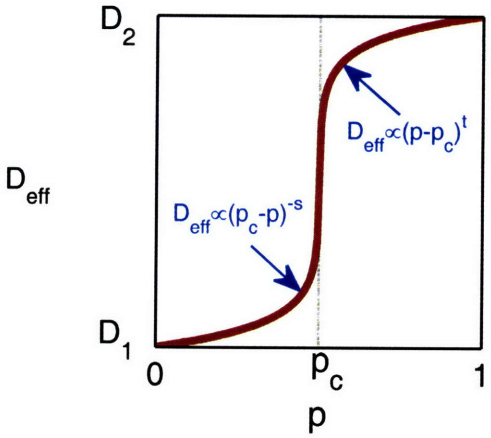

Figure 9. Percolation in effective diffusivities for a two-phase composite with finite phase diffusivities.

It is difficult to rigorously derive an equation to describe the effective diffusivity shown in Figure 9 because the curve exhibits a critical percolation transition and it should also reduce to simple power law scaling in the vicinity of the percolation threshold. However, the curve shown in Figure 9 looks very similar to the black lines in Figure 6, which are the predictions of the symmetric Effective Medium Theory (EMT) equation (Eq. (11)). It is this striking similarity that inspired McLachlan *et. al.* [47-49] to make use of Eq. (11) in deriving a semi-empirical equation to describe the curve in Figure 9. While preserving the basic features of Eq. (11), they have replaced the dimensionality d by $1/p_c$ and also directly introduced the scaling exponents s and t into Eq. (11). The resulting equation is usually referred to as the generalized effective-medium (GEM) equation. In the context of diffusion, this equation writes as

$$(1-p)\frac{D_1^{1/s}-D_{eff}^{1/s}}{D_1^{1/s}+(p_c^{-1}-1)D_{eff}^{1/s}}+p\frac{D_2^{1/t}-D_{eff}^{1/t}}{D_2^{1/t}+(p_c^{-1}-1)D_{eff}^{1/t}}=0 \qquad (36)$$

Although Eq. (36) is purely empirical, it has been shown both experimentally and numerically to yield good predictions for effective diffusivities as well as other transport properties for binary heterogeneous materials.

As discussed in section 1.2.2, the symmetric EMT Eq. (11) has been derived by embedding each particle independently into an effective medium. All possible interactions among particles are thus neglected in this embedding procedure. The series expansion methods (discussed in section 1.2.3) attempt to take into account these interactions by adding more complex terms. The coefficients for these additional terms are unfortunately difficult to obtain even for simple microstructures. Conversely, by introducing the percolation threshold and scaling exponents into the symmetric EMT equation, the GEM equation (Eq. (36)) is able to predict the correct percolation transition and scaling in materials properties. It is thus reasonable to infer that all the interactions among particles have been correctly captured by remarkably few percolation quantities. p_c, s and t are all what we need in order to predict the effective properties of heterogeneous materials, no matter how disordered the microstructures may seem to be. What is more, since s and t are effectively constants that do not change as we add local correlations in the microstructure, we only need to assess one parameter—the percolation threshold—to capture all the effects of microstructure topology in a complex material, and to make accurate predictions of properties at any phase fraction.

It would be premature, though, to draw the conclusion that Eq. (36) is the ultimate or perfect homogenization solution that we can ever expect. There are many complex microstructures or processes the equation may not be able to directly apply to. But at least it already has the essential feature of being able to reduce to percolation scaling laws similar to Eq. (27) and (28) in proper limits,

$$D_{eff} = D_1 \cdot [(p_c - p)/p_c]^{-s} \quad \text{for } |D_2| \to \infty \text{ and } p < p_c \tag{37}$$

$$D_{eff} = D_2 \cdot [(p - p_c)/(1 - p_c)]^{t} \quad \text{for } |D_1| \to 0 \text{ and } p > p_c \tag{38}$$

and we may further generalize it for specific cases. However, it is a central assertion of this thesis that understanding the percolation and scaling elements of the homogenization problem will be the key to a full solution.

1.4.2. Nonrandom Distribution of Microstructures

The largest body of knowledge about the specific values of percolation thresholds and scaling exponents are from studies specific to a random distribution of phase properties on lattices. As mentioned earlier, correlations among the occupation probabilities or phase distributions can shift the percolation threshold. If they are long-range, they may also possibly cause changes in the scaling exponents. Unfortunately, the exact quantitative effects of such correlations on percolation properties are largely unknown or unclear.

What makes things worse is that in real materials, correlations in microstructure distributions are not only common, but also very complex and thus difficult to directly characterize. Correlations exist when there are constraints that prevent the microstructural components from being randomly distributed, *e.g.*, disorientations of neighboring grain boundaries must satisfy crystallographic orientation constraints [50],

and when there are interactions between the components, *e.g.*, attraction causes positive correlation and repulsion causes negative correlation. Real materials often exhibit nonrandom microstructure morphologies due to processing.

It is possible to use computer simulations to calculate percolation properties for a few simple correlated systems or even digital images of some real microstructures [51-53]. But ultimately what would be most useful is some general understanding of how the percolation threshold and scaling properties change as a function of some simple correlation metrics such us a characteristic correlation length, particle size distribution etc.

1.4.3. Multicomponent (Multiphase) Systems

It is obvious that percolation thresholds are defined for binary systems. They may also apply to multiphase systems where the phase properties exhibit a sharp bimodal distribution. In reality, however, many complex composite systems are composed of phases with several distinctly different phase properties or even a continuous spectrum of phase properties. It is not clear how to define and use a percolation threshold for these multiphase composite systems, although it is very likely that a percolation threshold in this case will be compared to some integration of phase fractions. In addition, some percolation studies have found that complex continuous distributions of phase properties may cause non-universal scaling behaviors. The critical scaling exponents depend on the specific statistical distributions of the individual phase properties.

The possibility of non-universality poses many challenges to the evaluation of effective properties. Even if the scaling exponents (s and t) are known for a given spectrum of phase properties, The GEM equation Eq. (36) is written for binary systems only. Because the scaling exponent in each term is different, the equation is no longer symmetric. It cannot be directly generalized for multicomponent systems by adding a term for each additional component or phase. However, it is imperative to be able to generalize the equation for ternary, quaternary... systems and finally for systems with a continuous spectrum of phase properties.

1.4.4. Treating Heterogeneous Solids as True Continuum Media

Although lattice percolation has been generally well studied, one often has to deal with continuum percolation because most composite systems are solids and not lattices. Continuum percolation (for a review, see [54]), where all possible occupation positions of the phases fill the space, represents a more realistic percolation model for most real heterogeneous materials. Presently there is only limited understanding of continuum percolation. Existing works mainly study the geometric percolation threshold and cluster distribution of impermeable or overlapping objects [55, 56], mainly disks and spheres [57-59],

using cluster and correlation functions and Monte Carlo simulations. Attempts have also been made to estimate the scaling exponents for several properties by mapping the continuum problem to a discrete network problem [59, 60]. While the geometric scaling exponents seem the same as those for lattice percolation [58, 59, 61], the exponents for conductivity, permeability, and elasticity seem different from their lattice counterparts, except for conductivity in two dimensions [60, 62]. This inconsistency has stimulated a long dispute about whether, for the same problem, continuum and lattice percolation belong to the same universality class [61, 63, 64].

However, it is important to note that in a continuum composite there are contacts at faces, edges and corners. The geometric percolation threshold depends on the specific definition of connectivity, *i.e.*, which contacts are considered effective joints. In addition, it is not clear how these contacts affect materials properties and which contacts are more important for a certain property. Unfortunately the presence and effects of many contacts have been naturally neglected when a heterogeneous solid is mapped onto a lattice. A lot of uncertainties in continuum percolation in the literature can be attributed to ignoring or incorrectly assuming the effects of various contacts. Unfortunately, there has, to date, not been even a single work that systematically studied the percolation and critical scaling behavior of physical processes in continuum systems by strictly working on the continuum. This might be because efficient finite element codes for direct percolation study of such problems, over meaningful system sizes and with sufficient statistics, have only become readily available in recent years.

1.4.5. Complex Dependence of Physical Processes on Topology

In terms of percolation, linear transport properties are the simplest properties because they entirely depend on geometric connectivity. Their percolation threshold is usually the same as the geometric connectivity threshold. Other properties are rarely as simple. Usually the percolation thresholds for effective properties not only depend on the geometric connectivity among phases, but also possibly on the intrinsic correlations of the physical processes. For example, as mentioned in section 1.3.3, on a triangular network, while diffusion and geometric connectivity have the same percolation threshold $p_c \approx 0.35$, an elastic triangular network has a completely different threshold at $p_{ce} \approx 0.58$ [38] or 0.641 [40]. It is likely that other properties would show still different percolation thresholds for the same triangular network. In addition to the percolation threshold, different classes of properties may have different scaling exponents (such as those in Table 4), or in other words, may belong to different universality classes. For example, percolation of linear transport properties (scalar percolation) and elastic rigidity percolation (vector percolation) belong to different universality classes. Intuitively, we may wonder about some properties that involve both diffusional process and force transmission. Rheology, or stress-driven diffusion, would be one such complex property of tremendous practical importance, but nothing is known about percolation properties for this situation. As emphasized throughout this chapter, if the percolation behaviors of a property are unknown, we will certainly miss the opportunity to describe the effective property of composite systems simply and accurately.

As we switch from lattice to continuum, even the same type of property can become much more complex. For example, when we work with an elastic network, each bond can be characterized by an elastic constant. But in real solids, a phase needs to be characterized by at least two elastic constants, such as Young's modulus and Poisson's ratio, or Lamé constant and shear modulus, or bulk and shear moduli. There is no doubt that the percolation of elasticity on the continuum will be more complicated because the two elastic constants can certainly affect each others' percolation behaviors. This is, at present, an untouched research area full of opportunities. Understanding the percolation of elasticity in continuum solids will eventually shed light on how to estimate effective elastic constants of engineering composites. This is an old and difficult problem that numerous researchers have been working on for over half a century. But almost all of the studies have focused on bounds and series expansion methods, so essentially the problem remains unsolved. Introducing the percolation element into the problem may lead to practical solutions of technological significance.

1.5. Thesis Goal and Overview

The above challenges will be addressed to various degrees in this work. The eventual objectives are to characterize the effects of microstructural geometry and topology using percolation quantities, and to provide a new line of thought as well as some practical tools for evaluating the effective properties of real heterogeneous materials. Conversely, a deep understanding of the microstructure-property relationship on the "macro" scale (the scale above the characteristic length of heterogeneities) is crucial for microstructure design because mostly this is the scale directly related to the performance of engineering materials.

Because this thesis addresses the interface between traditional percolation and composite theories, it is hoped that this work will contribute to both fields in many aspects. The heterogeneous systems studied in the following chapters are listed in Table 5. As mentioned in section 1.3.3, lattice percolation with a random distribution of elements has been generally well studied, as have the linear transport properties of ideal binary networks. The present thesis will therefore seek to provide new data and understanding for (1) multicomponent percolation, (2) correlated percolation, (3) continuum percolation, and most importantly, (4) percolation in more complex and important materials properties such as diffusional creep and continuum elasticity.

In most existing composite theories (section 1.2), the issue of phase topology has been either explicitly or implicitly neglected. This thesis work will therefore also (1) demonstrate the effects of phase connectivity and emphasize that we need to take into account connectivity in order to correctly predict effective properties, and (2) use the percolation threshold and scaling laws to succinctly characterize the effects of connectivity and interactions among particles, and finally (3) use percolation-type finite-size scaling to extrapolate the effective properties for infinite systems sizes inaccessible to computer simulations.

We begin by considering diffusion on a lattice which is imagined to be a two-dimensional heterogeneous grain boundary network in section 2.1. Section 2.2 adds complexity to the percolation problem by studying the interplay of stress and diffusion in the process of Coble creep. Building on the basic understanding of discrete lattices in Chapter 2, we proceed to study diffusion in continuum composites in section 3.1 and determine the differences between the discrete and continuum systems. In all these studies the materials have been assumed isotropic so that each grain boundary or phase can be described by a single diffusion coefficient. Section 3.2 deals with a more complex situation: the effective elastic properties of continuum composites, where each phase is characterized by two independent elastic constants. In Chapter 2, different types of grain boundaries have been randomly distributed onto the lattice, and, in Chapter 3, particles in the continuum composites have been randomly assigned a phase as well. The more realistic, correlated distribution of grain boundaries is studied in section 4.1 and correlated continuum composites are studied in section 4.2. Finally, in Chapter 5, we will develop an analytical homogenization method for the perfectly correlated microstructure—periodic composite materials.

The heterogeneous grain boundary networks and continuum composites will be treated separately. The scenario where percolation occurs both on the network and on the continuum will be even more complicated. For example, if we consider diffusion through a two-phase composite solid with phase and grain boundaries, we basically need to treat a multicomponent strongly-correlated continuum percolation problem. But eventually, our understanding on correlated discrete and continuum percolation can be integrated together to treat complex microstructures.

Table 5. Heterogeneous systems studied in this thesis and the corresponding chapter number.

System	Spatial distribution	Number of phases	Property	Chpt.
Grain boundary network	Random	Binary & Multicomponent	Diffusion & Diffusoinal Creep	2
	Correlated (short-range)	Binary	Diffusion & Diffusoinal Creep	4.1
Composite solid	Random	Binary	Diffusion & Elasticity	3
	Correlated (short to long range)	Binary	Diffusion	4.2
	Periodic	Binary	Diffusion	5

Chapter 2. Homogenization of Random Multicomponent Interfacial Networks

2.1. Grain Boundary Diffusion

2.1.1. New Perspectives on Materials Kinetics Due to Grain Boundary Character Distribution

There is generally a wide distribution of grain boundary character (atomic structure) in polycrystalline materials, including variations in misorientation and plane inclination [65]. The properties of individual grain boundaries, such as grain boundary energy, mobility, and diffusivity, all depend on their specific atomic structures. Among these and other grain boundary properties, diffusivity is most exhaustively studied because it can be directly measured from experiments [66-75]. For example, Monzen *et al.* [71, 72] showed that the minimum cusps of grain boundary diffusivity occur at coincidence site lattice (CSL) misorientations for the case of Bi diffusing along both tilt and twist boundaries in Cu. Other experimental studies in the Cu-Ni system [73, 74] have found that the activation energy for grain boundary diffusion decreases with an increase in disorientation angle for the few grain boundary structures studied; the increased structural disorder in high angle grain boundaries generally accelerates material transport. In a recent kinetic Monte Carlo (KMC) simulation [75], grain boundary diffusivity was found to vary by almost four orders of magnitude at high temperatures and almost ten orders of magnitude at low temperatures, depending on the grain boundary structure.

Diffusion is a critical kinetic property in materials science and engineering. In particular, grain boundary diffusion plays a crucial role in a variety of important physical processes, such as discontinuous precipitation [76, 77], recrystallization and grain growth [78], sintering [79, 80], electromigration [81, 82], dynamic embrittlement [83], and Coble creep [84]. As regions of excess free volume and enhanced atomic mobility, grain boundaries are often fast diffusion paths in polycrystalline materials, with diffusivities several orders of magnitude greater than in the lattice [85-87]. Diffusion along grain boundaries becomes especially significant as grain size is refined to the nanoscale [88, 89]; the transport and deformation properties of nanocrystalline materials are, in many cases, dominated by grain boundary diffusion. In view of the dependence of grain boundary diffusivity on boundary character and the broad spectrum of grain boundary characters in polycrystals [65, 90, 91], understanding diffusion through a polycrystal requires knowledge of the overall transport behavior of a variety of grain boundaries connected to each other.

However, despite the understanding of structure-property relationship of individual grain boundaries, the differences among grain boundaries have been largely neglected in determining or understanding macroscopic properties of polycrystalline materials until recent years. The emergence of "grain boundary

engineering" techniques, which include cycles of deformation followed by annealing treatments, has attracted much attention lately because of their ability to change the fractions of different grain boundaries in a polycrystal. Grain boundary network science has emerged as a result. It is the study of the geometric properties of heterogeneous grain boundary networks, such as cluster distribution and geometric percolation (e.g. [29, 92, 93]), and the effects of this geometric heterogeneity on macroscopic properties of polycrystalline materials. In this context, understanding diffusion through a heterogeneous grain boundary network seems to be a good starting point because the dependence of grain boundary diffusion on individual grain boundary structure has been generally well understood.

Eventually, the goal is to obtain a fictitious, or effective, value for grain boundary diffusivity, defined in such a way that it can properly represent a global 'average' over the broad grain boundary character distribution in polycrystalline materials. This effective grain boundary diffusivity is directly applicable in the kinetic C-regime where diffusion exclusively takes place in grain boundaries. Even in cases where lattice diffusion is also important, such as in the kinetic A- and B-regimes[§] [94] or in the recently-developed D-regime [95-98], knowledge of the contribution from the grain boundary network as a whole is still needed in order to reasonably model the diffusion properties of real microstructures. There have been many efforts to couple grain boundary diffusion with lattice diffusion through general mixing rules [99] or Fisher-type models [100-103], where only a single value of grain boundary diffusivity has been adopted. We may improve upon these models by replacing this single value with the effective grain boundary diffusivity.

However, this 'average' grain boundary diffusivity is by no means a simple linear average, because the diffusion behavior not only depends on the statistical distribution of grain boundary diffusivities, but also on the topology of the heterogeneous grain boundary network. In other words, the grain boundary networks should not be treated simply as a multicomponent ensemble but rather a true network where the interconnectivity among grain boundaries plays an important role. Percolation theory is an appealing method for relating macroscopic properties such as diffusivity to the topology of grain boundary clusters and networks. However, the use of percolation theory to predict grain boundary diffusion-controlled properties is complicated by additional topological issues. Although many high-diffusivity boundaries may be connected together in a complex and tortuous cluster structure, generally only the backbone of the cluster is a path for fast diffusion, and dangling branches will not contribute materially to diffusion-controlled properties. The effects of percolation on diffusion need to be rigorously studied instead of being simply conjectured from geometry only.

[§] The kinetic regimes are usually classified according to the Harrison criterion (Harrison LG, 1961), which is based on a polycrystalline geometry containing parallel grain boundaries. In the kinetic-A regime, diffusion fields from adjacent grain boundaries overlap each other, forming a macroscopically homogeneous diffusion profile that can be described by an effective diffusion coefficient of the polycrystal. In the B regime (shorter diffusion time or larger distance between grain boundaries), diffusion occurs in grain boundaries and in the lattice regions close to grain boundaries. In the C regime, diffusion takes place only in defects; this is usually referred to as short-circuit diffusion.

2.1.2. Simulation Procedures

In order to directly compare to prior literature [104-107], we confine our attention to a simple, well-studied system: a two-dimensional honeycomb grain structure. The model system is a square domain containing 6853 grains and 20228 grain boundaries. The simulation method is based on the analogous network model for electrical conductivity of a bond network proposed by Kirkpatrick [5]. The diffusant concentration is a constant, C_0, at the left side of the network and zero at the right side, while a zero-flux condition is imposed at the top and bottom. Thus the macroscopic concentration gradient runs left-to-right (see Figure 10(a)). For simplicity we consider only the steady-state diffusion, although the present results are easily adapted to kinetic situations.

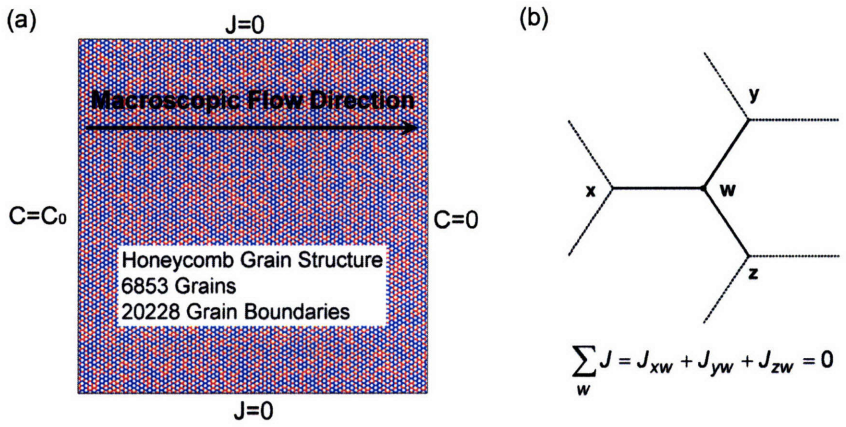

Figure 10. (a) Boundary conditions used to simulate the effective diffusivity of heterogeneous grain boundary networks. C is the diffusant concentration and J is the diffusional flux. (b) Requirement of mass balance at every triple junction.

We assume the material to be isotropic so that the second-rank diffusivity tensor can be reduced to a single diffusion coefficient. This limitation allows a more thorough focus on the effects of microstructure. We simplify the broad grain boundary character distribution according to a binary classification: "special" high coincidence boundaries of a low diffusivity D_1 and other "general" boundaries of a much higher diffusivity D_2 [108]. Here we assign grain boundary diffusivities in a random manner (uncorrelated): each boundary was assigned D_2 with a prescribed probability p', and D_1 otherwise. By varying p', we obtain systems with different grain boundary character distributions, characterized by the fraction of high-diffusivity (D_2) boundaries, p ($p \approx p'$). Later in Chapter 4.1 we will also introduce appropriate correlations for true polycrystals.

The diffusant concentration at a triple junction w is denoted as C_w, the concentration gradient along the boundary connecting the junctions x and w as ∇C_{xw}, and the corresponding mass flow rate J_{xw} is given by Fick's first law:

$$J_{xw} = -D_{xs}\nabla C_{xw} \tag{39}$$

We forbid mass accumulation at triple junctions, and thus mass balance is required at each junction, as shown in Figure 10(b). This results in a linear system of N equations with the unknowns being the concentrations at the N triple junctions. Each equation writes as

$$\left(\frac{D_{xw}}{L_{xw}}+\frac{D_{wy}}{L_{wy}}+\frac{D_{wz}}{L_{wz}}\right)C_w - \frac{D_{xw}}{L_{xw}}C_x - \frac{D_{wy}}{L_{wy}}C_y - \frac{D_{wz}}{L_{wz}}C_z = 0 \tag{40}$$

The coefficient matrix derived from these equations is sparse and weakly diagonally dominant, and the equation is numerically solved by Gaussian elimination. The solution gives the concentration C at every junction in the system, with which the concentration gradient ∇C and flux J along each boundary can be calculated. The "effective" diffusivity of an average boundary in the network is calculated as:

$$D_{eff} = -\frac{\langle J \rangle}{\langle \nabla C \rangle} \tag{41}$$

Where <> denotes an ensemble average. Since the macroscopic diffusion behavior is sensitive to network topologies that could be slightly different even for different network instances at the same boundary fraction, all of the reported values of D_{eff} are obtained by averaging results from many realizations of the network around the fraction of interest.

As mentioned earlier, many Fisher-type models [95-98] explicitly examine ranges over which D_{gb}. D_{bulk}, and D_{pipe} dominate the diffusion problem, using a simple microstructural geometry. They generally do not apply to systems containing large-scale heterogeneous grain boundary networks. Our approach is complimentary to these types of models. We have assumed any mass transport in the bulk or along dislocation cores to be negligible, and instead focus on the more complex long-range diffusion along grain boundaries in a large heterogeneous microstructure. This implies that for any case we have simulated, bulk and pipe diffusion are never faster than diffusion along the boundaries of a low-diffusivity in our network. Alternatively, one may regard the effective grain boundary diffusivity D_{eff} we calculate here as a macroscopic estimate of the contribution from grain boundaries to the overall diffusivity of polycrystalline materials. Contributions from bulk and pipe diffusion can then be introduced using the established Fisher-type models [95-98] or a composite model we have developed [109], with D_{gb} replaced by D_{eff} from this work.

2.1.3. Percolation Threshold of the Effective Grain Boundary Diffusivity

In Figure 11, the effective macroscopic diffusivity D_{eff}, normalized by the higher boundary diffusivity D_2, is plotted as a function of the fraction of general boundaries, p, for a broad range of diffusivity contrasts D_2/D_1. With an increase in p, D_{eff} increases monotonically but nonlinearly. The nonlinearity becomes more pronounced with increasing contrast ratios. Looking more closely, we note that the curves for $D_2/D_1 < 10^4$ appear continuous while for $D_2/D_1 > 10^4$, there is a discernible discontinuity in D_{eff}. At the highest contrast studied here, the increase in D_{eff} around a fraction of $p \approx 0.65$ becomes abrupt. This critical

fraction is almost the same as the percolation threshold for geometric connectivity, p_c = 1-2sin(π/18) ≈ 0.6527 [3, 30]. In other words, the sudden increase in D_{eff} at p_c is related to the emergence of a percolating (sample-spanning) cluster of general grain boundaries, which has a high-diffusivity D_2, in the network.

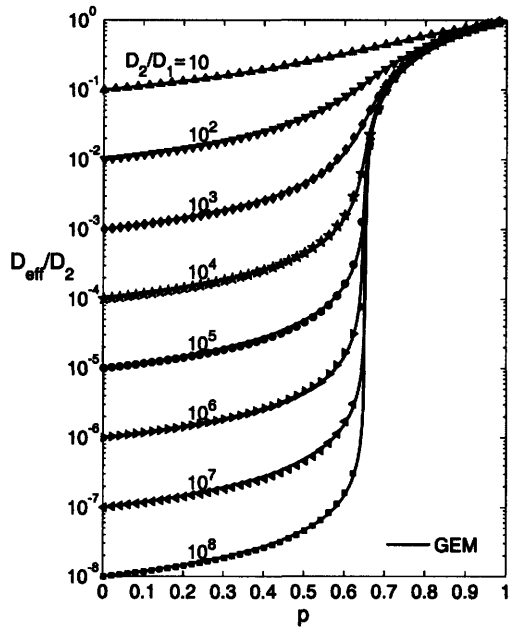

Figure 11. Dependence of the normalized effective diffusivity D_{eff}, normalized by D_2, on the fraction p of boundaries with diffusivity D_2 at various diffusivity contrast rations (D_2/D_1 = 10 to 10^8). The simulation results (averaged over many network realizations) are plotted as discrete data points. The solid lines are the prediction of the generalized effective medium (GEM) equation (Eq. (36)) that will be discussed later in section 2.1.4.

The dependence of diffusion on grain boundary networks on the network connectivity is further illustrated in Figure 12, which compares the diffusion profile in (a) with the percolating cluster in (b) for a random network with $D_2/D_1 = 10^8$ and $p \approx 0.67$ ($p > p_c$). The grey scale in (a) indicates the magnitude of diffusional flux along boundaries judged by comparing to appropriately chosen thresholds: black - high flux; deep grey - medium flux; light grey - low flux. The percolating cluster of general boundaries in (b) is identified using the Hoshen-Kopelman (HK) multiple labeling technique [110]. Further, the backbone of the percolating cluster has been identified using a custom Roux-Hansen type algorithm [111] that removes dangling ends of the percolating cluster through operations on the dual lattice. The identified backbone is highlighted in bold lines in Figure 12(b). Comparing Figure 12(a) and 4(b), it is clear that diffusion occurs primarily along the backbone of the percolating cluster of general boundaries.

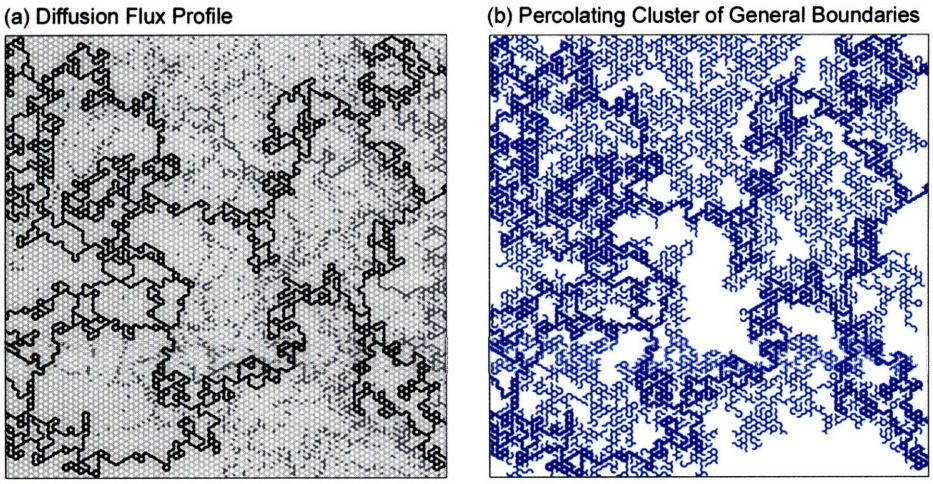

Figure 12. (a) Diffusion profile of all boundaries in the randomly distributed grain boundary network with the fraction of general fast-diffusing boundaries $p \approx 0.6601$ ($p > p_c$). The grey scale indicates the magnitude of the flux along boundaries distinguished by appropriately chosen thresholds: black - high flux; deep grey - medium flux; light grey - low flux. (b) The percolating cluster of general boundaries in the same network, with its backbone highlighted in bold lines.

2.1.4. Percolation Scaling

With the percolation threshold p_c fixed at 0.6527, the divergence of the effective diffusivity around this point can be fitted with conventional scaling laws below and above p_c:

$$D_{eff} \propto |p - p_c|^{-s} \quad (p < p_c) \tag{42}$$

$$D_{eff} \propto |p - p_c|^{t} \quad (p > p_c) \tag{43}$$

While most scaling laws emphasize near-threshold behavior, we have aimed at describing the effective diffusivity of the network over a wide composition range by fitting Eqs. (42) and (43) to $0 < p < 0.6$ and $0.7 < p < 1$, respectively. Although this reduces the fitting quality slightly, the fitted scaling laws match the simulation data quite well, as evident in Figure 13 where the fits at four different high contrast ratios are shown.

The scaling exponents obtained from the fitting are $s = 1.05 \pm 0.07$ and $t = 1.15 \pm 0.1$. The D_2/D_1 value has little effect on the fitted exponents. These values of s and t are in line with prior studies on the analogous problem of electrical conductivity in binary systems with component conductivities σ_1 and σ_2 [37, 112, 113]. In the limit $\sigma_2/\sigma_1 \to \infty$, s and t become the critical exponents for the conductor-superconductor mixture ($\sigma_2 = \infty$) and the insulator-conductor mixture ($\sigma_1 = 0$), respectively, and are equal to each other as already proven in Eq. (31) on Page 26. In this case, the reported values for s and t in two dimensions are approximately 1.3 [114-117]. The singularity that takes place when $\sigma_2/\sigma_1 \to \infty$ is broadened when both σ_1 and σ_2 are finite [118], and thus s and t depend on the definition of their respective validity ranges

[119]. Currently no consensus has been reached regarding the universal values of s and t for systems of imperfect contrast, but generally they are believed to be in the range of 1 to 2 [105, 120]. Some typical reported values are s = 1.0±0.1 and t = 1.1±0.1 [113], which are very close to the fitted exponents we obtain here.

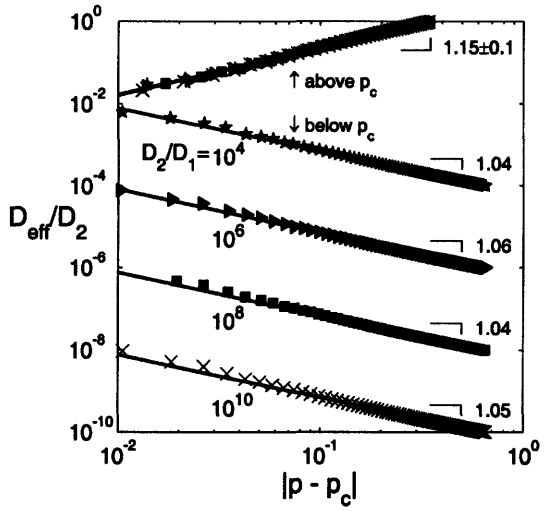

Figure 13. Fitting the normalized effective diffusivity D_{eff}/D_2 from simulation at four high contrast ratios to percolation scaling laws, Eq. (27) and (28). The fitted exponents are $s \approx 1.05\pm0.07$ below the percolation threshold p_c and $t \approx 1.15\pm0.1$ above p_c.

2.1.5. Predicting Effective GB Diffusivity by Combining Percolation and Effective Medium Theories

The symmetric effective medium theory (EMT) equation (Eqs. (11) and (12)) derived for composite solids without an obvious matrix phase was subsequently re-derived for a heterogeneous network by Kirkpatrick [5]. He derived a network EMT equation where the network interconnectivity is represented by the coordination number z of the vertices. The dimensionality d in Eqs. (11) and (12) is replaced by z/d in the new equation, which reads as

$$\int \frac{D - D_{eff}}{D + (z/d - 1)D_{eff}} f(D)dD = 0 \tag{44}$$

for heterogeneous networks with a continuous distribution of diffusivities. $f(D)$ is the diffusivity probability distribution function. For binary systems Eq. (44) reduces to

$$(1-p)\frac{D_1 - D_{eff}}{D_1 + (z/d - 1)D_{eff}} + p\frac{D_2 - D_{eff}}{D_2 + (z/d - 1)D_{eff}} = 0 \tag{45}$$

where p is the fraction of bonds (or boundaries in the present context of grain boundary networks) with diffusivity D_2.

For the hexagonal networks simulated in the present study, $z = 3$. Predictions form the network EMT equation, Eq. (45), are compared to the simulation data at several diffusivity contrast ratios (D_2/D_1) in Figure 14. Eq. (45) is in good agreement with simulation results when D_2/D_1 is very low (e.g., $D_2/D_1 < 10^2$). For the case $D_2/D_1=10^3$ and 10^4, the estimation of Eq. (8) is measurably lower than the simulation data for p in the range ~0.5-0.7. The reason for this disagreement is almost certainly the emergence of percolation-dominant behavior as the diffusivity contrast increases. Unfortunately EMT cannot capture such topological complexities.

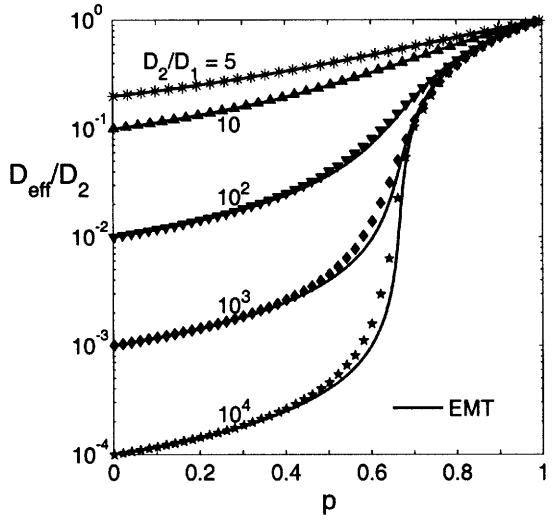

Figure 14. Prediction of the effective diffusivity from the network EMT (Eq. (45)) compared with simulation data.

It is obvious from Figure 6(b) and Figure 14 that whatever appears as the multiplying coefficient of D_{eff} in the denominator in EMT equations determines the critical fraction at which the effective diffusivity suddenly increases. In percolation theory, this critical fraction is considered as the percolation threshold. Therefore, although the symmetric EMT (Eq. (11) and (12)) and the network EMT (Eq. (45)) did not consider the effects of connectivity and percolation transition, both of them have implicitly assumed a percolation threshold, $1/d$ in the symmetric EMT and d/z in the network EMT. For a hexagonal network, the network EMT predicts a percolation threshold at 2/3, which is fairly close, but unfortunately not identical, to the true percolation threshold for random distributions, $p_c = 0.6527$. This can also be seen in Figure 14(a) where the network EMT equation predicts a critical transition at a fraction slightly higher than the true percolation threshold. In addition, both EMT theories have also implicitly assumed both scaling exponents to be unity. In fact, the scaling exponents should be $s \approx 1.05\pm0.07$ below p_c and $t \approx 1.15\pm0.1$ above p_c (see Figure 13).

The GEM equation (Eq. (36)), which is a combination of percolation and effective medium theories, can overcome both of these shortcomings. In Eq. (36), the percolation threshold and scaling exponents are explicitly included as materials parameters instead of being predefined. Therefore we can use true

percolation properties in the equation such as $p_c = 0.6527$, $s \approx 1.05 \pm 0.07$, and $t \approx 1.15 \pm 0.1$ to describe a randomly-distributed hexagonal network. The predictions from Eq. (36) are in good agreement with simulation results in the full range of p and at all diffusivity contrast ratios, as shown in Figure 11.

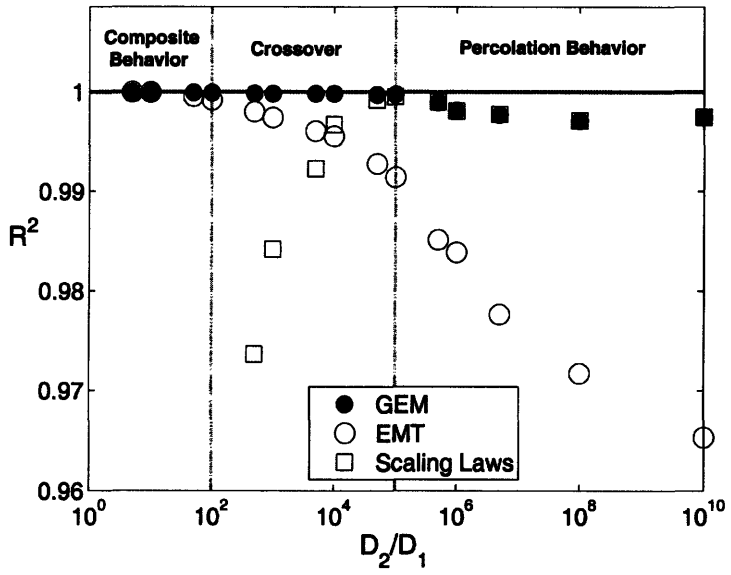

Figure 15. Coefficient of determination, R^2, as a function of the diffusivity ratio, D_2/D_1, for three different models: the GEM equation (Eq. (36)), the network EMT (Eq. (45)) and the percolation scaling laws (Eq. (27) and (28)).

To further compare the effectiveness of the percolation scaling laws (Eq. (27) and (28)), the network EMT (Eq. (45)) and the GEM equation (Eq. (36)), we plot in Figure 15 the coefficient of determination, R^2, a measure of how well the corresponding model fits the true response calculated rigorously from the network simulations, as a function of the diffusivity contrast. We can see that the quality of the fit provided by the percolation scaling laws drops quickly when D_2/D_1 is below ~10^5, while the effectiveness of the network EMT drops when D_2/D_1 is above ~10^2. Between these values is what we will term the "crossover" regime, in which the system exhibits behavior reminiscent of both percolating systems and composite materials, but cannot be simply described by either one of these approaches alone. The GEM equation, which combines the features of the percolation and effective medium theories, fits well to the simulation data for all diffusivity ratios.

2.1.6. Multicomponent Systems

Conventional effective medium theories (EMTs) fail to capture the percolation behavior of high-contrast systems [5, 6, 18], while the GEM equation (Eq. (36)), though capable of describing percolating systems,

is written only for binary cases [48, 121]. Here we extend the GEM equation to the multicomponent case in order to describe more realistic polycrystals in which there may be a wider spectrum of grain boundary character [65, 90, 91]. However, the GEM equation cannot be simply extended by adding one more term for each additional component because the terms are not symmetric anymore with two possibly different scaling exponents *s* and *t*.

2.1.5.1. Representing Topological Complexities in Percolation Quantities

We begin with a homogeneous medium with diffusivity D_{eff} and consider diffusion driven by a concentration gradient $\phi = \nabla C$ where C is the concentration of diffusant. Inserting a bond (grain boundary) with a different diffusivity D into the medium, under a conserved flux condition, will result in a deviation in the local ϕ [**] [5, 17, 122]:

$$\Delta\phi \propto \frac{D - D_{eff}}{D + AD_{eff}} \tag{46}$$

where the parameter A should depend on the dimensionality and system geometry. Following McLachlan [121, 123], we may write the deviation function in a more general form in order to incorporate the percolation scaling laws. For a binary system with phase diffusivities D_1 and D_2 ($D_1<D_2$), we have

$$\Delta\phi_1 \propto \frac{D_1^{1/s} - D_{eff}^{1/s}}{D_1^{1/s} + AD_{eff}^{1/s}} \quad \text{and} \quad \Delta\phi_2 \propto \frac{D_2^{1/t} - D_{eff}^{1/t}}{D_2^{1/t} + AD_{eff}^{1/t}} \tag{47}$$

where $A = p_c^{-1} - 1$ with p_c the percolation threshold; the subscripts 1 and 2 denote the two components. If the components are uncorrelated, we can insert them one by one into the medium; the average deviation is then $p_1\Delta\phi_1 + p_2\Delta\phi_2$. We require the final heterogeneous system generated by the insertion to be macroscopically equivalent to the original homogeneous system with diffusivity D_{eff}. The average deviation in ϕ thus has to vanish [17]:

$$p_1\Delta\phi_1 + p_2\Delta\phi_2 = 0 \tag{48}$$

where p_1 and p_2 are the fractions of phase 1 and 2, respectively. Eqs. (47) and (48) together are equivalent to the GEM equation (Eq. (36)).

If the two components are not randomly distributed but rather spatially correlated, they can no longer be inserted into the medium independently. In other words, the total fluctuation in ϕ not only includes a linear addition of individual deviations, $p_1\Delta\phi_1 + p_2\Delta\phi_2$, but also an additional cross-term that describes the correlations among the two components, $p_1p_2\Delta\phi_{1-2}$. The requirement of zero average deviation must still apply:

[**] Ideally both ϕ and $\Delta\phi$ should be vectors. But in mean field theories, coordinates or positions of the particles have not been taken into account (see section 1.2.2). The theories can be considered, alternatively, as being developed by assuming all particles are located at the same position. The average scheme thus does not have to consider the vector nature of the fields.

$$p_1\Delta\phi_1 + p_2\Delta\phi_2 + p_1p_2\Delta\phi_{1-2} = 0 \tag{49}$$

The analytical form of $\Delta\phi_{1-2}$ is not easy to determine because it depends on the detailed geometry of the components as well as the distances and correlations among them. An alternative strategy to calculating $\Delta\phi_{1-2}$ is to instead assume that the correlations can be properly captured by a shift in the percolation threshold p_c, as is the case for correlated percolation problems. The scaling exponents s and t should be independent of such correlations, provided they exist only over a finite length scale. In this scenario, the deviations still have the same forms as Eq. (47), and the GEM equation for correlated systems can still be written as:

$$p_1\frac{D_1^{1/s} - D_{eff}^{1/s}}{D_1^{1/s} + A'D_{eff}^{1/s}} + p_2\frac{D_2^{1/t} - D_{eff}^{1/t}}{D_2^{1/t} + A'D_{eff}^{1/t}} = 0 \tag{50}$$

except that $A' = (p_c')^{-1} - 1$ is calculated from the true percolation threshold p_c' of the correlated system. Comparing Eq. (50) with its counterpart Eq. (49), we obtain the analytical form of the cross-term:

$$\Delta\phi_{1-2} \propto (A - A')\cdot\left[\frac{\zeta_1 - 1}{p_2\cdot(\zeta_1 + A)\cdot(\zeta_1 + A')} + \frac{\zeta_2 - 1}{p_1\cdot(\zeta_2 + A)\cdot(\zeta_2 + A')}\right] \tag{51}$$

where $\zeta_1=(D_1/D_{eff})^{1/s}$ and $\zeta_2=(D_2/D_{eff})^{1/t}$. It is interesting to note that for high-contrast systems, at intermediate compositions around the percolation threshold p_c', $\zeta_1 << 1 << \zeta_2$, therefore Eq. (51) can be simplified to:

$$\Delta\phi_{1-2} \propto \frac{1}{p_2}\cdot\left(\frac{1}{p_c - 1} - \frac{1}{p_c' - 1}\right) \tag{52}$$

and we see that the cross-term directly stems from the difference in the percolation thresholds for correlated and random systems. For positive correlations that tend to cluster fast-diffusing boundaries together, the percolation threshold decreases ($p_c' < p_c$), resulting in a negative cross-term ($\Delta\phi_{1-2} < 0$). When the probability of finding boundaries of the same type in the same neighborhood is higher than average, the required driving force for diffusant flow will be lower than in the randomly-distributed networks. A positive cross-term would denote the opposite: there is an increase in the percolation threshold and accordingly, adjacent boundaries are more likely to be of different types.

2.1.5.2. Effective Medium Theory for Multicomponent Systems

Consider a network composed of n ($n\geq 2$) types of grain boundaries of diffusivity D_1, D_2 ...D_n ($D_1<D_2<...D_n$) with fractions p_1, p_2 ...p_n. As boundaries are placed into the effective medium, they cause concentration gradient fluctuations. Cross-term deviations are also produced as a consequence of correlations with other boundaries, and here we only consider pair-wise correlation effects. We divide type-k boundaries into n-1 parts, the fraction of those correlated with type-m boundaries being f_{km}:

$$f_{km} = p_k\cdot\frac{p_m}{1 - p_k} \tag{53}$$

and

$$\sum_{m=1,m\neq k}^{n} f_{km} = p_k \tag{54}$$

If we insert f_{km} type-*k* boundaries and f_{mk} type-*m* boundaries together into the effective medium, and assume as in section 2.1.5.1 that their correlations are captured properly by a new percolation threshold of the *k*-*m* binary system, p_c^{k-m}, the average deviation in concentration gradient ϕ is then $f_{km}\Delta\phi_{km} + f_{mk}\Delta\phi_{mk}$, where $\Delta\phi_{km}$ is the deviation arising from the introduction of a type-*k* boundary considering its correlation with type-m boundaries, and can be calculated from Eq. (47) using p_c^{k-m}. The zero average deviation requirement then gives:

$$\sum_{\langle k,m\rangle}(f_{km}\Delta\phi_{km} + f_{mk}\Delta\phi_{mk}) = 0 \tag{55}$$

where $\langle k,m\rangle$ denotes pair summation over all possible $n(n\text{-}1)/2$ component pairs. Since the two terms in Eq. (55) have equivalent forms, the pair summation can be rearranged into a double summation:

$$\sum_{k=1}^{n}\left(\sum_{m=1,m\neq k}^{n} f_{km}\Delta\phi_{km}\right) = \sum_{k=1}^{n}\left[\sum_{i=1}^{k-1}(f_{ki}\cdot\Delta\phi_{ki}) + \sum_{j=k+1}^{n}(f_{kj}\cdot\Delta\phi_{kj})\right] = 0 \tag{56}$$

As defined, $D_i<D_k<D_j$ when $i<k<j$, and therefore $\Delta\phi_{ki}$ and $\Delta\phi_{kj}$ respectively assume the two forms in Eq. (47). Further introducing Eq. (53) into Eq. (56), we find:

$$\sum_{k=1}^{n}\frac{p_k}{1-p_k}\cdot\left[\sum_{i=1}^{k-1}\left(p_i\cdot\frac{D_k^{1/t}-D_{eff}^{1/t}}{D_k^{1/t}+A_{ki}D_{eff}^{1/t}}\right) + \sum_{j=k+1}^{n}\left(p_j\cdot\frac{D_k^{1/s}-D_{eff}^{1/s}}{D_k^{1/s}+A_{kj}D_{eff}^{1/s}}\right)\right] = 0 \tag{57}$$

where $A_{ki} = (p_c^{k-i})^{-1} - 1 = A_{ik}$, and p_c^{k-i} is the percolation threshold for *k*-*i* binary system. *s* and *t* have the same values as in simple binary systems, i.e., they are independent of the number of components in the systems. Eq. (57) can be solved numerically to obtain the effective diffusivity of multicomponent heterogeneous networks.

Our multicomponent GEM equation, Eq. (57), reduces to McLachlan's generalized effective medium (GEM) equation (Eq. (36)) when $n = 2$. It is worth mentioning that Eq. (57) is very general: it can be applied to both random and correlated systems, and should also be applicable in various dimensions. Both the correlations and the dimensionality enter the equation via their influence on the percolation threshold p_c, and the dimension also affects the exponents *s* and *t*.

2.1.5.3. Comparison of Theory with Simulation

As an illustration, we apply Eq. (57) to the case of diffusion on a random two-dimensional ternary grain boundary network. Because the percolation threshold, p_c, is the same for every pair of components in a randomly-distributed system, Eq. (57) becomes:

$$\sum_{k=1}^{n}\frac{p_k}{1-p_k}\cdot\left[\left(\sum_{i=1}^{k-1}p_i\right)\cdot\frac{D_k^{1/t}-D_{eff}^{1/t}}{D_k^{1/t}+AD_{eff}^{1/t}} + \left(\sum_{j=k+1}^{n}p_j\right)\cdot\frac{D_k^{1/s}-D_{eff}^{1/s}}{D_k^{1/s}+AD_{eff}^{1/s}}\right] = 0 \tag{58}$$

where $A=p_c^{-1}-1$. For a ternary system, $n=3$ and so Eq. (58) can be further reduced to:

$$p_1\frac{D_1^{1/s}-D_{eff}^{1/s}}{D_1^{1/s}+AD_{eff}^{1/s}}+\frac{p_2}{1-p_2}\left(p_1\frac{D_2^{1/t}-D_{eff}^{1/t}}{D_2^{1/t}+AD_{eff}^{1/t}}+p_3\frac{D_2^{1/s}-D_{eff}^{1/s}}{D_2^{1/s}+AD_{eff}^{1/s}}\right)+p_3\frac{D_3^{1/t}-D_{eff}^{1/t}}{D_3^{1/t}+AD_{eff}^{1/t}}=0 \qquad (59)$$

For this simple case, all the percolation thresholds are $p_c=0.6527$, and the exponents $s=1.05$ and $t=1.15$ are the parameters from the binary problem.

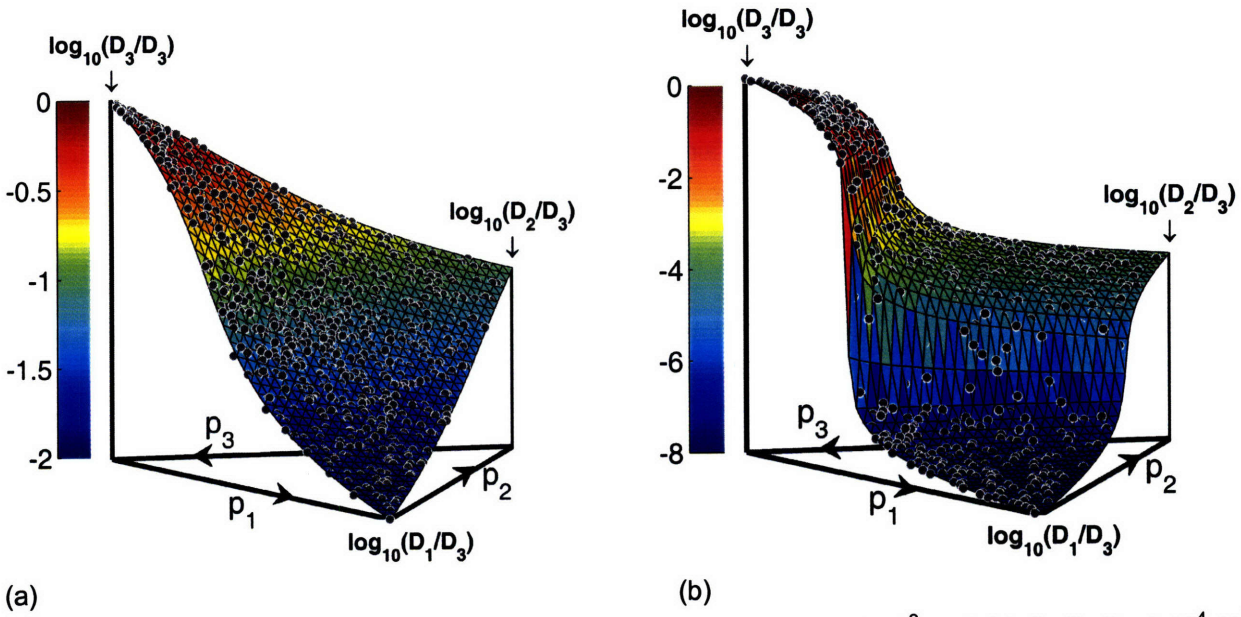

Figure 16. The effective diffusivity of ternary systems (a) D_1:D_2:D_3=1:10:10^2 and (b) D_1:D_2:D_3=1:10^4:10^8. Calculation from the derived multicomponent GEM equation (Eq. (59)) is plotted as the color surface while simulation data are plotted as black dots.

The predictions of Eq. (59) are compared with simulation results at low contrasts (D_1:D_2:D_3=1:10:10^2) in Figure 16(a) and at high contrasts (D_1:D_2:D_3=1:10^4:10^8) in Figure 16 (b). These are ternary diagrams of effective diffusivity with each axis of the triangle mapping to the fraction of boundaries of each type. Here the simulation data are shown as discrete points, while the prediction of Eq. (59) is shown as a triangulated color surface. The agreement is excellent for both diffusivity contrasts, indicating that our model captures both composite- and percolation-type systems.

Although the results in Figure 16 do not specifically address the complexities of true grain boundary networks (i.e., a realistic spectrum of boundary properties and crystallographic correlations), they do illustrate a general method by which the current literature on binary crystallographic networks can be adapted to incorporate advances in the understanding of the structure-property relationships of individual grain boundaries.

2.2. Grain Boundary Diffusional Creep (Coble Creep)

2.2.1. Coble Creep in Homogeneous and Locally-Heterogeneous Materials

Coble creep [84], or grain boundary diffusional creep, is a Newtonian deformation mechanism for polycrystals. Coble creep is an important deformation mechanism at relatively low stresses, warm temperatures (generally $T < 0.5T_M$) and small grain sizes, as revealed in common deformation mechanism maps [124]. It occurs via non-uniform mass transport along grain boundaries driven by gradients of the normal stress acting on the boundaries, which promotes preferential mass accumulation at those under tension. This stress-driven grain boundary diffusion arises from a vacancy concentration gradient, similar to the usual diffusion via a vacancy mechanism.

$$J_v(x) = -D_v \frac{dC_v}{dx} \xrightarrow{\Delta C_V \approx C_{V0}\frac{\sigma\Omega}{kT}} -\frac{D_v C_{V0}\Omega}{kT}\frac{d\sigma}{dx} \xrightarrow{D_{gb}=D_v C_{v0}\Omega} -\frac{D_{gb}}{kT}\frac{d\sigma}{dx} \tag{60}$$

where σ is the stress normal to the grain boundary, and x denotes a path coordinate along a grain boundary. Eq. (60) is equivalent to mass diffusion in the opposite direction.

$$J(x) = -J_v(x) = \frac{D_{gb}}{kT}\frac{d\sigma}{dx} \tag{61}$$

Here the flux has been defined as number of atoms passing through unit area per unit time, which results in a unit of $1/(m^2 s)$ for $J(x)$. Eq. (61) can be alternatively understood from a change in the mass diffusion potential due to the normal stresses acting on grain boundaries. The new diffusion potential is $\Phi = \mu^0 - \sigma\Omega$, where μ^0 is the chemical potential of an atom in a stress-free system, and the normal stress σ is considered positive if it is tensile, negative if it is compressive. The flux can then be written as

$$J(x) = -L\frac{\partial\Phi}{\partial x} = -M\cdot C\cdot\frac{\partial\Phi}{\partial x} = M\cdot C\cdot\Omega\frac{\partial\sigma}{\partial x} \tag{62}$$

Here $L = M\cdot C$ is the Onsager diffusion coefficient, $M = D_{gb}/(KT)$ is the mobility, and C is the atomic concentration defined as number of atoms per unit volume. Since we are only concerned with self-diffusion, to a good approximation, $C = 1/\Omega$ (there is one atom per atomic volume Ω). Introducing $M = D_{gb}/(KT)$ and $C = 1/\Omega$ back into Eq. (62), we obtain the same expression for diffusional flux as Eq. (61).

The mass redistribution due to grain boundary diffusion further induces grain movements that give rise to macroscopic deformation. Coble [84] derived a constitutive equation to predict the creep rate $\dot{\varepsilon}$:

$$\dot{\varepsilon} = \frac{1}{R}\frac{dR}{dt} \xrightarrow{\Omega\delta J = \pi R^2\frac{dR}{dt}} \frac{\Omega\delta}{\pi R^3}J \xrightarrow{R=d/2} \frac{8\Omega\delta}{\pi d^3}J \quad \propto \quad \frac{\Omega\delta D_{gb}}{KTd^3}\sigma_0 \tag{63}$$

$$\dot{\varepsilon} = \frac{A\Omega\delta D_{gb}}{kTd^3}\sigma_0 \tag{64}$$

Coble worked with a single spherical grain of radius R, considering its surface as the grain boundary. Ω is the atomic volume, δ is the grain boundary width, D_{gb} is the grain boundary self-diffusivity, K is Boltzmann's constant, T is the absolute temperature, d is the grain diameter, and σ_0 is the external stress. A is a parameter depending on the grain geometry and relaxation effects, and equals $A = 148/\pi \approx 47$ for

the spherical grain modeled by Coble. In this simple grain geometry, there is only one grain boundary, and thus only one grain boundary diffusivity D_{gb} shows up in the Coble equation Eq. (64).

Coble creep in a two-dimensional solid with perfectly hexagonal grain structures and a homogeneous grain boundary network has also been well studied [125, 126]. In this case, the creep rate can be derived analytically as well if the grain boundary sliding is assumed to be infinitely rapid, i.e., grain boundary sliding can occur instantly to accommodate mass redistribution, and shear stress along the grain boundaries is relieved instantaneously. In this case all grain boundaries have the same length L_{gb}, and thus the path coordinate x for every boundary in Eq. (61) can be expressed as $x = sL_{gb}$, where s is a unitless local path coordinate ranging from 0 to 1 along a boundary. Eq. (61) then becomes

$$J(s) = \frac{D_{gb}}{KT}\frac{\partial\sigma}{\partial(sL_{gb})} = \frac{D_{gb}}{KT}\frac{1}{L_{gb}}\frac{\partial\sigma}{\partial s} \qquad \left(\text{in } \frac{1}{\text{m}^2\text{s}}\right) \tag{65}$$

The atomic flux J is not uniform along the boundary. As a result, some diffusant in the boundary has to absorb onto the neighboring grains, or some matter in the lattice has to enter the boundary, at a rate V.

$$V(s) = -\delta\Omega\frac{\partial J}{\partial(sL_{gb})} = -\frac{\delta\Omega D_{gb}}{KT}\frac{1}{L_{gb}^2}\frac{\partial^2\sigma}{\partial s^2} \qquad \left(\text{in } \frac{\text{m}}{\text{s}}\right) \tag{66}$$

We assume that matter leaves or enters equally on both sides of the boundary, and that no overlap or void forms as a result of the plating process. Thus adjacent grains have to separate or approach each other at the speed V, and also rotate with respect to each other with a rate R.

$$R(s) = \frac{\partial V}{\partial(sL_{gb})} = -\frac{\delta\Omega D_{gb}}{KT}\frac{1}{L_{gb}^3}\frac{\partial^3\sigma}{\partial s^3} \qquad \left(\text{in } \frac{1}{\text{s}}\right) \tag{67}$$

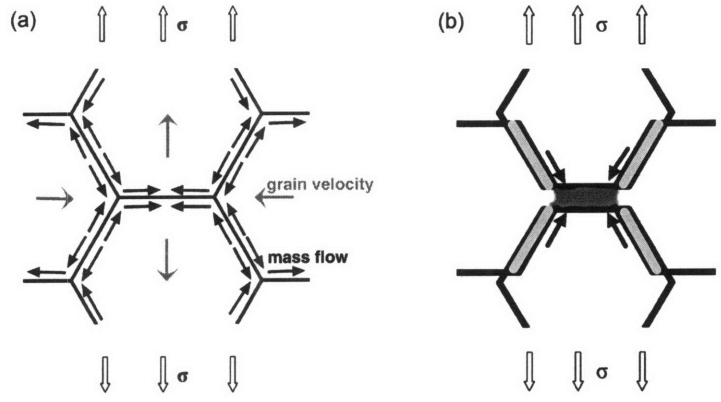

Figure 17. Schematic of the Coble creep process on a two-dimensional uniform honeycomb network of grain boundaries. (a) before deformation; (b) after deformation, where the shaded regions indicate the locations of matter redistribution, with the horizontal boundary being the energetically preferred site under creep conditions.

For a hexagonal grain structure with only one type of grain boundaries, the microstructure is perfectly symmetric and therefore grains do not rotate during the deformation. This is illustrated for a uniform

network of boundaries in Figure 17(a), and a corresponding deformed configuration is depicted in Figure 17(b). According to Eq. (67), $R(s) = 0$ can be satisfied by requiring $\partial^3\sigma/\partial s^3 = 0$ everywhere, which means that the normal stress σ should be a quadratic polynomial in s.

$$\sigma(s) = \alpha_2 s^2 + \alpha_1 s + \alpha_0 \tag{68}$$

Here the stress coefficients α_i, i = 0-2, are all in units of Pa. Because of the perfect symmetry shown in Figure 17, the stress coefficients α_i, i = 0-2, in Eq. (68) can be analytically solved from requirements such as mass balance, mechanical equilibrium, and deformation compatibility. Since every grain boundary has the same diffusivity, there are only two types of geometrically different grain boundaries, the horizontal ones which will be denoted by "h" and tilted ones which will be denoted by "t". The six unknown stress coefficients can be solved from six linear equations:

$$\text{Symmetry}: \quad J^h(s = 0.5) = 0 \tag{69}$$

$$\text{Symmetry}: \quad J^t(s = 0.5) = 0 \tag{70}$$

$$\text{Mass Conservation at triple junctions}: \quad J^h(s = 1) + 2J^t(s = 0) = 0 \tag{71}$$

$$\text{Stress Continuity at triple junctions}: \quad \sigma^h(s = 1) = \sigma^t(s = 0) \tag{72}$$

$$\text{Global Mass Conservation (Compatibility)}: \quad V^h = -2V^t \tag{73}$$

$$\text{Mechanical Equilibrium}: \quad \int_0^1 \sigma^h(s)ds + \int_0^1 \sigma^t(s)\cos(60^\circ)ds = 1.5\sigma_0 \tag{74}$$

where J, V, and σ are the diffusional flux in Eq. (65), the plating rate in Eq. (66) which is constant here, and the normal stress in Eq. (68), respectively. "h" and "t" denote horizontal and tilted grain boundaries. The stress distributions turn out to be

$$\sigma^h(s)/\sigma_0 = -6(s - 0.5)^2 + 2 \tag{75}$$

$$\sigma^t(s)/\sigma_0 = 3(s - 0.5)^2 - 0.25 \tag{76}$$

which are illustrated in Figure 18.

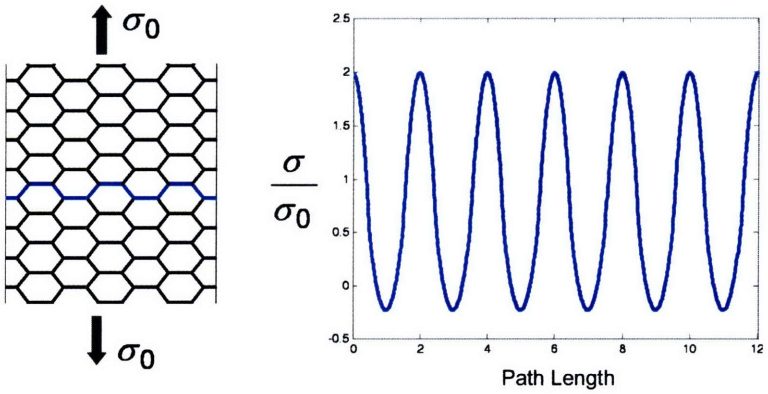

Figure 18. The distribution of the normal stress σ, normalized by the external stress σ_0, along a chosen path highlighted in blue in the honeycomb grain structure. The path length is in the unit of grain boundary length L_{gb} (edge length of the hexagons).

With the stress distributions known, the strain rate of the homogeneous microstructure can be determined from the plating of both horizontal and tilted boundaries described by Eq. (66) and the sliding of tilted grain boundaries. Introducing Eq. (75) and (76) into Eq. (66), we obtain the constant plating rate at horizontal and tilted boundaries as

$$V^h = 12\frac{\Omega\delta D_{gb}}{KTL_{gb}^2}\sigma_0 \tag{77}$$

$$V^t = -6\frac{\Omega\delta D_{gb}}{KTL_{gb}^2}\sigma_0 \tag{78}$$

It is noteworthy that although here grain boundary sliding is considered only as an accommodation process and thus the sliding rate is fully determined by the plating rate, sliding actually contributes to the macroscopic strain as well. We denote the sliding rate as V_s to distinguish it from the plating rate V. The total movement of a tilted boundary in the vertical direction (along stress axis) should be equal to half the plating rate of a horizontal boundaries, V^h, in order to avoid any void formation during the deformation.

$$V_s^t\cos(30°)+V^t\cos(60°)=\frac{1}{2}V^h \xrightarrow{\text{Eq.(73)}} -V^t \tag{79}$$

Thus

$$V_s^t = -\sqrt{3}V^t = 6\sqrt{3}\frac{\Omega\delta D_{gb}}{KTL_{gb}^2}\sigma_0 \tag{80}$$

Considering that there are in total N_{gb} grain boundaries, among which $N_{gb}/3$ are horizontal and $2N_{gb}/3$ are titled. The total strain rate of the system along the stress axis is

$$\begin{aligned}
\dot{\varepsilon} &= \frac{N_{gb}}{3}\int_0^1\left(\frac{V^h\cos(0°)}{L_y}\cdot\frac{L_{gb}\cos(0°)ds}{L_x}\right) && \text{(contribution from plating of horizontal boundaries)}\\
&+\frac{2N_{gb}}{3}\int_0^1\left(\frac{V^t\cos(60°)}{L_y}\cdot\frac{L_{gb}\cos(60°)ds}{L_x}\right) && \text{(contribution from plating of tilted boundaries)}\\
&+\frac{2N_{gb}}{3}\int_0^1\left(\frac{V_s^t\cos(30°)}{L_y}\cdot\frac{L_{gb}\cos(60°)ds}{L_x}\right) && \text{(contribution from sliding of tilted boundaries)}\\
&=(4-1+3)\frac{N_{gb}}{L_xL_y}\cdot\frac{\Omega\delta D_{gb}}{KTL_{gb}}\sigma_0\\
&\xrightarrow{N_{gb}=3N_{grain}\approx 3\frac{L_xL_y}{3\sqrt{3}L_{gb}^2/2}}\frac{12}{\sqrt{3}L_{gb}^2}\cdot\frac{\Omega\delta D_{gb}}{KTL_{gb}}\sigma_0\\
&\xrightarrow{d=\sqrt{3}L_{gb}}36\frac{\Omega\delta D_{gb}}{KTd^3}\sigma_0
\end{aligned} \tag{81}$$

where L_x and L_y are the system size in horizontal and vertical directions. Eq. (81) should be considered as the Coble equation for two-dimensional hexagonal grain structures with all grain boundaries being the same, i.e., having the same diffusivity. The proportionality, 36, obtained in this way is consistent with prior derivations using a different method [126], validating the present description of the problem that will be used later in our simulations.

However, all the symmetric mass flow and grain motion suggested in Figure 17, the periodic stress distribution shown in Figure 18, and the simple analytical constitutive equation Eq. (81) all become invalid for real polycrystalline materials because of the heterogeneity arising from both local geometric irregularities as well as the broad spectrum of grain boundary diffusivities. Some recent works [127, 128] have begun to address such heterogeneity on very local scales. For example, a grain of a different size or a grain boundary of a different diffusivity has been introduced into the otherwise perfectly uniform hexagonal structure. These studies have found that a larger grain and a special grain boundary with a lower diffusivity have similar effects on the creep response; they would both cause a stress concentration in order to achieve deformation rates comparable to those of the small grains or near general grain boundaries. We will confine our attention to the effects of grain boundary character distribution here.

Tong *et al.* [127] simulated Coble creep of a general boundary honeycomb network characterized by diffusivity D_g containing a single special boundary with diffusivity $D_s = 0.8D_g$, and showed that a subtle stress concentration develops at this special boundary. For the same system, Moldovan *et al.* [128] further demonstrated that the stress localization is more pronounced as D_s decreases; the local stress is enhanced by a factor of 2.25 for $D_s = 0.01D_g$. Interestingly, the opposite case of a special boundary network containing a single general boundary does not yield a quantitatively symmetric state: the local stress is decreased only by 50% [128]. This asymmetry suggests that special boundaries play a dominant role in determining the stress distribution. Asymmetry between the role of special and general boundaries has also been observed in terms of deformation homogeneity [129]. While introducing a general boundary into a special boundary network does not disturb the deformation pattern very much, the presence of a special boundary in a general boundary network substantially breaks the deformation regularity in its vicinity.

In short, all previous work on dilute binary networks has revealed that variations in grain boundary character lead to nontrivial stress or deformation localization during Coble creep. Even more pronounced effects can be expected for networks away from the dilute limit as the compatibility among grain boundaries will be satisfied in a much more complicated way.

Our interest in studying the effects of large scale topological disorder due to grain boundary character distribution (GBCD) was further stimulated by recent experimental evidence that GBCD does affect the creep rate. As far as creep is concerned, the structure-property relationships of the heterogeneous grain boundary networks can often be simplified by using a binary classification scheme for the grain boundary character. For example, high coincidence boundaries often exhibit "special" properties such as dramatically lower diffusivities [108] and sliding rates [130, 131] as compared to other more "general" boundaries. A number of investigators [132-135] have sought to experimentally correlate creep properties with simplified measures of the GBCD, e.g., the total fraction of special grain boundaries, p. Lehockey and Palumbo [132] found that an increase in p from 13% to 66% reduced the creep rate of Ni by a factor of 16 at 723K. Thaveeprungsriporn and Was [133] increased p from 16% to 35% in Ni-16Cr-9Fe, and found that the creep rate at 633K decreased by a factor of about 26 and 66 for grain sizes 330 μm and 35 μm, respectively. In a study on austenitic stainless steel, a grain boundary engineered alloy

with $p \approx 63\%$ exhibited creep rates (at 923K) more than two orders of magnitude lower than the same alloy with $p < 25\%$ [135]. These experiments are all carried out under different conditions, but they consistently indicate that special boundaries are more resistant to creep deformation than general boundaries. However, the available experimental data are very sparse, and a systematic understanding of the effect of special boundaries for specific creep deformation mechanisms, and over the full range of p, is not yet available. We hope that the present theoretical work will provide some basic understanding of the effects of GBCD on creep, which may further provide some guideline for microstructure design.

2.2.2. Simulation Procedures

The simulation procedures used in this work are essentially similar to those of Hazzledine and Schneibel [136] and Ford *et al.* [137]. The simulation cell is a two-dimensional honeycomb lattice covering a nearly square domain of size 105x104 (in units of grain boundary length L_{gb}), which contains 4331 grains and 12730 grain boundaries. The grain boundaries are classified into two types: general boundaries of a high diffusivity D_g, and special boundaries of a low diffusivity D_s. D_g/D_s is referred to throughout as the diffusivity contrast ratio. These two types of boundaries are distributed on the honeycomb network randomly. Coble creep of a correlated grain boundary network will be discussed later in section 4.1.3. The simulation cell and some important boundary conditions and parameters are shown in Figure 19.

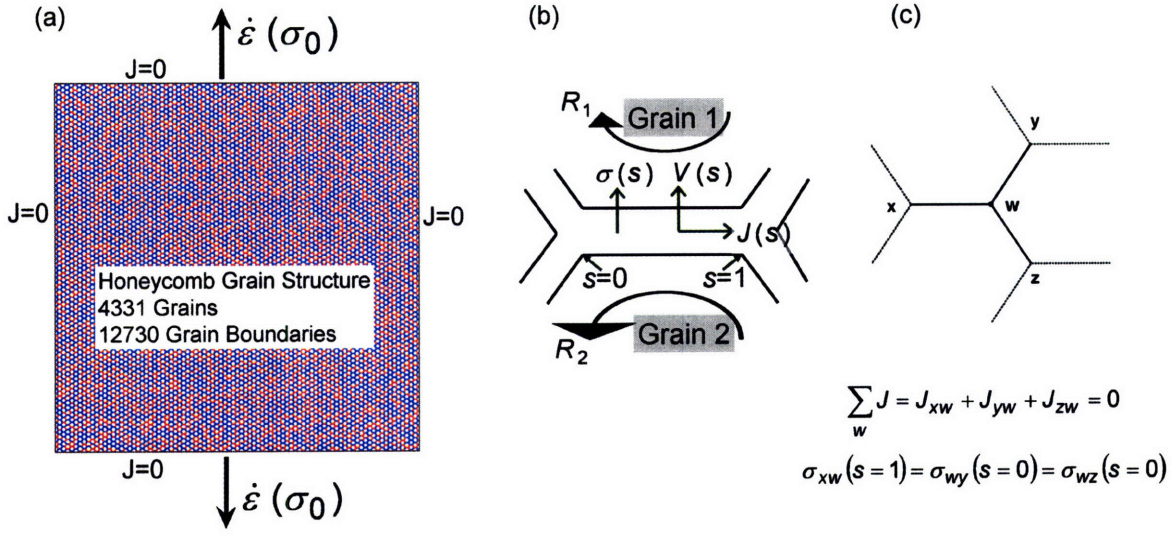

Figure 19. (a) Boundary conditions used to simulate grain boundary diffusional creep (Coble creep) for heterogeneous grain boundary networks. A constant strain rate $\dot{\varepsilon}$ is applied in the vertical direction while a zero-flux condition is imposed on all surfaces. (b) Directions of the four quantities important in the simulation. These include the normal stress σ, the diffusional flux J along the boundary, the plating rate V normal to the boundary, as well as the rotation rate R of the neighboring grains. (c) Mass conservation and stress continuity are required at every triple junction.

We perform uniaxial creep simulations under a constant strain rate condition, and focus on the response at zero strain. The top and bottom grains in the simulation cell are assigned a prescribed and a zero vertical velocity, respectively, and the side grains are constrained to move at the same horizontal velocity so as to preserve the rectangular shape of the system. Such velocity boundary conditions can lead to more accurate and reliable numerical results as compared to those obtained under other boundary conditions [137]. The applied external stress is calculated as the average of the stress acting on an arbitrary cross-section. The ratio of this external stress to the imposed strain rate is the creep viscosity η, which is a measure of the resistance to creep. Thus, the goal of the numerical procedure is basically to solve for the stress distribution in the system.

The diffusional flux J, plating rate V, and the rotation rate R are still described by Eq. (65), (66), and (67) on Page 49, except that D_{gb} in all these equations should be replaced by D_g or D_s depending on the assigned grain boundary character. Because of this, the microstructure is no longer symmetric and grains must rotate in order to prevent cracks or overlaps between them. $R(s)$ in Eq. (67) is no longer zero, but given that the grains are rigid, it should be constant along each boundary. According to Eq. (67), $\partial^4\sigma/\partial s^4 = 0$ which can be satisfied if the normal stress σ is a cubic function of s:

$$\sigma(s) = \alpha_3 s^3 + \alpha_2 s^2 + \alpha_1 s + \alpha_0 \tag{82}$$

Here the coefficients α_i, i = 1-4, are also all in units of Pa, and are unique for every grain boundary in the system. These stress coefficients, together with the translational and rotational velocities for every grain, are simultaneously obtained as the solution to a sparse linear system of equations. In addition to the boundary conditions stated above, these equations are built upon requirements of stress continuity and flux conservation at internal triple junctions, zero flux at the grain boundary–surface intersections, mechanical equilibrium, and deformation compatibility [136, 137]. These requirements are analogous to Eqs. (71) to (74), the requirements used to solve the homogeneous grain boundary network, but take on much more complicated forms because there is no longer any symmetry in the microstructure.

After the stress coefficients α_i are determined, the stress σ, the diffusional flux J, and the plating rate V along each grain boundary can then be directly obtained from Eqs. (82), (65), and (66). We first tested our code with a homogeneous grain boundary network by letting $D_g = D_s$, which led to numerical stress distributions essentially exactly matching the analytical predictions of Eq. (75) and (76). In fact Figure 18 is plotted from our simulation output for a small homogeneous system. We specifically obtained ~35.9 as the coefficient for Coble equation, very close to the analytical result, 36, in Eq. (81). (It is impossible to reach 36 in real simulations because of the finite size effect. 36 is obtained by assuming every grain to be a complete hexagon; in finite systems with straight edges the edge grains are all only part of a hexagon.) With our code tested, we now start simulating heterogeneous grain boundary networks. We calculate the external stress σ_0 by averaging the stress across the top surface of the simulation cell, and obtain a creep viscosity η for each network configuration of special boundary fraction p. η as a function of p reduces to a typical percolation problem.

2.2.3. Percolation Threshold of the Effective Creep Viscosity

We identify the ratio of the calculated stress σ_0 to the prescribed strain rate $\dot{\varepsilon}$ as the Newtonian viscosity:

$$\eta(p,L) = \langle \sigma_0(p,L)/\dot{\varepsilon} \rangle \tag{83}$$

where p is the fraction of special grain boundaries, L is the system size, and $\langle \cdots \rangle$ denotes an average over many network realizations. All the $\eta(p,L)$ values reported here will be normalized with respect to $\eta(1,L)$. In Figure 20, $\eta(p,L)$ is plotted versus p for L=21, 45 and 104 on a semi-logarithmic scale (with an inset on the linear scale), revealing the rapid change associated with a percolation transition in the vicinity of $p \approx 0.5$. Above the percolation transition the binary grain boundary network has a viscosity similar to that of a network of special boundaries. This transition occurs at higher p as the system size L is increased.

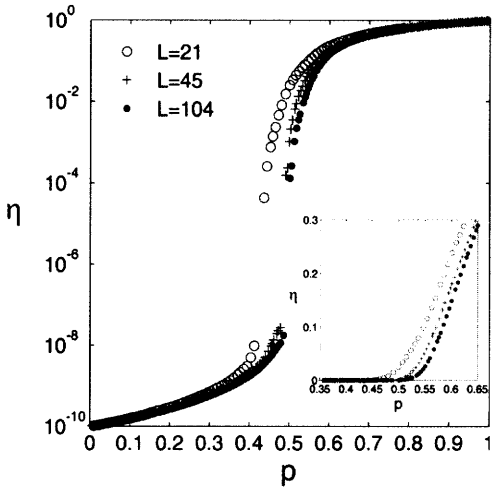

Figure 20. Normalized effective creep viscosity η as a function of the "special" boundary fraction p for three network sizes L = 21, 45, and 104. The inset is plotted in linear scale.

By assigning networks with high viscosity ($\eta(p,L) > \sqrt{\eta(0,L)\cdot\eta(1,L)}$) as "percolating", and as "not percolating" otherwise, and by averaging over many network configurations, we obtain the average probability $\Pi(p,L)$ with which a network of spatial size L percolates at fraction p [3]. This is plotted for p = 0.38-0.58 and several network sizes in Figure 21(a), where the average percolation threshold $p_{av}(L)$ is defined as the composition where $\Pi(p,L)$ = 0.5. Furthermore, the difference between the compositions corresponding to $\Pi(p,L)$=0.1 and 0.9 is defined as the 'width' of the percolation transition, $\Delta(L)$, as illustrated for the case of L = 21 in Figure 21(a). By extrapolating p_{av} to Δ = 0 (see Figure 21(b)), we obtain the percolation threshold for an infinite lattice: p_{cc}= 0.5416±0.0036.

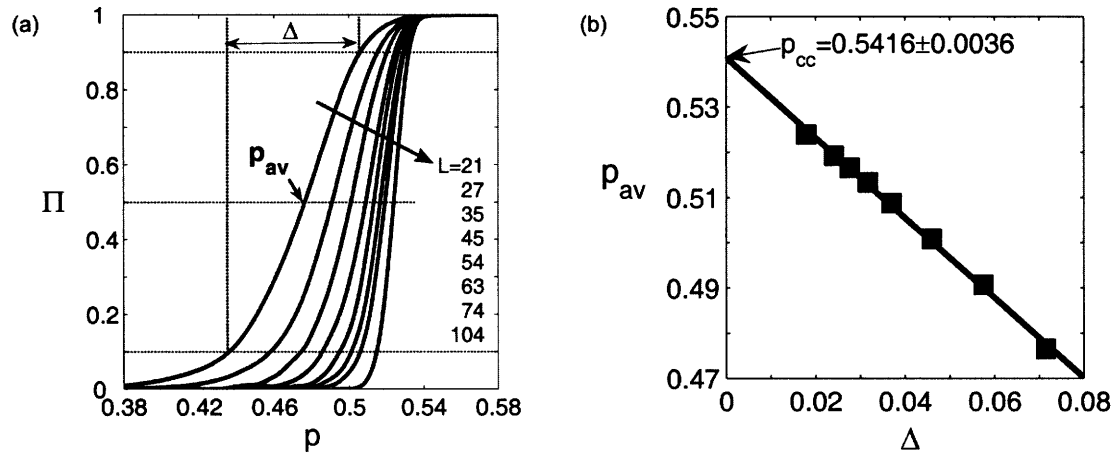

Figure 21. (a) Percolation probability Π as a function of p. (b) Average percolation threshold p_{av} versus the percolation transition width Δ of various system sizes, where extrapolation to Δ = 0 gives the percolation threshold p_{cc} of an infinite system.

This percolation threshold, p_{cc} = 0.5416±0.0036, for Coble creep on a heterogeneous honeycomb grain boundary network, is new. It has not been observed previously for any other properties. For example, geometric percolation and percolation of linear transport properties such as diffusion both have a percolation threshold at $p_c \approx 0.6527$. As discussed in section 1.3.1(Page 20), correlations could possibly cause a shift in the percolation threshold. In the present case the special and general boundaries are all randomly distributed on the network. So they must be correlated in terms of their behavior. Do such correlations change the scaling exponents? As we will see in the next section, they do!

2.2.4. Percolation Scaling and A New Universality Class

According to Eq. (19), the percolation transition width Δ scales with the system size as $\Delta(L) \propto L^{-1/\upsilon}$, where υ is the correlation length exponent defined in Eq. (23). In Figure 22(a), examination of the size scaling of Δ yields a correlation length exponent υ = 1.16±0.04.

The scaling of the creep viscosity η with respect to the special fraction p below and above the percolation threshold p_{cc} is

$$\eta(p) \propto (p_{cc} - p)^{-s} \quad \text{for } p < p_{cc} \tag{84}$$

$$\eta(p) \propto (p - p_{cc})^{t} \quad \text{for } p > p_{cc} \tag{85}$$

In the vicinity of the threshold, i.e., in the range $|p - p_{cc}| \le 0.1$, our simulation data can be fitted with approximate asymptotic exponents of $s \approx 1.88 \pm 0.12$ and $t \approx 1.69 \pm 0.09$, as we reported in Ref. [138].

These values of s and t are consistent with the values we obtain when we tuned the scaling of $L^{t/\upsilon}\eta(p,L)$ and $L^{-s/\upsilon}\eta(p,L)$ with respect to $L^{1/\upsilon}|p-p_{cc}|$ using all the finite-size results.

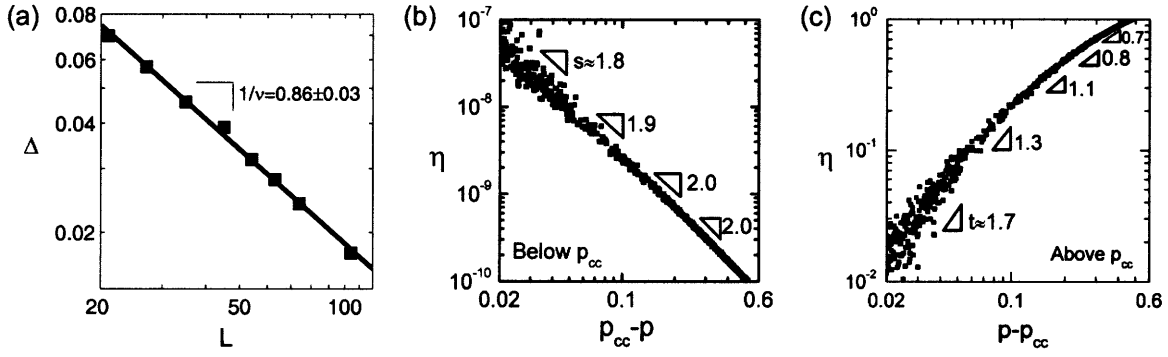

Figure 22. (a) Δ as a function of network size L, where the slope is related to the correlation length exponent υ. (b) Fitting of creep viscosity η to the power-law scaling for p below the percolation threshold p_{cc}. (c) Scaling above p_{cc}. Here we show the data for L = 104, using p_{av} for this lattice size as p_{cc}. Error ranges on the slopes $1/\upsilon$, s, and t are statistical results for the finite range of conditions tested here.

The scaling relationships over the full range of p are shown in Figure 22(b) and (c), where a series of local slope measurements is presented. Below the percolation threshold p_{cc}, the curve in Figure 22(b) generally has a well defined slope close to the asymptotic value around $s \approx 1.9$. As p approaches p_{cc} from below, s slightly decreases because the creep viscosity η below and above p_{cc} have to reconcile with each other at the threshold. In contrast, as p increases from the percolation threshold p_{cc} to 1 (Figure 22(c)), the scaling exponent t decreases substantially from ~1.7 to ~0.7. This large variation of t is well beyond what might be expected from the normal difference between near-threshold and far-from-threshold behaviors. For example, the drift is only about 0.1-0.2 for s in Figure 22(b), and even less than that in the simpler problem of concentration-gradient-driven diffusion (see Figure 13); in that case diffusion is governed by the geometric connectivity, and t is nearly a constant over the full range of p above the percolation threshold [139].

We have also examined the distribution of forces and flux that the grain boundaries carry, specifically, the moments of the force distribution [40, 46], $\{M_F(k)\}$, and moments of the flux distribution [140, 141], $\{M_J(k)\}$,

$$M_F(k) = \sum \left| L_{gb} \cdot \int_0^1 \sigma(s) ds \right|^k \propto L^{-\tilde{q}_F^k} \tag{86}$$

$$M_J(k) = \sum \left| \int_0^1 J(s) ds \right|^k \propto L^{-\tilde{q}_J^k} \tag{87}$$

where the summation runs over the ensemble of grain boundaries of interest, $\sigma(s)$ and $J(s)$ are the stress and flux defined in Eq. (82) and (65), respectively, $\tilde{q}_F^k$ and $\tilde{q}_J^k$ are the asymptotic exponents associated

with the finite-size scaling of $M_F(k)$ and $M_J(k)$ at the percolation threshold. The moments of the force distribution defined in Eq. (86) are analogous to the force moments defined in Eq. (34) for elastic spring networks (on Page 27). The only difference between them is that the stresses or forces in a system undergoing creep depend on many other quantities such as diffusional flux and plating rate, etc, while the forces in elastic networks are independent quantities. We find that the best fit of our data to Eq. (86) and (87) up to the fourth moment (k = 1-4) occurs at $p \approx 0.546$. This value is consistent with the percolation threshold, p_{cc} = 0.5416±0.0036, obtained from direct fitting in Figure 21(b). The fitting of $M_F(k)$ and $M_J(k)$, k = 1-4, to the size scaling at p = 0.546 are respectively plotted in Figure 23(a) and (b), and the corresponding scaling exponents $\tilde{q}_F^k$ and $\tilde{q}_J^k$ are presented in Table 6.

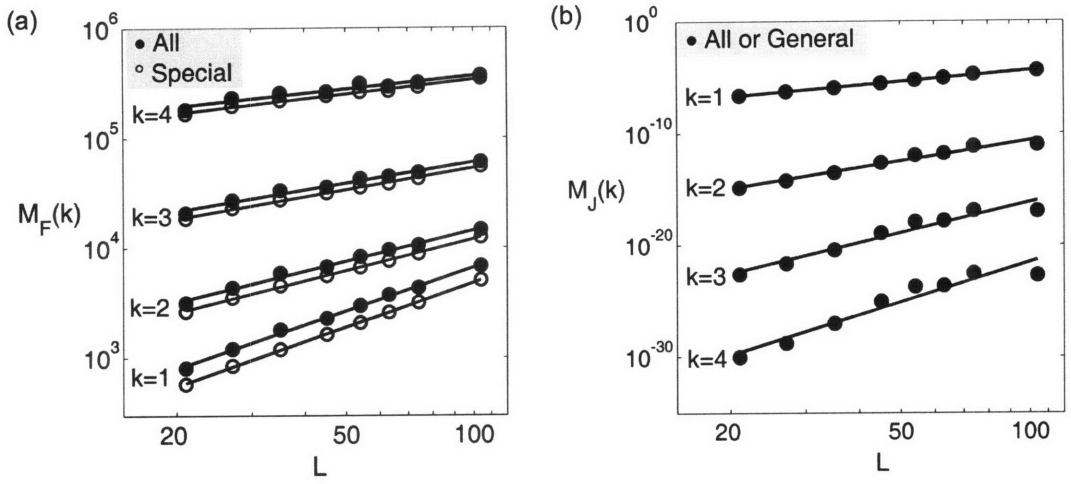

Figure 23. Moments of (a) the force distribution $M_F(k)$ and (b) the flux distribution $M_J(k)$, for orders k = 1-4, plotted against the network size L for Coble creep of the honeycomb network at p = 0.546. The data points are simulation results and the lines are least-squares fits to the data. Error analysis is not provided here due to the limited range and amount of data. In (a) results are shown for all of the grain boundaries as well as the special boundaries only; the results are similar because the special boundaries carry most of the force. Similarly, in (b) the flux distribution for the full network and just the high-diffusivity general boundaries exhibit indistinguishable scaling because most diffusional flow runs through the general boundaries.

All the parameters we have obtained to describe the threshold and scaling behavior of Coble creep are collected in Table I, and compared with their counterparts for both conductivity (or diffusivity) percolation and central-force elastic (rigidity) percolation [142], both of which have been discussed in the introduction (section 1.3.3 on Page 24). What is particularly noteworthy here is that the percolation of Coble creep, when free grain boundary sliding is assumed, exhibits a set of scaling exponents that are rather different from either conductivity or rigidity percolation; this may therefore constitute a new percolation universality class. Coble creep represents a unique type of percolation problem in that it encompasses characteristics both of and beyond the classic conductivity and rigidity problems. Grain boundaries not only provide diffusional paths (as in the conductivity problem), but also act as sources/sinks of matter due

to the variation of the flux along grain boundaries. The normal stress and the induced lateral plating seem analogous to the force and displacement of the central-force dual (triangular) lattice, and the mechanical equilibrium of grains during Coble creep also represents a force balance at vertices of the dual lattice. However, in both the conductivity and elasticity problems, a linear relationship is maintained both locally and globally between the driving force and the response (i.e., flux is proportional to the potential gradient; elastic displacement is proportional to force). In contrast, during Coble creep, the local plating rate (Eq. (66)) is not linearly proportional to, but instead is the second derivative of, the normal stress acting on the grain boundaries (Eq. (82)). In short, although we study the percolation aspect of Coble creep by varying the fraction of 'special' grain boundaries, the system under investigation is in fact more than a simple bond network. It is a continuum where both the grains and the surrounding grain boundaries are involved in the deformation process. As such, the system exhibits more complex behavior and a unique set of scaling exponents.

Table 6. Comparison of percolation parameters for Coble creep, conductivity, and central-force rigidity in two dimensions.

	Coble creep	Conductivity	Central-force Rigidity
p_c	0.5416±0.0036[a]	0.6527[b]	0.58[c] or 0.641[d]
ν	1.16±0.04	4/3[e]	1.14±0.1[f]
s	1.88±0.12	1.3[g]	1.12[h]
t	1.69±0.09	1.3[g]	2.4±0.4[c]
$\tilde{q}_F^1$	-1.31		0.76±0.05[i]
$\tilde{q}_F^2$	-0.93		2.95±0.25[i]
$\tilde{q}_F^3$	-0.64		4.94±0.45[i]
$\tilde{q}_F^4$	-0.40		7.05±0.75[i]
$\tilde{q}_J^1$	-3.32		
$\tilde{q}_J^2$	-6.11	-0.98±0.01[k]	
$\tilde{q}_J^3$	-9.06		
$\tilde{q}_J^4$	-11.89	-0.81±0.02[k]	

[a] Honeycomb lattice

[b] Honeycomb lattice. Ref. [143]

[c] Triangular bond lattice. Ref. [142]

[d] Triangular bond lattice. Refs. [40, 43]

[e] Ref. [30]

[f] Ref. [144]

[g] Ref. [116]

We want to point out that the present analysis involves a system of imperfect contrast, so the comparison of the present results to the perfect contrast conductivity or rigidity percolation problems is not necessarily straightforward. This situation is further complicated by the requirement of concurrent force and flux balance in the system. For example, all of the moment exponents are calculated under an imposed macroscopic strain rate and a high but finite diffusivity contrast (10^{10}), a condition different from any used in previous investigations of force and current (or voltage drop) distributions [46, 141, 147]. It is not clear how to simultaneously normalize force and flux conditions in the creep problem; on the other hand, it

does not seem appropriate to discard the interplay between force and flux in order to directly compare with other single-process percolation problems.

2.2.5. Understanding Percolation from Physical Correlations

2.2.5.1. Stress Concentration Due to Grain Boundary Character Distribution

During Coble creep, the internal stress distribution in the system is nonuniform due to variations in the grain boundary diffusivities, as well as topological heterogeneities such as a distribution of grain sizes or grain shapes [148]. It has been shown that the local stress enhancement at grain boundaries arising from a diffusivity variation is significantly higher than that caused by geometric irregularities [128]. While the presence of a single large grain yields a peak stress of about $2.7\sigma_0$, introducing a single special boundary into a honeycomb network with a diffusivity contrast ratio of 10^2 - 10^4 results in a concentrated stress as high as $4.6\sigma_0$ [128]. We have observed even greater stress concentrations in the more general case where the two types of grain boundaries are randomly distributed in the network.

Figure 24(a) and (b) show the distribution of stress, normalized by the external stress σ_0, along some selected paths in a random grain boundary network, which contains ~50% special boundaries ($p \approx 0.5$) with a diffusivity contrast ratio $D_g/D_s = 10^4$. Both paths are perpendicular to the applied stress (strain) axis, and lie in the middle of the sample. Special boundaries are in black and general ones are in grey, while the thickness of the boundaries distinguishes the upper and lower paths in each of the two figures. The first important point observed in Figure 24 is that the local normal stress along grain boundaries can be enhanced relative to σ_0 by a factor of about 20 or higher, for both tensile stress as in Grain 4 and compressive stress as in Grain 7. Such pronounced stress concentrations could be relevant to crack or cavity nucleation, although the worst situations mostly occur at special boundaries which are usually resistant to crack propagation. A second observation in Figure 24 is that, compared to a single species network where all horizontal boundaries (boundaries perpendicular to the stress axis) share the same distribution of tensile stress and all lateral boundaries also have the same distribution of mostly compressive stress [126, 136, 137], the presence of a second species not only modifies the magnitude of the stresses, but can also sometimes change the sign of the stresses. For example, stresses along the horizontal special boundary (in black) in Grains 1, 6, and 7 become compressive, and stresses along the top lateral special boundary in Grain 7 become tensile. A third message Figure 24 delivers is that there is a strong correlation between the stress distributions of either two opposing grain boundaries in the same grain, such as the boundaries marked by the arrows in Grains 2–5, or two or three second-nearest-neighbor boundaries, such as the marked boundaries in Grains 1 and 6–8.

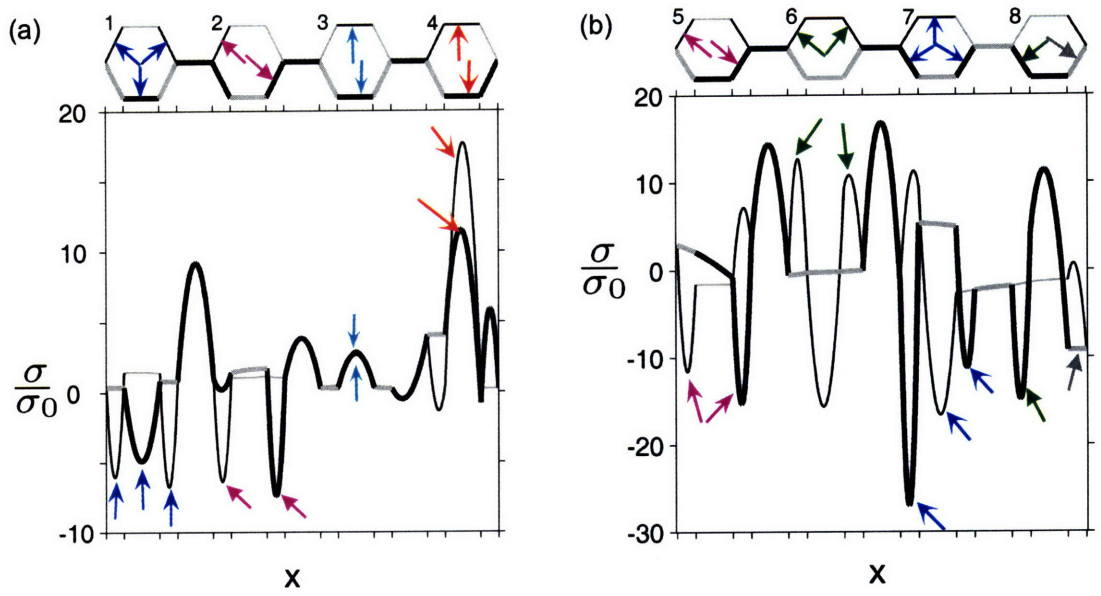

Figure 24. The distribution of stress σ, normalized by the external stress σ_0, along two chosen paths (a) and (b) in a random grain boundary network. The diffusivity ratio between general (in grey) and special (in black) boundaries is $D_g/D_s = 10^4$, and the special boundary fraction is $p \approx 0.5$. The thickness distinguishes the two paths (upper and lower) in each figure. The arrows point out stress concentrations and correlations as described in the text.

All these stress distribution irregularities and correlations can be explained by the imposed mechanical equilibrium. Force balance across the grain is most easily realized by balancing the stresses on opposing grain boundaries, as is the case for Grains 2–5. This is especially true when both of the opposing boundaries are special boundaries, which are more effective at carrying stress and are in fact the stress concentrators in the network. Another well balanced boundary distribution is where three special boundaries form a tripodal arrangement in a grain, such as Grain 1 and 7. In this case, these three special boundaries often adopt similar stress distributions in order to achieve force equilibrium; this is also why the stresses along the horizontal special boundaries in Grain 1 and 7 are compressive instead of being tensile, as would be typical for horizontal boundaries. A less common, but also effective way of balancing the force across a grain is exhibited in Grain 6 and 8, where two second-nearest-neighbor boundaries share similar stress distributions. It is worth mentioning that although stress concentration mostly occurs at special boundaries, occasionally general boundaries, such as that marked by a grey arrow in Grain 8, can have a high stress as well.

2.2.5.2. Correlations among Boundary Stresses

While Figure 24(a) and (b) provide strong evidence for correlations among grain boundary stresses, they are only specific examples of two small regions from a much bigger system. To better examine the stress (force) distribution for the whole system, we compare the force backbone with the diffusion backbone in

Figure 25 for a grain boundary network with 59% special boundaries. The diffusion backbone is made of those boundaries with an average diffusional flux above a chosen flux threshold and similarly, the average force on every boundary in the force backbone is above a chosen force threshold. Both thresholds are chosen so that about half of all boundaries will be shown in the figure.

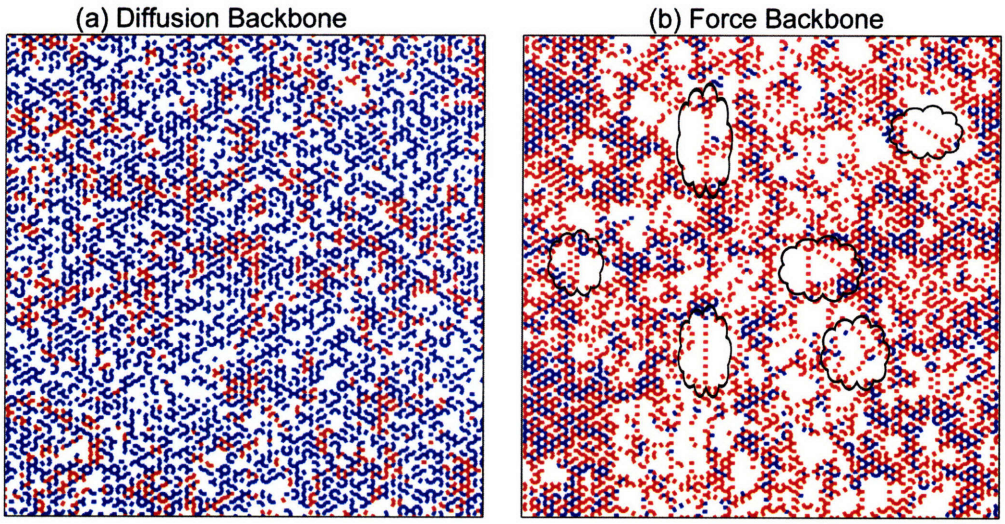

Figure 25. (a) The main flux-carrying part and (b) the main force-carrying part of the network at a special fraction $p \approx 0.595$. The flux and force threshold is chosen such that about half of the grain boundaries are shown in both figures, where red segments are the 'special' low-diffusivity grain boundaries and blue segments are the 'general' high-diffusivity boundaries.

A heterogeneous network undergoing Coble creep exhibits interesting geometric features arising from the imperfect contrast between species. For example, at $p \approx 0.59$, there is neither any sample-spanning cluster of purely low-diffusivity (strong) 'special' boundaries nor of high-diffusivity (weak) 'general' boundaries. However, both force transmission and mass transport are made possible by the mutual cooperation of these two types of boundaries. This is clearly seen in the 'diffusion backbone' (Figure 25(a)) and the 'force backbone' (Figure 25 (b)) of the network, where 'special' boundaries are in red and 'general' boundaries are in blue. The main flux-carrying part of the network shown in Figure 25(a) is made up of ~80% 'general' and ~20% 'special' boundaries. Here mass transport through the network is facilitated by the enhanced diffusion along many chains of 'special' boundaries lying between fast-diffusing 'general' boundaries. Meanwhile, about one third of the main force-carrying boundaries shown in Figure 25(b) are 'general' boundaries, which help form abundant loop structures effective in transmitting forces. Also as circled in the clouds, many bridges of 'special' boundaries across the loops are stressed to fulfill the force balance among the grains. These stressed loops and 'bridges' are quite reminiscent of the loops and cutting bonds in the rigid backbone of central-force networks [149, 150].

The statistics of the stress distribution can be quantitatively captured by a spatial correlation function. Integration of the normal stress $\sigma(s)$ in Eq. (82) over the range $0 \le s \le 1$ yields the average stress exerted

on a grain boundary. Because all boundaries in the network have the same length, this is essentially a force F. We choose the center of a boundary to define its position $\vec{r}_0$ in the network, and define the spatial autocorrelation function among boundary forces as

$$R(r) = \frac{\sum_{\vec{r}_0,\vec{r}_0+r}\left(F_{\vec{r}_0} - \bar{F}\right)\left(F_{\vec{r}_0+r} - \bar{F}\right)}{\sqrt{\sum_{\vec{r}_0,\vec{r}_0+r}\left(F_{\vec{r}_0} - \bar{F}\right)^2}\sqrt{\sum_{\vec{r}_0,\vec{r}_0+r}\left(F_{\vec{r}_0+r} - \bar{F}\right)^2}} \tag{88}$$

where $\bar{F}$ denotes the average F for all boundaries in the system, and $\vec{r}_0 + r$ denotes each boundary a distance r away from the boundary centered at $\vec{r}_0$. It is important to note that $R(r)$ is calculated from all appropriate pairs of two boundaries r distance apart from each other, regardless of their positions in the system and their orientations with respect to the external stress axis. $R(r)$ equals +1 if the forces on two boundaries r distance away from each other always covary positively and perfectly, -1 if they covary negatively and perfectly, and zero if they vary independently.

We first calculate the correlation coefficient $R(r)$ for the forces acting on two boundaries in the same grain. The sign and magnitude of R calculated this way characterize the frequencies of the force balance types shown in Figure 24, and indicate how the force equilibrium is, on average, achieved in the system. The diffusivity contrast ratio D_g/D_s is fixed at 10^4, while the special boundary fraction p covers the full range 0 – 1. The obtained R values are plotted in Figure 26 for all the three possible distances between two boundaries in the same grain, $r = \sqrt{3}$, 1.5, and $\sqrt{3}/2$ (in units of the grain boundary length L_{gb}).

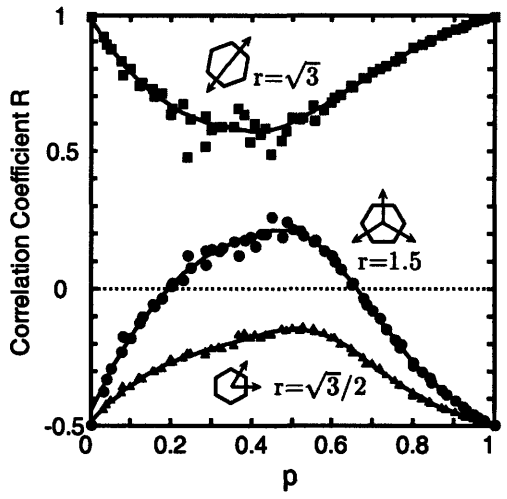

Figure 26. Correlation coefficient R of the grain boundary forces as a function of the special boundary fraction p for the distances $r = \sqrt{3}/2$, 1.5, and $\sqrt{3}$ (in units of grain boundary length). All three of these distances correspond to those connecting boundaries on the same grain, in the configurations shown by the inset diagrams.

In Figure 26, the data for $r = \sqrt{3}$ correspond to force transmission across two opposing boundaries in a grain (such as the cases of Grains 2–5 in Figure 24). Three points can be made from this set of data. First, R for $r = \sqrt{3}$ is higher than 0.5 over the full range of special fraction p (except for a few outlying data points). This is consistent with the observation in Figure 24 that force balance on opposing boundaries is the major mode of force equilibrium of a grain. The limiting cases at $p = 0$ and 1 present the extremes of this trend: the force balance in homogeneous networks is completely accomplished across opposite sides of the grain, leading to $R = 1$. Second, R for $r = \sqrt{3}$ shows an opposite trend with p to that for $r = 1.5$; as the network becomes more heterogeneous, the lines of force transmission are more often deflected by the force balance between second-nearest-neighbor boundaries. Third, R for $r = \sqrt{3}$ is asymmetric with respect to $p = 0.5$, for example, being higher at $p = 0.8$ than at $p = 0.2$. We believe that this asymmetry reflects special boundaries being more effective at transmitting forces.

In Figure 26, R values for $r = 1.5$ are negative when the fraction of special boundaries $p < 0.2$ or $p > 0.65$, and become positive in-between; from this we may state that tripodal force balance among second-nearest-neighbor boundaries across a grain becomes an effective path for force balance for $p \approx 0.2$–0.65. This is understandable based on the types of force balance seen in Grains 1 and 6–8 in Figure 24. As p approaches 0.5, the probability of having a force balance (similarity) among three special boundaries forming a tripodal configuration or among only two second-nearest-neighbor boundaries increases, and the correlation coefficients correspondingly increase above zero. R values for $r = \sqrt{3}/2$ are always negative, which means that the nearest-neighbor boundaries tend to have dissimilar stresses or forces.

We have also calculated the correlation coefficient $R(r)$ including all possible pairs of grain boundaries r distance apart from each other, without restricting both boundaries to be from the same grain. For $r = 1.5$ and $\sqrt{3}/2$, this procedure is the same as the previous calculation in Figure 26 because all possible pairs of boundaries at these two distances always belong to the same grain. For $r = \sqrt{3}$, however, this procedure includes numerous other configurations with the same characteristic separation, in addition to the case of two boundaries on opposite sides of a grain; for example, the distance $\sqrt{3}$ marked by the dashed arrows in Figure 27(c) does not correspond to a straightforward force transmission path across a grain, but it is also included in the calculation. In fact, all distances of $r \geq \sqrt{3}$ correspond to boundary pairs with more than one configuration (some are shown in Figure 27(c)). By averaging over all the possible configurations, the correlation coefficients R for these large distances at a certain p simply represent the degree of disorder in the force distribution, i.e., how much the regular force distribution on a homogeneous network has been disturbed by the random distribution of the boundary character. The remaining discussion in this section will focus on distances $r \geq \sqrt{3}$.

Figure 27(a) plots $R(r)$ for r from 0 to 6, which includes the 19 nearest neighbors, for a diffusivity contrast ratio $D_g/D_s = 10^4$. The five curves correspond to networks with different special boundary fractions, $p = 0$, 0.1, 0.2, 0.3, and 0.5. The condition $p = 0$ corresponds to a homogeneous network exclusively composed

of one type of grain boundary, in which the force distribution exhibits perfect positive correlation (R = 1) for $r = \sqrt{3}$, 3, $2\sqrt{3}$, $\sqrt{21}$, $3\sqrt{3}$, and 6. These specific separations all correspond to distances between two parallel boundaries, as illustrated in Figure 27(c). At p = 0, the forces on all horizontal boundaries are the same, and all lateral boundaries also have the same force. Thus two parallel boundaries, both horizontal or both tilted, always share the same stress distribution and force. Meanwhile, two nonparallel boundaries must comprise a pair of either horizontal/tilted or right-tilted/left-tilted boundaries; the probability of the former combination is higher than that of the latter, and therefore the forces on two nonparallel boundaries are more often dissimilar, resulting in a negative correlation coefficient for many distances.

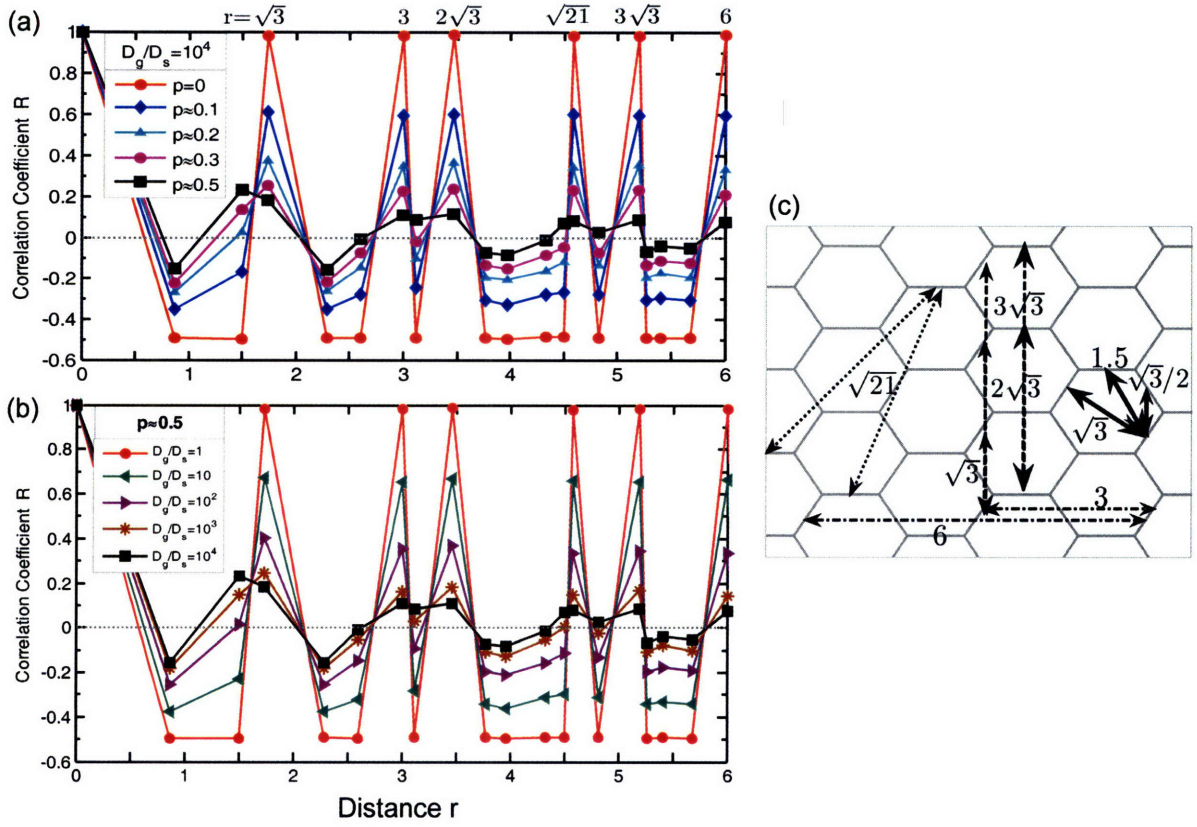

Figure 27. Correlation coefficient R of the grain boundary forces as a function of the distance r (in units of grain boundary length). R is computed for five special boundary fractions p = 0, $p \approx 0.1$, 0.2, 0.3, and 0.5 under a diffusivity ratio $D_g/D_s = 10^4$ in (a) and for diffusivity ratios D_g/D_s = 1, 10, 10^2, 10^3, and 10^4 at a special fraction $p \approx 0.5$ in (b). Examples of the various paths are illustrated in (c).

For binary networks, the values of R at all distances $r \geq \sqrt{3}$ simply indicate how reasonable it is to represent the force distribution for a binary network with the homogeneous network solution, i.e., a distribution with only two distinct values, one for all horizontal boundaries and the other for all tilted boundaries. The closer R is to zero, the worse such a simplified representation is for heterogeneous

networks. As the special fraction p increases to 0.5 (Figure 27(a)), both the positive correlations between parallel boundaries and the negative correlations between nonparallel boundaries gradually diminish; the correlation directionality gradually recovers as p keeps increasing above 0.5 (not shown in the figure). R for all distances $r \geq \sqrt{3}$ approaches zero as p approaches 0.5 from either below or above because the distinct difference between forces on horizontal and tilted boundaries is gradually reduced by the random distribution of the boundary character. The similar peak heights or depths at a certain p in Figure 27(a) can also be explained by the nature of R. A correlation coefficient that is essentially determined by geometric orientation (the boundaries being horizontal or tilted) should be similar on different length scales.

In addition to the distribution of grain boundary character described by the special boundary fraction p, the diffusivity contrast ratio between general and special boundaries, D_g/D_s, is another parameter that controls the degree of network randomization. The effect of D_g/D_s on the force correlations is illustrated in Figure 27(b). At $p \approx 0.5$, the force distributions in networks with higher D_g/D_s ratios are more random (i.e., less directional). As D_g/D_s decreases towards unity, the correlation coefficient R exhibits sharp peaks and valleys again; the network with $D_g/D_s = 1$ at any p is equivalent to a network of predominantly one boundary species.

In brief, because the requirement of force equilibrium for every grain is mandatory, strong correlations among boundary forces are manifested during Coble creep. Although special boundaries are usually the stress concentrators in the system, even for networks with randomly-distributed grain boundary character, the distribution of the average stresses (or forces) on boundaries are generally highly correlated.

2.2.5.3. Correlations among Plating Rates

In the honeycomb network, the first nearest neighbors of a boundary are those meeting it at the adjoining triple junctions. Each boundary has four nearest neighbors, which serve as sources or sinks for matter flow in the boundary of interest, and therefore the characters of the four neighbors may influence the rate of matter removal or deposition at a specific boundary. The distribution of the plating rate of a boundary in different surroundings is plotted in Figure 28, where 'S' denotes a special boundary and 'G' a general boundary. For example, "GS-S-SS" denotes a special boundary meeting one general and one special boundary at one triple junction, and meeting two special boundaries at the other triple junction. Figure 28 is computed for a network composed of half general and half special boundaries ($p \approx 0.5$), where the diffusivity contrast has been increased to 10^{10} in order to make the correlation effect evident. The x-axis is the absolute value of the plating rate V (Eq. (66)) (in units of m/s) excluding the prefactor constants $\delta\Omega / KTL_{gb}^2$ (in units of 1/(m·Pa)), and therefore the x-axis labels are in units of N/s; the y-axis is the cumulative fraction of boundaries exhibiting that rate. Each curve corresponds to a different neighborhood. The data for special boundaries with different neighbors are plotted in Figure 28(a), and those for general boundaries in Figure 28(b).

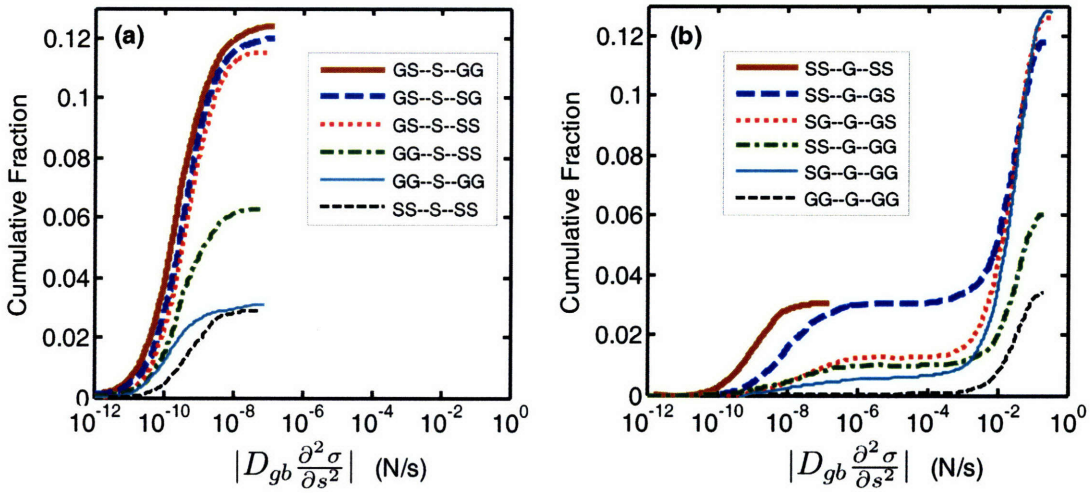

Figure 28. The distribution of the absolute value of the plating rate V, excluding the prefactor constants, for a boundary in different surroundings. The data for special boundaries with different nearest neighbors are plotted in (a) and general boundaries in (b). "S" denotes special boundary and "G" general boundary. In this example the network has a special boundary fraction $p \approx 0.5$ and a diffusivity ratio $D_g/D_s = 10^{10}$.

In Figure 28(a), special boundaries surrounded by different neighbors have quite similar average plating rates, which are generally distributed on the range 10^{-12} – 10^{-7}. Special boundaries have a much lower diffusivity than general boundaries, and are the plating rate-limiting species in the system. It therefore seems reasonable that the plating rates of special boundaries do not depend very much on the character of neighboring boundaries. In contrast, the average plating rate of a general boundary is substantially impacted by its surroundings (Figure 28(b)). The general boundaries with four general boundary neighbors ("GG-G-GG") have very high plating rates above 10^{-3}, while those surrounded by four special boundaries ("SS-G-SS") all have very low plating rates below 10^{-7}, of similar magnitude to the plating rates of special boundaries (cf. Figure 28(a)). Special boundaries are poor conduits (Eq. (65)) and are less active in exchanging matter with the grains (Eq. (66)). They generally cannot provide sufficient matter to accommodate fast plating at their neighboring general boundaries. In other words, general boundaries surrounded by four special boundaries have low plating rates because they lack available sources or sinks for diffusion; their neighborhood coerces them to exhibit apparently special behavior.

The plating rates of other general boundaries almost all show a bimodal distribution. Take for example the case of a general boundary surrounded by one general and three special boundaries, labeled as "SS-G-GS" (see blue curve in Figure 28(b)). In this family of general boundaries, the plating rates of some boundaries are below 10^{-7} and others are above 10^{-3} with almost none in between. Those with plating rates above 10^{-3} are likely connected to a fairly large cluster of general boundaries by their single general neighbor; those with plating rates below 10^{-7} are probably part of a very small cluster of general boundaries, bounded by special boundaries at the second- or further-nearest-neighbor level.

To this point, we have explored the strong correlations in the creeping system in terms of both the stress (force) and plating rate distributions. Next we shall examine the correlations in the energy dissipation rate or power dissipation, which is more directly related to the effective creep viscosity.

2.2.6. Understanding Percolation from Energy Dissipation

2.2.6.1. Energy Dissipated in General and Special Boundaries

As an atom diffuses down the chemical potential gradient, the work done on the atom is finally dissipated as heat. Because we have assumed free grain boundary sliding, i.e., shear stress is relieved instantaneously and performs no work, the supplied external work is all dissipated via diffusion along the grain boundaries. The rate of energy dissipation in one boundary, E, is

$$E = \frac{\delta L_{gb}}{\Omega} \int_0^1 \frac{KT}{D_{gb}} \Omega^2 J^2 ds \tag{89}$$

with the diffusional flux J defined in Eq. (65). Thus E can be reduced as

$$E = \frac{\delta \Omega D_{gb}}{KTL_{gb}} \int_0^1 \left(\frac{\partial \sigma}{\partial s} \right)^2 ds \tag{90}$$

The stress σ is given by the cubic function in Eq. (82), and therefore Eq. (90) becomes

$$E = \frac{\delta \Omega D_{gb}}{KTL_{gb}} \left(\frac{9}{5} \alpha_3^{\,2} + 3\alpha_3 \alpha_2 + 2\alpha_3 \alpha_1 + \frac{4}{3} \alpha_2^{\,2} + 2\alpha_2 \alpha_1 + \alpha_1^{\,2} \right) \tag{91}$$

The rate of energy dissipation E in Eq. (91) has the unit of J/(m·s) in two dimensions. The multiplicative prefactors $\delta\Omega / KTL_{gb}$ (in units of 1/Pa) have been neglected in the present calculation, and thus the E values reported here are all in units of Pa^2m^2/s.

In
Figure 29, we show the summations of E over all general boundaries, all special boundaries, and all the grain boundaries in the network, for a contrast ratio $D_g/D_s = 10^{10}$. The $\sum E$ values have all been normalized with respect to $\left(\sum E\right)_{p=1}$. The summation of E over all the grain boundaries is equal to the external work, which is proportional to the creep viscosity η under constant strain rate conditions. Therefore, the dotted curve in
Figure 29 has the same shape as the η curve in Figure 20, and also exhibits the same percolation transition point pcc. However, in
Figure 29, we now see the basic physical shift that underlies the percolation transition. Below p_{cc}, energy is dissipated predominantly in general boundaries, and the energy dissipation in special boundaries is trivial, while above p_{cc}, energy dissipation mainly takes place in special boundaries. An interesting secondary observation pertains to the two trivial contributions, which each exhibit additional discontinuities. The trivial dissipation in special boundaries has a discontinuous jump around $p \approx 0.15$-

0.3, while in the general boundaries a similar discontinuity occurs at $p \approx 0.75$-0.85. The origin of these unusual secondary discontinuities is not clear, but might be related to a change of the role of the dilute species in the network: the possibility of stress or deformation concentration decreases as p approaches the dilute limits of zero or one.

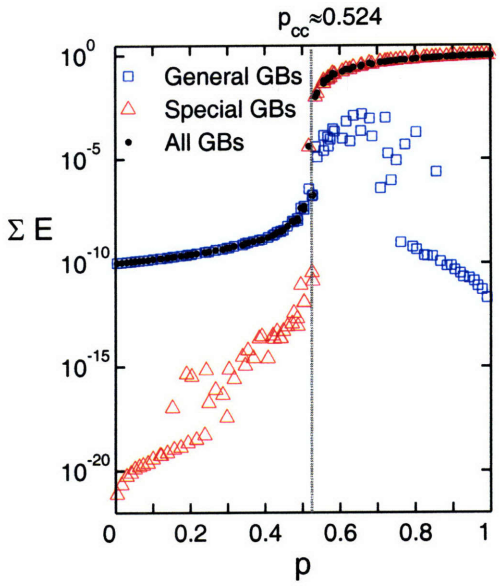

Figure 29. Summations of the dissipated energy over all grain boundaries in the network, only all the special boundaries, and only all the general boundaries, for a constant diffusivity contrast ratio $D_g/D_s=10^{10}$.

As E in Eq. (91) represents each boundary's contribution to the overall energy dissipation, the distribution of E reflects the behavioral heterogeneity in the network. Histograms of E for general boundaries and for special boundaries are respectively plotted in Figure 30(a) and Figure 30(b) at several special fractions below and above the percolation threshold, $p_{cc} \approx 0.524$. For general boundaries (Figure 30(a)), as p approaches p_{cc} from below (dashed curves), the distribution shifts to the right, and the primary peak reduces in height. The distribution even becomes bimodal for the case of $p \approx 0.522$ plotted with the red dashed line. Above p_{cc}, the distribution peak shifts back to the left as p increases, suggesting a decrease in the energy dissipated in general boundaries. The trend is opposite for special boundaries (Figure 30(b)). The distribution is broadened and shifted to the right as p increases below p_{cc} (dashed curves), and becomes bimodal right above p_{cc} (solid curves). As p further increases, the peak corresponding to low energies gradually diminishes while the other peak at higher energies grows in magnitude and shifts to the right. This is consistent with
Figure **29** which shows that as p increases above p_{cc}, more energy is dissipated in special boundaries.

To better compare between general and special boundaries, we have normalized the E value of every boundary with respect to the average energy dissipation rate of a boundary, $\overline{E}$, at the specific p value,

and plot the normalized histogram of $E/\overline{E}$ for general boundaries in Figure 30(c) and for special boundaries in Figure 30(d). The distribution of $E/\overline{E}$ for general boundaries below p_{cc} (dashed lines in Figure 30(c)) and that for special boundaries above p_{cc} (solid lines in Figure 30(d)) are strikingly similar. Firstly, the main histogram peak is always centered around $E/\overline{E}=1$, which confirms that the main energy dissipation species is general boundaries below p_{cc}, and special boundaries above p_{cc}. Secondly, as p approaches p_{cc} from below for general boundaries and from above for special boundaries, the height of the main peak decreases, and meanwhile, a second peak emerges and grows at much lower $E/\overline{E}$ values. This near-threshold bimodal distribution for both species will be further explored in the following. The single peak for general boundaries above p_{cc} (solid lines in Figure 30(c)) and that for special boundaries below p_{cc} (dashed lines in Figure 30(d)) show similar trends as well.

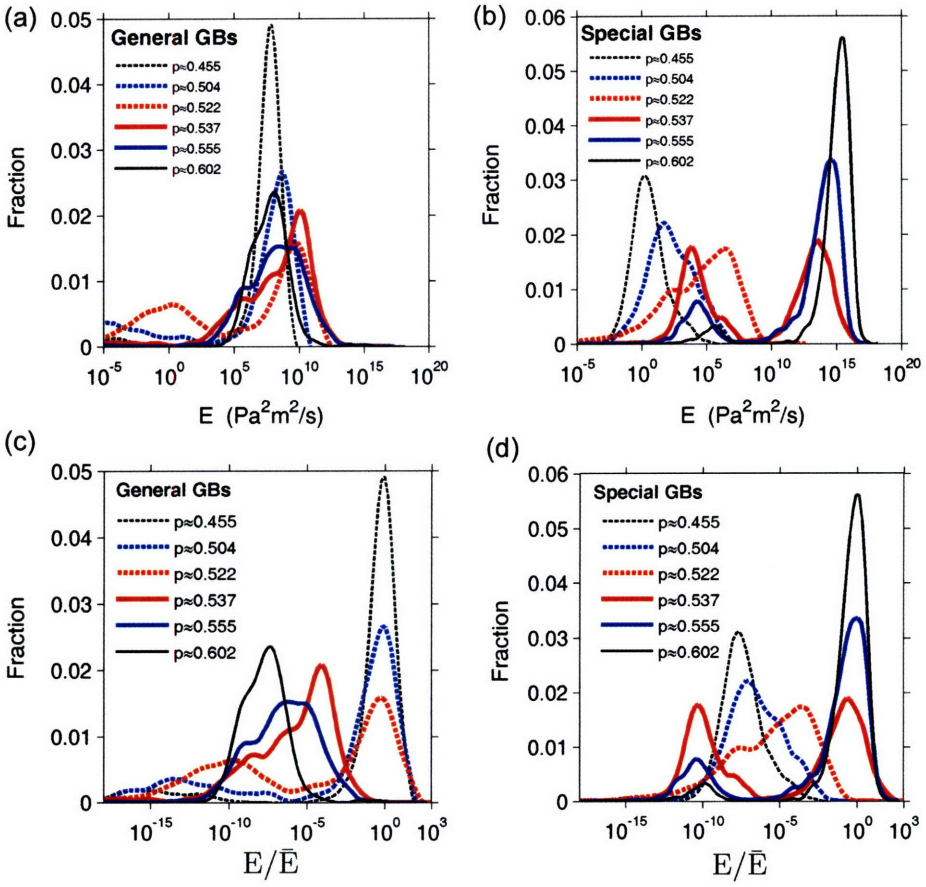

Figure 30. The histograms of the dissipated energy E for (a) general boundaries and (b) special boundaries below (dashed curves) and above (solid curves) the percolation threshold ($p_{cc} \approx 0.524$) for a diffusivity ratio $D_g/D_s = 10^{10}$. The E value of every boundary is further normalized with respect to the average energy dissipation rate of a boundary, $\overline{E}$, at each special fraction. The histogram of $E/\overline{E}$ are plotted in (c) for general boundaries and (d) for special boundaries.

2.2.6.2. Geometric Connectivity of the "Energy Backbone"

The distribution of the dissipated energy E on networks with $p \approx 0.522$ ($< p_{cc}$) and $p \approx 0.537$ ($> p_{cc}$) are respectively plotted in Figure 31(a) and (c). The E values marked on the scale bar do not include the prefactor constants in Eq. (91) and have the unit of Pa^2m^2/s. In Figure 31(a), the energy dissipation level throughout the network is generally very low, in accordance with the low creep viscosity of the system below the percolation threshold p_{cc}. In Figure 31(c), the overall E level is much higher, indicating an increase in the creep viscosity above p_{cc}. In both Figure 31(a) and (c), some of the boundaries dissipate energy at a rate many orders of magnitude higher than others. Although these fast dissipating boundaries appear, at a coarse level, to connect the opposite sides of the system, they are actually not connected into a sample-spanning cluster. In fact, neither any sample-spanning cluster of general boundaries nor special boundaries could form for both special fractions considered in Figure 31, as both fractions are significantly lower than the geometric connectivity threshold. Thus the percolation transition and the dramatic change in the energy dissipation distribution are not induced by geometric connectivity on the honeycomb lattice.

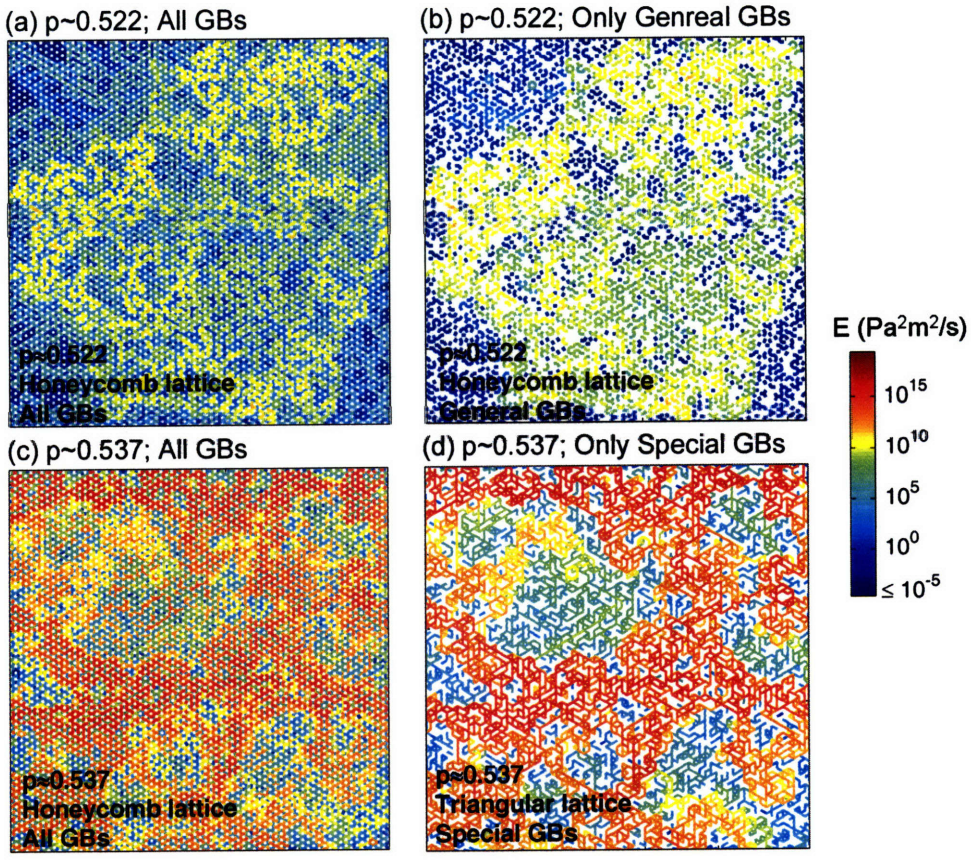

Figure 31. The spatial distribution of the dissipated energy E on the network. (a) All grain boundaries on the honeycomb lattice at the special fraction $p \approx 0.522$ (below percolation threshold). (b) Only general boundaries on the honeycomb lattice at $p \approx 0.522$. (c) All boundaries on the honeycomb lattice at $p \approx 0.537$ (above percolation threshold). (d) Only special boundaries on the triangular (dual) lattice at $p \approx 0.537$.

There is a strong correlation between the magnitude of E for a boundary and its species. Below p_{cc}, the boundaries with relatively fast energy dissipation are mainly general boundaries and exhibit winding morphologies (yellow boundaries in Figure 31(a)). These general boundaries dissipate energy faster mainly because of their higher diffusivity (Eq. (89) - (91)). Thus the energy dissipation distribution should be correlated with the connectivity and clustering of general boundaries. This is clearly seen in Figure 31(b) which plots the dissipated energy in all the general boundaries at $p \approx 0.522$ on the honeycomb lattice. In general, the energy dissipation rates of the general boundaries belonging to the same small cluster are either all very high or all very low.

Above p_{cc}, the boundaries with relatively fast energy dissipation are mainly special boundaries and form long chains of small rings (red boundaries in Figure 31(c)). Special boundaries become the main energy dissipating location because of the higher stress gradients they sustain (see Eq. (90) and Figure 24), and such higher stress gradients usually correlate with higher absolute magnitudes of the average stress or force on these boundaries. As described in Section 2.2.5.1, mechanical equilibrium of each grain is achieved by the balance of the forces among the boundaries around a grain, mainly connecting second- and third-nearest neighbor bonds on the honeycomb lattice. Therefore above the percolation threshold, the true connections among boundaries are not those where the boundaries meet at triple junctions, but rather those defining the force network across the grains. This definition of artificial connectivity across grains corresponds to true connectivity on the dual lattice—for the honeycomb network the dual is the triangular lattice. We can map each boundary in the honeycomb lattice onto the triangular dual lattice by assigning a dual bond connecting the center of its two adjacent grains, while keeping its species identity. The distribution of E for special boundaries at $p \approx 0.537$ on the triangular lattice is plotted in Figure 31(d). The special boundaries with high E values in Figure 31(d) now form a sample-spanning connected cluster. What is more, the shape of this cluster closely resembles the morphology of the rigid backbone in elastic networks [2, 42, 151], which is in line with our assertion that force balance and transmission play an important role in the percolation transition of Coble creep.

Finally, we recall that in Figure 30 at $p \approx 0.522$, the energy dissipated in general boundaries exhibited a bimodal distribution, and at $p \approx 0.537$, the energy dissipation in special boundaries was bimodal. Such bimodal distributions are obvious in Figure 31(b) and (d).

2.2.6.3. Energy Dissipation versus "Internal Work"

Here the relationship between energy and percolation is examined from a complementary perspective. We have also observed an additional energy inflection at p_{cc}, in the fraction of boundaries that expend vs. absorb energy during creep. The total energy dissipation is the summation of E over all grain boundaries,

$$\sum E = \sum_{GB} \int_0^1 d\Omega \left(J \frac{\partial \sigma}{\partial s} \right) ds = \sum_{GB} \int_0^1 d\Omega \frac{\partial (J\sigma)}{\partial s} ds - \sum_{GB} \int_0^1 d\Omega \left(\sigma \frac{\partial J}{\partial s} \right) ds \tag{92}$$

Applying the divergence theorem [152] to the first term, we find

$$\sum_{GB}\int_0^1 \delta\Omega\frac{\partial(J\sigma)}{\partial s}ds = \sum_{\text{junction}}\delta\Omega(J_1\sigma_1 + J_2\sigma_2 + J_3\sigma_3) \tag{93}$$

The integral over grain boundaries reduces to the summation over the junctions in the network; J_1, J_2, and J_3 are the fluxes going from the boundaries into the junction; σ_1, σ_2, and σ_3 are the stresses acting on the three adjoining boundaries at the junction. At internal triple junctions, $\sigma_1 = \sigma_2 = \sigma_3$ since the stress has to be continuous, and $J_1 + J_2 + J_3 = 0$ because mass must be conserved. At surface junctions, we have imposed a zero flux boundary condition, $J_1 = J_2 = J_3 = 0$. Thus Eq. (93) is equal to zero and Eq. (92) reduces to

$$\sum E = -\sum_{GB}\int_0^1 \delta\Omega\left(\sigma\frac{\partial J}{\partial s}\right)ds = \sum_{GB} L_{gb}\int_0^1 \sigma V ds = \sum W \tag{94}$$

Here W is defined as the integration of the product of the normal stress σ (Eq. (68)) and the plating rate V (Eq. (66)) over one boundary, and is analogous to the concept of internal work in continuum mechanics. Upon the application of the external stress, internal stress is developed in the system and enables the matter plating to occur. As the global summations $\sum W$ and $\sum E$ are both equal to the applied external work, the local value W conceptually represents how much energy one boundary gains and the local value E represents how much energy one boundary dissipates via diffusion per unit time. Thus W - E is a measure of the local energy balance at one boundary. Introducing Eqs. (66) and (82) into Eq. (94), we have

$$W = -\frac{\delta\Omega D_{gb}}{KTL_{gb}}\left(\frac{6}{5}\alpha_3^{\,2} + 2\alpha_3\alpha_2 + 2\alpha_3\alpha_1 + 3\alpha_3\alpha_0 + \frac{2}{3}\alpha_2^{\,2} + \alpha_2\alpha_1 + 2\alpha_2\alpha_0\right) \tag{95}$$

and by subtracting Eq. (91), we obtain

$$W - E = -\frac{\delta\Omega D_{gb}}{KTL_{gb}}\left(3\alpha_3^{\,2} + 5\alpha_3\alpha_2 + 4\alpha_3\alpha_1 + 3\alpha_3\alpha_0 + 2\alpha_2^{\,2} + 3\alpha_2\alpha_1 + 2\alpha_2\alpha_0 - \alpha_1^{\,2}\right) \tag{96}$$

In Figure 32, the fraction of boundaries that "gain" energy (with $W - E > 0$) is denoted as f, which is plotted for all boundaries as well as for only general boundaries and only special boundaries. Interestingly, the total fraction of energy-gaining boundaries reaches a maximum of ~0.5 at the percolation threshold p_{cc}. This singular point apparently arises from the divergence of the fraction of special boundaries with $W > E$ at p_{cc} (see triangular points in Figure 32). Clearly, there is a sudden energy redistribution among the special boundaries at p_{cc}. This is associated with both the increase in W due to the increase of the creep viscosity of the system and the increase and bifurcation in E as shown in Figure 30. We suspect that there might be some desired arrangement of the local energy balance in the network that governs the physically percolating event, but more work is needed to clarify the nature of the percolation transition.

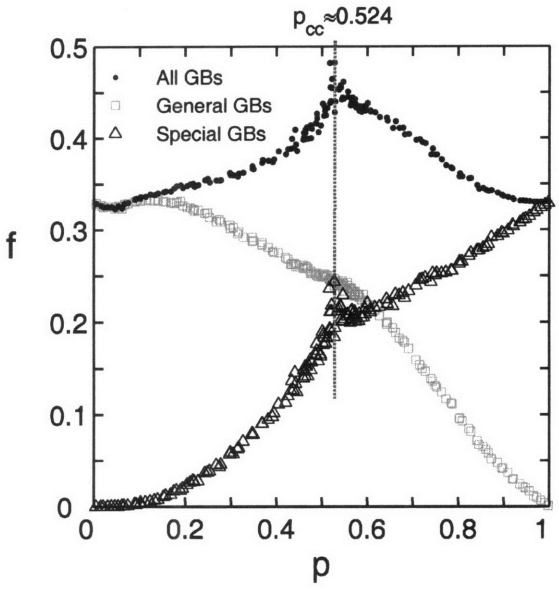

Figure 32. The fraction f of boundaries with $W - E > 0$. The three curves correspond to f of all boundaries as well as for only special boundaries and only general boundaries. The first two cases show a singularity point around the percolation threshold $p_{cc} \approx 0.524$.

2.2.7. Predicting Effective Creep Response by Modifying the Coble Equation

Although there are many complexities associated with the percolation transition, the calculation of the creep viscosity η of the binary grain boundary network is basically a composite problem that may also be addressed by conventional effective medium averaging schemes. These provide a practical tool for predicting the creep behavior for a material with known grain boundary character distribution (GBCD), and can be extended easily to more complex GBCDs that are non-binary or nonrandom [139]. We use McLachlan's generalized effective medium (GEM) equation (Eq. (36)) [63, 153] because it includes the percolation threshold and the scaling exponents. For the present creep problem, the GEM equation writes as

$$(1-p)\frac{\eta_g^{1/s} - \eta_{eff}^{1/s}}{\eta_g^{1/s} + (p_{cc}^{-1} - 1)\eta_{eff}^{1/s}} + p\frac{\eta_s^{1/t} - \eta_{eff}^{1/t}}{\eta_s^{1/t} + (p_{cc}^{-1} - 1)\eta_{eff}^{1/t}} = 0 \tag{97}$$

where η_g and η_s are the creep viscosities of the purely general boundary network and purely special boundary network, respectively. We have fitted Eq. (97) to the simulation data using p_{cc}, s, and t as adjustable parameters, and the best fits yield $p_{cc} \approx 0.524 \pm 0.003$, $s \approx 2.08 \pm 0.16$, and $t \approx 1.26 \pm 0.16$. The fitted percolation threshold and the exponent s are quite close to those obtained earlier by direct percolation analysis, while t is between the minimum and maximum value obtained from fitting to the scaling law in Figure 22(c). As there is a large variation in t as p increases, $t \approx 1.26 \pm 0.16$ from the GEM fitting may be regarded as an appropriate average that generally reflects the creep properties for the whole range of p above the percolation threshold.

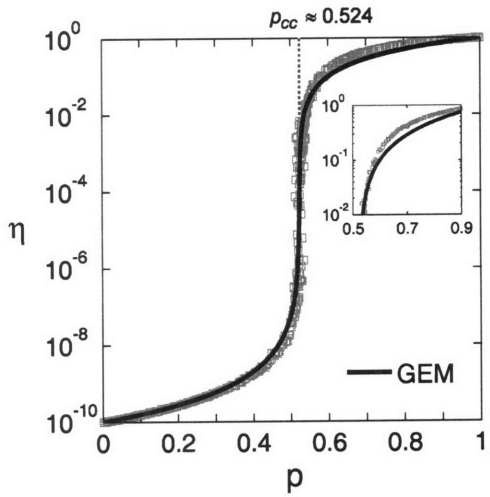

Figure 33. The normalized creep viscosity η as a function of the special boundary fraction p for a diffusivity ratio $D_g/D_s = 10^{10}$. The square points are the simulation data, and the solid line is the prediction of the GEM equation Eq. (36).

The GEM fitting result is plotted in Figure 33 as the solid line. Eq. (97) generally fits well to the simulation data over the full range of p. However, as shown in the inset, there is some deviation above the percolation threshold. This is because a single value of exponent t cannot accurately capture the behavior above the percolation threshold. This slight disagreement notwithstanding, Eq. (97) may be used in conjunction with the conventional Coble equation (the general equation Eq. (64) or the specific one for hexagonal grains, Eq. (81)) [84] to predict the creep behavior of a heterogeneous grain boundary network.

To show how this works, we first write the Coble equation in a form slightly different from the usual presentation, by separating it into two parts. The first equation (Eq. (98)) expresses the strain rate $\dot{\varepsilon}$ as a function of the creep viscosity η, the same quantity used in all of our previous discussion, while the second equation (Eq. (99)) relates this creep viscosity η to the grain boundary diffusivity D_{gb}.

$$\dot{\varepsilon} = \frac{1}{\eta}\sigma_0 \tag{98}$$

$$\eta = \frac{kTd^3}{A\Omega\delta D_{gb}} \tag{99}$$

If we now consider the grain boundary character distribution in the materials, we may use Eq. (99) to evaluate the creep viscosity characteristic of each type of grain boundary by substituting D_{gb} with the specific grain boundary diffusivity. Then we may use the generalized effective medium equation (the binary equation Eq. (97) or the multicomponent version analogous to Eq. (57)) to calculate the effective viscosity η_{eff} of the heterogeneous grain boundary network. Finally replacing η in Eq. (98) with η_{eff}, we obtain the constitutive law for Coble creep in a heterogeneous system. This process is further illustrated

in Eq. (100) for a binary grain boundary network composed of general boundaries with diffusivity D_g and special boundaries with diffusivity D_s.

$$\eta_g = \frac{kTd^3}{A\Omega\delta D_g} \qquad \eta_s = \frac{kTd^3}{A\Omega\delta D_s}$$

$$\downarrow$$

$$(1-p)\frac{\eta_g^{1/s} - \eta_{eff}^{1/s}}{\eta_g^{1/s} + (p_{cc}^{-1} - 1)\eta_{eff}^{1/s}} + p\frac{\eta_s^{1/t} - \eta_{eff}^{1/t}}{\eta_s^{1/t} + (p_{cc}^{-1} - 1)\eta_{eff}^{1/t}} = 0 \tag{100}$$

$$\downarrow$$

$$\eta_{eff}$$

$$\downarrow$$

$$\dot{\varepsilon} = \frac{1}{\eta_{eff}}\sigma_0$$

So our results for the effective creep viscosity can be used together with the Coble equation to predict stress-strain rate relationships for heterogeneous grain boundary networks. As mentioned earlier, in addition to the variation in grain boundary diffusivities, heterogeneities can also arise from geometric irregularities such as a distribution of grain sizes and shapes. This common type of heterogeneity may be addressed in two ways. One is to map the irregular grain structure into an uniform one but with all diffusivities of grain boundaries modified according to the geometries of their neighboring grains, as it has been shown that the stress concentrations at larger grains are similar to those at special grain boundaries [128]. Another approach is to directly homogenize the grain shapes and sizes to provide an effective grain shape and size, analogous to obtaining an effective grain boundary diffusion coefficient for a grain boundary network containing boundaries of different diffusivities. After all, the grain size that appears in various constitutive laws should be the effective value averaging over many shapes and sizes. It is not clear at present how to reduce a broad distribution of grain shapes and sizes to one or only a few effective parameters, with the connectivity and percolation effects taken into account. This is a very interesting, important, and challenging problem that, if solved, will lead to better understanding and predictions of the microstructure-property relationships for essentially all polycrystalline materials.

2.3. Summary

This chapter has studied diffusion and diffusional creep in a hexagonal grain structure containing several types of grain boundaries. With the kinetic differences among grain boundaries taken into account, we have observed some new and interesting physical phenomena that are practically relevant but would be otherwise overlooked. These phenomena are mostly correlated with microstructural connectivity, i.e., how different types of grain boundaries are distributed in materials and how some of them form a percolating cluster.

Diffusion in heterogeneous grain boundary networks belongs to the usual percolation universality class of linear transport properties. The critical scaling exponents for the effective diffusivity are the same as

those for effective electrical and thermal conductivities. The percolation threshold is consistent with the geometric percolation threshold at which a percolating cluster of grain boundaries with high diffusivities emerges in the microstructure. The paths of mass transport coincide with geometric clusters.

In contrast, grain boundary diffusional creep exhibits a new percolation threshold and a new set of scaling exponents. It is a new universality class of percolation. The percolation threshold is much lower than the geometric percolation threshold (or the one for diffusion). The creep process is not entirely determined by the formation of a percolating cluster of some type of grain boundaries, but rather also depends on the mechanical equilibrium of every grain and the deformation compatibility among grains. These additional conditions exert strong correlations on the actual behavior of each grain boundary; the behavior of a grain boundary can no longer be predicted solely based on the grain boundary type.

The percolation of Coble creep is found to be induced by the development of a force backbone on the dual of the original grain boundary network. The forces developed during Coble creep can be described by the force scaling laws used frequently in elastic networks such as Eq. (35). However, during Coble creep, the balance of forces normal to grain boundaries is correlated with diffusion along grain boundaries, a coupling entirely new to the percolation field. Examination of the energy dissipation in the system also reveals a transition from a diffusion-dominated process to a force-dominated process across the percolation threshold.

Despite all the complexities discussed above, both the effective grain boundary diffusivity and effective Coble creep viscosity can be well described by a generalized effective medium equation (Eq. (36)) adapted for specific situations (Eq. (45) and (100)). That equation was proposed over thirty years ago, but unfortunately has attracted little attention over the years. We find the equation very useful for describing the effective properties of any heterogeneous system that exhibits a critical percolation transition with constant critical scaling exponents. We have also generalized the equation, which was originally written for binary systems, to the multicomponent case so that it can be used to assess the effective properties of many real multicomponent systems.

Chapter 3. Homogenization of Random Multiphase Composite Solids

In addition to the distribution of different types of grain boundaries (Chapter 2), another more common form of heterogeneity in materials is the presence of different solid phases. Both the geometries of the phase particles and the connectivity among them play an important role in most materials properties. While the effects of the particle shapes have been long recognized, the role of the phase connectivity has been largely overlooked and only in recent years has this started to be quantitatively appreciated. On the other hand, the concept of "continuum percolation" has existed for several decades, and attracted a lot of attention, mainly within the percolation community, in the 1980s. Some work estimated the percolation scaling exponents by mapping the continuum problem to a discrete network problem. The major concern for the mapping approach is that one must decide beforehand a connectedness criterion, which depends on the physical context and is rarely known. In this chapter, the effective diffusivity and elastic properties of two-dimensional composite materials with randomly distributed phases will be studied using finite element simulation. The study will mainly focus on the percolation threshold and scaling behaviors of two-phase composite materials.

3.1. Linear Transport Properties

Many linear transport properties are mathematically analogous, such as mass diffusion, heat transfer, electrical conduction, magnetic permeation, etc. They can generally be described by

$$J(x) = -D(x)\nabla C(x) \tag{101}$$

where J represents the flow, D the transport coefficient, and C the potential. So the effective transport coefficient is usually defined by

$$\langle J(x)\rangle = -D_{eff}\langle \nabla C(x)\rangle \tag{102}$$

where < > denotes a volume average over the whole sample. These transport properties are generally in the same percolation universality class, given the same Euclidean dimensionality and microstructure type (discrete or continuous). In other words, if we know the percolation threshold and scaling exponents for one property, they are equally valid for the other properties mentioned above.

3.1.1. Finite Element Simulation Procedures

In order to connect to and compare with lattice percolation properties, we study continuum percolation for a family of two-dimensional symmetric-cell materials in this chapter. Symmetric-cell composite materials are constructed by partitioning a continuum into cells of specified shape and size and then randomly assigning phase properties to each cell. Therefore neither phase may be clearly defined as the matrix or the inclusion, although we will name phase 1 as the matrix phase and phase 2 as the inclusion phase to

facilitate discussion. We simulate effective transport properties for three cell geometries: triangular, square[††], and hexagonal tessellations (Figure 34), which are all special cases for the general Voronoi tessellation. Because we are only concerned with number fractions or area fractions of the phases, the unit of the length scale is irrelevant to the results. If we consider the length of the cell edge to be one unit, then the system sizes we have simulated are 90x90 (18824 cells), 80x80 (6400 cells), and 105x105 (4367 cells) for triangular, square, and hexagonal tessellations, respectively. The total number of cells used in the simulation has been decreased a bit from triangular to square and to hexagonal cells because the adaptive meshing procedure used here (and to be described in more detail later) becomes more time-consuming as the cell has more corners. In order to focus on the effects of the contacts and connectivity between phase cells, we assume perfect bonding everywhere and do not consider short circuit transport along phase or grain boundaries.

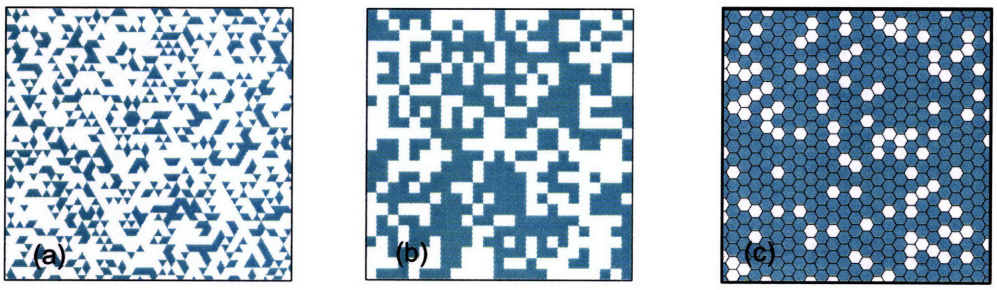

Figure 34. The topologies of the two-phase symmetric-cell composite materials in our simulations. The cell geometries are triangular, square, and hexagonal in (a), (b), and (c), respectively.

The microstructures are constructed and solved in ABAQUS, a commercial finite element software package. Specifically, we use Abaqus/CAE to run our PYTHON code without opening the Graphic User Interface so that we can acquire sufficient data for percolation analysis efficiently. Using finite element simulation to determine the effective diffusivity is more efficient and reliable than the widely used Monte Carlo random walk method [154, 155].

We have used 8-node quadratic elements (DC2D8) for square cells, 6-node quadratic elements (DC2D6) for triangular cells, and both types of elements for hexagonal cells. To minimize the effect of singularity (to accurately capture the stress concentrations around sharp corners of the cells), we do not use one uniform mesh for the whole system but instead remesh the model adaptively according to previous solution distributions. We apply the adaptive remeshing technique to the whole model targeting an uniform error distribution, so that the process progressively drives the elements near the singularity points to smaller and smaller sizes while making elements coarser elsewhere. We start with three mesh seeds per edge, which is a coarse, but reasonably refined, initial mesh in order to keep the computation cost low. To prevent unbounded element minimization around the corner regions in the remeshing process, we apply a minimum element size of 1% of the predefined mesh size and a maximum remeshing iteration

[††] The square tetessellation is also called the *random checkerboard model*.

number of 5. Figure 35 shows an example of the resulting mesh that we finally use to calculate the effective properties.

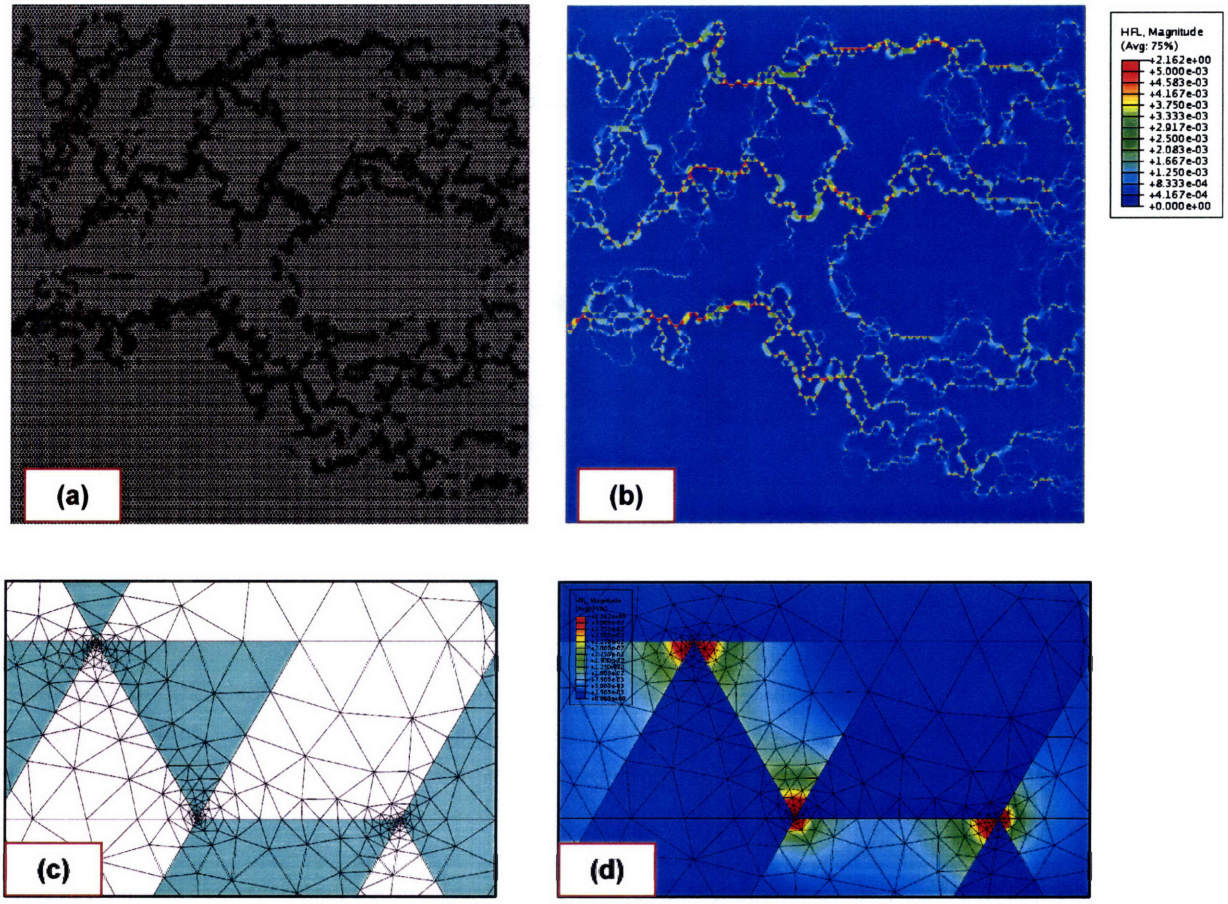

Figure 35. (a) Adaptive mesh for the two-phase composite material with triangular particle shapes. The regions with ultra-fine meshes correspond to connected clusters of the phases of higher conductivity as can be seen in (b), where the color scale reflects the magnitude of the heat flow (HFL). (c) and (d) are close-ups of (a) and (b), respectively. We can see that the adaptive remeshing technique mainly refines meshes in regions where the phases of higher conductivity (in green in (c)) make corner contacts.

In Abaqus, the adaptive remeshing technique is only available for heat transfer problems among the linear transport properties, so we have generated the mesh by considering J to be the heat flow, D to be the heat conductivity, and C to be the temperature in Eq. (101). However, because of the mathematical analogy, the results can be directly translated into equivalent quantities for mass diffusion, i.e., J becomes the mass flow, D diffusivity, and C the concentration of the diffusant. We are therefore able to present all the results here in terms of diffusivity so as to be consistent with the diffusion topics in previous chapters. In order to clearly observe a percolation transition, we assume a high diffusivity contrast ratio between the two phases, $D_I/D_M=10^8$, where "I" denotes the inclusion and "M" the matrix.

The boundary conditions are similar to those used to study the effective grain boundary diffusivity in Chapter 2. The diffusant concentration is a constant, C_0, at the left side of the simulation domain and zero at the right side, while a zero-flux condition is imposed at the top and bottom. (We have also run simulations for a concentration gradient running top-to-bottom for hexagonal and triangular cells. The results are indistinguishable from the data for a left-to-right concentration gradient.) The requirement of mass balance at the nodes results in a set of linear equations that are solved by the finite element solver. The average flux <J> in Eq. (102) is directly determined from the reaction flux[#], which is a standard output in ABAQUS.

3.1.2. Percolation Threshold of the Effective Diffusivity

Although prior to this study there have not been any direct numerical data for the effective properties of symmetric-cell composites, researchers in the field have realized that percolation in continuum composites is different from discrete lattice (bond or site) models because of geometric effects. For example, since continuum phases fill space (or area in two dimensions) and can make face, edge, and corner contacts (or edge and corner contacts in two dimensions), the criterion for connectivity is no longer definitive and has to be examined specifically for a certain property. It has been speculated that for the symmetric-cell composites, transport properties might exhibit two percolation thresholds in two dimensions, one caused by the connectivity among both nearest- and second-nearest- neighbors and the other caused by the connectivity among solely the nearest neighbors [156, 157]. In other words, transport through corner contacts can lead to an additional percolation threshold beyond the conventional one caused by edge contacts.

Our study is the first to examine the percolation behaviors of such composite materials by directly working on the continuum. However, we only observe one percolation threshold for the effective diffusivity in the whole range of the phase fractions (see Figure 36). The effective diffusivities for composites with triangular cells exhibit a percolation threshold at $p_c \approx 0.3$; $p_c \approx 0.4$ for composites with square cells, and $p_c \approx 0.5$ for composites with hexagonal cells. It is important to first extract p_c as accurately as possible in order to obtain good estimation of the scaling exponents later. We calculate p_c based on the percolation probability $\Pi(p)$. The system is considered "percolating" when its effective diffusivity $D_{eff} > \sqrt{D_1 D_2}$ such as those data points in the top part in Figure 36. By averaging over many realizations at the same p, we obtain the percolation probability $\Pi(p)$ which is plotted in Figure 37. In percolation theory, $d\Pi/dp$ is supposed to behave like the Gaussian distribution with a characteristic width (standard deviation) Δ [3]:

$$\frac{d\Pi}{dp} = \frac{1}{\sqrt{2\pi}\Delta} \exp\left(-\frac{(p-p_c)^2}{2\Delta^2}\right) \tag{103}$$

[#] In finite element simulations, the unknowns at the positions where boundary conditions are imposed are excluded from the linear equations to avoid singularity. After the equations are solved, the responses at the domain boundary (flux in the present case) can be calculated and are usually termed as *reaction* quantities.

Integrating Eq. (103) from 0 to p, we obtain

$$\Pi(p) = 0 + \int_0^p \left(\frac{d\Pi}{dp}\right) dp = \frac{1}{2}\mathrm{erf}\left(\frac{p_c}{\sqrt{2}\Delta}\right) + \frac{1}{2}\mathrm{erf}\left(\frac{p - p_c}{\sqrt{2}\Delta}\right) \tag{104}$$

where erf denotes the error function.

$$\mathrm{erf}(x) = \frac{2}{\sqrt{\pi}} \int_0^x \exp\left(-t^2\right) dt \tag{105}$$

The fit of Eq. (104) to the percolation probability obtained from simulation data is plotted in black lines in Figure 37, where the percolation threshold p_c and the distribution width Δ from the fitting are also listed.

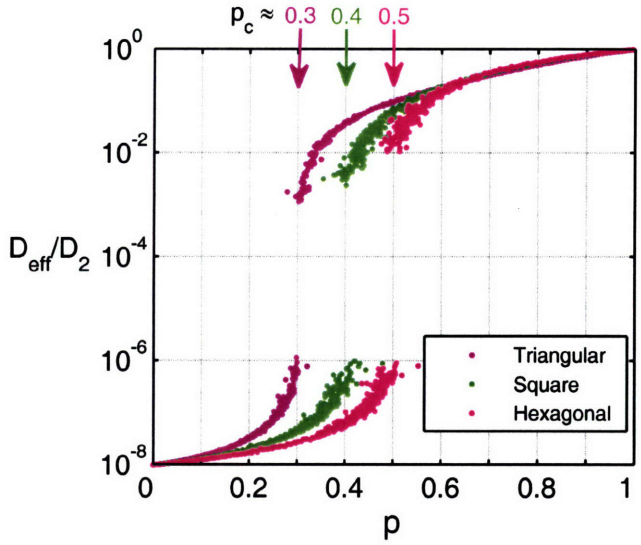

Figure 36. Normalized effective diffusivity of the two dimensional two-phase composites (shown in Figure 34) as a function of the area fraction of the fast-diffusing phase.

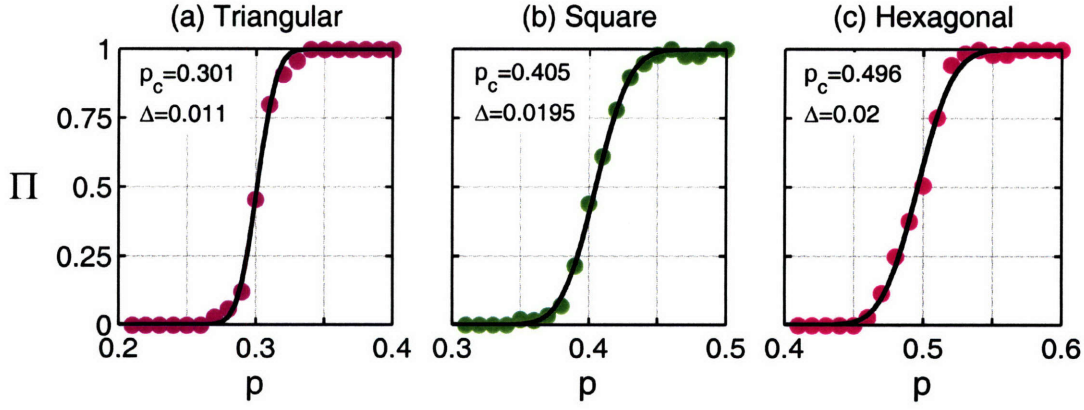

Figure 37. Percolation probability Π as a function of p, the fraction of the phase with a higher diffusivity D_2, for composites with (a) triangular, (b) square, and (c) hexagonal cells. The black line in each figure is the fitting of the simulation results to Eq. (104) in order to extract the percolation threshold p_c.

The percolation thresholds obtained from the fitting in Figure 37 are compared with known percolation thresholds for site percolation on discrete lattices in Table 7. Interestingly, the percolation thresholds we obtain for diffusion in continuum composites are very close to some percolation thresholds on dual lattices (bold numbers in the table).

Table 7. Comparison between site percolation thresholds for discrete lattices and the percolation thresholds for diffusion in the present continuum composites.

Site percolation on discrete lattices				Diffusion in continuum composites	
Lattice	p_c for NN	p_c for NN+NNN	p_c for NN+NNN+4N	Cell Shape	p_c
Triangular	**0.5** (6)	0.289 (12)	N/A (18)	Hexagonal	0.496 (6)
Square	0.592 (4)	**0.407** (8)	0.288 (12)	Square	0.405 (8)
Honeycomb	0.697 (3)	N/A (9)	**0.288*** (12)	Triangular	0.301 (12)

Note:
1. "NN" denotes connectivity among nearest neighbors, "NNN" next-nearest neighbors, and "4N" next-next-nearest neighbors. The numbers in the parenthesis are the new coordination numbers. Results for square lattices are from Ref. [34, 158] and while p_c for NN+NNN on the triangular lattice is from Ref. [159].
2. * means there is no direct theoretical or numerical result for the site percolation threshold on a honeycomb lattice considering connectivity beyond the nearest neighbors. However, considering that p_c for a coordination number of 12 on both triangular (NN+NNN) and square (NN+NNN+4N) lattices are both ~0.289, we may conjecture that p_c for NN+NNN+4N on the honeycomb lattice may be 0.288 as well because of the same new coordination number.

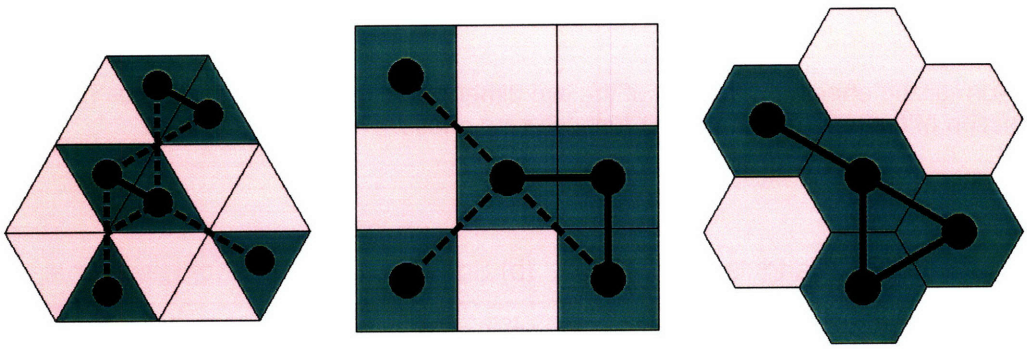

(a) (b) (c)

Figure 38. Schematic illustration of mapping the connectivity of symmetric-cell composite materials to the connectivity on corresponding site lattices for (a) triangular, (b) square, and (c) hexagonal cell shapes. The cells are mapped into sites on a dual lattice. Specifically, triangular cells are mapped into a honeycomb lattice, square cells into square lattice, and hexagonal cells into triangular lattice. Edge contacts between cells are mapped into connections between nearest-neighbor sites (in solid lines). Corner contacts are mapped into connections between next-nearest-neighbor sites (in dashed lines).

The percolation thresholds for composites with triangular and square cells are both consistent with corresponding discrete site percolation thresholds, when allowing for simultaneous connections among nearest and further neighbors. This may be because so far as the transport properties are concerned,

the connectivity of these two types of composites can be simplified as a site percolation problem, where each site represents one cell/particle and can connect to all neighboring sites sharing a cell edge or corner. This mapping process is further illustrated in Figure 38. For triangular cells, both the next-nearest (NNN) and the next-next nearest (4N) neighbors can connect to each other by corner contacts, and the diffusion lengths for these cases are actually the same since diffusion almost exclusively takes place in the fast-diffusing phase (green phase). Thus hereafter these two interconnections will both be referred to as next-nearest neighbor connectivity. The percolation threshold for composites with hexagonal cells, $p_c \approx 0.5$, is the same as the site percolation threshold on a triangular lattice only allowing for nearest-neighbor connections (NN). This is because hexagonal particles have to meet each other at edges; they cannot have corner contacts without sharing an edge.

The percolation thresholds for square and triangular site lattices considering only the nearest-neighbor connectivity are 0.59 and 0.5, respectively. We do not observe any discontinuity at these values. This result is somewhat surprising, considering that transport across the edge contacts should be more effective than through corner contacts. Many researchers (e.g., Refs. [160, 161]) seem to have expected a second inflection at the volume fraction where edge contacts become the dominant diffusion path. Here we find that additional edge contacts represent an apparently minor change in the system as compared to the change from having no percolation path to the emergence of a percolation path.

3.1.3. Percolation Scaling

The scaling properties we are most concerned with are the scaling of the effective diffusivity with respect to the distance from the percolation threshold, i.e., $D_{eff} \propto (p_c - p)^{-s}$ for $p < p_c$ and $D_{eff} \propto (p - p_c)^t$ for $p > p_c$, as the scaling exponents s and t can be directly used to predict the effective properties.

The above results for the percolation threshold open up the question of whether the scaling behaviors for these symmetric-cell composite materials are the same as the discrete lattice percolation. On the one hand, we have shown that the present percolation thresholds are equivalent to the site percolation thresholds including next-nearest neighbor connectivity for square and triangular cells; this should be considered a short-range correlation. In percolation theory, a short range correlation is not expected to change the percolation universality class, i.e., the scaling of our current problem should be the same as the site percolation problem. But on the other hand, our system is actually a continuum system and cannot be simply anticipated based on lattice observations even though the percolation thresholds align between the two problems. Although the coexistence of corner and edge contact does not result in two percolation thresholds, they may affect the percolation scaling exponents.

The scaling of the effective diffusivity D_{eff} (normalized by D_2) with respect to $|p\text{-}p_c|$, the distance from the percolation threshold, is shown in Figure 39(a) for p below the percolation threshold p_c. Compared to diffusion on heterogeneous grain boundary networks (cf. Figure 13), now the scaling exponent s is slightly

less uniform as p changes. $s \approx 1.2$ for p close to p_c and $s \approx 1$ for p far away from p_c. As the magnitude of the scaling exponent reflects the connectivity, we may infer that the biggest cluster of the fast-diffusing phase does not grow at a constant rate as p increases, which is normal and reasonable. Data for the three cell-shapes all show such a trend, although the difference between s close to and far from p_c is the biggest for triangular cells. We suspect the bigger difference for triangular cells results from the higher probability of connecting to neighbors via corner contacts (Figure 38) at higher p.

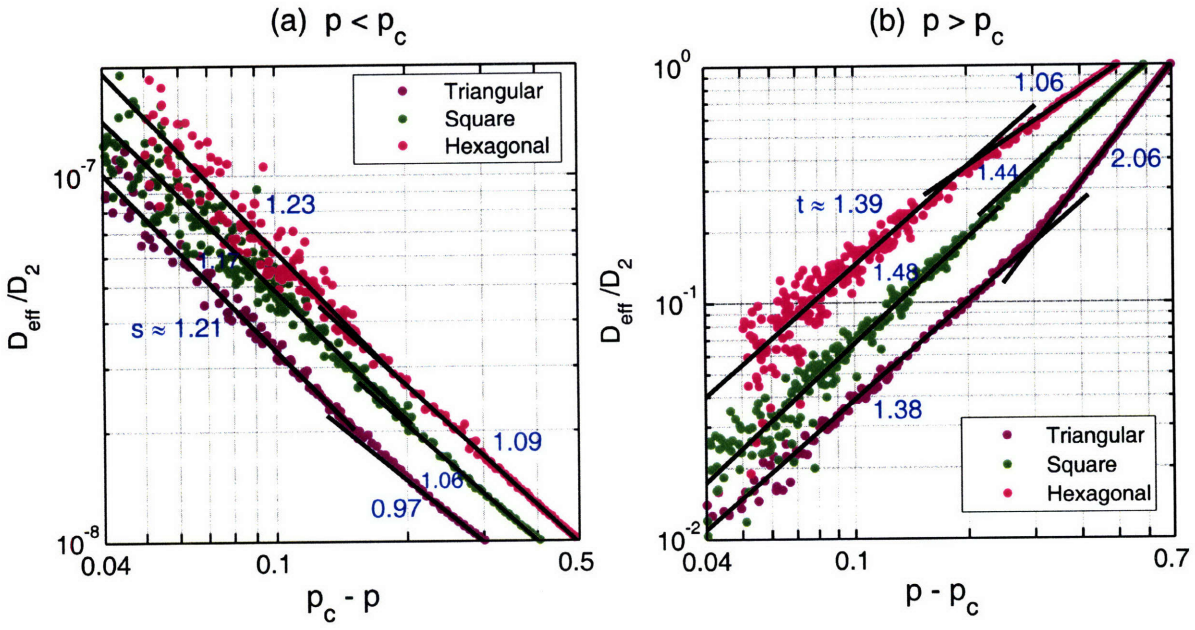

Figure 39. Scaling of the effective diffusivity with respect to the distance from the percolation threshold p_c for the three types of composites materials. (a) is for the data below p_c and therefore provide the scaling exponent s, and (b) is for data above p_c and provide the scaling exponent t.

The scaling behavior for p above the percolation threshold p_c is plotted in Figure 39(b). The scaling exponent $t \approx 1.4$ for p close to p_c for all the three data sets. It has been proven in Eq. (31) that for diffusion on a strict two-dimensional network, s and t in the vicinity of p_c should be equal to each other. Some numerical simulations yield $s = t \approx 1.3$. However, we have found that for diffusion on the continuum, $s \approx 1.2$ and $t \approx 1.4$ for p close to p_c. It is interesting that these exponents are no longer symmetric in two dimensions.

The trend in the scaling exponent t as p increases is now different for the three cell shapes. For composites with hexagonal cells, t decreases from ~1.39 for p close to p_c to ~1.06 for p far away from p_c. Since hexagonal cells never meet at corners without also meeting at an edge, we may consider such a decrease in t as normal behavior analogous to the decrease in s when p moves away from p_c in Figure 39(a). However, for composites with square cells, t remains almost the same (1.44-1.48) at all fractions.

For composites with triangular cells, t even increases significantly from ~1.38 to ~2.06. These two distinctly different slopes are very obvious in Figure 39(b).

The abnormal trend in t for square and triangular shapes may be attributed to diffusion through corner contacts in addition to the normal contacts in two dimensions, as illustrated in Figure 38. For these two cell shapes, the single percolation threshold ($p_c \approx 0.405$ for square and 0.301 for triangular cells) we have observed corresponds to the phase fraction at which a percolating cluster of cells connected at both edges and corners first appears. The later formation of a percolating cluster of cells exclusively connected via edges at higher p (~0.593 for square and ~0.696 for triangular cells, which correspond to normal site percolation threshold on square and hexagonal lattices, respectively (see Table 2)) has not resulted in any additional percolation threshold in effective diffusivity. However, such formation of a more effective diffusion path seems to tend to cause an increase in the percolation scaling exponent t. In composites with square cells, each cell connects to four neighboring cells via corners and four others via edges. So the formation of a percolating cluster of cells all connected at edges does not represent a big change in connectivity and may only result in a small increase in t. However, this small increase can be offset by the normal decreasing trend, such as what occurred in composites with hexagonal cells, and therefore t remains almost constant at all fractions. In composites with triangular cells, however, each cell connects with only three neighboring cells at edges while connecting with nine neighbors at corners. In this case the later formation of a percolating cluster of cells all connected at edges significantly increases the connectivity on the continuum. It is thus not surprising that t can still increase from ~1.38 to ~2.06 even after subtracting ~0.3, the normal amount by which t would decrease if not for the change in connectivity.

It thus seems that continuum percolation should be considered belong to a different universality class from lattice percolation or even possibly be nonuniversal. Effective properties of heterogeneous solids cannot be inferred from any network generated from mapping. Instead they should be studied strictly on the continuum. The unusual scaling behaviors of composite solids make it difficult for us to accurately predict their effective properties, and will stand as a major challenge to the effective use of percolation theory in materials science.

3.1.4. Predicting Effective Diffusivity of Composite Solids: Difficulty Due to Multiconnectivity

We may use the generalized effective medium (GEM) equation (Eq. (36)) to predict effective properties of binary heterogeneous materials. A prerequisite, though, is that the scaling exponents s and t should be constant below and above the percolation threshold, respectively. In Chapter 2.1, the GEM equation has been proven able to yield reasonably good predictions for the effective diffusivities of heterogeneous grain boundary networks. Its success in this case should be attributed to the almost constant values of s and t for all p below and above the percolation threshold p_c, respectively. In Chapter 2.2, the scaling

behaviors of grain boundary diffusional creep are a bit more complex. While s is still almost constant, t gradually decreases from ~1.7 to ~0.7 as p increases from p_c to 1. When we use an average value, 1.26, to represent the scaling exponent above p_c, the GEM equation generally fits well to the simulation data except that there is some obvious deviation above the percolation threshold. This is because using a single average value as the exponent cannot capture all the physics associated with the gradual change in t. Now we find that the scaling exponents for composite solids are similarly, if not more, complicated. Even if we neglect the small decrease in both s and t as p moves away from the percolation threshold (see Figure 39), we still need to deal with the large increase in t for composites with triangular cells or more generally, composites with particles making point contacts in two dimensions and point and/or edge contacts in three dimensions.

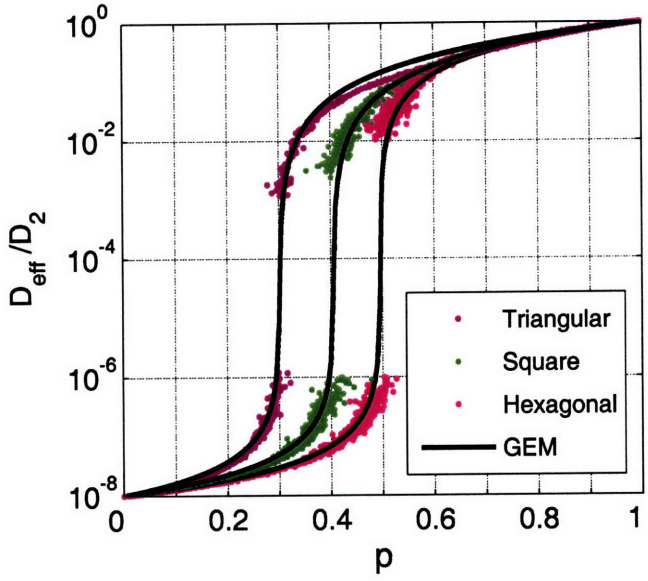

Figure 40. Comparing the predictions of the GEM equation (Eq. (36)) using averaged exponents to the simulation data.

We may for the moment again ignore all the variations in s and t as a function of p and only use an average value to represent them in the GEM equation, by fitting with s and t as adjustable parameters. The resulting fits of the GEM equation are plotted in black lines in Figure 40. Estimations from the GEM equation in general agree well with the simulation data for composites with hexagonal and square cells because for these two cell shapes, the variations in the scaling exponents are relatively small. This fortuitous agreement does not hold for triangular cells, unfortunately. The use of an average exponent t (~1.55) results in a large deviation from the simulation data at large values of p. The deviation seems even much larger than that observed earlier for diffusional creep when an average t is also used. This might be because in the case of creep, t gradually changes as p increases so an average t can somewhat represent the system on a coarse level. On the contrary, diffusion in composite solids with triangular cells shows a more abrupt discontinuity and two distinctly different values of t instead of a continuous variation

above the percolation threshold. An average value of t is thus much less representative of the true responses of the system.

To summarize the above discussion, we find that the new element of effective connectivity at corners in two dimensional composite solids has resulted in new scaling behaviors. The nonuniform scaling exponent t presents a challenge to evaluating the effective diffusivities or other properties because the convenient and powerful tool that is the GEM equation (Eq. (36)) requires a single value for each scaling exponent. Extending the GEM equation for such complex situations is necessary, but will be undoubtedly difficult. In the original GEM equation, s and t are the scaling exponent below and above the percolation threshold p_c, respectively. It is not clear, at least to the present author, how to introduce an additional value of t for p above a critical value yet without invoking a second percolation threshold into the equation. It is as challenging as the idea of extending the equation for a continuously changing scaling exponent, such as in the case of Coble creep.

3.2. Linear Elastic Properties

Previously we have studied linear diffusion properties of discrete heterogeneous grain boundary networks in Chapter 2.1 and composite solids in Chapter 3.1, as well as grain boundary diffusional (Coble) creep in Chapter 2.2. In all these cases, each boundary or phase has been characterized by one diffusion coefficient, under our assumption of isotropy. In this section, we will study the effective elastic properties of composite solids, where each phase should be characterized by at least two independent elastic constants. In the composite community, numerous efforts have been devoted to developing a rigorous and practical method to evaluate the effective elastic properties. Despite all the progresses made in developing high-order bounds and effective medium theories, this goal is yet to be achieved.

In a continuum composite, each phase is characterized by a stiffness tensor $C(x)$:

$$\sigma_{ij}(x) = C_{ijkl}(x)\varepsilon_{kl}(x) \tag{106}$$

with σ the stress tensor and ε the strain tensor. The tensor C has only two independent components for isotropic materials. The stress-strain relationships are usually described by a few common pairs of parameters, including the Lamé constant λ and the shear modulus G, or the Young's modulus E and Poisson's ratio v, or the bulk modulus K and the shear modulus G. We use the bulk and shear modulus to characterize the phases,

$$\sigma_{ij}(x) = K\delta_{ij}\varepsilon_{kk} + 2G\varepsilon'_{ij} \tag{107}$$

where $\varepsilon_{kk} = \varepsilon_{11} + \varepsilon_{22} + \varepsilon_{33}$ is the volumetric strain, ε'_{ij} is the deviatoric strain, and δ_{ij} is the Kronecker delta. Therefore the effective bulk modulus K_{eff} and effective shear modulus G_{eff} can be defined through

$$\langle\sigma_{ij}(x)\rangle = K_{eff}\delta_{ij}\langle\varepsilon_{kk}\rangle + 2G_{eff}\langle\varepsilon'_{ij}\rangle \tag{108}$$

where <> denotes an average over the whole sample.

3.2.1. Finite Element Simulation Procedures

We study two-dimensional isotropic elasticity by applying a plane strain condition. It is physically relevant to materials with one dimension significantly thicker than the other two, such as fiber-reinforced composite materials. Simulating two-dimensional microstructures also allows us to obtain physically meaningful data by studying large systems with sufficiently refined meshes. For a single phase, the plane strain bulk modulus K^{PE} and shear modulus G^{PE} are related to their three dimensional counterparts K and G by:

$$K^{PE} = K + G/3$$
$$G^{PE} = G \tag{109}$$

and the stress-strain relationship can be described as

$$\sigma_{ij}(x) = K^{PE}\delta_{ij}\varepsilon_{kk} + 2G^{PE}\varepsilon'_{ij} \tag{110}$$

where all the indices i, j, k can be 1 or 2. We define the plane strain effective bulk and shear moduli using the strain energy density U.

$$U = \frac{1}{2}\left[K^{PE}_{eff}\langle\varepsilon_{kk}\rangle^2 + 2G^{PE}_{eff}\langle\varepsilon'_{ij}\rangle\langle\varepsilon'_{ij}\rangle\right] \tag{111}$$

There are usually three types of boundary conditions [162, 163]: (1) static (also called uniform traction or Neumann) boundary conditions; (2) kinematic (also called uniform displacement or Dirichlet) boundary conditions; (3) Orthogonal mixed boundary conditions, where displacements are applied on all sides of the specimen without friction. The static and kinematic uniform boundary conditions are usually considered to provide a lower and upper bound estimation for the effective elastic properties while the orthogonal mixed boundary conditions provide better estimations. Meanwhile, the mixed boundary condition is also closer to the conditions achieved in common experimental setups. The mixed boundary conditions we use to obtain the effective bulk and shear modulus are illustrated in Figure 41 (a) and (b), respectively.

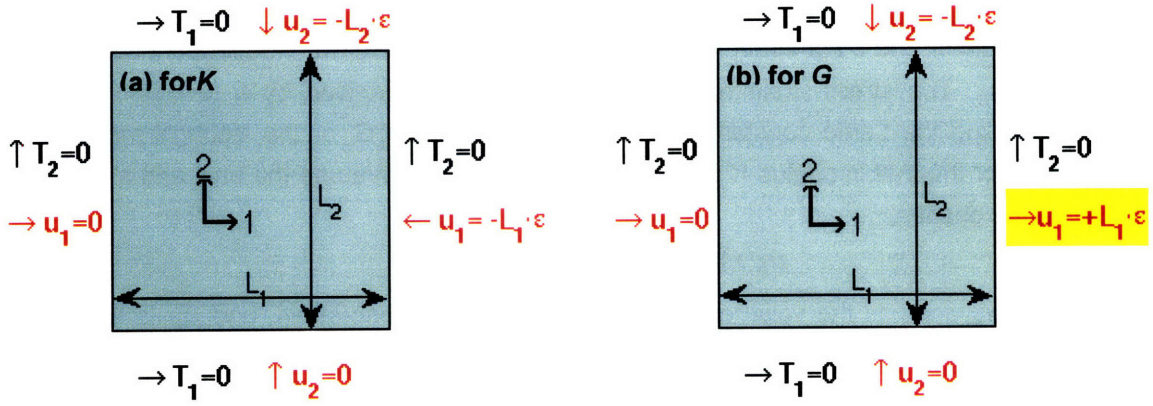

Figure 41. Orthogonal mixed boundary conditions used in calculating effective bulk modulus (a) and shear modulus (b). T denotes surface traction and u surface displacement.

When calculating the effective bulk modulus K_{eff}^{PE}, we have applied an equibiaxial compression, $\varepsilon_{11} = \varepsilon_{22} = -\varepsilon$ while requiring all surface shear forces to be zero (Figure 41(a)). If we ignore the microstructural heterogeneity for the moment and consider the system to be a homogeneous material with a bulk modulus K_{eff}^{PE}, then only hydrostatic pressure would develop under these boundary conditions and the strain energy would be purely volumetric, i.e., $K_{eff}^{PE}\langle\varepsilon_{kk}\rangle^2/2$. This strain energy should be equal to the total strain energy U of the composite material, and this defines the effective bulk modulus of the composite material as [164]

$$K_{eff}^{PE} = \frac{2U}{\langle\varepsilon_{kk}\rangle^2} = \frac{U}{2\varepsilon^2} \tag{112}$$

When calculating the effective shear modulus G_{eff}^{PE}, we have used a biaxial loading, $\varepsilon_{11} = \varepsilon$ and $\varepsilon_{22} = -\varepsilon$, and also require the shear stresses on surfaces to vanish (Figure 41(b)). Again we invoke the idea of homogenization and view the composite material as a homogeneous material with an effective shear modulus G_{eff}^{PE}, then the strain state in the coordinate system rotated by 45° is pure shear according to

$$\begin{bmatrix} \cos 45° & -\sin 45° & 0 \\ \sin 45° & \cos 45° & 0 \\ 0 & 0 & 0 \end{bmatrix} \begin{bmatrix} \varepsilon & 0 & 0 \\ 0 & -\varepsilon & 0 \\ 0 & 0 & 0 \end{bmatrix} \begin{bmatrix} \cos 45° & \sin 45° & 0 \\ -\sin 45° & \cos 45° & 0 \\ 0 & 0 & 0 \end{bmatrix} = \begin{bmatrix} 0 & \varepsilon & 0 \\ \varepsilon & 0 & 0 \\ 0 & 0 & 0 \end{bmatrix} \tag{113}$$

Therefore the strain energy would be purely deviatoric, i.e., $G_{eff}^{PE}\langle\varepsilon'_{ij}\rangle\langle\varepsilon'_{ij}\rangle$. This strain energy should be equal to the total strain energy U of the composite material, and this defines the effective shear modulus of the composite material as

$$G_{eff}^{PE} = \frac{U}{\langle\varepsilon'_{ij}\rangle\langle\varepsilon'_{ij}\rangle} = \frac{U}{2\varepsilon^2} \tag{114}$$

The strain energy density U in Eqs. (112) and (114) are obtained from a standard output, the recoverable strain energy "ALLSE for Whole Model", in Abaqus.

We have not directly used a pure or simple shear strain state as the boundary condition because in these two cases, the large shear strains at the four sample corners would induce unphysically large stress concentrations, especially when there are phases with higher modulus at or close to these corners (see Figure 42). Such highly localized nonuniform strain distribution close to the surfaces would significantly affect the simulation results, particularly for small specimen sizes.

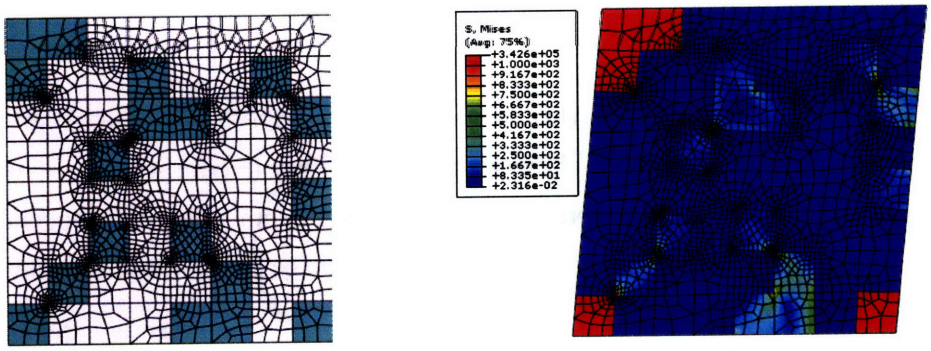

(a) (b)

Figure 42. An example of the stress concentrations at corners under simple shear boundary conditions. (a) The phase distribution. The green phase has higher bulk and shear moduli than the other phase. (b) The distribution of Von Misses stress. Notice that the stresses at the three corners occupied by the phase with higher moduli are two orders of magnitude higher (in red) than in other cells.

We have simulated symmetric-cell composite materials comprised of 6400 square cells (shown in Figure 34(b)). The two phases are randomly distributed over the cells, and are assumed to be perfectly bonded. In order to show the percolation on the effective modulus – phase fraction curve, we use a high modulus contrast ratio. K_2^{PE}/K_1^{PE} is fixed at 10^4 when obtaining the effective bulk modulus and G_2^{PE}/G_1^{PE} is also fixed at 10^4 when obtaining the effective shear modulus.

Since the plane strain bulk and shear moduli are related to the elastic modulus and Poisson's ratio,

$$K^{PE} = \frac{E}{2(1+\upsilon)(1-2\upsilon)}$$
$$G^{PE} = \frac{E}{2(1+\upsilon)} \tag{115}$$

the Poisson's ratio is related to the two moduli through

$$\upsilon = \frac{1-G^{PE}/K^{PE}}{2} \tag{116}$$

Therefore if the ratio of these two moduli for a given phase approaches zero ($G^{PE}/K^{PE} \to 0$), the Poisson's ratio v approaches 0.5, the incompressible limit. In fact, when $v > 0.49$ (or $G^{PE}/K^{PE} < 0.02$), the material should be considered as nearly incompressible. As a result, a purely hydrostatic pressure can be applied to the phase without having to change the displacements much, or conversely, a solution based on the idea of virtual displacement only would be too sensitive as a subtle change in solution (such as computer round-off) could induce an enormous change in pressure. We avoid this problem by using hybrid elements in nearly incompressible phase(s). The hybrid elements are "mixed formulation" elements using a mixture of displacement and stress variables with an augmented Variational principle to approximate the equilibrium equations and compatibility conditions. The pressure stresses are treated as a basic solution variable independently interpolated instead of being calculated from the solved displacements [165].

We have used a free meshing technique for all of the composite materials studied here. The element shapes are quadrilateral dominated, and are either 8-node biquadratic quadrilaterals or 6-node triangles, with reduced integration. The quadratic (second-order) elements provide higher accuracy in Abaqus. They capture stress concentrations more effectively and are better for modelling geometric features than first-order elements. Reduced integration uses a lower-order integration to form the element stiffness matrix, and can reduce running time. Also second-order reduced-integration elements generally provide more accurate results than the corresponding fully integrated elements. The materials parameters (plane strain bulk modulus K^{PE}, plane strain shear modulus G^{PE}, the Poisson's ratio v) as well as the corresponding elements used in our simulations are listed in Table 8. The unit of all moduli presented in the table can be considered as MPa, although the specific unit does not affect any conclusions.

Table 8. Elastic properties of each phase and the corresponding element types used in finite element simulations for obtaining the effective bulk and shear moduli.

Purpose	Phase 1			Phase 2			Phase Ratio		Elements[a]
	K_1^{PE}	G_1^{PE}	υ_1	K_2^{PE}	G_2^{PE}	υ_2	$\frac{K_2^{PE}}{K_1^{PE}}$	$\frac{G_2^{PE}}{G_1^{PE}}$	
K_{eff}^{PE}	6.25×10^{2}	5×10^{2}	0.1	6.25×10^{6}	5×10^{2}	0.49996	10^4	1	CPE8RH, CPE6H
	6.25×10^{2}	5×10^{2}	0.1	6.25×10^{6}	5×10^{3}	0.4996	10^4	10	CPE8RH, CPE6H
	6.25×10^{2}	5×10^{2}	0.1	6.25×10^{6}	5×10^{4}	0.496	10^4	10^2	CPE8RH, CPE6H
	6.25×10^{2}	5×10^{2}	0.1	6.25×10^{6}	5×10^{5}	0.46	10^4	10^3	CPE8R, CPE6
	6.25×10^{2}	5×10^{2}	0.1	6.25×10^{6}	5×10^{6}	0.1	10^4	10^4	CPE8R, CPE6
G_{eff}^{PE}	6.25×10^{2}	5×10^{2}	0.1	6.25×10^{6}	5×10^{6}	0.1	10^4	10^4	CPE8R, CPE6
	6.25×10^{3}	5×10^{2}	0.46	6.25×10^{6}	5×10^{6}	0.1	10^3	10^4	CPE8R, CPE6
	6.25×10^{4}	5×10^{2}	0.496	6.25×10^{6}	5×10^{6}	0.1	10^2	10^4	CPE8RH, CPE6H
	6.25×10^{5}	5×10^{2}	0.4996	6.25×10^{6}	5×10^{6}	0.1	10	10^4	CPE8RH, CPE6H
	6.25×10^{6}	5×10^{2}	0.49996	6.25×10^{6}	5×10^{6}	0.1	1	10^4	CPE8RH, CPE6H
	1.25×10^{8}	5×10^{2}	0.499998	1.25×10^{8}	5×10^{6}	0.1	1	10^4	CPE8RH, CPE6H

[a] In the notation for elements, 'C' stands for continuum, 'PE' plane strain, 'R' reduced integration, 'H' hybrid elements.

As we use a high phase contrast ratio (up to 10^4), stress concentrations are inevitable, particularly when the phases with higher modulus meet at corners. In order to sufficiently capture the stress concentrations, we again used the adaptive remeshing technique to automatically obtain an ultra fine mesh at locations with a high stress concentration (similar to Figure 35). We use element energy density ("ENDENERI" in Abaqus) as the error indicator and aim for a uniform error distribution in the specimen. We start with 4 mesh seeds per edge, and specify a minimum element size of 0.15% of the original element size to prevent unbounded element minimization. Although the presence of the sharp corners in

the model will inevitably lead to stress singularities, we believe that, with a sufficiently refined remesh at those locations, they have only a negligible effect on the overall response of the model.

For simplicity, we will use K and G to denote the plane strain bulk and shear moduli, instead of the more thorough notation K^{PE} and G^{PE}, in the remainder of this chapter.

3.2.2. Effective Shear Modulus

3.2.2.1. Effective Shear Modulus of Composite Materials with Equal Phase Bulk Moduli

To understand the effect of phase bulk moduli on the effective shear modulus G_{eff}, we first start with simple cases where the two phases comprising the composite have equal bulk moduli ($K_1 = K_2 = K$) but different shear moduli ($G_1 = 5\text{x}10^2$ and $G_2 = 5\text{x}10^6$). According to Eq. (116), $K_i = G_i/(1-2\nu_i)$, where $i = 1$ or 2 indicating the specific phase, and v is the Poisson's ratio. Since $0 < v < 0.5$ for most materials, the accessible values for K are very limited when both G_1 and G_2 are fixed and are held at a high contrast ratio such as 10^4 in the present case. By requiring υ_1 to approach the incompressible limit ($\upsilon_1 = 0.49996$ and 0.499998), we are able to obtain two sets of simulation parameters, $K_1 = K_2 = 6.25\text{x}10^6$ and $1.25\text{x}10^8$, which are different by a factor of 20. The complete simulation parameters have been included in Table 8. Hybrid elements are used in the simulation in order to accurately calculate the pressure in these nearly incompressible composite materials.

The effective shear modulus G_{eff} for these two cases are shown in Figure 43, where the simulation results for composites with $K_1 = K_2 = K = 6.25\text{x}10^6$ are plotted as black circles while green dots are results for composites with $K_1 = K_2 = K = 1.25\text{x}10^8$. For both cases, G_{eff} increases nonlinearly with the fraction of phase 2, p. It is really interesting that for $p < 0.4$, the values of G_{eff} for the two sets of data are almost the same; the specific value of the common bulk modulus of the phases does not seem to play a role. The effect of K only becomes discernible when p increases above 0.5. In this regime, the values of G_{eff} for composites with higher common K are slightly higher; the difference between the two curves is actually very large, although it doesn't appear so because of the wide axis range, considering that K is only 20 times different between the two cases. For example, the difference between G_{eff} for the two curves is even more than 20 times different when p is between 0.6 and 0.7. Because $K_1 = K_2 = K$ holds at any volume fraction p, G_{eff} for the two curves being the same at low p and being very different at higher p cannot be explained directly by the volume fractions, i.e., dilute limit vs. non-dilute fractions. One possibility is that G_{eff} is coupled with K. When G_{eff} is low, as is the case at low p, the effect of K is much smaller compared to when G_{eff} is high.

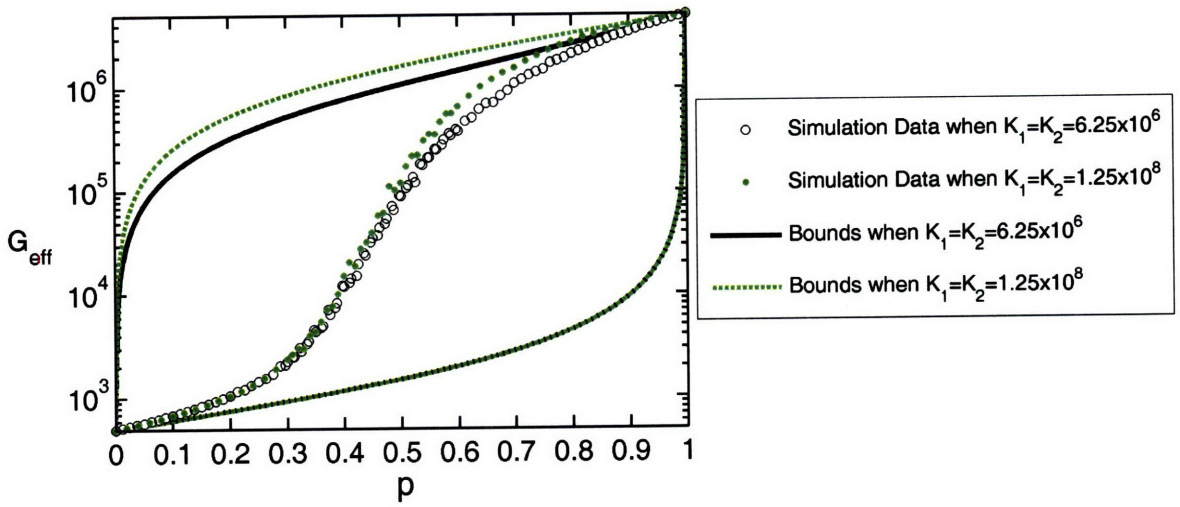

Figure 43. Effective shear modulus G_{eff} of two composite materials with two phases having the same bulk moduli (K_1 = K_2). Data points are simulation results while the lines are upper and lower bounds for G_{eff} calculated from Eq. (117) and (118). p is the fraction of phase 2.

Analogous to the bounds for linear transport properties presented in Eq. (1) to (4) in section 1.2.1, bounds have also been developed for linear elastic properties. The lower and upper bounds derived by Hashin [166] for effective shear modulus are

$$G^{(-)} = G_1 + \frac{p}{\frac{1}{G_2 - G_1} + \frac{(1-p)(K_1 + 2G_1)}{2G_1(K_1 + G_1)}} \tag{117}$$

$$G^{(+)} = G_2 + \frac{1-p}{\frac{1}{G_1 - G_2} + \frac{p(K_2 + 2G_2)}{2G_2(K_2 + G_2)}} \tag{118}$$

if $G_1 < G_2$. In contrast to the bounds for linear transport properties, Eq. (117) and (118) are not considered as the best possible bounds given the volume fraction p only in the entire range of p; there are not such "best" bounds yet. The bounds for the above two cases of $K_1 = K_2 = K$ are also plotted in Figure 43. Our simulation results always lie between the upper and lower bounds. Somewhat surprisingly, the lower bounds (Eq. (117)) for the two K values are almost identical while the upper bounds (Eq. (118)) for the two cases are very different from each other, different from the upper and lower bounds for transport properties which are always symmetric respect to each other (e.g., see Figure 3). On the other hand, however, the different behaviors of the upper and low bounds for G_{eff} are consistent with our prior observation that G_{eff} values for composites with a low and a high common bulk modulus K are almost the same at low p and are very different at high p. When p is low, G_{eff} of the composite material is very close to the lower bound; the value of K does not seem to affect the lower bound, thus it does not affect G_{eff}. When p is high, G_{eff} becomes much closer to the upper bound; since the higher K is, the higher the upper bound becomes, it seems reasonable to obtain higher G_{eff} for higher K. As mentioned in the previous paragraph, G_{eff} and K are very likely coupled. They might be coupled in a way similar to how K_i and G_i are coupled in Eq. (117) or (118); that is, $(aK + bG_{eff})/(K + cG_{eff})$, where a, b, and c are constants.

Similar to the derivation of the symmetric effective medium theory (EMT) of Eq. (11) or (12) for linear transport properties (discussed in section 1.2.2), the EMT for effective elastic properties has also been derived by Budiansky [167] from the exact solution for an isolated spherical inclusion embedded in an infinite matrix. Eshelby [168] solved the single inclusion problem and provided the stress-strain relationship for the inclusion. Budiansky [167] assumed that each particle can be considered embedded in an effective medium (similar to the self-consistent idea illustrated in Figure 5) so that the stress and strain in the particle can be described by the Eshelby solution. Using plain strain bulk and shear moduli, this EMT equation writes as

$$\frac{1-p}{1+\beta\left(\frac{G_1}{G_{eff}}-1\right)}+\frac{p}{1+\beta\left(\frac{G_2}{G_{eff}}-1\right)}=1 \tag{119}$$

where β is a proportionality between two strains in Eshelby's derivation. For the case of $K_1 = K_2 = K$, β takes on the form

$$\beta=\frac{6K+10G_{eff}}{15K+15G_{eff}} \tag{120}$$

We can consider the unity on the right side of Eq. (119) as (1-p)+p, and further rearrange Eq. (119) into a familiar form

$$(1-p)\frac{G_1-G_{eff}}{G_1+\left(\frac{1}{\beta}-1\right)G_{eff}}+p\frac{G_2-G_{eff}}{G_2+\left(\frac{1}{\beta}-1\right)G_{eff}}=0 \tag{121}$$

It is interesting to note that β in Eq. (120) looks consistent with our previous conjecture that K and G_{eff} may be coupled in the form of $(aK+bG_{eff})/(K+cG_{eff})$. Eq. (121) can be solved numerically for G_{eff}, which are plotted in Figure 44 for the same materials parameters as in Figure 43. Predictions from Eq. (121) agree with simulation results well when $p < 0.4$, but are too high at higher p.

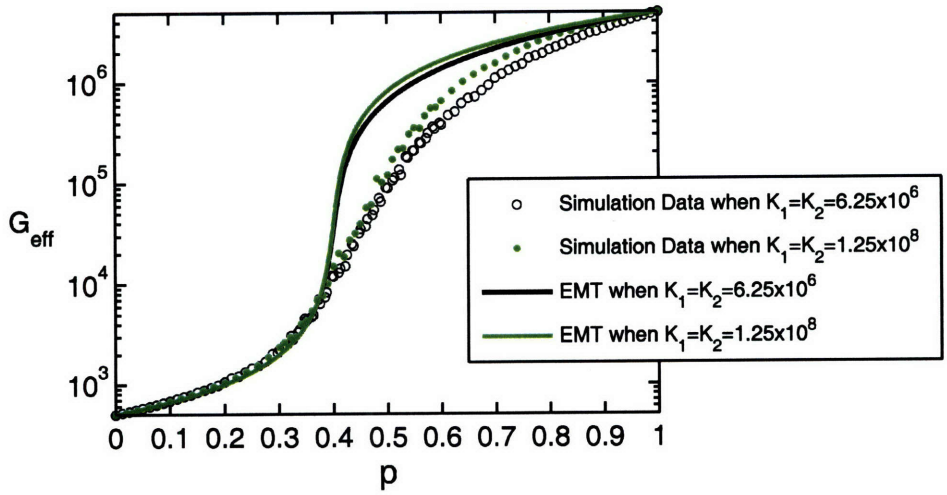

Figure 44. Predictions from the EMT equation (Eq. (121)) compared to simulation results.

Predictions from the EMT equation for effective shear modulus, Eq. (121), exhibit a discontinuity at $p \sim 0.4$. Eq. (121) actually appears very similar to the EMT equations for effective diffusivity, Eq. (11) and (45), which, as discussed in section 2.1.5, have implicitly assumed a percolation threshold. It is the same with Eq. (121). It has implicitly assumed a percolation threshold at $p_c = \beta$. For both sets of materials parameters, $K_1 = K_2 = K > G_2 >> G_1$, and therefore $K >> G_{eff}$. So p_c is approximately

$$p_c = \beta = \frac{6K + 10G_{eff}}{15K + 15G_{eff}} \xrightarrow{K>>G_{eff}} \sim \frac{6}{15} = 0.4 \tag{122}$$

a value consistent with the discontinuity in Figure 44, which is also fortuitously close to the true percolation threshold for the present simulation geometry—square cells with phases randomly distributed. Also in Eq. (121), the scaling exponents are all one, the same drawback as other types of EMT. The large deviations in the predictions from the equation from the simulation data may be attributed to these predefined scaling exponents of one.

It is for these reasons that the following GEM equation (similar to Eq. (36)),

$$(1-p)\frac{G_1^{1/s} - G_{eff}^{1/s}}{G_1^{1/s} + (p_c^{-1} - 1)G_{eff}^{1/s}} + p\frac{G_2^{1/t} - G_{eff}^{1/t}}{G_2^{1/t} + (p_c^{-1} - 1)G_{eff}^{1/t}} = 0 \tag{123}$$

is used instead to fit the simulation data. In Eq. (123), the percolation threshold p_c and the scaling exponent s and t are explicit included which we can use as fitting parameters. We for the moment assume that the effects of the bulk moduli are properly captured by the percolation threshold. The fittings of Eq. (123) to the simulation data are shown in Figure 45. For the two curves, the percolation threshold p_c and scaling exponent s are similar, but t is very different.

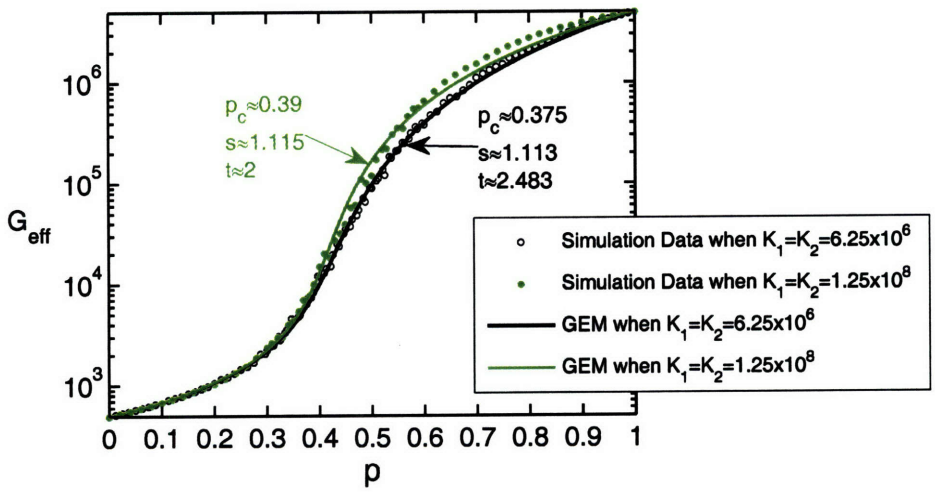

Figure 45. Fitting of effective shear modulus G_{eff} to the generalized effective medium equation (Eq. (123)). The fitted percolation properties p_c, s, and t for each curve are included in the figure.

The agreement of Eq. (123) with simulation results is better than Eq. (121), but is not perfect. It is extremely difficult to obtain good fittings at high p; there is no single value of t that can make the fitting good for the entire range of p! If the percolation threshold p_c as well as the data below p_c are required to be accurately described by the GEM equation, the resulting fit always predicts values of G_{eff} much lower than the simulation results at high p. Corner contacts may be an issue; however, t is almost a constant for diffusion in the same type of composites (Figure 39). Another possibility is that the effects of bulk moduli cannot be represented by the same percolation threshold; the large disagreement of Eq. (123) with simulation results at high p may be due to the stronger coupling between K and G_{eff} at high p. Eq. (123) needs to be modified to take into account this effect, possibly by including a term in the denominator like $(aK + bG_{eff})/(K + cG_{eff})$. Then the resulting new equation which combines the features of Eq. (121) and Eq. (123) may provide better predictions. This work is currently in progress.

3.2.2.2. Effective Shear Modulus of Composite Materials with Different Phase Bulk Moduli

We have studied the effective shear modulus G_{eff} of composite materials with two phases having the same bulk moduli ($K_1 = K_2$). The higher the magnitude of this common bulk modulus is, the higher the resulting G_{eff} is. So phase bulk moduli do affect composite materials' ability to change shape. Next we study the effects of the contrast in phase bulk moduli, K_2/K_1, on the effective shear modulus by gradually decreasing K_1 while keeping all other phase parameters such as K_2, G_1, and G_2 fixed.

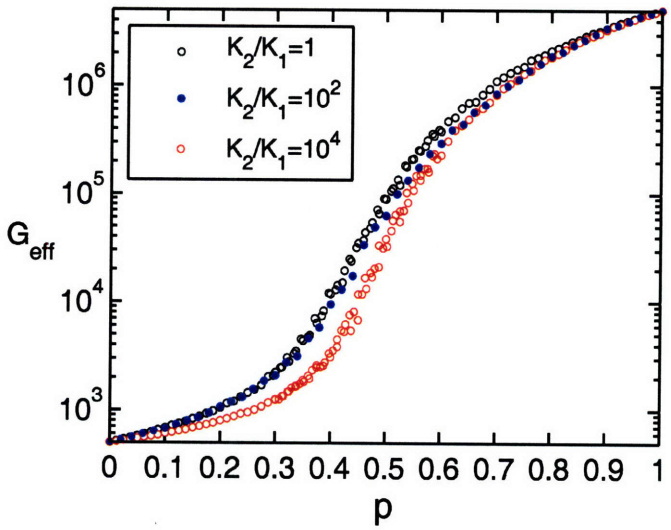

Figure 46. The dependence of the effective shear modulus G_{eff} of the composite materials on the ratio of the bulk modulus K_2/K_1 (K_2 is fixed while K_1 is different for these three curves). p is the fraction of phase 2 (with bulk modulus K_2 and shear modulus G_2).

Shown in Figure 46 are the values of G_{eff} for three different K_1 values, K_1 = 6.25x10^6, 6.25x10^4, and 6.25x10^2, which correspond to bulk modulus contrasts of K_2/K_1 = 1, 10^2, and 10^4, respectively. The overall trend is that as K_1 decreases, G_{eff} decreases (for example, from black to red data points in the figure), consistent with our previous observation that G_{eff} seems to change in the same direction as the phase bulk moduli. However, G_{eff} does not change linearly with K_2/K_1. The values of G_{eff} when K_2/K_1 = 10^2 (blue data points in the figure) do not always lie in between those for K_2/K_1 = 1 and 10^4, but rather seem to coincide with the data for K_2/K_1 = 1 at low p, and coincide with the data for K_2/K_1 = 10^4 at high p. This, again, implies that if there is to be an equation for G_{eff} as a function of phase properties, K and G must be coupled in a very complicated way in the equation.

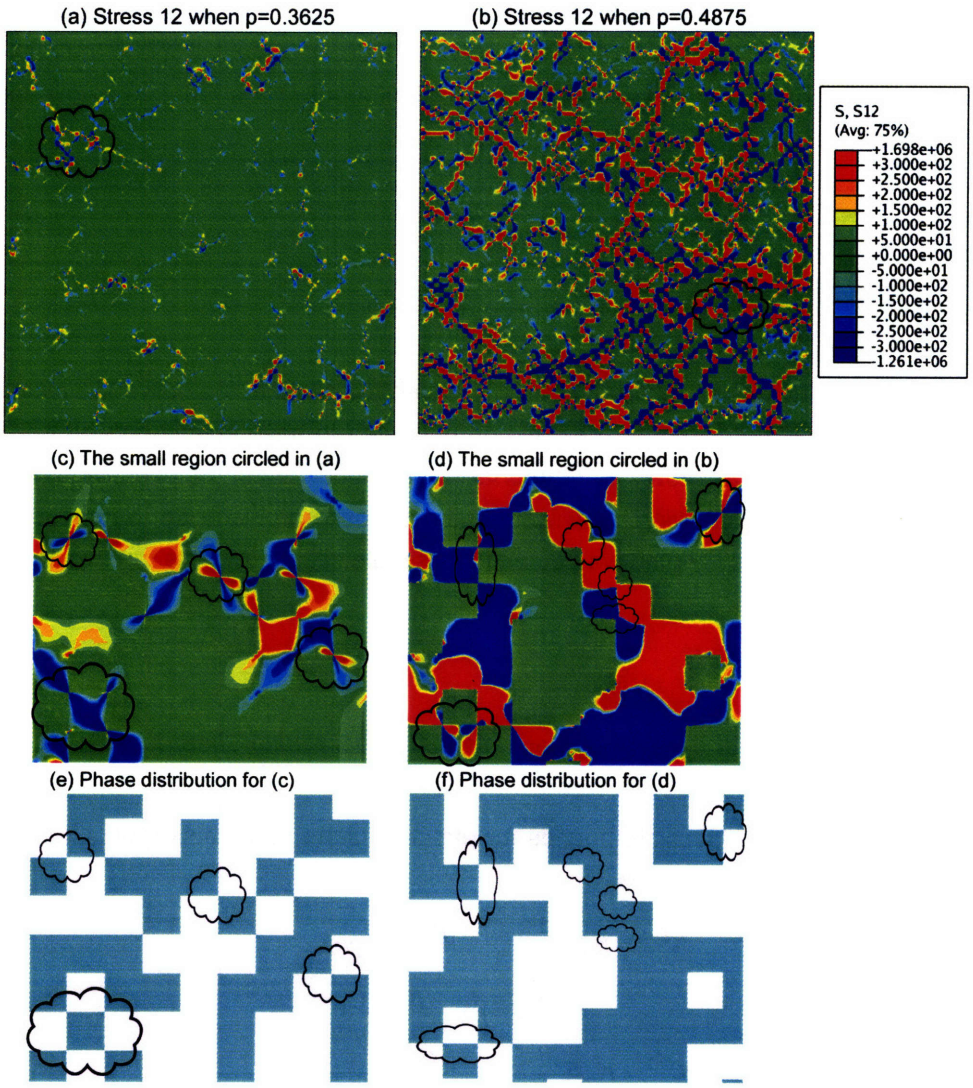

Figure 47. Distribution of shear stresses for composite materials with G_2/G_1 = 10^4 and K_2/K_1 = 10^4 at (a) p = 0.3625 and (b) p = 0.4875, with p being the fraction of phase 2. The small region circled in (a) is magnified in (c) whose corresponding phase distribution is provided in (e). Similarly the small region circled in (b) is maginified in (d) whose phase distribution is shown in (f). Advances of the shear stress through corners are highlighted in black circles in (c-f).

Finally, before we move on to the effective bulk modulus, let's look at how the shear stresses are distributed in the heterogeneous microstructure. The distributions of shear stresses for composite materials with $G_2/G_1 = 10^4$ and $K_2/K_1 = 10^4$ (same material parameter as the red data points in Figure 46) at two phase fractions, $p = 0.3625$ and 0.4875, are provided in Figure 47. The two phase fractions should be on opposite sides of the percolation threshold as can be seen in Figure 46. Below the percolation threshold, the shear stresses at most places are close to zero although some small, localized regions are under high shear stresses, such as the circled region in Figure 47(a). Above the percolation threshold, the stressed regions seem to form percolating paths in the material (Figure 47(b)); regions under positive stresses often accompany regions under negative stresses because of the deformation compatibility. Some details of the stress distributions can be seen in Figure 47(c) and (d) and the corresponding phase distributions are shown in Figure 47(e) and (f), respectively. Corner contacts among the square cells still play an important role in transmitting the stress, but exhibit different stress features below and above the percolation threshold.

3.2.3. Effective Bulk Modulus

While the shear modulus indicates materials' resistance to shape change, the bulk modulus measures the materials' resistance to volume changes. The two do not seem to have anything to do with each other, but in the above section we have shown that the phase bulk moduli affect the effective shear modulus in a very interesting way. In the following we will study the opposite problem: do the phase shear moduli affect the effective bulk modulus? Again we begin with a simple situation where the two phases have the same shear moduli.

3.2.3.1. Effective Bulk Modulus of Composite Materials with Equal Phase Shear Moduli

Hashin [166] proposed the best possible bounds for effective plane strain bulk modulus in terms of only phase moduli and phase volume fractions.

$$K^{(-)} = K_1 + \frac{p}{\frac{1}{K_2 - K_1} + \frac{1-p}{K_1 + G_1}} \tag{124}$$

$$K^{(+)} = K_2 + \frac{1-p}{\frac{1}{K_1 - K_2} + \frac{p}{K_2 + G_2}} \tag{125}$$

The upper and lower bounds coincide ($K^{(-)} = K^{(+)}$) when $G_1 = G_2 = G$ [166, 169-171]. This means that the effective bulk modulus can be calculated exactly from either equation when the two phases have the same shear modulus, regardless of the phase geometry.

$$K_{eff} = K_1 + \frac{p}{\frac{1}{K_2 - K_1} + \frac{1-p}{K_1 + G}} = K_2 + \frac{1-p}{\frac{1}{K_1 - K_2} + \frac{p}{K_2 + G}} \tag{126}$$

Eq. (126) is invariant upon the interchange of indices 1 and 2.

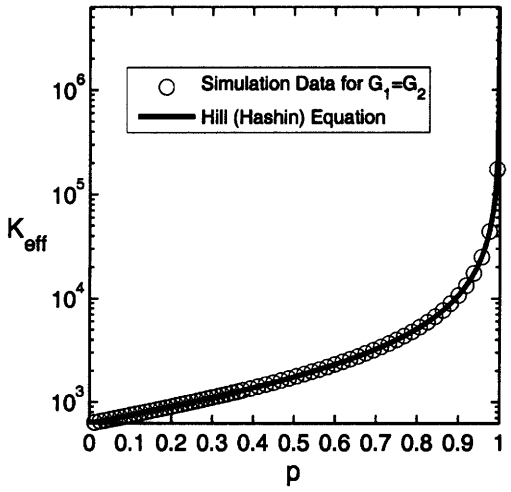

Figure 48. Effective bulk modulus of composite materials composed of two phases that have the same shear moduli ($G_1 = G_2$). Our simulation data are in excellent agreement with predictions from the Hill (or Hashin) Equation (Eq. (126)) plotted as the solid line.

We compare our simulation data for this specific case with the predictions from Eq. (126) in Figure 48. The excellent agreement between our simulation results and Eq. (126) assures us that our simulation procedures are correct on the one hand, and on the other hand, makes us wonder why Eq. (126) works so well. It is remarkable that this equation is valid for two-phase composites with any phase geometry if the two phases have the same shear moduli. Hill [169, 170] showed that a sufficient condition for Eq. (126) to be true is to have piecewise constant volumetric strain (or pressure) in each phase. If the volumetric strains are e_1 and e_2 in the two phases respectively, and the pressures are P_1 and P_2, then the effective bulk modulus is

$$K_{eff} = \frac{f_1 P_1 + f_2 P_2}{f_1 e_1 + f_2 e_2} = \frac{f_1 (K_1 e_1) + f_2 (K_2 e_2)}{f_1 e_1 + f_2 e_2} \tag{127}$$

The equivalence between Eq. (126) and Eq. (127) requires that

$$\frac{e_1}{e_2} = \frac{K_2 + G}{K_1 + G} \tag{128}$$

which is the same as

$$\frac{P_1}{P_2} = \frac{K_1 (K_2 + G)}{K_2 (K_1 + G)} \tag{129}$$

It turns out that the piecewise condition can satisfy the equilibrium and compatibility requirements, and the ratio of e_1 to e_2 in Eq. (128) (or the ratio of P_1 to P_2 in Eq. (129)) can make the displacements and

normal tractions at phase boundaries continuous. Eq. (128) and Eq. (129) seem good solutions to the problem. We are able to confirm in our simulations that the pressure distribution in the composite is indeed piecewise constant, such as shown in Figure 49(c), although the individual stress components are not uniform or piecewise at all (Figure 49(a) and (b)).

So theoretically Eq. (128) (or Eq. (129)) is a sufficient condition for the accurate analytical solution of the effective plane strain bulk modulus in Eq. (126), but may not be a necessary condition. We have found in our simulation (in Figure 49(c)) that it is indeed true and conclude that it must be a necessary condition. But to our knowledge there is no theoretical work yet that rigorously proves the piecewise constant assumption to be a necessary condition.

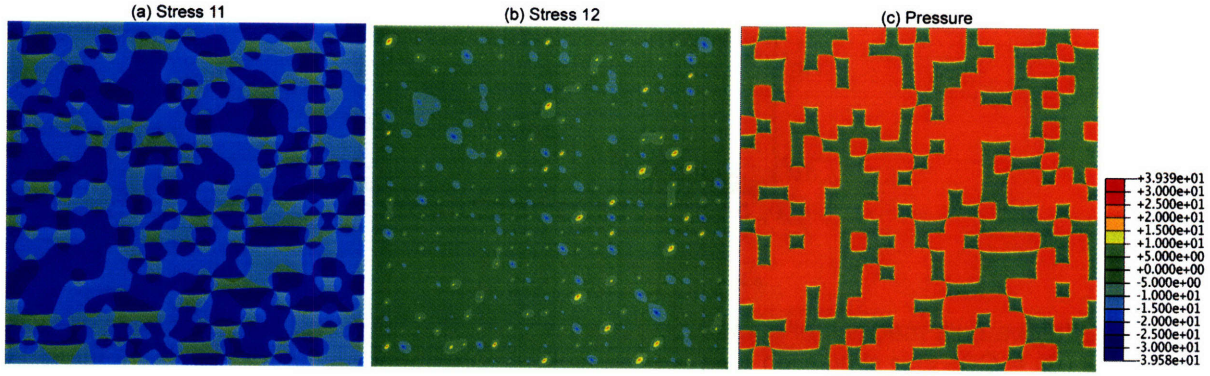

Figure 49. (a) Stress 11, (b) stress 12, and (c) pressure distribution in part of a composite material with two phases having equal shear moduli under the equibiaxial loading condition illustrated in Figure 41(a). The distribution of σ_{22} is not shown because it is very similar to the distribution of σ_{11} in (a) rotated by 90°. Although the stress distributions are not uniform, the pressure is uniform inside each phase, i.e., the pressure or the volumetric strain is piecewise constant for this case. In all of these figures the deformation has been magnified by a factor of 20 in order to show the local shape changes.

Although here the shear moduli of the two phases are the same, the shear stress σ_{12} is not uniform in the material, as shown in Figure 49(b). The variation in shear stress is due to the significant shape change at corners, which can be seen in Figure 49(c). Under an applied equibiaxial strain (Figure 41(a)), the phase with lower bulk modulus (green in Figure 49(c)) tends to shrink more than the other phase, causing severe deformations in corner regions.

3.2.3.2. Effective Bulk Modulus of Composite Materials with Different Phase Shear Moduli

Next we gradually increase the shear modulus of phase 2, G_2, to study the effects of contrasts in phase shear moduli on the effective bulk modulus K_{eff}, keeping all other phase properties such as K_1, K_2 and G_1 constant. The specific values of these parameters used in the simulations have been listed in Table 8.

The simulation results are shown in Figure 50. The simulation data for the case of $G_1 = G_2$ obtained previously are also included for comparison.

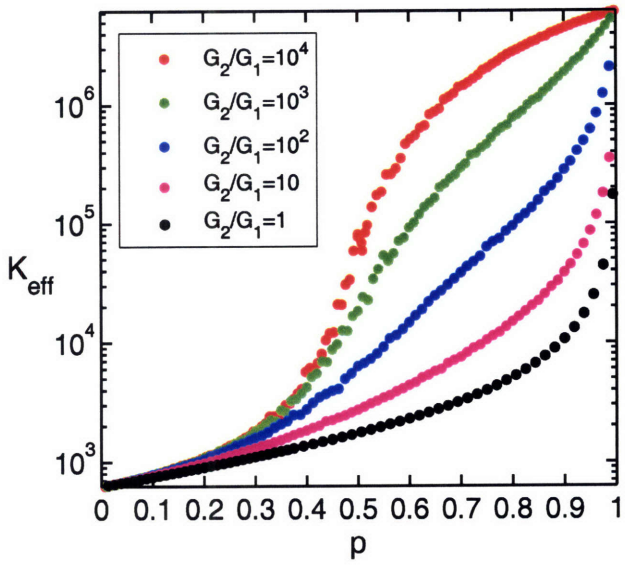

Figure 50. Dependence of the effective bulk modulus K_{eff} on the ratio of the shear modulus, G_2/G_1 (G_1 is fixed for all these curves while G_2 is gradually changed by a factor of 10).

It is known, and also intuitively evident, that K_{eff} will increase when any of K_1, K_2, G_1, or G_2 is increased. Thus we are not surprised at all to observe an increase in K_{eff} as G_2 is increased, especially at high fractions of phase 2 (at high p). What is surprising, though, is a dramatic change in the curve shape as G_2 increases, from having one curvature to having an inflection in curvature. In particular, the red data points for the case of $G_2/G_1 = 10^4$ show a shape clearly indicating a percolation transition. But it is then unclear why the other curves don't exhibit the same shape.

We will conjecture for a moment that Eq. (126) is still accurate even when $G_1 \neq G_2$, provided that G in the equation is replaced by a fictitious effective shear modulus $\tilde{G}_{eff}$.

$$K_{eff} = K_1 + \frac{p}{\frac{1}{K_2 - K_1} + \frac{1-p}{K_1 + \tilde{G}_{eff}}} = K_2 + \frac{1-p}{\frac{1}{K_1 - K_2} + \frac{p}{K_2 + \tilde{G}_{eff}}} \tag{130}$$

from which we can obtain an expression for $\tilde{G}_{eff}$,

$$\tilde{G}_{eff} = \frac{p}{\frac{1-p}{K_{eff} - K_2} - \frac{1}{K_1 - K_2}} - K_2 \tag{131}$$

Using the simulation data shown in Figure 50 as K_{eff} in Eq. (131), we obtain the values for $\tilde{G}_{eff}$ if Eq. (130) indeed works for cases when $G_1 \neq G_2$. The obtained $\tilde{G}_{eff}$ values are plotted in Figure 51. All curve shapes in Figure 51 are consistent and reflect a percolation transition. And, as we have seen repeatedly throughout this thesis and particularly in Figure 45 for the effective shear modulus, the generalized effective medium (GEM) equation is quite useful for describing such shapes:

$$(1-p)\frac{G_1^{1/s}-\tilde{G}_{eff}^{1/s}}{G_1^{1/s}+(p_c^{-1}-1)\tilde{G}_{eff}^{1/s}}+p\frac{G_2^{1/t}-\tilde{G}_{eff}^{1/t}}{G_2^{1/t}+(p_c^{-1}-1)\tilde{G}_{eff}^{1/t}}=0 \qquad (132)$$

The fittings of Eq. (132) to the data points are plotted as lines in Figure 51. The agreement is good in general except when p is close to 1. As already pointed out earlier in the discussion of Figure 45, an obvious deficiency of using the GEM equation for the effective shear modulus is that it does not explicitly include the effects of phase bulk moduli.

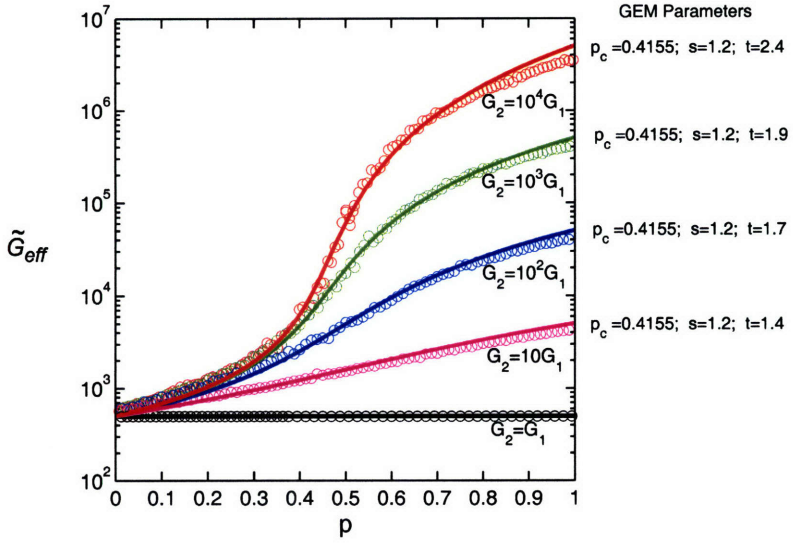

Figure 51. (a) $\tilde{G}_{eff}$ calculated from Eq. (131) using K_{eff} from simulation results in Figure 50. The lines are predictions from the GEM equation Eq. (132).

We propose that the effective bulk modulus K_{eff} can be described by the combination of Eq. (130) and (132). For example, if we use the fitted percolation parameters from Figure 51, Eq. (130) and (132) together yield predictions of the effective bulk modulus that are in good agreement with the simulation results, as shown in Figure 52. The good agreement is quite encouraging. We find that the original Hill equation (Eq. (126)), which is written for the case where two phases have the same shear modulus, can be applied to composites with phases of different shear moduli as well, with the common shear modulus replaced by a fictitious effective shear modulus. Currently we evaluate this effective shear modulus using the GEM equation, which provides reasonably good, but not perfect, results. An improvement that needs to be pursued is to incorporate the effects of phase bulk moduli, or more conveniently, the effective bulk

modulus K_{eff}, into the GEM equation. This new procedure will not only yield better predictions for G_{eff} than Figure 45, but will also provide more accurate estimations for K_{eff} than Figure 52. What is more, including a coupling term of G_{eff} and K_{eff} in the GEM equation may lead to the discovery of a true percolation threshold and scaling exponents that are invariant with respect to the phase bulk moduli.

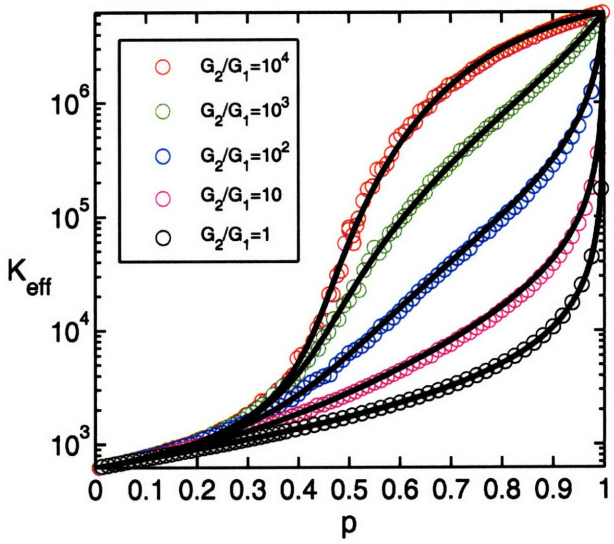

Figure 52. Effective bulk modulus K_{eff} of composite materials with the two phases having different shear moduli (G_2/G_1 values are shown in the legend), compared with the predictions of the combination of Eq. (130) and (132) which are plotted as solid lines.

3.3. Summary

Topology in continuum solids is fundamentally different from that of discrete lattices, e.g., the grain boundary networks studied in the previous chapter, in that there are multiple connectivity paths, such as contacts at edges and corners. This different topology results in new percolation thresholds and critical scaling exponents for diffusion in continuum composites. For several different particle geometries simulated, the new percolation thresholds are all the same as the critical fractions at which a percolating cluster with particles connected at both edges and corners emerges in the composite microstructure. However, we found that the formation of another percolating cluster composed of particles solely connected at edges at a higher fraction does not lead to another critical percolation transition, i.e, a second percolation threshold, as previously conjectured/believed in the literature. The appearance of this second percolating cluster, which is obviously a faster diffusion path, only causes a change in the critical scaling exponents at high phase fractions. Evaluating the effective diffusivities of continuum composites thus becomes difficult; the GEM equation has to be modified somehow in order to include the change in the scaling exponent above the percolation threshold.

In addition to this complexity induced by the corner contacts, the second problem we studied in this chapter—the effective shear modulus G_{eff} and bulk modulus K_{eff}—is even more complicated because each phase is characterized by two independent elastic constants. Our simulations provide the very first sets of data for a percolation problem of this kind. Although the bulk modulus and shear modulus can be considered independent materials parameters, G_{eff} depends on the phase bulk moduli, and similarly, K_{eff} of composite solids is affected by the shear moduli of the two phases as well. We find that, on a coarse level, the GEM equation can describe G_{eff} reasonably well, with the effects of phase bulk moduli captured by the percolation threshold and scalinge exponents. And with G_{eff} well described, we can predict K_{eff} of any composite using the Hill equation originally derived for composites with equal shear moduli, by replacing the common shear modulus with G_{eff}.

However, this procedure is not perfect yet. The problem lies in the lack of K_{eff} in the GEM equation. K_{eff} and G_{eff} should be coupled in the equation because the current GEM equation alone cannot fit the simulation data perfectly at all phase fractions. This forms the topic of further work underway right now.

Chapter 4. Effects of Spatial Correlations on Percolation and Homogenization

In both the heterogeneous grain boundary networks studied in Chapter 2 and the composite solids studied in chapter 3, grain boundaries or phases have been randomly distributed. The probability of each element to be a specific type is the same everywhere and is independent of location. The random distribution (sometimes referred to as Bernoulli percolation) is, however, often too ideal for many natural and engineering materials. The occupation probability is often not independent but rather correlated due to time or space constraints. Some works have focused on the geometric properties of correlated systems (e.g., Ref. [172]), but the effects of these constraints on materials' critical behaviors remain largely unknown. In this chapter, we will introduce spatial correlations into grain boundary networks by requiring the grain boundary character distribution to be crystallographically consistent, and introduce spatial correlations into composite solids by promoting the tendency to form a periodic distribution, which imposes strong constraints among phase distributions. In order to focus on the effects of microstructure distribution, we restrict ourselves to a relatively simple materials property—the effective diffusivity which has been extensively studied for both the random grain boundary networks in section 2.1 and for random composite solids in section 3.1. It is hoped that, by comparing the effective diffusivities of correlated and random systems, the effects of microstructural correlations will be revealed and quantitatively described.

4.1. Crystallographically-correlated Grain Boundary Networks

4.1.1. Correlations in Grain Boundary Character Distribution Due to Consistency in Crystallography

While the study of randomly-assembled networks in Chapter 2 captures the essential features of the diffusion properties of grain boundary netwoks, recent literature on grain boundary networks has emphasized that grain boundaries in true polycrystals are actually not distributed in a random manner [29, 107, 173-178]. The crystallography of polycrystals imposes a correlation between the character of adjacent grain boundaries, particular those meeting at triple junctions or quadruple nodes. The fundamental correlation in grain boundary character distribution is illustrated in Figure 53. Three neighboring grains are characterized by an orientation matrix O_1, O_2, and O_3, respectively. The misorientation matrixes of the grain boundaries between each two of them are thus $M_A = O_1 O_3^{-1}$, $M_B = O_2 O_1^{-1}$, and $M_C = O_3 O_2^{-1}$. If we consecutively apply a rotation M_A, M_B, and then M_C to Grain 3, we have to come back to the same orientation O_3 of Grain 3 because the total rotation is 2π. This consistency requires that

$$M_c M_B M_A = \left(O_3 O_2^{-1}\right)\left(O_2 O_1^{-1}\right)\left(O_1 O_3^{-1}\right) = I \tag{133}$$

where I is the identity matrix. Therefore the misorientation of grain boundaries meeting at a triple junction is fundamentally correlated according to Eq. (133). This local correlation can be captured by deriving grain boundary misorientations from known grain orientations instead of treating each grain boundary independently.

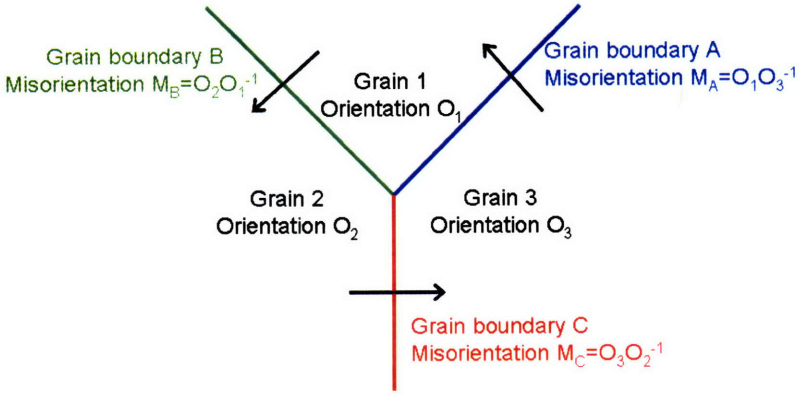

Figure 53. Illustration of the crystallographic correlations in a two dimensional section.

We construct a simple "fiber-textured" family of microstructures [179], where grain boundary characters are assigned in a crystallographically consistent manner. The starting microstructure comprises grains of the same common orientation. Each grain is rotated about a shared axis by an angle θ which is randomly chosen between 0 and $\pi/3$. The misorientation between grains is then compared to a prescribed threshold angle ϕ. Grain boundaries with misorientation angles lower than ϕ are treated as special boundaries with a low diffusivity D_1, and others are considered general boundaries with a higher diffusivity D_2. By varying ϕ, we generate crystallographically-correlated networks of desired special boundary fractions. Although in this case, classification of grain boundaries only involves the misorientation angle and thereby does not necessarily reflect the true structure-property relationship for every specific boundary, comparison of the properties between correlated and random networks can effectively reveal the effects of crystallographic constraints which must appear in any microstructure.

Figure 54 compares the topology of a crystallographically-correlated grain boundary network (c & d) with a randomly-distributed network (a & b) at the same fraction. For clarity, general boundaries and special boundaries are plotted in separate figures. Comparing (c) to (a), we can see that general boundaries in a correlated network are better connected to each other and tend to form long stretched clusters. Comparing (d) and (b), it is also obvious that special boundaries in a correlated network are more correlated at triple junctions. This can be understood from the simple geometry shown in Figure 53. For example, if grain boundary A is special, then the rotation angle θ of grain 1 and 3 must be similar. Let's assume that θ_1 and θ_3 are similarly low (we will reach the same conclusion if we assume they are both

large angles). Then grain boundaries B and C will tend to be both special when the rotation angle θ_2 of grain 2 is low, and both general when θ_2 is high. Thus in this type of correlated network, a special boundary is very likely to be either completely segregated or connected to two other special boundaries at the triple junction. This in turn explains the long stretched configuration of general boundaries. A special boundary being segregated is equivalent to two general boundaries meeting at a triple junction. In summary, the crystallographic correlations we have introduced into the grain boundary network promote two types of triple junctions, those formed by three special boundaries and those formed by one special and two general boundaries.

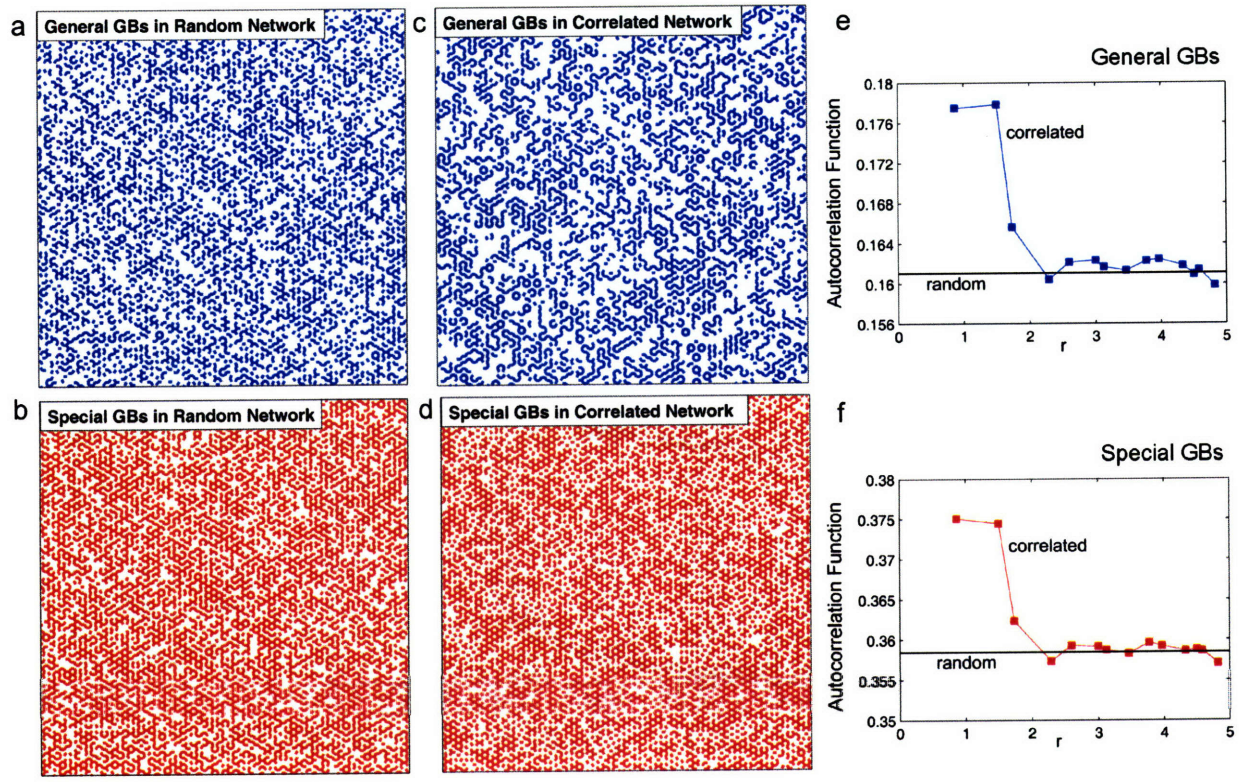

Figure 54. Comparison between configurations of randomly-distributed (a & b) and crystallographically-correlated (c & d) grain boundary networks at $p \approx 0.5987$ (fraction of special boundaries $1 - p \approx 0.4013$). General and special boundaries have been plotted separately in order to show the difference clearly. The short-range correlation imposed by the crystallographic consistency can also been seen in e & f where the autocorrelation functions for general and special boundaries are plotted, respectively.

Although general and special boundaries are correlated in different ways in the correlated network, their correlation lengths are similar, as revealed by the autocorrelation function in Figure 54(e) and (f). The probability of finding a boundary of the same type is higher than average (the case for random networks) for both types of grain boundaries. The correlation is confined to the first few nearest neighbors and is thus short-ranged.

4.1.2. Effects of Crystallographic Correlation on Grain Boundary Diffusion

Figure 55 compares the normalized effective diffusivity of the correlated networks (solids symbols) with that of the random networks (hollow symbols). At intermediate general boundary fractions (p~0.35-0.7) the correlated networks have higher effective diffusivities than random networks. This behavior reflects a difference in percolation thresholds: in the correlated network percolation initiates at $p_c^{crys} \approx 0.6$ while in the random network $p_c^{rand} \approx 0.6527$. The better linear connectivity among general boundaries in the correlated network (see Figure 54(c)) allows for easier diffusional flow through the network. Thus the percolation threshold for diffusion is reduced from ~0.65 to ~0.6, a result consistent with one previous investigation [107] on geometric percolation of the same type of correlated networks, where p_c was reported to shift by 0.052±0.005 due to crystallographic consistency.

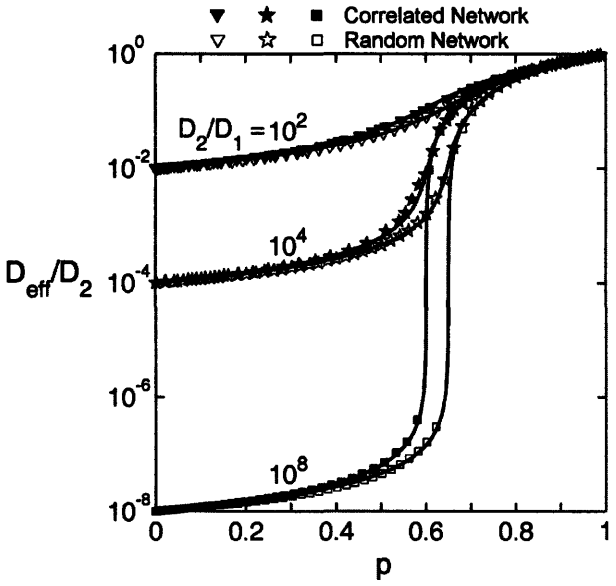

Figure 55. Effective diffusivities for crystallographically-correlated grain boundary networks (filled symbols) compared with those for randomly-distributed networks (open symbols). p is the fraction of general boundaries whose diffusivity is D_2. The solid lines are the predictions of the GEM equation (Eq. (36)) using the specific percolation threshold, $p_c \approx 0.6$ for correlated networks and 0.6527 for random networks. However, the critical exponents used in the GEM equation are the same for both correlated and random networks: $s = 1.05$ and $t = 1.15$.

Taking into account the threshold shift in correlated networks, we can compare the simulation data with predictions of the GEM equation (Eq. (36)). The predictions of Eq. (36) are shown as solid lines in Figure 55, using $p_c = 0.6527$, $s = 1.05$, and $t = 1.15$ for random networks, and $p_c = 0.6$ with the same critical exponents for correlated networks. It is obvious that the GEM equation, without any change in the scaling exponents, is able to predict the effective diffusivity of correlated networks. The only effect of the correlations is to cause a shift in the percolation threshold. This result is consistent with our previous

conclusion in section 4.1.1 or Figure 54(e) and (f) that the crystallographic correlations we have introduced into the network are short-ranged. In percolation theory, a short-range correlation does not change the percolation universality class, *i.e.*, the values of the critical scaling exponents.

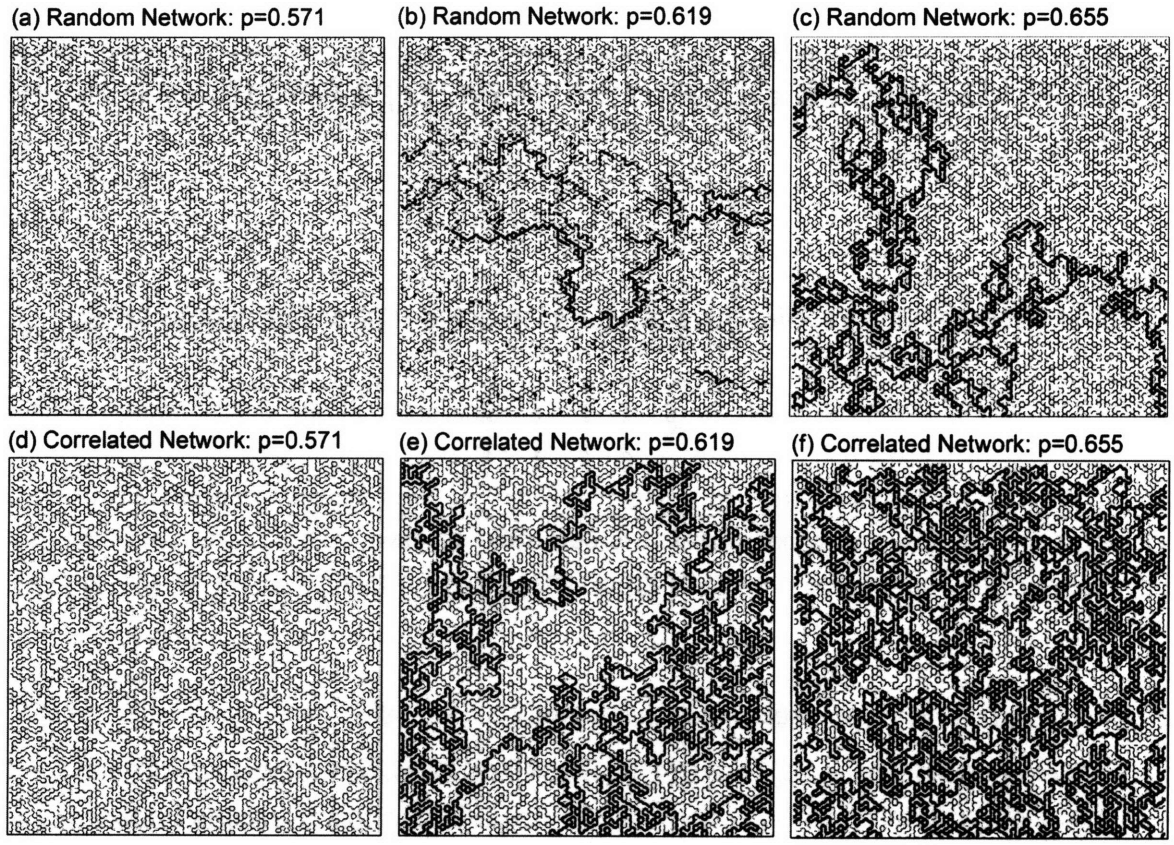

Figure 56. Examples of the difference between the diffusion flux distribution in randomly-distributed (a-c) and crystallographically-correlated (d-f) networks at three different fractions of general boundaries: p = 0.571 in (a & d); 0.619 in (b & e); 0.655 in (c & f). For clarity, only the general boundaries are plotted because they are the fast-diffusing ones and therefore are effective diffusion paths in the networks. The line widths are log-proportional to the magnitude of diffusional fluxes in the boundaries, *i.e.*, thicker lines indicate higher fluxes.

The effects of crystallographic correlation on diffusion behavior are illustrated graphically in Figure 56, where we compare the diffusional flux of random and correlated networks at three different general boundary fractions ($p \approx 0.571$, 0.618 and 0.655) for special/general grain networks with a high diffusivity contrast ($D_2/D_1 = 10^8$). Here only the general boundaries are shown, with each boundary's width log-proportional to the magnitude of the flux along it. At $p \approx 0.571$ ($p < p_c^{crys} < p_c^{rand}$), as shown in Figure 56(a) for random and (d) for correlated networks, the mass flow is low in both networks. However, the better connectivity among general boundaries in the correlated network results in a higher effective diffusivity, $D_{eff}^{crys} = 5.58 \times 10^{-7} D_2$, compared to that of the random network, $D_{eff}^{rand} = 8.64 \times 10^{-8} D_2$. At $p \approx$

0.618 ($p_c^{crys} < p < p_c^{rand}$), as shown in Figure 56(b) and (e), the fast-diffusing general boundaries in the correlated network already form a spanning cluster with a well-defined backbone, while only a few general boundaries in the random network have a high diffusional flux in them, and these are poorly connected. This difference in connectivity results in a significant difference in their effective diffusivities: $D_{eff}^{crys} = 2.36 \times 10^{-2} D_2$ and $D_{eff}^{rand} = 3.79 \times 10^{-7} D_2$. At $p \approx 0.655$ ($p_c^{crys} < p_c^{rand} < p$), as shown in Figure 56(c) and (f), both networks contain a spanning cluster of general boundaries, but the one in the correlated network is much larger, leading to a higher effective diffusivity ($D_{eff}^{crys} = 6.03 \times 10^{-2} D_2$) than the random network ($D_{eff}^{rand} = 1.01 \times 10^{-2} D_2$).

4.1.3. Effects of Crystallographic Correlation on Grain Boundary Diffusional Creep

Following the results above for diffusion, we proceed to consider the role of crystallographic correlations on grain boundary diffusional (Coble) creep. Percolation of Coble creep on honeycomb grain boundary networks with randomly assigned grain boundary character has been studied in section 2.2. Using the same simulation procedures described therein, we obtain the effective creep viscosity for networks with grain boundary character assigned in a crystallographically consistent manner which has been elaborated in section 4.1.1.

As shown in Figure 57(a), the creep viscosity η exhibits a percolation transition at $p_{cc}^{crys} \approx 0.555$ for crystallographic networks, and at $p_{cc}^{rand} \approx 0.524$ for random networks, at the same network size $L \approx 104$. The percolation threshold for Coble creep has shifted by an amount of ~0.031 towards a higher fraction of special boundaries, due to correlations induced by the crystallographic constraints. More special boundaries are required to achieve the same creep resistance as the random network, particularly for p between 0.4 and 0.7.

Prior studies [179] of geometric connectivity on essentially the same correlated grain boundary networks as ours have found that the geometric percolation threshold for special boundaries is ~0.6888, which is about 0.036 higher than the percolation threshold for random network, ~0.6527. Although, according to Figure 54(f), special boundaries in the correlated network are more locally correlated than in the random network, the local correlations are mainly due to triple junctions composed of three special boundaries; this kind of clustering does not promote the formation of a percolating cluster, causing the geometric percolation threshold to increase. The shift in the creep percolation threshold, +0.031, is very close to the shift in the geometric percolation threshold for special boundaries, +0.036, but is not exactly the same. The reasons are that there might a finite size effect and more likely that Coble creep is not entirely controlled by the connectivity on the original honeycomb lattice, but rather also depends on the force network and thus connectivity on the dual triangular network. In other words, the effects of crystallographic correlations are modified by the physical correlations of creep.

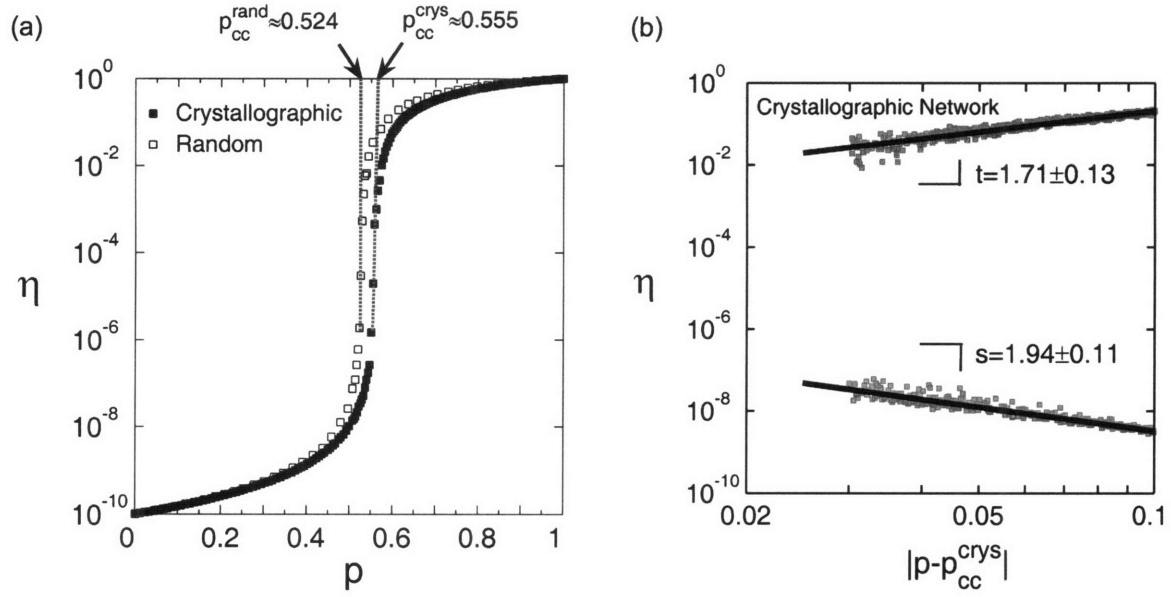

Figure 57. (a) The normalized effective creep viscosity η as a function of the special boundary fraction p. η exhibits a percolation transition at $p_{cc}^{crys} \approx 0.555$ for the crystallographic network and at $p_{cc}^{rand} \approx 0.524$ for the random network. (b) η is fitted to the power-law scaling above and below p_{cc}^{crys}.

In Figure 57(b), the creep viscosity η is fitted to the scaling laws of Eqs. (84) and (85) below and above the percolation transition point p_{cc}^{crys} within the range $\left|p - p_{cc}^{crys}\right| \leq 0.1$. The scaling exponents are s = 1.94±0.11 and t = 1.71±0.13, which are consistent with the critical exponents for random networks, 1.88±0.12 below and 1.69±0.09 above the percolation threshold (see Figure 22(b) and (c)). These scaling exponents are specific to a certain class of percolation problems, and it has been observed for geometric and diffusion percolation that crystallographic constraints do not alter the percolation universality class [29, 139]. The results in Figure 57(b) conform to this notion, but extend it to the percolation of Coble creep.

4.2. Composite Solids with Nonrandom Phase Distributions

In Chapter 3 we studied composites with cells randomly populated by two phases. This represents only one, extreme condition on the possible phase distribution—the random limit. The opposite limit, which is characterized by complete order, occurs when one phase is always entirely surrounded by the other, such as composites containing a periodic array of small inclusions. In this chapter we will study microstructures with correlated phase distributions between these two limits. This will enable us to systematically study the effects of correlations among phase distributions on macroscopic effective properties. Another goal for this section is to identify the critical length scale (or a range of length scales)

at which the percolation scaling behaviors change from being universal to nonuniversal. As mentioned in section 1.3.2 and 1.4.2, short-ranged correlations do not alter the scaling exponents while long-range correlations may. By studying a series of microstructures with increasing spatial correlations, we will be able to correlate the change in scaling exponents, if there are any, with an increase in microstructural correlations.

4.2.1. Microstructure Design and Simulation Procedures

All the microstructures in this section are generated based on hexagonal cells. An advantage of working with hexagonal cells is that we do not have to worry about the additional complexities associated with corner contacts, as discussed at length in section 3.1.

We will define an order parameter, h, that indicates the correlation state of the phases in the microstructure. In an ideally periodic microstructure, such as the one shown in Figure 58 (h = 0), each cell contains a small hexagonal inclusion of phase 2 (in green) embedded in a matrix of phase 1 (in pink). Consider a microstructure where each cell is assigned a phase randomly, such as the one shown in Figure 58 (h = 1), has the same phase fractions p as the periodic microstructure. There are N_1 cells occupied by phase 1 and N_2 cells occupied by phase 2 in this randomly distributed microstructure. Thus the fraction of phase 2 in both the periodic and random microstructures is $p = N_2/(N_1+N_2)$.

Now, returning to the periodic microstructure, we remove N_1h small inclusions randomly chosen (these cells thus become cells of phase 1), and deposit the removed amount of volume onto other small inclusions so that all the cells formerly containing these small inclusions are now filled with phase 2. These small inclusions to be coated are also randomly chosen, and there should be

$$\frac{(N_1h)A_{\text{small inclusion}}}{A_{\text{cell}} - A_{\text{small inclusion}}} = \frac{(N_1h)p}{1-p} = (N_1 + N_2)ph = N_2h \tag{134}$$

such small inclusions in order to conserve the volume removed previously. We are then left with a microstructure containing three types of cells. There are N_1h cells completely filled with phase 1, N_2h cells filled with phase 2, and $(N_1+N_2)(1-h)$ cells containing a small inclusion of phase 2 embedded in phase 1. The fraction of phase 2 in the new microstructure is still p. Although this method of generating the microstructure has not explicitly assumed correlations in the phase occupation probability, it actually generates correlated microstructures in an alternative, efficient way—by promoting order or the periodic element in the microstructure.

It is obvious that h = 0 corresponds to the periodic microstructure while h = 1 corresponds to the random distribution. By varying h between 0 and 1, we are able to generate a series of microstructures containing features of both the asymmetric (inclusion-matrix type) distribution and the symmetric (random) distribution of phases, at the same phase fraction. Examples of the microstructures with h = 0, 0.2, 0.4, 0.6, 0.8, and 1 at a phase 2 fraction p = 0.4 are shown in Figure 58. As h increases, the big cells filled

with phase 2 become better connected to each other, so we expect a percolation transition for microstructures with high h, while those with low h can never percolate simply because the small inclusions do not contribute to connectivity.

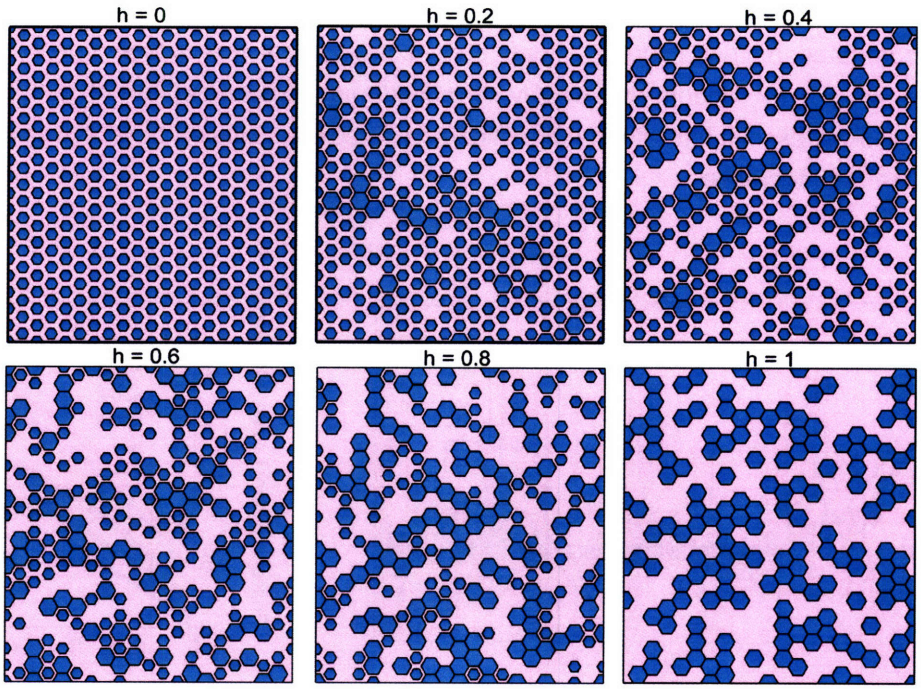

Figure 58. Illustration of a quarter of the correlated microstructures in our simulations. $h = 0$ corresponds to a perfectly periodic microstructure while $h = 1$ corresponds to a random distribution. All these microstructures have the same phase fraction, $p = 0.4$ (the green phase).

The overall correlations in the phase distribution may be described by the autocorrelation function, the same technique used to characterize correlated grain boundary networks in Figure 51. But it is more difficult to calculate this two-point correlation function for a continuum microstructure since ideally the ensemble average needs to be obtained from infinite pairs of points in the microstructure. We have simplified this process by partitioning the microstructure into cells much smaller than the characteristic particle sizes, with the positions of these cells represented by their center point coordinates. Although some microstructure information is lost when the continuum microstructure is discretized in this way, the most critical information such as connectivity among particles is retained. Because the mesh size used in this calculation should be uniform everywhere, the mesh size we use to partition the microstructure depends on the specific phase fraction. An example of the autocorrelation function calculated from the discretized structures at a phase fraction $p = 4/9 \approx 0.444$ is shown in Figure 59(a). The curves would be smoother if even finer meshes were used. But we can already see in Figure 59(a) that microstructures with $h < 0.6$ exhibit strong correlations while those with $h > 0.6$ seem more random.

An alternate and simpler way to characterize microstructural correlations is to examine the specific surface S, which is the total length of phase boundaries per unit area in the present two dimensional microstructures. S is high in the periodic microstructure (h = 0) because there are many small inclusions separated from each other. On the contrary, S is expected to be low in the randomly distributed microstructure (h = 1) because two unit lengths of phase boundary are eliminated whenever two cells of the same phase are connected to each other. S as a function of the phase fraction p is plotted in Figure 59(b) for a few correlated microstructures. S for strongly-correlated microstructures (low h) monotonically increases with p, while S for random and weakly-correlated microstructures (high h) generally exhibits a peak. The peak is likely associated with the formation of a percolating cluster, beyond which adding more particles will cause S to decrease.

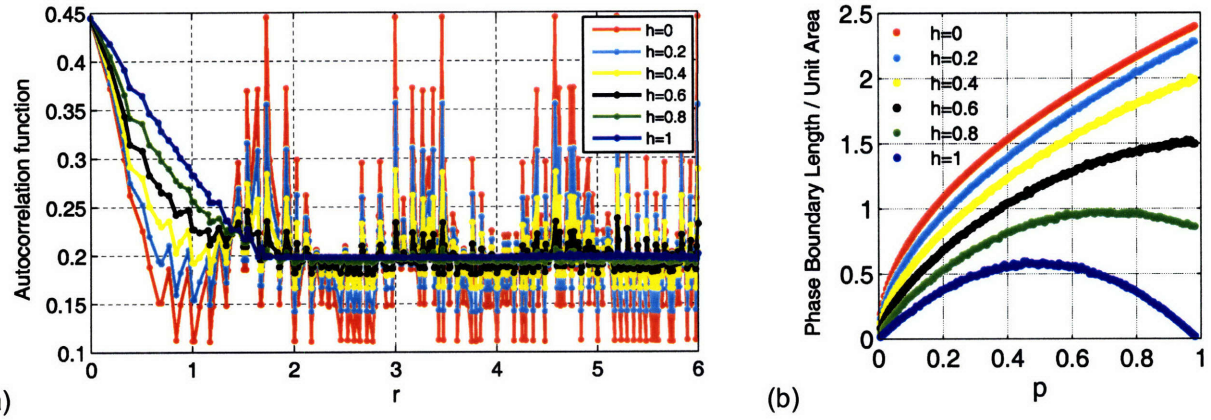

Figure 59. Correlation analysis of the microstructures. (a) Autocorrelation function for phase 2 in correlated microstructures at a phase fraction $p = 4/9 \approx 0.444$. (b) Specific surface (total length of phase boundaries per unit area) of the correlated microstructures at essentially all phase fractions.

Phase 2 (the green phase in Figure 58) is assigned a diffusivity D_2 that is much higher than the diffusivity D_1 of phase 1. The simulation procedures are the same as those used to calculate the effective diffusivities of randomly distributed microstructures described in Chapter 3.1.1. As it takes more time to generate and properly refine a mesh for such large scale disordered microstructures, the current system size (1620 cells) is smaller than the system (4367 cells) used in Chapter 3.1. This way we can simulate the correlated microstructures thousands of times for each h in order to obtain good percolation statistics.

4.2.2. Effects of Correlations on Percolation Threshold

The effective diffusivities D_{eff} for a series of microstructures with different levels of correlations are plotted in Figure 60. The discontinuity seen in D_{eff} in each set of data signifies a percolation transition. We have already shown in Chapter 3.1.2 that the percolation threshold for diffusion on the honeycomb cell

structure with random phase distributions (h = 1) is $p_c \approx 0.496$ (Figure 36 and Figure 37), and at high h values, we observe that the data in Figure 60 are approaching this value. Now as the correlation parameter h decreases from one towards zero, the percolation transition shifts progressively towards higher p. The percolation threshold is approaching unity for h = 0.5, and should in fact converge to exactly one for the ideal periodic microstructure at h = 0. This is consistent with our prior observations that microstructures with low h can rarely percolate because of the poor connectivity among phase 2, and also agrees with Figure 59 which shows that microstructures with low h are more correlated (closer to the periodic microstructures where phase 2 particles are all segregated).

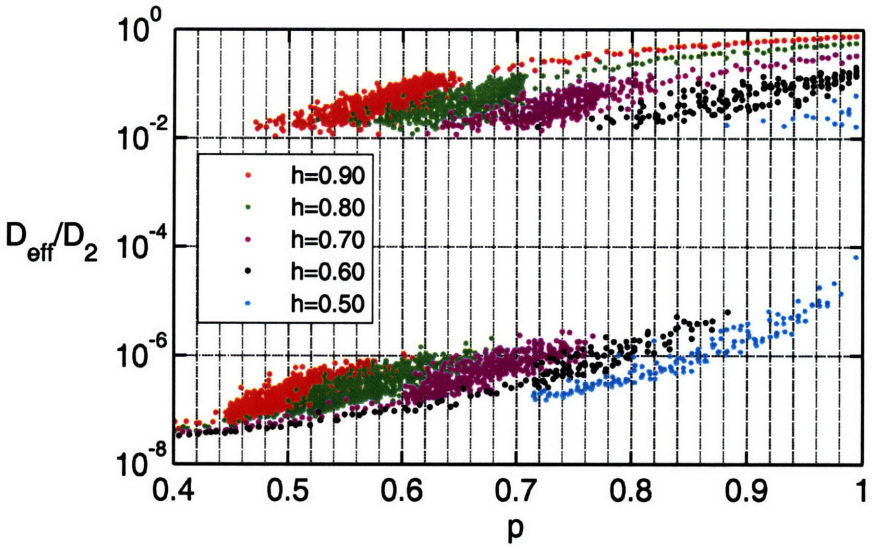

Figure 60. The effective diffusivity D_{eff}, normalized by the diffusivity of Phase 2, D_2, as a function of the fraction of Phase 2, p, for a series of microstructures with different degrees of spatial correlations characterized by the parameter h (h = 1: random distribution; h = 0: periodic distributions).

The data are somewhat scattered in Figure 60 because of finite size effects, making it difficult to directly obtain a percolation threshold. Accordingly, we convert the effective diffusivity plot to the percolation probability Π in Figure 61, as done previously in section 3.1.2. Π is calculated as a moving average of the Heaviside step function converted from the effective diffusivity. Finally we fit $\Pi(p)$ with Eq. (104) to extract the average percolation threshold p_c for microstructures with a fixed h. The fitted p_c values are written in the legend in Figure 61. We already know that for h =1 (random distribution), $p_c \approx 0.496$. As h decreases, p_c increases. However, p_c is not a linear function of h.

$p_c(h)$ can in fact be rationalized from the types of cells in the microstructures. At an infinite system size, randomly assigning each cell with a phase will result in a percolation threshold at $p_c(h = 1) = 0.5$. Half of the cells have to be phase 2, the phase with higher diffusivity, in order to make the system percolate. For correlated microstructures, there are $N_2 h$ cells filled with phase 2. Only the connectivity of these cells

contributes to the percolation transition, as the smaller inclusions of phase 2 are segregated from each other. So the system does not percolate until

$$\frac{N_2 h}{N_1 + N_2} = p_c(h = 1) \tag{135}$$

$$p_c(h) = \frac{p_c(h = 1)}{h} = \frac{0.5}{h} \tag{136}$$

As shown in Figure 62(a), the predictions of $p_c(h)$ from Eq. (136) are in good agreement with the values obtained from our simulations listed in Figure 61. When h = 0.95, 0.9, 0.85, 0.8, 0.7, 0.6, $p_c(h)$ should be $0.5/h$ = 0.526, 0.555, 0.588, 0.625, 0.714, 0.833, respectively. Our simulation results are slightly different from these predictions because, again, the systems simulated are finite.

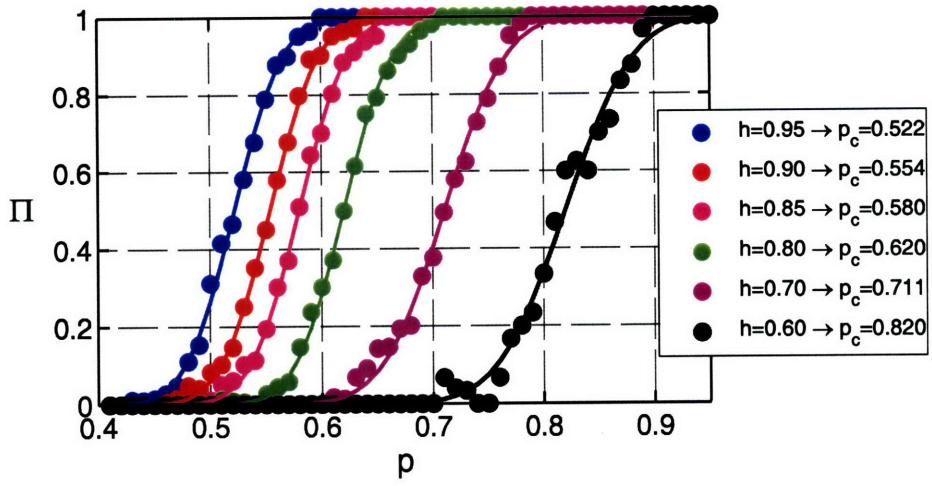

Figure 61. Percolation probability π as a function of phase fraction p. The data generated from simulation results are plotted in dots. The lines are the fit to Eq. (104) which relates π to the percolation threshold p_c through error functions. The fitted p_c values are included in the legend.

4.2.3. Effects of Correlations on Percolation Scaling

The percolation thresholds we obtain for this series of increasingly correlated microstructures once more confirm our previous claim that connectivity among microstructural elements is the key to understanding and predicting effective properties of disordered materials. Another critical element of the problem is the percolation scaling. Using the effective diffusivities of a series of correlated microstructures ranging from being close to random distribution to being close to periodic distribution, we can study the percolation scaling behaviors as a function of the degree of correlations among phase distributions.

We fit the effective diffusivities to the power scaling laws $D_{eff} \propto (p_c - p)^{-s}$ for $p < p_c$ and $D_{eff} \propto (p - p_c)^t$ for $p > p_c$ to extract the percolation scaling exponents s and t. The fitting results are plotted in Figure 62(b) and are also presented in Table 9. When $p < p_c$, only those data points with $D_{eff} < \sqrt{D_1 D_2}$ are used in the fitting, and similarly, only data with $D_{eff} > \sqrt{D_1 D_2}$ are used when $p > p_c$. In general, a few data points in the very proximity of p_c must be neglected in the fitting process because they induce large fluctuations in p-p_c. Because the range of p for $p < p_c$ increases as p_c shifts to higher values (as h decreases), we further fit to the scaling law $D_{eff} \propto (p_c - p)^{-s}$ for p far away from p_c ($p < p_c$ - 0.2) and close to p_c (p_c - 0.12 < p < p_c) in addition to the fit in the whole range. These local exponents are shaded in gray in Table 9. On the other hand, the range of p for $p > p_c$ decreases so it is not that necessary to fit for t locally.

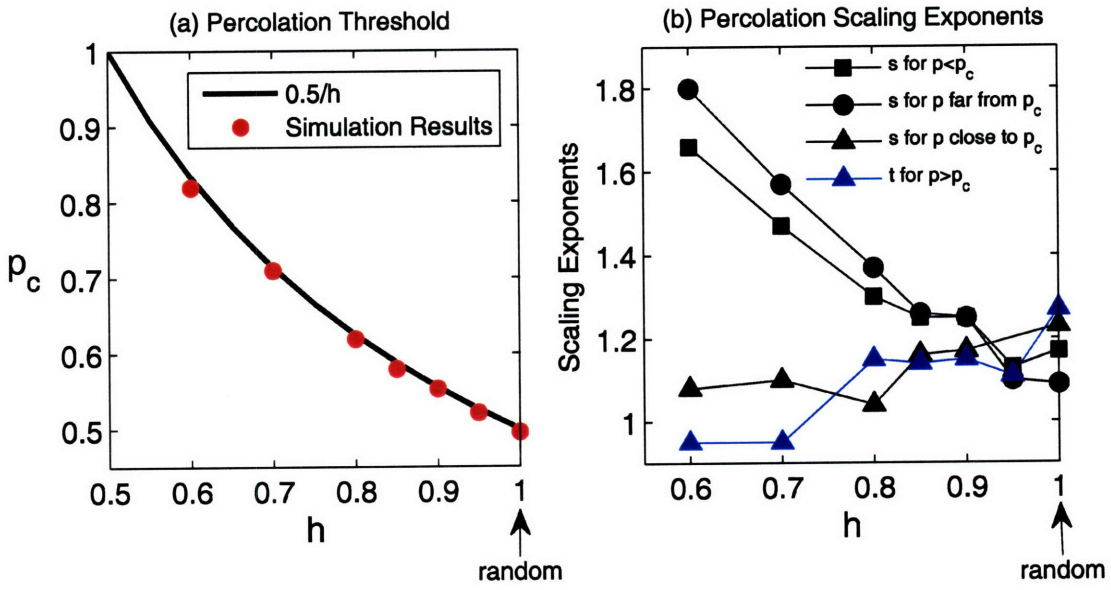

Figure 62. (a) Percolation threshold and (b) scaling exponents for a series of microstructures characterized by a correlation or order parameter h. h = 0 denotes an ideally periodic structure while h = 1 denotes a randomly distributed structure.

Globally s increases from ~1.17 to ~1.66 while t decreases from ~1.27 to ~0.95 when h decreases from 1.0 to 0.6, i.e., when the percolation threshold p_c of the microstructure increases from 0.496 to 0.82. The difference between s and t widens when the microstructures are more correlated; they become asymmetric exponents in strongly-correlated systems.

Interestingly, neither of these exponents changes linearly with p_c. $s \approx 1.15$ for h = 1 and 0.95, 1.25 for h = 0.8-0.9, and then keeps increasing as h further decreases. Meanwhile, $t \approx 1.27$ when h = 1, 1.15 when h = 0.8-0.95, and 0.95 when h = 0.6-0.7. These almost constant exponents for certain h, which is

equivalent to certain levels of correlation, may allow us to differentiate short-range, medium-range, and long-range correlations in phase distributions. It is widely recognized that short-range correlations do not alter the scaling exponents while little is known about the effects of even stronger correlations. Table 9 seems to suggest that there may be another set of exponents, which may still be universal, for medium-range correlations, while scaling exponents for long-range correlations are nonuniversal, i.e., are functions of the correlation length.

Table 9. Percolation threshold and scaling exponents for diffusion in composites with correlated microstructures.

h	p_c	s			t
		$p<p_c$	$p<p_c$-0.2	p_c-0.12<p<p_c	($p>p_c$)
1 (random)*	0.496	1.17	1.09	1.23	1.27
0.95	0.522	1.13	1.10	N/A**	1.11
0.9	0.554	1.25	1.25	1.17	1.15
0.85	0.580	1.25	1.26	1.16	1.14
0.8	0.620	1.30	1.37	1.04	1.15
0.7	0.711	1.47	1.57	1.10	0.95
0.6	0.82	1.66	1.80	1.08	0.95
0 (periodic)	1		About 2 to1 as p increases from 0 to 1		N/A

* The data for h = 1 (random distribution) are taken from Figure 39.

** Not available due to the discreteness of the data set. For convenience we have required both N_1h and N_2h to be integers. When h = 0.95 or 0.85, the minimum increment in N_1 or N_2 is 20 and the resulting increment in p is close to 20/1620=0.0123 (not exact because p reported here denotes area fractions. Since we have half grains at edges, the area fraction can be slightly different from number fraction). Thus in this limited range of p, the data are simply too discrete to get good fittings. We are able to fit the curve for h = 0.85 because we have already run simulations for this case for many more times.

Now we turn our attention to the local scaling exponent s for p far away from the percolation threshold p_c ($p < p_c$ -0.2) and close to p_c (p_c -0.12 < p < p_c) shaded in gray in Table 9. When h decreases from 1.0 to 0.6, s for p far away from p_c is increasing very fast, from ~1.09 to 1.89, while s for p in the vicinity of p_c keeps decreasing from ~1.23 to 1.08. Therefore the increase in s for the whole range of p is caused by the increase of s for p far from p_c (p close to 0).

What is even more interesting is the comparison between s and t in the vicinity of p_c. When the phases are randomly distributed, s and t should be equal to each other in theory ($s = t \approx 1.3$, proved in Chapter 1.3.3). Our simulation results (for h = 1), $s \approx 1.23$ and $t \approx 1.27$, are consistent with such symmetric requirements. As we gradually introduce more correlations into the microstructure, both s and t decrease. When h = 0.6 (strong correlation), $s \approx 1.08$ while $t \approx 0.95$. As shown in Figure 60 and Eq. (136), for $h \leq$ 0.5, the percolation threshold becomes one, which means that t must disappear.

We have also simulated periodic microstructures similar to Figure 58 ($h = 0$), but with square cell shapes. The effective diffusivities show a percolation threshold at one. The scaling exponent s is about 2 when p is close to 0, and is about 1 when p is close to 1 (p_c). The value of $s \approx 2$ for p far from p_c and 1 for p close to p_c are consistent with the trend we observe in the data. As h decreases towards zero, s increases towards 2 for $p << p_c$ and decreases towards 1 when p is close to p_c.

4.3. Summary

Correlations among grain boundary character distribution imposed by crystallographic consistency constraints are short-range correlations. The percolation scaling exponents of both grain boundary diffusion and diffusional creep in correlated systems are the same as their counterparts in systems with random boundary or phase distributions. Thus the properties remain in the same universality class. The grain boundary network in the fiber-textured microstructures used in our simulations is in fact one of the most correlated grain boundary networks generated in a crystallographically consistent manner. The evidence is that the shift in geometric percolation threshold caused by the present crystallographic constraints is ~0.05, which is almost the largest among the percolation shifts of many types of correlated grain boundaries networks studied in the literature [50]. Therefore it is very likely that correlations in the grain boundary character distribution in most materials are short ranged. This has important implications for predicting effective properties associated with the grain boundary networks. Provided the percolation quantities of a property on random grain boundary networks are known, only the percolation threshold needs to be re-assessed for crystallographically correlated networks. The seemingly difficult problem of capturing all effects of microstructure connectivity and predicting effective properties of real correlated interfacial networks reduces to the evaluation of a single percolation parameter.

The amount of shift in the percolation threshold due to spatial correlations in the occupation probability depends on the specific property of interest. The exact effects of correlations are property dependent. The crystallographic correlations in the present grain boundary networks caused the percolation threshold of grain boundary diffusion to shift by ~0.05 and that of diffusional creep to shift by ~0.03. This difference may be attributed to the asymmetry in both the topology and the property of special and general grain boundaries.

Strong, or long-range, correlations may exert different effects on materials' critical behaviors. It is necessary to generate a series of correlated microstructures with different correlation lengths to reveal their effects. A simple and useful method has been developed in this work to generate correlated microstructures with correlations anywhere between the random and the periodic phase distributions. We found that, for diffusion, the percolation threshold is determined by the fraction of particles that can possibly contribute to microstructural connectivity; particles that are always segregated do not play a role in determining the percolation threshold, but they affect the scaling behaviors.

In addition to causing a shift in the percolation threshold, strong correlations also change the critical scaling exponents which have been identified here for the first time for all ranges of correlations. These scaling exponents become functions of the correlation length. This non-universality presents a great challenge for predicting effective properties of strongly correlated heterogeneous materials—the scaling exponents have to be evaluated for each specific case. Alternatively, this problem may possibly be avoided by interpolating between effective properties of random systems and those of periodic systems.

Chapter 5. Homogenization of Periodic Composite Materials

In Chapter 3 we studied the effective diffusivity and elastic properties of composite solids with phases randomly distributed in space. Later in Chapter 4.2 we also introduced correlations into the composite and studied the effective diffusivity as a function of the correlations among phase distributions. The extreme case of a correlated distribution is a periodic distribution, i.e., composite materials with periodically distributed inclusions, which will be the subject of this chapter.

5.1. Need for an Accurate and Simple-to-implement Technique

Periodic composite materials can be completely specified by the phase distributions in one unit cell, which is repeated periodically in space to generate the microstructure. Periodicity not only significantly simplifies the microstructure representation, but even allows for analytical homogenization solutions. These solutions can be used to predict the effective properties of some real microstructures that may be approximated as periodic, e.g., the transverse sections of many fiber-reinforced composites. Additionally, such analytical homogenization procedures can be potentially useful for extrapolating the properties of an infinite system from those of one finite system; assuming a periodic stacking of the representative volume element (RVE) might be a more efficient and accurate method than just working on the RVE itself, particularly when the convergence with respect to the RVE size is slow.

Existing methods for deriving the effective properties of periodic composite materials mostly rely on certain representations in the Fourier space [180-185]. Using the Fourier expansion of the field quantities can automatically satisfy the continuity or equilibrium boundary conditions that are otherwise difficult to fulfill, and can also convert an integral equation into a system of linear equations for the unknown Fourier coefficients. For example, Helsing [183] expanded a displacement descriptor (interface force density) in two dimensions in a Fourier series and solved the resulting set of linear equations for the Fourier coefficients. Bergman and Dunn [180] and Cohen and Bergman [181] used the Fourier expansion for the displacements, but instead of solving for the Fourier coefficients directly, they progressively tightened the upper and lower bounds by including more power expansion coefficients for an intermediate function. Nemat-Nasser *et al.* [184, 185] calculated the overall elastic properties of materials with periodically-distributed inclusions and voids by expanding Eshelby's transformation strain tensor [168] in Fourier series.

In solving for the elastic field of an inclusion embedded in an infinite matrix, Eshelby [168] introduced an imaginary transformation strain in the inclusion region so that the stress-strain relationships in the matrix and in the inclusion could both be described by the elastic constants of the matrix. For periodic composite materials, Nemat-Nasser *et al.* [184, 185] expressed the spatially varying transformation strain as well as other field quantities as Fourier series, derived an integral equation from the consistency and equilibrium

requirements, and further proposed several solution methods. Nemat-Nasser and co-workers' idea is theoretically rigorous and conceptually straightforward. Consequently, the idea has been subsequently used for a variety of specific problems, such as for the elastic properties of solids with periodically distributed cracks [186] and periodic masonry structures [187], elastic stiffness and relaxation moduli of linear viscoelastic periodic composites [188, 189], stress-strain relations of rate-dependent elastic-plastic periodic composites [190], electrical conductivity [191], thermal conductivity [192], effective dielectric, elastic, and piezoelectric constants of periodic piezoelectric composites [193], and the dielectric response of isotropic graded composites [194].

However, the derivation of Refs. [184, 185] contains one considerably simplifying assumption, which has unfortunately propagated through the line of work mentioned above [184-186, 190, 195]. This simplification arises specifically in deriving the relationship between the Fourier coefficients for the transformation strain, $\hat{\varepsilon}^*(\xi)$, and those for the true deformation field, $\hat{u}^*(\xi)$, where ξ is the reciprocal vector. The equilibrium condition in the r_{th} direction (Eq. (2.5) in Ref. [184]) should be strictly obeyed as

$$\sum_{\xi\neq(0,0,0)} C_{rjkl}\xi_j\hat{u}_k^*(\xi)\xi_l e^{i\xi\cdot x} + i\sum_{\xi\neq(0,0,0)} C_{rjkl}\xi_j\hat{\varepsilon}_{kl}^*(\xi)e^{i\xi\cdot x} = 0 \tag{137}$$

where i is the imaginary unit ($i=\sqrt{-1}$) and in each term, the repeated subscripts, j, k, and l, sum over 1, 2, 3; C_{rjkl} is the elastic stiffness tensor. The above condition was however simply interpreted as (see Eq. (2.8) in Ref. [184]):

$$-C_{rjkl}\xi_j\xi_l\hat{u}_k^*(\xi) = iC_{rjkl}\xi_j\hat{\varepsilon}_{kl}^*(\xi) \tag{138}$$

for every ξ. So when an infinite summation over ξ is equal to zero, it was assumed that each individual term in the summation should be equal to zero. Consequently, the two essential features, the infinite summation and particularly the position dependence, in Eq. (137) were essentially discarded, and thus the ultimate solution obtained in this way may not be the true general solution for the field quantities.

In addition, in the original work [184, 185], although several approximations to the spatial distribution of the transformation strain were proposed in order to solve the equations, the one most frequently used is the hypothesis of a constant or piecewise constant transformation strain within the inclusion(s) in the unit cell. This assumption neglects the interactions among inclusions in the composite, which make the transformation strain position-dependent, an effect which becomes quite dominant at moderate to high volume fractions. Another solution method recommended by Nemat-Nasser *et al.* [184, 185] is to additionally expand the transformation strain as a polynomial series and solve for the polynomial coefficients. This method is viable, but is not as efficient as it involves a power series in addition to the initial Fourier series. The "complete solution method" [184, 185], which does not rely on any assumption on the distribution of the transformation strain and is thus most accurate among all the solution methods, has, however, seldom been used, probably because of the complexity in constructing and solving the system of linear equations with a full coefficient matrix.

Therefore, despite the large volume of work in the literature devoted to the homogenization of periodic composites, there is still a need for some simple, straightforward, and rigorous analytical methods to

evaluate effective properties of periodic composite materials. In the following, we will derive the effective properties of periodic composite materials using Eshelby's concept of the transformation field and the Fourier series representation, but offer a new approach, and avoid oversimplifying assumptions.

5.2. Analytical Derivation

We specifically consider the effective diffusivity, and our solution can be easily adapted to other analogous properties. For clarity, the equations presented below are written for composites with isotropic matrix and inclusion properties so that the diffusivity reduces to a scalar, but the same procedures should apply to anisotropic constituent properties materials as well. The unit cell is a rectangular prism with dimensions L_1, L_2, and L_3 along the Cartesian coordinate axes. The total volume of the unit cell, $V = L_1L_2L_3$, is partitioned into the matrix region V_M and the inclusion region V_I (here the subscript "M" denotes matrix and "I" inclusion). The phase boundaries are assumed to be perfectly bonded.

5.2.1. Expressing Perturbation and Eshelby Transformation Fields in Fourier Series

Consider an infinite, isotropic material with diffusivity D_M placed in a concentration field $C^0(\vec{R})$ that induces a uniform concentration gradient $E^0 = -\nabla C^0(\vec{R})$, where $\vec{R} = (x_1, x_2, x_3)$ is the position vector in three dimensions. Inserting a periodic distribution of isotropic inclusions with diffusivity D_I into the matrix changes the concentration field to $C(\vec{R}) = C^0(\vec{R}) + C^d(\vec{R})$ and the concentration gradient to $E(\vec{R}) = E^0 + E^d(\vec{R})$, where $C^d(\vec{R})$ and $E^d(\vec{R})$ are the perturbations in the concentration field and gradient, respectively, due to the presence of inclusions, and $E^d(\vec{R}) = -\nabla C^d(\vec{R})$. Because the inclusion distribution is periodic, both $C^d(\vec{R})$ and $E^d(\vec{R})$ are periodic functions with periodicity L_α in the α (α=1, 2, 3) direction. In short, the concentration field $C(\vec{R})$ can be split into a linear part $C^0(\vec{R})$ and a periodic part $C^d(\vec{R})$, and accordingly, the concentration gradient $E(\vec{R})$ is composed of a constant vector $E^0 = (E_1^0, E_2^0, E_3^0)$ and a periodic vector $E^d(\vec{R}) = \left(E_1^d(\vec{R}), E_2^d(\vec{R}), E_3^d(\vec{R})\right)$. Since the periodicity of $C^d(\vec{R})$ guarantees the periodicity of $E^d(\vec{R})$ while the converse is not necessarily true (e.g., a constant $E^d(\vec{R})$ would indicate a linear, instead of periodic, $C^d(\vec{R})$), we first write $C^d(\vec{R})$ as a Fourier series,

$$C^d(\vec{R}) = \sum_{\xi} \hat{C}^d(\xi) e^{i\xi\cdot\vec{R}} \tag{139}$$

where the reciprocal vector $\xi = (\xi_1, \xi_2, \xi_3) = (2\pi n_1 / L_1, 2\pi n_2 / L_2, 2\pi n_3 / L_3)$ with n_1, n_2, n_3 = 0,±1,±2,.... Then the perturbation in the concentration gradient in the α direction is the gradient of Eq. (139).

$$E_\alpha^d(\vec{R}) = -i\sum_\xi{}' \xi_\alpha \hat{C}^d(\xi) e^{i\xi\cdot\vec{R}} \tag{140}$$

where the prime on the summation symbol $\sum_\xi{}'$ denotes a summation excluding $\xi = (0,0,0)$, because the constant term $\hat{C}^d(\xi = (0,0,0))$ in Eq. (139) does not contribute to the differentiation with respect to position.

The diffusional flux in the composite in the α direction, $J_\alpha(\vec{R})$, can simply be written as:

$$J_\alpha(\vec{R}) = \begin{cases} D_M\left[E_\alpha^0 + E_\alpha^d(\vec{R})\right] & \text{in } V_M \\ D_I\left[E_\alpha^0 + E_\alpha^d(\vec{R})\right] & \text{in } V_I \end{cases} \tag{141}$$

Now introduce a transformation gradient $E^*(\vec{R})$ so that with the modified concentration gradient $E^0 + E^d(\vec{R}) - E^*(\vec{R})$, the whole composite can be described as the homogeneous matrix material with diffusivity D_M everywhere.

$$J_\alpha(\vec{R}) = D_M\left[E_\alpha^0 + E_\alpha^d(\vec{R}) - E_\alpha^*(\vec{R})\right] \tag{142}$$

Because the original flux must be preserved, Eq. (141) and Eq. (142) should be equivalent. This defines the transformation gradient $E^*(\vec{R})$ as

$$E_\alpha^*(\vec{R}) = \begin{cases} 0 & \text{in } V_M \\ (1 - D_I / D_M)\left[E_\alpha^0 + E_\alpha^d(\vec{R})\right] & \text{in } V_I \end{cases} \tag{143}$$

Because of the geometric periodicity, $E^*(\vec{R})$ is also periodic and can be written as a Fourier series as well.

$$E_\alpha^*(\vec{R}) = \sum_\xi \hat{E}_\alpha^*(\xi) e^{i\xi\cdot\vec{R}} \tag{144}$$

with each Fourier coefficient defined as

$$\hat{E}_\alpha^*(\xi) = \frac{1}{V}\int_V E_\alpha^*(\vec{R}) e^{-i\xi\cdot\vec{R}} d\vec{R} = \frac{1}{V}\int_{V_I} E_\alpha^*(\vec{R}) e^{-i\xi\cdot\vec{R}} d\vec{R} \tag{145}$$

The second equality in Eq. (145) results from the fact that $E^*(\vec{R})$ is always zero for any $\vec{R}$ in V_M according to Eq. (143).

The above definitions of the perturbation concentration gradient $E_\alpha^d(\vec{R})$ (Eq. (140)) and the transformation gradient $E_\alpha^*(\vec{R})$ (Eq. (143) and (144)) are analogous to the definitions in the work of Nemat-Nasser *et al.* [184]. In the following, we shall use a new, more rigorous, method to solve for the Fourier coefficients for these unknown field quantities.

5.2.2. Solution Technique

Replacing $E_\alpha^d(\vec{R})$ in Eq. (143) with the Fourier series in Eq. (140), we have

$$E_\alpha^*(\vec{R}) = (1 - D_I / D_M)\left[E_\alpha^0 - i\sum_{\xi'}{}' \xi'_\alpha \hat{C}^d(\xi') e^{i\xi'\cdot\vec{R}}\right] \qquad \text{in } V_I \tag{146}$$

Here the original symbol ξ in Eq. (140) is changed to ξ', which is the same reciprocal vector as ξ. $\xi' = (2\pi n'_1 / L_1, 2\pi n'_2 / L_2, 2\pi n'_3 / L_3)$ with n'_1, n'_2, n'_3=0,±1,±2,.... Multiplying both sides of Eq. (146) by $e^{-i\xi\cdot\vec{R}}$ and integrating $\vec{R}$ over V_I, we have

$$\int_{V_I} E_\alpha^*(\vec{R}) e^{-i\xi\cdot\vec{R}} d\vec{R} = (1 - D_I / D_M)\left[E_\alpha^0 \int_{V_I} e^{-i\xi\cdot\vec{R}} d\vec{R} - i\sum_{\xi'}{}' \xi'_\alpha \hat{C}^d(\xi') \int_{V_I} e^{-i(\xi-\xi')\cdot\vec{R}} d\vec{R}\right] \tag{147}$$

The left side of Eq. (147) is equal to $V\hat{E}_\alpha^*(\xi)$ according to Eq. (145). As a result,

$$\hat{E}_\alpha^*(\xi) = f_I(1 - D_I / D_M)\left[E_\alpha^0 g_{V_I}(\xi) - i\sum_{\xi'}{}' \xi'_\alpha g_{V_I}(\xi - \xi')\hat{C}^d(\xi')\right] \tag{148}$$

where the geometric factor $g_{V_I}(\xi)$ is

$$g_{V_I}(\xi) = \frac{1}{V_I}\int_{V_I} e^{-i\xi\cdot\vec{R}} d\vec{R} \tag{149}$$

Eq. (148) provides each Fourier coefficient for the transformation gradient, $\hat{E}_\alpha^*(\xi)$, as a function of the Fourier coefficients for the perturbation concentration field, $\hat{C}^d(\xi)$. So, in our method, each $\hat{E}_\alpha^*(\xi)$ value is an infinite summation over ξ' for terms containing $\hat{C}^d(\xi')$, in contrast to the spirit of Eq. (138) which would improperly suggest that each $\hat{E}_\alpha^*(\xi)$ can be fully determined by the corresponding $\hat{C}^d(\xi)$ with the same reciprocal vector ξ.

The steady-state condition requires that $\nabla \cdot J(\vec{R}) = 0$. Using the expression for $J(\vec{R})$ in Eq. (142), we obtain

$$\nabla \cdot \left[E^d(\vec{R}) - E^*(\vec{R})\right] = 0 \tag{150}$$

Substitute $E_\alpha^d(\vec{R})$ and $E_\alpha^*(\vec{R})$ in Eq. (150) with the series expression in Eq. (140) and Eq.(144), respectively:

$$\sum_{\xi}{}' \left[(\xi\cdot\xi)i\hat{C}^d(\xi) + \xi\cdot\hat{E}^*(\xi)\right] e^{i\xi\cdot\vec{R}} = 0 \tag{151}$$

where $\hat{E}^*(\xi) = \left(\hat{E}_1^*(\xi), \hat{E}_2^*(\xi), \hat{E}_3^*(\xi)\right)$. Multiply both sides of Eq. (151) by $e^{-i\eta\cdot\vec{R}}$ and integrate $\vec{R}$ over an arbitrary volume Ω.

$$\sum_{\xi}{}' \left[(\xi\cdot\xi)i\hat{C}^d(\xi) + \xi\cdot\hat{E}^*(\xi)\right] g_\Omega(\eta - \xi) = 0 \tag{152}$$

where the geometric integration function g has already been defined in Eq. (149). This procedure introduces into the equation a virtual vector parameter $\eta = (2\pi m_1 / L_1, 2\pi m_2 / L_2, 2\pi m_3 / L_3)$, where m_1, m_2, and m_3 can be any integer) and a virtual integration volume Ω. As Eq. (151) holds for any $\vec{R}$ in the unit cell, the integration can be performed over any finite volume Ω inside the unit cell in order to convert Eq. (151) to a position-independent equation. But Ω cannot be the whole unit cell volume V because the integration of $e^{i\xi\cdot\vec{R}}$ over V is zero. We choose Ω in the range $V_I \le \Omega < V$.

Replacing $\hat{E}^*(\xi) = \left(\hat{E}_1^*(\xi), \hat{E}_2^*(\xi), \hat{E}_3^*(\xi)\right)$ in Eq. (152) with Eq. (148) results in a linear equation whose only unknowns are the $\hat{C}^d(\xi)$ values, the coefficients for the Fourier expansion of the perturbation concentration field $C^d(\vec{R})$ in Eq. (139).

$$\sum_{\xi}{}' \left[\frac{1}{f_I(1-D_I/D_M)} (\xi\cdot\xi)\hat{C}^d(\xi) - \sum_{\xi'}{}' (\xi\cdot\xi') g_{V_I}(\xi-\xi')\hat{C}^d(\xi') \right] g_\Omega(\eta-\xi) = i\sum_{\xi}{}' (\xi\cdot E^0) g_{V_I}(\xi) g_\Omega(\eta-\xi) \qquad (153)$$

In the second term on the left side of Eq. (153), we first exchange the symbols ξ and ξ' and next exchange the sequence of summation to make the outer summation the one over ξ. Then we group the two terms on the left side of Eq. (153) and obtain the final equation for the unknowns $\hat{C}^d(\xi)$.

$$\sum_{\xi}{}' \left[\frac{1}{f_I(1-D_I/D_M)} (\xi\cdot\xi) g_\Omega(\eta-\xi) - \sum_{\xi'}{}' (\xi'\cdot\xi) g_{V_I}(\xi'-\xi) g_\Omega(\eta-\xi') \right] \hat{C}^d(\xi) = i\sum_{\xi}{}' (\xi\cdot E^0) g_{V_I}(\xi) g_\Omega(\eta-\xi) \qquad (154)$$

where $\xi = (2\pi n_1 / L_1, 2\pi n_2 / L_2, 2\pi n_3 / L_3)$, $\xi' = (2\pi n_1' / L_1, 2\pi n_2' / L_2, 2\pi n_3' / L_3)$; the summations $\sum_{\xi}{}'$ and $\sum_{\xi'}{}'$ sum over all possible integer combinations for (n_1, n_2, n_3) and (n_1' n_2', n_3'), respectively, except (0,0,0). If the infinite series is truncated beyond Nth order, n and n' can be any value among 0, ±1, ±2... ±N. As each n and n' can take 2N+1 values, there are $(2N+1)^3$-1 ξ and ξ' vectors in the summations. Thus there are $(2N+1)^3$-1 unknown $\hat{C}^d(\xi)$ values in Eq. (154). Accordingly, we can choose $(2N+1)^3$-1 arbitrary η vectors to build a system of linear equations with a square coefficient matrix, as Eq. (154) leads to one equation for each independent η vector. In theory the specific choices of the virtual vector η and the integration volume Ω will not affect the solution, but they do influence the condition number of the coefficient matrix of the linear equations. As a result, we can obtain a well-conditioned coefficient matrix by choosing appropriate η and Ω for a certain diffusivity contrast D_I/D_M and inclusion volume fraction f_I. For convenience, we confine η to be in the same range as ξ and ξ', i.e., η = ($2\pi m_1/L_1$, $2\pi m_2/L_2$, $2\pi m_3/L_3$), where m_1, m_2, and m_3 = 0,±1,±2...±N. And we properly adjust Ω between V_I and V (not equal to V) to optimize the conditioning of the coefficient matrix.

Our solution method presented above directly solves for the unknown Fourier coefficients from the governing equations without first approximating the field to a simpler form, such as constant, piecewise constant or polynomial position-dependent as used previously [191], at the expense of accuracy. The method reflects the idea of the "complete solution method" proposed by Nemat-Nasser *et al.* [184], but is derived in a rigorous and simple way. We have derived the strict relationship between the Fourier

coefficients $\hat{E}^*_\alpha(\xi)$ and $\hat{C}^d(\xi)$ as presented in Eq. (148) from the definition of the transformation gradient in Eq. (143), which naturally connects the transformation field to the true field. Then we constructed the governing equations for the unknown coefficients from the equilibrium or steady-state condition. The series of studies that followed Nemat-Nasser and co-workers' method have all worked in the opposite way and used the simplification elaborated in Section 5.1 (Eq. (137) and (138)). Furthermore, we have introduced a virtual integration volume Ω, which does not have to be the inclusion volume V_I and can be varied to optimize the conditioning of the matrix of the final linear equations.

5.2.3. Analytical Solution for the Effective Diffusivity

The effective diffusivity of the composite, D_{eff}, is defined as

$$D_{eff} = \frac{\left\langle J_\alpha(\vec{R})\right\rangle_V}{\left\langle E^0_\alpha + E^d_\alpha(\vec{R})\right\rangle_V} \tag{155}$$

where $\langle\ \rangle_V$ denotes a volume average in the unit cell. Here α can be any direction for which the original (or macroscopic) applied concentration gradient $E^0_\alpha \neq 0$. Introducing the expression for the flux $J(\vec{R})$ from Eq. (142) into Eq. (155),

$$D_{eff} = D_M\left(1 - \frac{\left\langle E^*_\alpha(\vec{R})\right\rangle_V}{E^0_\alpha + \left\langle E^d_\alpha(\vec{R})\right\rangle_V}\right) \tag{156}$$

where

$$\begin{aligned}\left\langle E^*_\alpha(\vec{R})\right\rangle_V &= \frac{1}{V}\int_V E^*_\alpha(\vec{R})d\vec{R} \\ &= \hat{E}^*_\alpha(\xi=(0,0,0)) \\ &= f_I(1-D_I/D_M)\left[E^0_\alpha g_{V_I}((0,0,0)) - i{\sum_{\xi'}}' \xi'_\alpha g_{V_I}(-\xi')\hat{C}^d(\xi')\right] \\ &= f_I(1-D_I/D_M)\left[E^0_\alpha - i{\sum_{\xi}}' \xi_\alpha g_{V_I}(-\xi)\hat{C}^d(\xi)\right]\end{aligned} \tag{157}$$

In Eq. (157), the second equal sign is due to Eq. (145), the third is due to Eq. (148), and the forth introduces a notation change from ξ' back to ξ in the second term. From Eq. (140), the volume average of $E^d_\alpha(\vec{R})$ vanishes because $\int_V e^{i\xi\cdot\vec{R}}d\vec{R}=0$.

$$\left\langle E^d_\alpha(\vec{R})\right\rangle_V = \frac{1}{V}\int_V E^d_\alpha(\vec{R})d\vec{R} = -\frac{1}{V}i{\sum_{\xi}}' \xi_\alpha \hat{C}^d(\xi)\left(\int_V e^{i\xi\cdot\vec{R}}d\vec{R}\right) = 0 \tag{158}$$

Introducing Eqs. (157) and (158) back into Eq. (156), we obtain an explicit expression for the effective diffusivity:

$$D_{eff} = (1-f_I)D_M + f_I D_I + \frac{f_I(D_M - D_I)}{E_\alpha^0} i \sum_{\xi}{}' \xi_\alpha g_{V_I}(-\xi)\hat{C}^d(\xi) \tag{159}$$

where the set of $\hat{C}^d(\xi)$ values are the solutions of the governing equation Eq.(154). In Eq. (159), the effective diffusivity is decomposed into two parts, the first being a volumetric average of the matrix and inclusion diffusivities and the second being a series summation. The series summation results from the periodicity of the inclusion distribution, and depends on the inclusion geometry via the integration function g and the g-dependent $\hat{C}^d(\xi)$ values.

5.3. Numerical Examples of a Cubic Array of Cubic and Spherical Inclusions

We shall examine the convergence of the effective diffusivity with respect to the truncation order N, the highest order of the Fourier series included in the calculation, and compare our results with the predictions from some other theories. We specifically evaluate the effective diffusivities of composite materials containing cubic arrays of either cubic or spherical inclusions. In these cases the unit cell for the periodic composite is cubic so that $L_1 = L_2 = L_3 = L$ in all previous equations in Section 5.2. The symmetries present in the cubic lattice and the phase geometry can significantly reduce the number of unknowns and equations, and thus reduce the computing expense and enable a rapid solution to the problem.

The geometric factor g (defined in Eq.(149)) for a cuboid inclusion of volume V_I is

$$g_{V_I}(\xi) = \frac{1}{V_I}\int_{V_I} e^{-i\xi\cdot\vec{R}} d\vec{R} = \prod_{\alpha=1}^{3}\left(\frac{1}{L_{I\alpha}}\int_{-\frac{L_{I\alpha}}{2}}^{\frac{L_{I\alpha}}{2}} e^{-i\xi_\alpha x_\alpha} dx_\alpha\right) \tag{160}$$

where $L_{I\alpha}$ is the size of the inclusion in the α direction. Each term in Eq. (160)is

$$\frac{1}{L_{I\alpha}}\int_{-\frac{L_{I\alpha}}{2}}^{\frac{L_{I\alpha}}{2}} e^{-i\xi_\alpha x_\alpha} dx_\alpha = \begin{cases} 1 & \text{if } \xi_\alpha = 0 \\ \dfrac{2}{L_{I\alpha}\xi_\alpha}\sin\left(\dfrac{L_{I\alpha}\xi_\alpha}{2}\right) & \text{if } \xi_\alpha \neq 0 \end{cases} \tag{161}$$

For the case of a cubic array of cubic inclusions, L_1=L_2=L_3=L and L_{I1}=L_{I2}=L_{I3}=L_I in Eq.(160) and (161).

The geometric factor g for a spherical inclusion with radius r ($4\pi r^3/3 = V_I$) is [184]:

$$g_{V_I}(\xi) = \frac{1}{V_I}\int_{V_I} e^{-i\xi\cdot\vec{R}} d\vec{R} = \begin{cases} 1 & \text{if } \xi = (0,0,0) \\ \dfrac{3}{(|\xi| r)^3}\left[\sin(|\xi| r) - |\xi| r\cos(|\xi| r)\right] & \text{if } \xi \neq (0,0,0) \end{cases} \tag{162}$$

The maximum radius of the sphere in the cubic unit cell $r_{max} = L/2$, so the maximum possible volume fraction of the spherical inclusions in this case is $f_{I\max} = 4\pi r_{\max}^3 / L^3 = \pi/6 \approx 0.5236$. Our method should work for overlapping spheres as well, except that the integration function g in Eq. (154) and (159) can no longer be calculated from Eq. (162) and needs to be specifically evaluated.

Figure 63 presents the effective diffusivities calculated at increasing truncation order N for composites containing a cubic array of cubic (data are plotted as squares) or spherical (plotted as circles) inclusions at various inclusion volume fractions f_I.

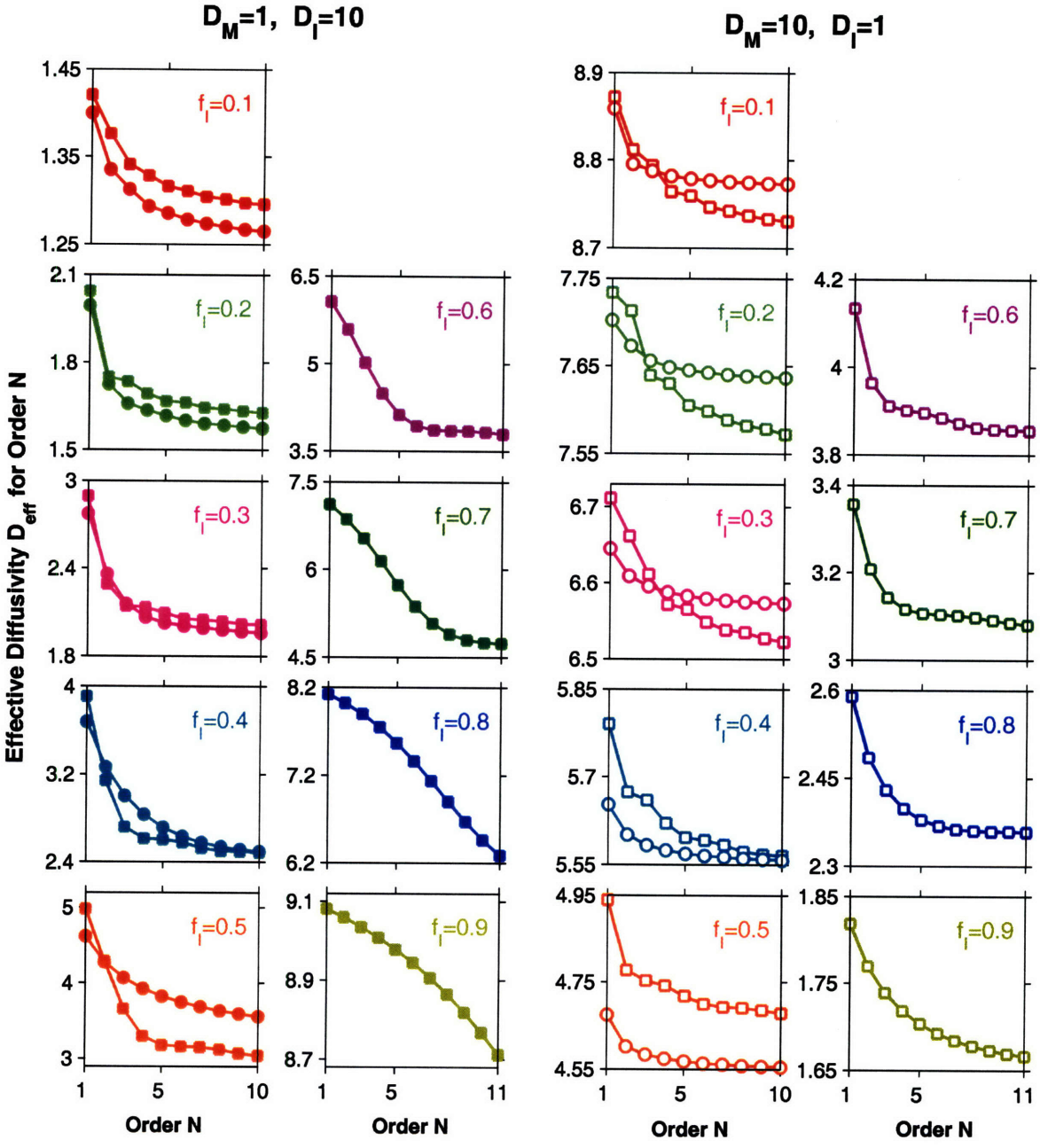

Figure 63. Convergence of the calculated effective diffusivity with respect to the truncation order N at various inclusion volume fractions f_I = 0.1, 0.2 ... 0.9. The squares (■ and □) denote data for cubic inclusions while the circles (● and ○) are the data points for spherical inclusions. The filled symbols (■ and ●) are for the case D_M=1 and D_I=10, and the open symbols (□ and ○) are for the case D_M=10 and D_I=1.

For both diffusivity contrast ratios, D_I/D_M = 10 and 0.1, the calculated effective diffusivities always monotonically decrease with increasing order N. This is because, as shown in Eq.(159), the 0^{th} order solution is simply a linear average of the phase diffusivities, $D_{eff} = (1-f_I)D_M + f_I D_I$, which is an upper bound. As we include more and more high-order terms, more interaction effects are progressively taken into account. We can see that the resulting diffusivities converge quite fast as we increase the truncation order N. When the inclusions have a higher diffusivity (D_I/D_M = 10), the interactions among them become increasingly strong at high volume fractions, making it more difficult to achieve convergence at high inclusion fractions; we need to include more higher-order terms in order to capture the strong interactions. These trends are generally true for both inclusion shapes, except that for spheres, for which the transition to a "high" volume fraction occurs much sooner than for cubic inclusions because the maximum volume fraction of non-overlapping spheres is only about 0.52.

When D_I/D_M = 10, D_{eff} for composites with spherical inclusions is lower than for composites with cubic inclusions at f_I = 0.1, 0.2, and 0.3, but becomes higher when f_I = 0.4 and 0.5. This might be because at the same volume fraction, the minimum distance between spherical inclusions is much smaller than that between cubic inclusions. Since the diffusivity of the segregated inclusions is higher, the effective diffusivities of the composite material will be higher when the inclusions are closer to each other. This effect becomes prominent at high volume fractions. It is the opposite case when D_I/D_M = 0.1. Now the matrix phase is the main diffusion path and the narrow necks of the matrix material may limit the diffusional flow. Therefore D_{eff} for composites with spherical inclusions is higher than for composites with cubic inclusions at f_I = 0.1, 0.2, and 0.3, and becomes lower when f_I = 0.4 and 0.5.

In Table 10, we compare the highest-order numerical results we currently have with the predictions of some earlier models, including the Maxwell-Garnett (MG) formula (Eq. (8)), which coincides with the Hashin-Shtrikman (HS) bounds (Eqs. (3) and (4)) [10], Rayleigh's method, and McKenzie and McPhedran's model [196, 197]. It is generally recognized that the MG formula, Rayleigh's method, and McKenzie *et al.*'s model are of order 1, 2, and 4, respectively [196]. Rayleigh's method and McKenzie *et al.*'s model are specifically derived for a periodic cubic lattice of spheres.

When D_M = 1 and D_I = 10, our results are slightly above the predictions of the MG formula (or HS lower bound). Both phases in the composite are isotropic and the diffusivity of the isolated inclusions is higher than the diffusivity of the surrounding matrix material, so the microstructure is very close to realizing the HS lower bound (Figure 2(d)). The results are in fact slightly higher than the lower bound because the present cubic array is not an ideally isotropic geometry, and this difference increases with the inclusion volume fraction. Comparing results from Rayleigh's method, McKenzie et al.'s model and our results for spherical inclusions, it is seen that higher order evaluations generally result in higher effective diffusivities. Although our results may vary a few thousandths considering the convergence trend shown in Figure 63, this variation is marginal and the trend still holds. For the same type of composite microstructures, Gu *et al.* [198] also observed that predictions from homogenization approaches that include higher-order interactions are in general higher than the lower bound.

Table 10. Effective diffusivities of periodic composites containing a cubic array of spherical or cubic inclusions calculated using our homogenization method (at 10^{th} or 11^{th} order) compared with predictions from other theories.

D_M=1, D_I=10

f_I	0^{th} Order (Rule of Mixture)	1^{st} Order (MG or HS$^-$)	2^{nd} Order (Rayleigh)	4^{th} Order (McKenzie *et al.*)	Present Method	
					Spherical Inclusion	Cubic Inclusion
0.1	1.9	1.2432	1.2433	1.2433	1.2651	1.2959
0.2	2.8	1.5294	1.5317	1.5317	1.5738	1.6275
0.3	3.7	1.8710	1.8870	1.8876	1.9610	2.0164
0.4	4.6	2.2857	2.3567	2.3631	2.4969	2.4877
0.5	5.5	2.8000	3.0532	3.1133	3.5276	3.0358
0.6	6.4	3.4545				3.7959
0.7	7.3	4.3158				4.7331
0.8	8.2	5.5000				6.2888 ↓
0.9	9.1	7.2308				8.7124 ↓

D_M=10, D_I=1

f_I	0^{th} Order (Rule of Mixture)	1^{st} Order (MG or HS$^+$)	2^{nd} Order (Rayleigh)	4^{th} Order (McKenzie *et al.*)	Present Method	
					Spherical Inclusion	Cubic Inclusion
0.1	9.1	8.7671	8.7669	8.7669	8.7728	8.7307
0.2	8.2	7.6316	7.6280	7.6280	7.6363	7.5719
0.3	7.3	6.5823	6.5630	6.5632	6.5730	6.5229
0.4	6.4	5.6098	5.5468	5.5480	5.5581	5.5660
0.5	5.5	4.7059	4.5496	4.5519	4.5551	4.6744
0.6	4.6	3.8636				3.8547
0.7	3.7	3.0769				3.0801
0.8	2.8	2.3404				2.3577
0.9	1.9	1.6495				1.6659

When D_M = 10 and D_I = 1, the results are very close to the HS upper bound because now the percolating matrix phase has a higher diffusivity (see the geometry realizing HS upper bound in Figure 2(c)). For cubic inclusions, our high order results converge well to below the upper bound at volume fractions f_I = 0.1-0.6, but seem to stay a little above the upper bound even though convergence has almost been reached at f_I = 0.8 and 0.9, as shown in Figure 63. For spherical inclusions, although the results seem to have almost converged at all inclusion fractions (see Figure 63), D_{eff} at f_I = 0.1 and 0.2 remain slightly above the upper bound while D_{eff} at f_I = 0.3-0.5 are far below the upper bound. It is not clear whether

higher-order calculations should result in an effective property above the HS upper bound for a cubic array of inclusions, which is not a strictly isotropic structure and thus not required to fall within the HS bounds.

5.4. Summary

We have proposed a technique for calculating the effective properties of composite materials with periodic microstructures. It is based on the idea of expanding the imaginary transformation "strain" in Fourier series and constructing equations from consistency and equilibrium requirements. But we derive the equations in a different, rigorous way, as compared with prior literature, without making any assumptions that oversimplify the solution or render it accurate only for special circumstances. The results are exact to a given order and converge approximately at ninth or tenth order, which are computationally achievable. The method is in theory applicable to any microgeometry in a parallelepiped unit cell, and is easiest for a single centered inclusion contained in a cubic unit cell. The method is rigorous, easy to implement, and reasonably efficient.

The coefficient matrix in the governing equation (Eq. (154)) is not sparse, and intuitively it might seem to require a lot of computer memory and CPU time to directly solve for the Fourier coefficients [180]. This is not necessarily the case. Even if all the geometric symmetries are neglected, the calculation would take only ~1 GB of memory and ~20 hours using a desktop PC for the tenth order if the coefficient matrix is built using row vectors, instead of element-by-element, and would take ~2 GB of memory and ~8-10 hours if column vectors are used instead (although the equations were presented on a row basis). The computation expense could be significantly reduced if symmetries are taken into account, such as the cubic symmetry in our numerical examples and inversion symmetry. With today's powerful computers with high memory limits and parallel computing capabilities, computing cost is much less a concern as compared to the accuracy and simplicity of the method.

What is more, the simple form of the final governing equation indicates that an analytical exact (or at least exact to a high order not available presently) solution might be possible, though not yet available, for some simple inclusion geometries.

Chapter 6. Conclusions

Heterogeneous materials are everywhere, and it is a central interest of materials scientists to be able to predict their macroscopic effective properties based on knowledge of the distribution of the heterogeneities or phases. Many composite theories have been developed for this purpose and are widely known in the field, including the simple rule-of-mixtures, the seminal Hashin-Shtrikman bounds, the widely-used Maxwell-Garnett formula, Bruggeman's effective medium approximation, series expansions.... Numerous other methods comprise a list that can go on and on. However, one important element—microstructure connectivity—is missing in essentially all these models. This thesis has considered one possible approach to introduce the effects of microstructure connectivity on effective property prediction, and to develop practical theoretical tools to evaluate effective properties for a variety of complicated heterogeneous microstructures.

The materials properties studied in this thesis include the effective diffusivity, effective diffusional creep viscosity, and effective bulk and shear moduli. The heterogeneous microstructures studied include two-phase composite solids and binary as well as multicomponent grain boundary networks. The spatial distributions of phases studied include an ideally random phase distribution, short-range to long-range correlated distributions, and a perfect periodic phase distribution.

A main theme of this thesis is the use of the formal apparatus of percolation theory as a means of capturing microstructural connectivity, and then introducing the percolation concepts into composite-type theories for specific properties. The effects of microstructure connectivity are sufficiently captured by only a few percolation quantities such as the percolation threshold and critical scaling exponents. These important percolation parameters have been identified for all of the microstructures and materials properties studied in this work (most for the first time). Further, these parameters are incorporated into an effective medium equation which is then able to predict the effective properties correctly and in particular capture the percolation transition accurately. This is critical because macroscopic effective properties can change dramatically when the phase fraction crosses the percolation threshold, an effect that is not captured by composite models of the types noted above.

This thesis has also considered a variety of additional complexities that may arise in real materials, such as correlated phase distributions, multicomponent systems, multiconnectivity in continuum solids, and each phase being characterized by multiple materials parameters instead of one. All these complicated but important issues have been carefully studied.

The specific conclusions of this thesis are as follows.

1. The mathematical form of the physical laws governing a property usually determines the percolation universality class the property belongs to. Our percolation scaling results for diffusion on randomly-distributed grain boundary networks are consistent with literature data on other linear transport properties

such as conductivity. Grain boundary diffusional creep and continuum elasticity, however, have their own scaling exponents, reported here for the first time.

2. Percolation properties of composite solids are different from discrete systems such as grain boundary networks. Multiconnectivity on the continuum, such as edge and corner contacts, affects both the percolation threshold and critical scaling exponents.

3. Multicomponent heterogeneous systems are very common, but unfortunately the very powerful theoretical tool we have discovered in the literature, the GEM equation that couples percolation with traditional effective theory, is only written for binary systems. By assuming that all microstructural effects can be properly captured by the percolation threshold and scaling exponents, and by incorporating our understanding of percolation properties of binary systems, we are able to generalize the GEM equation for multicomponent cases. The predictions of the generalized equation are in excellent agreement with our simulation results for ternary systems.

4. All correlations in phase distributions change the percolation threshold, but whether they affect the scaling behaviors depends on the correlation length. Short-range correlations do not alter the scaling exponents; in other words, the problem remains in the same universality class. This is the case found for grain boundary networks, where crystallographic consistency requirements induce correlations, but do not change the scaling behavior seen in diffusion or diffusional creep. On the other hand, long-range correlations make the percolation scaling nonuniversal; the scaling exponents become functions of the correlation length. This is the case for composites with some tendency to form periodic arrangements of the reinforcement phase, as shown here for diffusion and other linear transport properties.

These specific results are significant in light of the current state of understanding in the field, for the following reasons:

1. The kinetic differences among different types of grain boundaries have been largely neglected in various materials models that involve grain boundary diffusion. Our results for the effective grain boundary diffusivities not only provide a homogenized diffusivity that can be used in these models, but also introduce a useful theoretical framework largely unknown in materials research before.

2. The percolation threshold and scaling exponents of Coble creep are all different from diffusion on the same type of heterogeneous grain boundary networks; Coble creep is a new universality class of percolation. This result speaks to strong correlations, but not those due to constraint in spatial distributions, but rather correlations imposed by the equilibrium and compatibility requirements of the creep process itself. Our results for the effective creep viscosity and the famous Coble equation together make a good practical tool that can be used to predict stress-strain rate relationships for heterogeneous materials.

3. Evaluating effective elastic properties is a difficult problem numerous researchers have been working on for a long time. Since each phase is characterized by several independent elastic constants, which

are bulk and shear moduli in this work, the percolation in one effective elastic constant will be affected by all other constants. Using large-scale finite element simulations, we have collected two series of interesting data, one for effective shear modulus and the other for effective bulk modulus. Very interesting trends have been observed that are not anticipated by conventional modeling approaches. In particular, we are the first to introduce into this old problem the percolation element, which may finally lead to analytical solutions for effective elastic properties.

4. Luckily, we do not have to worry about the effects of microstructure topology for periodic composite materials. Periodicity makes it possible to directly develop a rigorous homogenization procedure. By using Eshelby's transformation field and Fourier series, we are able to obtain a short expression for the effective diffusivity that is considerably simpler and efficient to evaluate as compared with existing theories. Our procedure can be further modified for other materials properties such as elasticity.

Finally, the search for accurate descriptions of microstructure-property relationships has never stopped and will never stop. A lot of future research topics can be generated from this work, and of course there remains a lot of work to do. This author, for one, will keep pursuing these topics, and it is hoped that more people will join in this challenging and exciting area.

References

[1] Koplik, J., Homogenization and effective medium methods for transport in disordered granular systems, in *Physics of granular media* (Nova, New York, 1991), p. 215

[2] Sahimi, M., Heterogeneous materials 1: Linear transport and optical properties (Springer, New York, 2003)

[3] Stauffer, D., Aharony, A., Introduction to percolation theory (Taylor & Francis, London, 1992)

[4] Choy, T.C., Effective medium theory: Principles and applications (Oxford University Press, New York, 1999)

[5] Kirkpatrick, S., Percolation and conduction, *Reviews of Modern Physics* 45, 574 (1973)

[6] Landauer, R., Electrical conductivity in inhomogeneous media, *AIP Conference Proceedings* 40, 2 (1978)

[7] Batchelor, G.K., Transport properties of two-phase materials with random structure, *Annu. Rev. Fluid Mech.* 6, 227 (1974)

[8] Torquato, S., Random heterogeneous materials: Microstructure and macroscopic properties (Springer, New York, 2002)

[9] Hashin, Z., Shtrikman, S., A variational approach to the theory of the effective magnetic permeability of multiphase materials, *Journal of Applied Physics* 33, 3125 (1962)

[10] Hashin, Z., Shtrikman, S., Conductivity of polycrystals, *Physical Review* 130, 129 (1963)

[11] Karkkainen, K.K., Sihvola, A.H., Nikoskinen, K.I., Effective permittivity of mixtures: Numerical validation by the fdtd method, *Ieee Transactions on Geoscience and Remote Sensing* 38, 1303 (2000)

[12] Berryman, J.G., Bounds and estimates for transport coefficients of random and porous media with high contrasts, *Journal of Applied Physics* 97, 063504 (2005)

[13] Helsing, J., Bounds to the conductivity of some two-component composites, *Journal of Applied Physics* 73, 1240 (1993)

[14] Milton, G.W., Bounds on the complex permittivity of a two-component composite material, *Journal of Applied Physics* 52, 5286 (1981)

[15] Walpole, L.J., On bounds for the overall elastic moduli of inhomogeneous systems--ii, *Journal of the Mechanics and Physics of Solids* 14, 289 (1966)

[16] Walpole, L.J., On bounds for the overall elastic moduli of inhomogeneous systems--i, *Journal of the Mechanics and Physics of Solids* 14, 151 (1966)

[17] Choy, T.C., Effective medium theory (Clarendon Press, Oxford, 1999)

[18] Landauer, R., The electrical resistance of binary metallic mixtures, *Journal of Applied Physics* 23, 779 (1952)

[19] Maxwell, J.C., Treatise on electricity and magnetism (Clarendon Press, Oxford, 1873)

[20] Maxwell-Garnett, J.C., Colours in metal glasses and in metallic films, *Philosophical Transactions of the Royal Society of London A* 203, 385 (1904)

[21] Bruggeman, D.A.G., *Ann. Physik. Leipzig* 24, 636 (1935)

[22] Torquato, S., Bulk properties of 2-phase disordered media .1. Cluster-expansion for the effective dielectric-constant of dispersions of penetrable spheres, *Journal of Chemical Physics* 81, 5079 (1984)

[23] Felderhof, B.U., Ford, G.W., Cohen, E.G.D., Cluster-expansion for the dielectric-constant of a polarizable suspension, *Journal of Statistical Physics* 28, 135 (1982)

[24] Jeffrey, D.J., Group expansions for bulk properties of a statistically homogeneous, random suspension, *Proceedings of the Royal Society of London Series A* 338, 503 (1974)

[25] Brown, J.W.F., Solid mixture permittivities, *The Journal of Chemical Physics* 23, 1514 (1955)

[26] Ramshaw, J.D., Dielectric polarization in random media, *Journal of Statistical Physics* 35, 49 (1984)

[27] Torquato, S., Effective electrical-conductivity of 2-phase disordered composite media, *Journal of Applied Physics* 58, 3790 (1985)

[28] Sahimi, M., Non-linear and non-local transport processes in heterogeneous media: From long-range correlated percolation to fracture and materials breakdown, *Physics Reports* 306, 213 (1998)

[29] Frary, M., Schuh, C.A., Grain boundary networks: Scaling laws, preferred cluster structure, and their implications for grain boundary engineering, *Acta Materialia* 53, 4323 (2005)

[30] Isichenko, M.B., Percolation, statistical topography, and transport in random media, *Reviews of Modern Physics* 64, 961 (1992)

[31] Stauffer, D., Scaling theory of percolation clusters, *Physics Reports (Review Section of Physics Letters)* 54, 1 (1979)

[32] Bunde, A., Kantelhardt, J.W., Diffusion and conduction in percolation systems -- theory and application, in *Diffusion in condensed matter* (Springer Verlag, Berlin, 2005), p.

[33] Chaves, C.M., Koiller, B., Universality, thresholds and critical exponents in correlated percolation, *Physica A* 218, 271 (1995)

[34] Petrov, I.V., Stoynev, II, Babalievskii, F.V., Correlated 2-component percolation, *Journal of Physics A* 24, 4421 (1991)

[35] Prakash, S., Havlin, S., Schwartz, M., Stanley, H.E., Structural and dynamical properties of long-range correlated percolation, *Physical Review A* 46, R1724 (1992)

[36] Sahimi, M., Mukhopadhyay, S., Scaling properties of a percolation model with long-range correlations, *Physical Review E* 54, 3870 (1996)

[37] Straley, J.P., Critical exponents for the conductivity of random resistor lattices, *Physical Review B (Solid State)* 15, 5733 (1977)

[38] Feng, S., Sen, P.N., Percolation on elastic networks - new exponent and threshold, *Physical Review Letters* 52, 216 (1984)

[39] Arbabi, S., Sahimi, M., Elastic properties of 3-dimensional percolation networks with stretching and bond-bending forces, *Physical Review B* 38, 7173 (1988)

[40] Arbabi, S., Sahimi, M., Mechanics of disordered solids .1. Percolation on elastic networks with central forces, *Physical Review B* 47, 695 (1993)

[41] Bergman, D.J., Elastic-moduli near percolation in a two-dimensional random network of rigid and nonrigid bonds, *Physical Review B* 33, 2013 (1986)

[42] Day, A.R., Tremblay, R.R., Tremblay, A.M.S., Rigid backbone - a new geometry for percolation, *Physical Review Letters* 56, 2501 (1986)

[43] Hansen, A., Roux, S., Universality class of central-force percolation, *Physical Review B* 40, 749 (1989)

[44] Moukarzel, C., Duxbury, P.M., Leath, P.L., Infinite-cluster geometry in central-force networks, *Physical Review Letters* 78, 1480 (1997)

[45] Sahimi, M., Arbabi, S., Mechanics of disordered solids .2. Percolation on elastic networks with bond-bending forces, *Physical Review B* 47, 703 (1993)

[46] Sahimi, M., Arbabi, S., Force distribution, multiscaling, and fluctuations in disordered elastic media, *Physical Review B* 40, 4975 (1989)

[47] McLachlan, D.S., A new interpretation of percolation conductivity results with large critical regimes, *Solid State Communications* 60, 821 (1986)

[48] McLachlan, D.S., An equation for the conductivity of binary-mixtures with anisotropic grain structures, *Journal of Physics C* 20, 865 (1987)

[49] McLachlan, D.S., Blaszkiewicz, M., Newnham, R.E., Electrical resistivity of composites, *Journal of the American Ceramic Society* 73, 2187 (1990)

[50] Frary, M., Schuh, C.A., Percolation and statistical properties of low- and high-angle interface networks in polycrystalline ensembles, *Physical Review B* 69, (2004)

[51] Garboczi, E.J., Day, A.R., An algorithm for computing the effective linear elastic properties of heterogeneous materials: Three-dimensional results for composites with equal phase poisson ratios, *Journal of the Mechanics and Physics of Solids* 43, 1349 (1995)

[52] Langer, S.A., Fuller, E., Carter, W.C., Oof: An image-based finite-element analysis of material microstructures, *Computing in Science & Engineering* 3, 15 (2001)

[53] Singh, H., Gokhale, A.M., Mao, Y., Spowart, J.E., Computer simulations of realistic microstructures of discontinuously reinforced aluminum alloy (dra) composites, *Acta Materialia* 54, 2131 (2006)

[54] Balberg, I., Recent developments in continuum percolation, *Philosophical Magazine B* 56, 991 (1987)

[55] Bug, A.L.R., Safran, S.A., Webman, I., Continuum percolation of permeable objects, *Physical Review B* 33, 4716 (1986)

[56] Baker, D.R., Paul, G., Sreenivasan, S., Stanley, H.E., Continuum percolation threshold for interpenetrating squares and cubes, *Physical Review E* 66, (2002)

[57] Lee, S.B., Universality of continuum percolation, *Physical Review B* 42, 4877 (1990)

[58] Gawlinski, E.T., Stanley, H.E., Continuum percolation in 2 dimensions - monte-carlo tests of scaling and universality for non-interacting disks, *Journal of Physics A* 14, L291 (1981)

[59] Elam, W.T., Kerstein, A.R., Rehr, J.J., Critical properties of the void percolation problem for spheres, *Physical Review Letters* 52, 1516 (1984)

[60] Halperin, B.I., Feng, S., Sen, P.N., Differences between lattice and continuum percolation transport exponents, *Physical Review Letters* 54, 2391 (1985)

[61] Lee, S.B., Torquato, S., Monte-carlo study of correlated continuum percolation - universality and percolation thresholds, *Physical Review A* 41, 5338 (1990)

[62] Feng, S., Halperin, B.I., Sen, P.N., Transport properties of continuum systems near the percolation threshold, *Physical Review B* 35, 197 (1987)

[63] Wu, J.J., McLachlan, D.S., Percolation exponents and thresholds obtained from the nearly ideal continuum percolation system graphite-boron nitride, *Physical Review B* 56, 1236 (1997)

[64] Petersen, J., Roman, H.E., Bunde, A., Dieterich, W., Nonuniversality of transport exponents in continuum percolation systems - effects of finite jump distance, *Physical Review B* 39, 893 (1989)

[65] Saylor, D.M., El Dasher, B.S., Rollett, A.D., Rohrer, G.S., Distribution of grain boundaries in aluminum as a function of five macroscopic parameters, *Acta Materialia* 52, 3649 (2004)

[66] Kaur, I., Handbook of grain and interphase boundary diffusion data (Ziegler Press, Stuttgart, 1989)

[67] Li, X.M., Chou, Y.T., High angle grain boundary diffusion of chromium in niobium bicrystals, *Acta Materialia* 44, 3535 (1996)

[68] Li, X.M., Chou, Y.T., Low angle grain boundary diffusion of cr in nb bicrystals, *Philosophical Magazine a-Physics of Condensed Matter Structure Defects and Mechanical Properties* 73, 1303 (1996)

[69] Balandin, I.L., Bokshtein, B.S., Temperature and orientation dependences of the grain-boundary diffusion coefficient of antimony in copper bicrystals, *Physics of the Solid State* 39, 1019 (1997)

[70] Budke, E., Herzig, C., Prokofjev, S., Shvindlerman, L.S., Orientation dependence of au and cu diffusion along symmetric [001] tilt grain boundaries in cu, *Materials Science Forum* 207-209, 465 (1996)

[71] Monzen, R., Kuze, T., Misorientation dependence of grain-boundary diffusion of bi in cu bicrystals, *Journal of the Japan Institute of Metals* 63, 1224 (1999)

[72] Monzen, R., Takada, Y., Kita, K., Misorientation dependence of diffusion of bi in [0 0 1] symmetric tilt boundaries of cu, *Journal of Materials Science Letters* 17, 283 (1998)

[73] Schwarz, S.M., Kempshall, B.W., Giannuzzi, L.A., Stevie, F.A., Utilizing the sims technique in the study of grain boundary diffusion along twist grain boundaries in the cu(ni) system, *Acta Materialia* 50, 5079 (2002)

[74] Bernardini, J., Cabane, J., Diffusion du ruthenium et du nickel le long des dislocations dans le cuivre: Ruthenium and nickel pipe diffusion in copper, *Acta Metallurgica* 21, 1571 (1973)

[75] Suzuki, A., Mishin, I.M., Diffusion mechanism in grain boundaries, *Journal of Metastable and Nanocrystalline Materials* 19, 1 (2004)

[76] Yang, C.F., Sarkar, G., Fournelle, R.A., Discontinuous precipitation and coarsening in al-zn alloys, *Acta Metallurgica* 36, 1511 (1988)

[77] Manna, I., Gust, W., Predel, B., Discontinuous precipitation in zn---al alloys, *Scripta Metallurgica et Materialia* 24, 1635 (1990)

[78] King, A.H., Diffusion induced grain-boundary migration, *International Materials Reviews* 32, 173 (1987)

[79] Suryanarayana, C., Korth, G.E., Consolidation of nanocrystalline powders, *Metals and Materials-Korea* 5, 121 (1999)

[80] Suryanarayana, C., Yoo, S.H., Groza, J.R., Consolidation of mechanically alloyed cu-in-ga-se powders, *Journal of Materials Science Letters* 20, 2179 (2001)

[81] Trattles, J.T., Oneill, A.G., Mecrow, B.C., Computer-simulation of electromigration in thin-film metal conductors, *Journal of Applied Physics* 75, 7799 (1994)

[82] Ghiti, A., Oneill, A.G., The effects of grain boundary diffusion anisotropy on via electromigration failure, *Journal of Applied Physics* 81, 3064 (1997)

[83] Pfaendtner, J.A., McMahon Jr., C.J., Oxygen-induced intergranular cracking of a ni-base alloy at elevated temperatures--an example of dynamic embrittlement, *Acta Materialia* 49, 3369 (2001)

[84] Coble, R.L., A model for boundary diffusion controlled creep in polycrystalline materials, *Journal of Applied Physics* 34, 1679 (1963)

[85] Kaur, I., Wolfgang, G., Fundamentals of grain and interphase boundary diffusion (Ziegler Press, Stuttgart, 1989)

[86] Peterson, N.L., Diffusion mechanisms and structural effects in grain boundaries, *Journal of Vacuum Science & Technology A: Vacuum, Surfaces, and Films* 4, 3066 (1986)

[87] Fernandez, J.R., Monti, A.M., Pasianot, R.C., Grain-boundary diffusion by vacancy mechanism in alpha-ti and alpha-zr, *Metallurgical and Materials Transactions a-Physical Metallurgy and Materials Science* 33, 791 (2002)

[88] Suryanarayana, C., Koch, C.C., Nanocrystalline materials - current research and future directions, *Hyperfine Interactions* 130, 5 (2000)

[89] Beke, D.Journal of metastable and nanostructured materials192004

[90] Rohrer, G.S., Saylor, D.M., El Dasher, B., Adams, B.L., Rollett, A.D., Wynblatt, P., The distribution of internal interfaces in polycrystals, *Zeitschrift Fur Metallkunde* 95, 197 (2004)

[91] Kim, C.S., Hu, Y., Rohrer, G.S., Randle, V., Five-parameter grain boundary distribution in grain boundary engineered brass, *Scripta Materialia* 52, 633 (2005)

[92] Basinger, J.A., Homer, E.R., Fullwood, D.T., Adams, B.L., Two-dimensional grain boundary percolation in alloy 304 stainless steel, *Scripta Materialia* 53, 959 (2005)

[93] Minich, R.W., Schuh, C.A., Kumar, M., Role of topological constraints on the statistical properties of grain boundary networks, *Physical Review B* 66, (2002)

[94] Harrison, L.G., Influence of dislocations on diffusion kinetics in solids with particular reference to the alkali halides, *Transactions of the Faraday Society* 57, 1191 (1961)

[95] Kondratev, V.V., Trachtenberg, I.S., Intergranular diffusion in real polycrystals, *Physica Status Solidi B* 171, 303 (1992)

[96] Klinger, L., Rabkin, E., Diffusion along the grain boundaries in crystals with dislocations, *Interface Science* 6, 197 (1998)

[97] Klinger, L., Rabkin, E., Beyond the fisher model of grain boundary diffusion: Effect of structural inhomogeneity in the bulk, *Acta Materialia* 47, 725 (1999)

[98] Divinski, S.V., Geise, J., Rabkin, E., Herzig, C., Grain boundary self-diffusion in alpha-iron of different purity: Effect of dislocation enhanced diffusion, *Zeitschrift Fur Metallkunde* 95, 945 (2004)

[99] Belova, I.V., Murch, G.E., Diffusion in nanocrystalline materials, *Journal of Physics and Chemistry of Solids* 64, 873 (2003)

[100] Fisher, J.C., Calculation of diffusion penetration curves for surface and grain boundary diffusion, *Journal of Applied Physics* 22, 74 (1951)

[101] Whipple, R.T.P., Concentration contours in grain boundary diffusion, *Philosophical Magazine* 45, 1225 (1954)

[102] Levine, H.S., MacCallum, C.J., Grain boundary and lattice diffusion in polycrystalline bodies, *Journal of Applied Physics* 31, 595 (1960)

[103] Suzuoka, T., Exact solutions of two ideal cases in grain boundary diffusion problem and the application to sectioning method, *Journal of the Physical Society of Japan* 19, 839 (1964)

[104] Yonezawa, F., Sakamoto, S., Hori, M., Percolation in two-dimensional lattices. I. A technique for the estimation of thresholds, *Physical Review B (Condensed Matter)* 40, 636 (1989)

[105] Li, P.S., Strieder, W., Critical exponents for conduction in a honeycomb random site lattice, *J. Phys. C: Solid State Phys.* 15, L1235 (1982)

[106] Joy, T., Strieder, W., Effective-medium theory of the conductivity for a random-site honeycomb lattice, *Journal of Physics C: Solid State Physics* L279 (1979)

[107] Frary, M., Schuh, C.A., Percolation and statistical properties of low- and high-angle interface networks in polycrystalline ensembles, *Physical Review B* 69, 134115 (2004)

[108] Kaur, I., Gust, W., Kozma, L., Handbook of grain and interface boundary diffusion data (Ziegler Press, Stuttgart, 1989)

[109] Chen, Y., Schuh, C.A., Geometric considerations for diffusion in polycrystalline solids, *Journal of Applied Physics* 101, (2007)

[110] Hoshen, J., Kopelman, R., Percolation and cluster distribution. I. Cluster multiple labeling technique and critical concentration algorithm, *Physical Review B (Solid State)* 14, 3438 (1976)

[111] Roux, S., Hansen, A., A new algorithm to extract the backbone in a random resistor network, *Journal of Physics a-Mathematical and General* 20, L1281 (1987)

[112] Sahimi, M., On the relationship between the critical exponents of percolation conductivity and static exponents of percolation, *Journal of Physics A: Mathematical and General* L601 (1984)

[113] Webman, I., Jortner, J., Cohen, M.H., Critical exponents for percolation conductivity in resistor networks, *Physical Review B (Solid State)* 16, 2593 (1977)

[114] Bunde, A., Havlin, S., Fractals and disordered systems (Berlin; New York: Springer, c1996, 1996)

[115] Bunde, A., Dieterich, W., Percolation in composites, *Journal of Electroceramics* 5, 81 (2000)

[116] Clerc, J.P., Giraud, G., Laugier, J.M., Luck, J.M., The electrical conductivity of binary disordered systems, percolation clusters, fractals and related models, *Advances in Physics* 39, 191 (1990)

[117] Sahimi, M., Hughes, B.D., Scriven, L.E., Davis, H.T., Critical exponent of percolation conductivity by finite-size scaling, *Journal of Physics C: Solid State Physics* L521 (1983)

[118] Efros, A.L., Shklovskii, B.I., Critical behavior of conductivity and dielectric-constant near metal-non-metal transition threshold, *Physica Status Solidi B-Basic Research* 76, 475 (1976)

[119] Jonckheere, T., Luck, J.M., Dielectric resonances of binary random networks, *Journal of Physics A: Mathematical and General* 3687 (1998)

[120] Straley, J.P.Annals of the Israel Physical Society51983

[121] McLachlan, D.S., Analytical functions for the dc and ac conductivity of conductor-insulator composites, *Journal of Electroceramics* 5, 93 (2000)

[122] Vrettos, N.A., Imakoma, H., Okazaki, M., An effective medium treatment of the transport properties of a voronoi tesselated network, *Journal of Applied Physics* 66, 2873 (1989)

[123] McLachlan, D.S., Priou, A., Chenerie, I., Issac, E., Henry, F., Modeling the permittivity of composite-materials with a general effective medium equation, *Journal of Electromagnetic Waves and Applications* 6, 1099 (1992)

[124] Frost, H., Ashby, M., Deformation-mechanism maps: The plasticity and creep of metals and ceramics (Pergamon Pr, 1982)

[125] Kim, B.N., Hiraga, K., Morita, K., Ahn, B.W., Analysis of creep due to grain-boundary diffusion in hexagonal microstructures, *Philosophical Magazine* 84, 3251 (2004)

[126] Spingarn, J.R., Nix, W.D., Diffusional creep and diffusionally accommodated grain rearrangement, *Acta Metallurgica* 26, 1389 (1978)

[127] Tong, W.S., Rickman, J.M., Chan, H.M., Harmer, M.P., Coble-creep response and variability of grain-boundary properties, *J. Mater. Res.* 17, 348 (2002)

[128] Moldovan, D., Wolf, D., Phillpot, S.R., Mukherjee, A.K., Gleiter, H., Grain-boundary diffusion-controlled stress concentration in polycrystals, *Philosophical Magazine Letters* 83, 29 (2003)

[129] Ding, R., Moldovan, D., Yamakov, V., Wolf, D., Phillpot, S.R., Effects of microstructural inhomogeneity on dynamic grain growth during large-strain grain boundary diffusion-assisted plastic deformation, *Modelling and Simulation in Materials Science and Engineering* 13, 1129 (2005)

[130] Monzen, R., Suzuki, T., Nanometre-scale grain-boundary sliding in copper bicrystals with [001] twist boundaries, *Philosophical Magazine Letters* 74, 9 (1996)

[131] Watanabe, T., Yamada, M., Shima, S., Karashima, S., Misorientation dependence of grain-boundary sliding in (1010) tilt zinc bicrystals, *Philosophical Magazine A* 40, 667 (1979)

[132] Lehockey, E.M., Palumbo, G., On the creep behaviour of grain boundary engineered nickel, *Materials Science and Engineering A* 237, 168 (1997)

[133] Thaveeprungsriporn, V., Was, G.S., The role of coincidence-site-lattice boundaries in creep of ni-16cr-9fe at 360 degrees c, *Metallurgical and Materials Transactions A* 28, 2101 (1997)

[134] Alexandreanu, B., Sencer, B.H., Thaveeprungsriporn, V., Was, G.S., The effect of grain boundary character distribution on the high temperature deformation behavior of ni-16cr-9fe alloys, *Acta Materialia* 51, 3831 (2003)

[135] Spigarelli, S., Cabibbo, M., Evangelista, E., Palumbo, G., Analysis of the creep strength of a low-carbon aisi 304 steel with low-sigma grain boundaries, *Materials Science and Engineering A* 352, 93 (2003)

[136] Hazzledine, P.M., Schneibel, J.H., Theory of coble creep for irregular grain structures, *Acta Metallurgica et Materialia* 41, 1253 (1993)

[137] Ford, J.M., Wheeler, J., Movchan, A.B., Computer simulation of grain-boundary diffusion creep, *Acta Materialia* 50, 3941 (2002)

[138] Chen, Y., Schuh, C.A., Percolation of diffusional creep: A new universality class, *Physical Review Letters* 98, 035701 (2007)

[139] Chen, Y., Schuh, C.A., Diffusion on grain boundary networks: Percolation theory and effective medium approximations, *Acta Materialia* 54, 4709 (2006)

[140] Arcangelis, L.d., Redner, S., Coniglio, A., Anomalous voltage distribution of random resistor networks and a new model for the backbone at the percolation threshold, *Physical Review B* 31, 4725 (1985)

[141] Blumenfeld, R., Meir, Y., Aharony, A., Harris, A.B., Resistance fluctuations in randomly diluted networks, *Physical Review B* 35, 3524 (1987)

[142] Feng, S., Sen, P.N., Percolation on elastic networks: New exponent and threshold, *Physical Review Letters* 52, 216 (1984)

[143] Sykes, M.F., Essam, J.W., Some exact critical percolation probabilities for bond and site problems in two dimensions, *Physical Review Letters* 10, 3 (1963)

[144] Marshall, E.W., Harris, A.B., Scaling of splay and total rigidity for elastic percolation on the triangular lattice, *Physical Review B* 38, 4929 (1988)

[145] Sahimi, M., Goddard, J.D., Superelastic percolation networks and the viscosity of gels, *Physical Review B* 32, 1869 (1985)

[146] Rammal, R., Tannous, C., Breton, P., Tremblay, A.M.S., Flicker (1/f) noise in percolation networks: A new hierarchy of exponents, *Physical Review Letters* 54, 1718 (1985)

[147] de Arcangelis, L., Redner, S., Coniglio, A., Multiscaling approach in random resistor and random superconducting networks, *Physical Review B* 34, 4656 (1986)

[148] Kim, B.N., Hiraga, K., Morita, K., Chen, I.W., Rate of creep due to grain-boundary diffusion in polycrystalline solids with grain-size distribution, *Philosophical Magazine* 85, 2281 (2005)

[149] Day, A.R., Tremblay, R.R., Tremblay, A.M.S., Rigid backbone: A new geometry for percolation, *Physical Review Letters* 56, 2501 (1986)

[150] Moukarzel, C., Duxbury, P.M., Stressed backbone and elasticity of random central-force systems, *Physical Review Letters* 75, 4055 (1995)

[151] Moukarzel, C., Duxbury, P.M., Comparison of rigidity and connectivity percolation in two dimensions, *Physical Review E* 59, 2614 (1999)

[152] Needleman, A., Rice, J.R., Plastic creep flow effects in the diffusive cavitation of grain-boundaries, *Acta Metallurgica* 28, 1315 (1980)

[153] McLachlan, D.S., Heiss, W.D., Chiteme, C., Wu, J.J., Analytic scaling functions applicable to dispersion measurements in percolative metal-insulator systems, *Physical Review B* 58, 13558 (1998)

[154] Belova, I.V., Murch, G.E., The effective diffusivity in polycrystalline material in the presence of interphase boundaries, *Philosophical Magazine* 84, 17 (2004)

[155] Belova, I.V., Murch, G.E., Calculation of the effective conductivity and diffusivity in composite solid electrolytes, *Journal of Physics and Chemistry of Solids* 66, 722 (2005)

[156] Sheng, P., Kohn, R.V., Geometric effects in continuous-media percolation, *Physical Review B* 26, 1331 (1982)

[157] Nettelblad, B., Martensson, E., Onneby, C., Gafvert, U., Gustafsson, A., Two percolation thresholds due to geometrical effects: Experimental and simulated results, *Journal of Physics D* 36, 399 (2003)

[158] Malarz, K., Galam, S., Square-lattice site percolation at increasing ranges of neighbor bonds, *Physical Review E (Statistical, Nonlinear, and Soft Matter Physics)* 71, 016125 (2005)

[159] Reimann, S., Bendisch, J., On global site-percolation on the correlated honeycomb lattice, *Physica A* 296, 391 (2001)

[160] Nettelblad, B., Martensson, E., Onneby, C., Gafvert, U., Gustafsson, A., Two percolation thresholds due to geometrical effects: Experimental and simulated results, *Journal of Physics D: Appl. Phys.* 36, 399 (2003)

[161] Sheng, P., Kohn, R.V., Geometric effects in continuous-media percolation, *Physical Review B* 26, 1331 (1982)

[162] Pecullan, S., Gibiansky, L.V., Torquato, S., Scale effects on the elastic behavior of periodic andhierarchical two-dimensional composites, *Journal of the Mechanics and Physics of Solids* 47, 1509 (1999)

[163] Hazanov, S., Hill condition and overall properties of composites, *Archive of Applied Mechanics* 68, 385 (1998)

[164] Hashin, Z., Analysis of composite materials-a survey, *Journal of Applied Mechanics* 50, 481 (1983)

[165] Sahimi, M., Arbabi, S., Mechanics of disordered solids .3. Fracture properties, *Physical Review B* 47, 713 (1993)

[166] Hashin, Z., On elastic behaviour of fibre reinforced materials of arbitrary transverse phase geometry, *Journal of the Mechanics and Physics of Solids* 13, 119 (1965)

[167] Budiansky, B., On the elastic moduli of some heterogeneous materials, *Journal of the Mechanics and Physics of Solids* 13, 223 (1965)

[168] Eshelby, J.D., The determination of the elastic field of an ellipsoidal inclusion, and related problems, *Proceedings of the Royal Society of London A* 241, 376 (1957)

[169] Hill, R., Theory of mechanical properties of fibre-strengthened materials: I. Elastic behaviour, *Journal of the Mechanics and Physics of Solids* 12, 199 (1964)

[170] Hill, R., Elastic properties of reinforced solids: Some theoretical principles, *Journal of the Mechanics and Physics of Solids* 11, 357 (1963)

[171] Thorpe, M.F., Jasiuk, I., New results in the theory of elasticity for two-dimensional composites, *Proceedings: Mathematical and Physical Sciences* 438, 531 (1992)

[172] Coniglio, A., Stanley, H.E., Klein, W., Site-bond correlated-percolation problem: A statistical mechanical model of polymer gelation, *Physical Review Letters* 42, 518 (1979)

[173] Schuh, C.A., Minich, R.W., Kumar, M., Connectivity and percolation in simulated grain-boundary networks, *Philosophical Magazine* 83, 711 (2003)

[174] Schuh, C.A., Kumar, M., King, W.E., Analysis of grain boundary networks and their evolution during grain boundary engineering, *Acta Materialia* 51, 687 (2003)

[175] Randle, V., Crystallographically-necessary constraints at triple junctions in grain boundary engineered alloys, *Mat. Res. Soc. Symp. Proc.* 819, (2004)

[176] Miyazawa, K., Ito, K., Ishida, Y., Branching rule of coincidence boundaries in cubic polycrystals, in *Intergranular and interphase boundaries in materials, pt 1* (TRANSTEC PUBLICATIONS LTD, Zurich-Uetikon, 1996), p. 301

[177] Gertsman, V.Y., Zhilyaev, A.P., Pshenichnyuk, A.I., Valiev, R.Z., Modeling of grain-boundary misorientation spectrum in polycrystals with crystallographic texture, *Acta Metallurgica Et Materialia* 40, 1433 (1992)

[178] Zhilyaev, A.P., Gertsman, V.Y., Mishin, O.V., Pshenichnyuk, A.I., Aleksandrov, I.V., Valiev, R.Z., Grain-boundary misorientation spectra (gbms) determined by real odf in fcc-materials susceptible to annealing twinning, *Acta Metallurgica Et Materialia* 41, 2657 (1993)

[179] Frary, M., Schuh, C.A., Percolation and statistical properties of low- and high-angle interface networks in polycrystalline ensembles, *Physical Review B* 69, 134115 (2004)

[180] Bergman, D.J., Dunn, K.-J., Bulk effective dielectric constant of a composite with a periodic microgeometry, *Physical Review B* 45, 13262 (1992)

[181] Cohen, I., Bergman, D.J., Effective elastic properties of periodic composite medium, *Journal of the Mechanics and Physics of Solids* 51, 1433 (2003)

[182] Bonnet, G., Effective properties of elastic periodic composite media with fibers, *Journal of the Mechanics and Physics of Solids* 55, 881 (2007)

[183] Helsing, J., An integral equation method for elastostatics of periodic composites, *Journal of the Mechanics and Physics of Solids* 43, 815 (1995)

[184] Nemat-Nasser, S., Taya, M., On effective moduli of an elastic body containing periodically distributed voids, *Quarterly of Applied Mathematics* 39, 43 (1981)

[185] Nemat-Nasser, S., Iwakuma, T., Hejazi, M., On composites with periodic structure, *Mechanics of Materials* 1, 239 (1982)

[186] Nemat-Nasser, S., Yu, N., Hori, M., Solids with periodically distributed cracks, *International Journal of Solids and Structures* 30, 2071 (1993)

[187] Wang, G., Li, S., Nguyen, H.-N., Sitar, N., Effective elastic stiffness for periodic masonry structures via eigenstrain homogenization, *Journal of Materials in Civil Engineering* 19, 269 (2007)

[188] Luciano, R., Barbero, E.J., Formulas for the stiffness of composites with periodic microstructure, *International Journal of Solids and Structures* 31, 2933 (1994)

[189] Luciano, R., Barbero, E.J., Analytical expressions for the relaxation moduli of linear viscoelastic composites with periodic microstructure, *Journal of Applied Mechanics* 62, 786 (1995)

[190] Fotiu, P.A., Nemat-Nasser, S., Overall properties of elastic-viscoplastic periodic composites, *International Journal of Plasticity* 12, 163 (1996)

[191] Gu, G.Q., Tao, R.B., New method for evaluating the dc effective conductivities of composites with periodic structure, *Physical Review B* 37, 8612 (1988)

[192] Gu, G.Q., Calculation methods for effective constants of periodic composite media, *Journal of Physics D* 26, 1371 (1993)

[193] Wei, E.B., Poon, Y.M., Shin, F.G., Gu, G.Q., Effective properties of piezoelectric composites with periodic structure, *Physical Review B* 74, 014107 (2006)

[194] Wei, E.-B., Gu, G.Q., Yu, K.W., Transformation field method for calculating the effective properties of isotropic graded composites having arbitrary shapes, *Physical Review B* 76, 134206 (2007)

[195] Iwakuma, T., Nemat-Nasser, S., Composites with periodic microstructure, *Computers & Structures* 16, 13 (1983)

[196] McKenzie, D.R., McPhedran, R.C., Exact modeling of cubic lattice permittivity and conductivity, *Nature* 265, 128 (1977)

[197] McPhedran, R.C., McKenzie, D.R., Conductivity of lattices of spheres .1. Simple cubic lattice, *Proceedings of the Royal Society of London Series a-Mathematical Physical and Engineering Sciences* 359, 45 (1978)

[198] Gu, G.-Q., Tao, R., New method for evaluating the dc effective conductivities of composites with periodic structure, *Physical Review B* 37, 8612 (1988)